Axial stretching, viscosity, surface tension and turbulence in free surface vortices at low-head hydropower intakes

Frank Suerich-Gulick

Doctor of Philosophy

Department of Civil Engineering and Applied Mechanics
Faculty of Engineering
McGill University, Montreal

August 2013

A thesis submitted to McGill University in partial fulfillment
of the requirements of the degree of Doctor of Philosophy

"*Gardening. No hope for the future.*"

Franz Kafka diary entry

Abstract

Axial stretching, viscosity, surface tension and turbulence in free surface vortices at low-head hydropower intakes

Frank Suerich-Gulick

Free surface vortices at low-head hydropower intakes can harm plant performance or cause premature failure of mechanical components by inducing unsteady or non-uniform flow or by entraining air, ice or floating debris down towards the turbines. Laboratory-scale physical modelling to assess vortex activity in proposed intakes is effective and remains the standard practice in industry, but it is costly and uncertainty remains as to how viscosity, turbulence and surface tension influence the translation of observed vortex characteristics from the laboratory model to the full-scale intake. Computational fluid dynamics (CFD) has been proposed as a potentially cheaper alternative without scale effects, but it requires further validation.

This work sheds additional light on scale effects in laboratory-scale models and assesses the ability of a widely used commercial CFD package to predict vortex characteristics within the constraints of the hydraulic engineering context. A physical laboratory-scale model of a simplified intake is constructed with piers that produce vortices in their wake and that roughly resemble those that support trash racks at hydropower intakes. Instantaneous measurements of the three-dimensional velocity field inside the vortex are taken over a range of vortex intensities produced by eight operating conditions, with simultaneous recording of the free surface depression. The collected data are used to adapt Burgers's vortex model to link vortex characteristics (the characteristic radius, the bulk circulation, the depth and shape of the free surface depression, and the size of the largest floating particles entrained) to the operating conditions and intake geometry. The resulting model is then used to examine how viscosity, turbulence and surface tension influence vortex characteristics and their scaling behaviour. Finally, three operating conditions documented experimentally are numerically modelled using CFD with a simplified custom turbulence modelling strategy.

The experimental results indicate that the axial profile of axial velocity in the vortex core, in combination with effective radial diffusivity due to viscosity and/or turbulence, plays a key role in determining the vortex characteristic radius. The magnitude of surface tension effects is shown to be relatively easily predicted and possibly far less important than scale effects associated with viscosity and turbulence. The CFD results further support the conclusion that modelling turbulence in interaction with the vortices remains one of the principal hurdles to overcome in predicting vortex characteristics at intakes in an industrial context.

Abrégé

L'étirement axial, la viscosité, la tension superficielle et la turbulence dans les tourbillons à surface libre à l'entrée de centrales hydroélectriques à basse chute

Frank Suerich-Gulick

La présence de tourbillons à l'amont de prises d'eau de centrales hydroélectriques à basse chute peut nuire à la performance de la centrale ou causer le bris prématuré de composants mécaniques, en provoquant des conditions d'écoulement non uniformes ou en entraînant de l'air, de la glace ou des débris flottants vers les turbines. Les modèles physiques à échelle réduite sont efficaces pour évaluer la présence de tourbillons à l'amont de prises d'eau proposées et ce mode d'évaluation demeure la pratique courante en industrie. C'est par contre une technique coûteuse et des incertitudes demeurent quant à l'influence de la viscosité, la turbulence et la tension superficielle sur le transfert des caractéristiques de tourbillons observés en modèle de laboratoire vers l'échelle de la centrale à grandeur nature.

L'analyse numérique de dynamique des fluides (CFD) est souvent proposée comme alternative moins coûteuse et sans les effets d'échelle, mais le besoin d'une évaluation plus détaillée demeure. Le travail présenté ici apporte des nouvelles idées sur les effets d'échelle dans les modèles physiques à échelle réduite et évalue la capacité d'un logiciel commercial de CFD couramment utilisé pour prédire les caractéristiques de tourbillons dans les limites du contexte de génie hydraulique. Un modèle physique simplifié d'une prise d'eau à échelle réduite est construit avec des piliers provoquant un décollement qui génère des tourbillons. Ces piliers reproduisent approximativement ceux qui retiennent les grilles qui filtrent les gros débris dans les centrales hydroélectriques.

Des mesures tridimensionnelles du champ de vitesse instantané sont collectées à l'intérieur des tourbillons de diverses intensités produits par huit conditions d'exploitation étudiées, avec enregistrement simultané de la dépression de la surface libre produite par le tourbillon. Les données ainsi collectées sont utilisées pour adapter le modèle de vortex de Burgers afin de lier les

caractéristiques des tourbillons (le rayon caractéristique, la circulation totale, la profondeur et la forme de la dépression de la surface libre, et la dimension des plus grandes particules flottantes entraînées par le tourbillon) à la géométrie de la prise d'eau et aux conditions d'exploitation. Ce modèle adapté est ensuite utilisé pour examiner l'influence de la viscosité, de la turbulence et de la tension superficielle sur les caractéristiques des tourbillons et les lois de changement d'échelle. Enfin, trois conditions d'exploitation documentées expérimentalement sont simulées par CFD en utilisant une stratégie simplifiée de modélisation de turbulence adaptée pour cette étude.

Les résultats expérimentaux indiquent que le profil de vitesse axiale le long de l'axe du du tourbillon en son centre, en combinaison avec la diffusivité radiale réelle due à la viscosité et/ou à la turbulence, a une influence déterminante sur la dimension du rayon caractéristique du tourbillon. L'amplitude des effets de tension superficielle peut être prédite relativement facilement et serait possiblement beaucoup moins importante que l'amplitude des effets d'échelle liés à la viscosité et à la turbulence. Les résultats des simulations par CFD renforcent la conclusion que la modélisation de la turbulence en interaction avec les tourbillons demeure un des obstacles principaux à surmonter afin de pouvoir prédire les caractéristiques de tourbillons aux prises d'eau dans un contexte industriel.

Acknowledgements

This research project was initiated by Étienne Parkinson from Andritz Hydro and Marc Villeneuve, of Groupe-Conseil Lasalle, with the goal of beginning to bridge the gap that exists between the civil and mechanical engineers who work on the design and optimization of hydropower intakes. Etienne and Marc and their respective companies provided me with financial resources and as well as guidance in designing and running the experiments and simulations work so that it would provide results that were useful for engineers working in the hydropower industry. During my time at Andritz I got much support from Hélene Garcin in learning how to use the free surface components of CFX.

At Groupe-Conseil Lasalle, Pierre Tadeo gave me many useful suggestions in devising experimental methods, and Jacques helped me build the different devices. Jean-Philippe Saucier, Graham Holder, Tristan Aubeb and Wael Taha also gave me invaluable advice. David Morissette collaborated with me to devise the ADV measurement methodology and helped collect much of the ADV data. At IREQ, Maryse Page, Anne-Marie Giroux, Sébastien Houde and Martin Beaudouin were extremely helpful in setting me up to run simulations on the IREQ computer cluster and discussing numerical challenges with me. Phil Zwart and Andrew Krucker also provided useful comments and suggestions on running the the CFD simulations.

I'm especially grateful to Alison Carpenter for her support and guidance that helped me get through a very challenging time of my life and helped me to grow into a stronger, happier person. I thank Jesse Olszynko-Gryn, Andrea Miller-Nesbitt, Rachel Sandwell, Rachel Heap-Lalonde, Troy Davis, Ian Bradley-Perrin, Bill Hébert, Patricia Bailey, Vicki Marcok, Emmanuelle Champion, Hanna Caplan and Ariane Cavalli, Mandy Kemper for being great friends to me at different points over the years and for reminding me what is important. Each provided me with the support and perspective I needed to get through some tough times. I thank my parents, Hannelore Suerich and Sid Gulick for their love, encouragement and the deep respect for creativity, curiosity and quality which they instilled in me.

I thank the folks at PolitiQ, Radical Queer Semaine, and Pervers/cité, for helping me find a place for myself and the residents at Coteau Vert for giving me something to come home to!

I wish to thank Vicki Marcok and Sid Gulick for the tremendous last-minute proof-reading and I take full responsibility for any mistakes that remain.

Finally and most importantly, I wish to thank my supervisor Professor Susan Gaskin, who was both collaborator and guide through every stage of the research, from the experimental and numerical work to the analysis and the writing of the thesis and manuscripts. She was a full partner in the research and her contributions to it were crucial. I believe that I have become a better researcher and much clearer communicator through this work, and I owe much of what I have learned to the extensive and always incisive commentary and suggestions she offered me over the past 8 years. I am deeply grateful to her for her wisdom, her patience and her humanity. I would not have completed this thesis had it not been for her her support, kindness, and faith in my ability to see it through to the end. I have tremendous respect for her as a researcher and as a human being and I hope we will have the opportunity to collaborate again in the future!

Preface and Contribution of Authors

The four manuscripts presented as part of this thesis were written by myself, Frank Suerich-Gulick, with much guidance from my supervisor, Professor Susan Gaskin, and some feedback from the industrial partners who initiated the project, Dr. Étienne Parkinson from Andritz Hydro and Marc Villeneuve from Groupe-Conseil Lasalle. All the analytical and modelling work was done by myself, with comments and feedback from Professor Gaskin, Dr. Parkinson and M. Villeneuve.

Dr. Parkinson and Mr. Villeneuve both contributed insight and knowledge about the industrial context and constraints within which low-head hydropower intakes are designed, optimized and built. Dr. Parkinson and his team at Andritz Hydro shared their experience working with the CFX multiphase flow solver modelling the free surface jets in Pelton turbines and gave me suggestions as I tried to run free surface simulations of intake flow. Mr. Villeneuve played a significant role in designing the physical intake model, relying on his extensive experience designing and operating physical laboratory-scale models in a consulting context to assess and optimize hydropower intakes for vortex activity. The physical test bench was built by the team of carpenters at Groupe-Conseil Lasalle. Mr. Villeneuve also contributed significant input in determining the appropriate operating conditions to study, emphasizing the importance of examining a range of vortex intensities. Dr. Parkinson and Mr. Villeneuve provided feedback at several points during the research process, regularly posing questions as to how observations and theoretical conclusions could be applied and made relevant to practicing engineers working in the design and optimization of hydropower intakes.

The main contributions of this thesis can be summarized as follows:

1. Measurements of the flow velocity inside and outside the free surface vortices that form in a simplified hydropower intake model were taken for eight operating conditions with a range of vortex intensities. The resulting database of measured approach flow and vortex velocity fields constitutes a useful set of test cases for numerical modelers to test the ability of CFD codes to predict the characterics of free surface vortices at intakes. As far

as I know, this database is unique in providing both approach flow and three-dimensional vortex velocity data with simultaneous measurements of the axial and azimuthal velocity profiles in the vortex core as well as the free surface depression for a wide range of operating conditions and vortex intensities in a realistic intake geometry.

2. Burgers's 1948 relation for the vortex characteristic radius $r_o = 2(\nu/a)^{1/2}$ with $a = \partial V_z/\partial z$ was demonstrated to hold true for a vortex in turbulent flow using simultaneous measurements of the axial profile of axial velocity $V_z(z)$ and of the radial profile of azimuthal velocity $V_\theta(r)$ in the vortex. ν is the kinematic viscosity of the fluid. This extends Petitjeans's (2003) demonstration using measurements of a vortex in laminar flow in the wake of a step.

3. The vertical velocity profile of the flow directly in front of the intake was shown to drive axial stretching of the vortex (thereby influencing its characteristic radius) by comparing time-averaged vertical profiles of the velocity outside the vortex to the instantaneous axial profile of V_z inside the vortex. The axial velocity inside the vortex was observed to tend towards a more linear axial profile than that outside the vortex. This produces a higher V_z in the vortex core and a steeper axial gradient of V_z at the free surface; the intensified axial stretching in turn leads to a more concentrated vortex. These observations constitute a subtle difference compared to Odgaard's (1986) model, which assumed that the axial velocity in the vortex was linear all the way from the free surface to the intake opening; the predicted scaling behaviour differs qualitatively as a result.

4. The scaling behaviour of surface tension effects on the free surface profile was shown quantitatively to vary with both the scale and the shape of the free surface depression by performing a parametric calculation of the free surface profiles produced with and without surface tension over a wide range of vortex scales and profile shapes. This expands on the results of Stepanyants and Yeoh (2008a) who focused on dimple vortices, and of Yıldırım and Jain (1981) who examined surface tension effects on free surface profiles for three different circulation values Γ_∞.

5. The insights drawn from the analysis of the measured vortex characteristics were used to estimate how vortex characteristics might scale from the laboratory to prototype scale,

highlighting the necessity to examine the possible transition of viscous- to turbulence-dominated diffusion in the vortex core.

6. Insights into the processes governing vortex characteristics were drawn from both theoretical work on vortex dynamics and from other applications such as wing-tip vortices, and the results of the analysis were formulated in terms of observable vortex characteristics that are relevant and accessible to practicing engineers. In particular, the crucial process of turbulence suppression inside the vortices has been extensively discussed in the wing-tip literature but has not been explicitly addressed in the literature addressed to practicing hydraulic engineers who deal with intake vortices in their consulting or design work. The CFD simulation results and analysis presented here clearly demonstrate the need for turbulence suppression to be accounted for and verified in a turbulence modelling strategy for free surface intake vortices. The thesis also presents techniques engineers can use to evaluate and extract useful information from even rough or simplified simulations of intakes.

7. A series of simple numerical test cases was defined to test free surface modelling with the CFD software and to develop the most appropriate boundary conditions and numerical and startup strategies to run free surface simulations of vortices at hydropower intakes. These test cases were disseminated to CFX developers at ANSYS and researchers at Hydro-Québec's research who used them to test multiphase solvers in CFX and in other software packages.

Contents

List of Figures

List of Tables

Abbreviations

1D	one-dimensional
2D	two-dimensional
3D	three-dimensional
ADV	Acoustic Doppler Velocimetry
CFD	Computational Fluid Dynamics
LDA	Laser Doppler Anemometry
PIV	Particle Image Velocimetry
PTV	Particle Tracking Velocimetry
SNR	signal-to-noise ratio
tiff	Tagged Image File Format

Symbols

A	= scaling factor in s'_c dependence on Fr [-]
A_{cs}	= particle cross-sectional area [m^2]
a	= axial gradient of axial velocity [s^{-1}]
a_1	= $\partial V_z/\partial z$ obtained from fit to selected trajectories [s^{-1}]
a_2	= $\partial V_z/\partial z$ obtained from fit to all trajectories [s^{-1}]
b	= value of V_z at $z = 0$ in fitted $V_z(z)$ profile [ms^{-1}]
B	= exponent in s'_c dependence on Fr [-]
c_{1-6}	= non-dimensional model coefficients
d	= intake pipe inner diameter [m]
dr	= length of free surface profile segment [m]
dt	= local time-step for CFD simulation [s]
F_σ	= force exerted by surface tension [N]
F_b	= force exerted by buoyancy [N]
F_d	= drag force [N]
F_p	= force exerted by pressure differential [N]
Fr	= Froude number [-]
f_σ	= surface tension correction function [-]
g	= gravitational acceleration [ms^{-2}]
H	= nominal flow depth [m]
$h1$	= imposed water depth at domain inlet [m]
$h2$	= imposed water depth at domain outlet [m]
h_0	= tip depth of free surface depression [m]

h' = non-dimensional depression tip depth [-]

h_r = local derivative of h w.r.t. r [-]

h_{rr} = local second derivative of h w.r.t. r [m^{-1}]

K = viscous correction factor [-]

k = distance between the piers [m]

l_p = pier length [m]

ℓ_{part} = particle diameter [m]

l_σ = air-water interface characteristic length [m]

ℓ = intake characteristic length [m]

m = iteration number [-]

N_ν = non-dimensional vicosity parameter [-]

$N_{\Gamma *}$ = non-dimensional circulation [-]

p_{hydr} = hydrostatic pressure [Pa]

p_{out} = pressure imposed at pipe exit [Pa]

$p_{\mathrm{out,0}}$ = initial pressure imposed at pipe exit [Pa]

$p_{\mathrm{out,F}}$ = final pressure imposed at pipe exit [Pa]

Q = intake flow rate [$\mathrm{m}^3\mathrm{s}^{-1}$]

R^2 = coefficient of determination of a curve fit []

R_1 = first radius of curvature of the free surface profile [m]

R_2 = second radius of curvature of the free surface profile [m]

Re = Reynolds number [-]

r = vortex radial coordinate [m]

r_o = vortex characteristic radius [m]

SE_a = standard error on the slope a [s^{-1}]

s = intake submergence [m]

s'_{c} = non-dimensional critical submergence [-]

t_0 = initial time [-]

t_{final} = final time [-]

$\mathbf{U}$ = velocity vector in the channel [ms^{-1}]

U_i = mean intake velocity [ms^{-1}]

U_m = mean channel velocity [ms^{-1}]

$\mathbf{V}$ = velocity vector inside the vortex [ms^{-1}]

$\forall$ = particle volume [m^2]

$V_{z,\text{avg},j}$ = V_z values averaged over trajectory segments [ms^{-1}]

$V_{z,\text{all}}$ = raw V_z values obtained from PTV x [ms^{-1}]

We = intake Weber number

w.v.f. = water volume fraction

X = global longitudinal coordinate [m]

Y = global span-wise coordinate across the channel[m]

y = horizontal coordinate on PTV image [m]

Z = global vertical coordinate [m]

z = vortex axial coordinate [m]

α = model-to-prototype scaling factor [-]

α_R = relaxation factor in free surface computation [-]

β = ratio of distance from free surface to intake [-]

χ = eddy diffusivity scaling coefficient [-]

δ = relative surface tension effect [-]

$\triangle h$ = tip depth difference due to surface tension [m]

$\triangle p_{\text{loss}}$ = head loss in pipe [Pa]

$\triangle \rho$ = increment in r_o value [m]

$\triangle t_{meas}$ = time-span of measurement [s]

$\triangle t$ = length of time-step [s]

$\triangle X$ = ADV measurement line offset [m]

$\triangle Z$ = vertical distance between ADV measurements [m]

Γ_∞ = vortex bulk circulation [m^{2}s^{-1}]

η = total distance from top of intake pipe [m]

κ = local mean free surface curvature [m^{-1}]

ν = water molecular viscosity [m^{2}s^{-1}]

ν_{eff} = effective viscosity [m^{2}s^{-1}]

ν_T = eddy diffusivity [$m^2 s^{-1}$]

ν_i = imposed eddy viscosity distribution [$m^2 s^{-1}$]

π = trigonometric constant

θ = vortex azimuthal coordinate [rad]

ρ = water density [kg m^{-3}]

ρ_i = particle density [kg m^{-3}]

ρ_w = water density [kg m^{-3}]

σ = surface tension coefficient [N/m]

τ = particle trajectory period [s]

ω = vorticity vector [s^{-1}]

ζ = nominal depression slope [-]

Subscripts

0 = value at ($r = 0$) or at time t=0

comp = computed value

ch value based on mean channel velocity

d = value based on intake diameter

est = estimated value

exp = measured value

fit = fitted value

j = particle number

m = mean value

m = value at the *m*-th iteration

max = maximum value

min = minimum value

M = laboratory model value

n = without surface tension effect

P = prototype value

s = value based on intake submergence

σ = with surface tension effect

To the Montréal queers who helped me learn to be myself.

Chapter 1

Introduction

The catalyst for this project was a desire to bridge the gap that exists between the civil and mechanical engineers who design and optimize hydropower plants. Traditionally, civil enginneers optimize the intake structure, while mechanical engineers design and optimize the turbines; there is little communication between the two during the design and optmimzation processes with members of each discipline working in isolation from each other in different companies. The approach flow conditions produced by the intake structure can have a significant impact on turbine performance, so greater collaboration should lead to improved design and performance and might help avoid unpleasant surprises.

One of the obstacles to increased collaboration between the two disciplines is the use of different terminology and numerical tools to analyse and describe the flow in their respective sub-domains. Civil engineers focus mainly on open channel flow and must evaluate flow conditions that are often influenced by the shape of river reaches that are often several kilometers in length. In comparison, the domains examined by the turbine engineers are much smaller in size and they concern pressure flow, without a free surface, in most cases. At the time this project was intiated in 2004, three-dimensional (3D) CFD was an established and essential tool in turbine optimization, whereas its use in civil engineering assessments was in its infancy, partly due to the challenges of modelling low-Froude number open channel flow over large domains. Simulations of flow upstream from intake structures tended to be limited to quasi-3D simulations where

the vertical transfer of momentum is neglected. Recent years have seen greater use of CFD to model flow at hydropower intakes, but physical scale modelling still remains the standard tool for assessing and optimizing hydropower intakes when resources permit it.

Intake optimization is particularly important and challenging for run-of-river hydropower plants, which have seen increased development in recent years because they cause less massive disturbance to the environment than projects with large reservoirs. Figure 1.1 shows plan and section views of sample run-of-river plants. The absence of large impoundment reservoirs in run-of-river plants increases the likelihood of flow asymmetries at the entrance to the power plant, and absent or limited flow-aligning devices make these asymmetries more likely to reach and affect the turbines. Run-of-river plants are often smaller in scale and in budget than impoundment projects, so budgets for optimization studies are often more limited in just those cases where they are most needed and may have the greatest impact on performance.

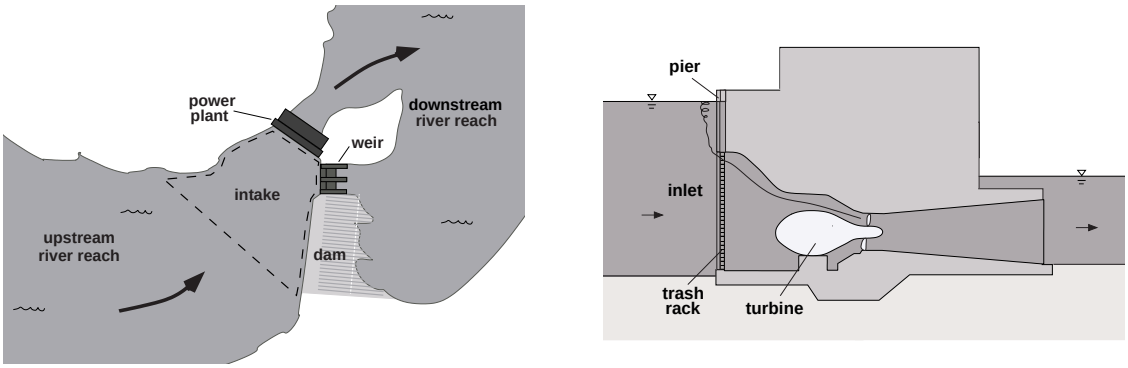

FIGURE 1.1: Plan (left) and section (right) views of sample run-of-river hydropower plants.

Free surface vortices are more likely to occur at the intake of run-of-river plants because of low submergence and approach flow asymmetries. Vortices are of concern because they can entrain air or floating debris or ice down to the turbines or generate flow asymmetry or unsteadiness, all of which can harm plant performance or cause premature failure of mechanical components. Free surface vortices at hydropower and pump intakes have been studied extensively since the 1950s, but this complex phenomenon is still not fully understood. The intake Froude number and submergence (distance from the free surface to the intake opening) were established early on to be key parameters determining vortex activity, but the exact relation was

found to depend on both the geometry and approach flow conditions for a given intake. General consensus therefore remains that physical scale modelling of proposed intakes is required to assess and optimize the intake. Uncertainty about scale effects in translating results from laboratory-scale models to the full prototype scale has led to extensive experimental work with models constructed at different scales and with fluids of different viscosities and surface tension coefficients. Measurements of velocity profiles and of the free surface deformation produced by the vortices were used to develop analytical models that describe the vortex structure to better understand how geometry, approach flow and scale influence vortex characteristics.

This work addresses two recurring questions for hydraulic engineers who assess and optimize low-head hydropower intakes – one long-standing and one relatively new:

1. How do scale effects influence the translation of vortex activity observed in physical laboratory-scale models to the full prototype scale?
2. How well can CFD predict free surface vortex activity at low-head hydropower intakes in a typical industrial hydraulic consulting context? Can CFD be a viable alternative or complement to physical scale modelling?

In order to examine these questions, detailed velocity and free surface profile measurements made in a physical model of a simplified intake are used to acquire greater insight into the processes that link intake geometry to vortex characteristics. An existing simple analytical vortex model (Burgers, 1948) is adapted to include the influence of geometry and approach flow, and the adapted model is then used to estimate how vortex characteristics observed in a laboratory-scale model might appear in the prototype-scale version of the same intake. The predictive ability of a commercial CFD package is evaluated by modelling the flow in the intake at three operating conditions documented in the experiment, comparing the simulated vortex characteristics with the measured ones. Techniques are suggested by which expected vortex characteristics can be approximately predicted from CFD results that capture the intake flow structure but that cannot predict the vortex characteristics due to poor grid resolution or turbulence modelling.

This thesis is organized in a manuscript format divided into seven sections. It begins with a review of relevant existing work, including a survey of experimental work, analytical vortex

models, and numerical modelling work. The physical model and the methodology used to collect and analyse the experimental data are presented, as well as the axisymmetric one-dimensional (1D) numerical model used to compute the free surface profile.

Chapter 4 (Manuscript 1) describes the measurements and the adapted vortex model. Among other things, it examines how the intake velocity field surrounding the vortex drives axial stretching of the vortex and how the profile of the axial velocity along the vortex axis inside the vortex shifts from the non-linear shape of the external flow to a more linear one.

Chapter 5 (Manuscript 2) uses the observations and vortex model developed in the first manuscript to examine how scale effects influence vortex characteristics in laboratory-scale physical models and to estimate how viscosity and turbulence might influence these characteristics at the prototype scale. Limitations of the resulting predictions are discussed, including possible transition from viscosity- to turbulence-dominated radial diffusion of vorticity in the vortex. Scaling trends predicted using a one-dimensional axisymmetric numerical model of the free surface profile indicate that the effect of surface tension varies with both the scale and shape of the free surface depression, and that these effects are likely to be significantly smaller than scale effects due to viscosity.

Chapter 6 (Manuscript 3) interprets the results and conclusions of the first two manuscripts in terms that are more relevant and accessible to consulting engineers working in an industrial context, with a short discussion of the particle entrainment characteristics of the vortices.

Chapter 7 (Manuscript 4) presents and evaluates the results of the CFD simulations. The challenges are discussed associated with capturing the free surface deformation and modelling the interaction of turbulence with the vortices within the constraints of an industrial context, and strategies that were developed to address them are presented. The results obtained using the standard k-ε turbulence model compared to those obtained with an imposed eddy viscosity field demonstrate the key role played by diffusion in determining the vortex structure and characteristics.

Chapter 8 concludes the thesis and suggests avenues for future work. The experimental results, codes used to track particles and compute the free surface profile, and an extract of the script use to set up the CFD simulations, are included in the appendices.

Chapter 2

Literature Review

2.1 The Civil engineering problem

2.1.1 Introduction and motivation

There is growing interest in smaller-scale low-head hydropower development because its environmental impact is judged to be lesser or more acceptable than that of larger-scale projects with reservoirs that impound large volumes of water (Bhat and Prakash, 2008). Though definitions vary by jurisdiction, hydropower plants with a power production capacity of less than 50 MW are often considered "small", while those with a capacity greater than 100 MW are considered "large". Similarly, plants with a head of 1 to 5 m are considered "low-head" is many jurisdictions in Canada, while in British-Columbia, where large the terrain is mountainous, plants with heads up to 15 m are considered "low-head" (Hatch Engineering, 2008). The head is defined as the difference the level of the water directly upstream and downstream from the power plant. By definition, run-of-river plants do not impound any water, so the flow rate upstream and downstream from the plant are always roughly equal. In the absence of a reservoir, they tend to have a low head. and be more sensitive to upstream flow conditions. The low head makes them more likely to encounter problems with free surface vortices forming directly above the intake leading to the turbines (Fisher and Franke, 1987). The intake structure guides the water as it accelerates

through the transition from the open channel (free surface) flow approaching the plant to the faster (confined) pressure flow in the submerged pipe or penstock that leads to the turbines. Intakes to hydropower plants and pumping stations share many common physical traits and both experience difficulties with free surface vortices. This work focuses on hydropower intakes, but it draws on much past research on vortices that form at pump intakes (for example Denny, 1995;Markland and Pope, 1965; Schäfer and Hellman,2005). The term 'intake vortices' is used hereafter to refer to vortices that form at either hydropower or pump intakes.

It is widely recognized that free surface vortices should be avoided when possible at hydropower intakes because they can have significant negative impacts on plant performance and longevity (Denny, 1956; Fisher and Franke, 1987; Johnson, 1988). The vortices can cause head losses, reduce the flow rate (Pavelyev and Shtarev, 2005), reduce the performance of turbines (Fisher and Franke, 1987) or pumps (Schäfer and Hellman, 2005) through nonuniform flow conditions or entrained air (Papillon and Sabourin, 2000), they can provoke audible vibrations leading to premature failure of mechanical components (Jiming *et al.*, 2000), or entrain floating debris (Fisher and Franke, 1987) or ice down from the free surface that then accumulates on the trash racks at the intake entrance, producing significant head losses (Jiming *et al.*, 2000) or non-uniform flow that degrades performance or causes premature mechanical failure such as turbine blade cracking (Fisher and Franke, 1987). In cold climates the entrainment of frazil ice from near the free surface is a particular concern, since it agglomerates and sticks to surfaces such as trash racks (Carriveau *et al.*, 2002).

The vortices are much smaller in scale than the intake (the vortex characteristic radius can easily be 2 orders of magnitude smaller than the diameter of the intake opening), and they are usually transient in location and intensity, which makes them quite difficult to measure and characterize in quantitative terms. It is therefore common to classify them by qualitative vortex 'type', based on the shape of the free surface depression they produce, their ability to entrain floating particles or air bubbles, and how dye injected into the vortex is diffused. (Denny, 1956; Padmanabhan and Hecker, 1984; Eguchi *et al.*, 1994; Schäfer and Hellman, 2005; Mercier *et al.*, 2008). The classification most commonly employed is attributed to George Hecker (Padmanabhan and Hecker, 1984) from the Alden Research Laboratory; it is also referred to as the ARL

classification (Hite, 1991; Schäfer and Hellman, 2005; Möller *et al.*, 2012a). At the 'weak' end of vortex types, the 'dye core' vortex produces a mild or negligible free surface depression but dye injected into the vortex at the free surface forms a clearly visible dye core, while dye injected outside the vortex is diffused by background turbulence. The 'strongest' most intense vortex type produces a funnel-shaped free surface depression that reaches all the way down to the intake pipe opening. Intermediate vortex types are classified by their ability to entrain debris or air bubbles down from the free surface and/or the generation of a funnel-shaped depression that does not necessarily reach all the way down to the intake.

Entrainment of air by the vortices is of particular concern in both hydropower and pumping stations (Möller *et al.*, 2012a) since even a small amount of air (1.5% air-water ratio by volume) in the flow can reduce turbine efficiency by 15% (Papillon and Sabourin, 2000) and/or cause harmful vibrations. Gas entrainment by vortices in nuclear reactor vessels has severe security risks, so the conditions for gas entrainment have been studied extensively in that context as well (Eguchi *et al.*, 1994; Ezure *et al.*, 2008; Kimura *et al.*, 2008; Ito *et al.*, 2010b,a).

Many experimental studies document vortex activity for a given configuration in terms of a critical submergence $(s/d)_c$ for each studied flow rate Q, where s is the submergence (distance from the free surface to the intake), and d is the intake pipe diameter. The critical submergence is defined as the submergence where either vortices judged to be 'problematic' occur, vortex intensity passes from one type to another (for example, dimple to funnel-shaped depression (Anwar *et al.*, 1978; Anwar and Amphlett, 1980; Anwar, 1983)), bubble entrainment begins to occur (Denny, 1956; Markland and Pope, 2003; Eguchi *et al.*, 1994; Kimura *et al.*, 2008), or when the air core reaches the intake (Daggett and Keulegan, 1974; Jain *et al.*, 1978; Anwar, 1983; Odgaard, 1986; Gulliver, 1988; Hite and Mih, 1994; Yıldırım *et al.*, 2012).

There is general consensus that the most significant non-dimensional parameter determining $(s/d)_c$ is the Froude number, defined as $\mathrm{Fr}_s = U_i/(gd)^{1/2}$ or $\mathrm{Fr}_s = U_i/(gs)^{1/2}$, where g is the gravitational acceleration, U_i is the mean velocity in the intake pipe, s is the submergence, and d is the intake pipe diameter (Quick, 1962b; Toyokura and Akaike, 1970; Jain *et al.*, 1978; Blaisdell, 1982; Anwar, 1983; Chang and Prosser, 1987; Schäfer and Hellman, 2005). The slope and shape of the curve relating $(s/d)_c$ to Fr varies with the intake configuration and geometry

(Knauss, 1987; Kocabaş and Yıldırım, 2002) and imposed circulation (Jain *et al.*, 1978; Kocabaş and Yıldırım, 2002). Many expressions for $(s/d)_c$ take the form $(s/d)_c \sim \mathrm{BFr}^A$. 'B' may incorporate the influence of factors such as viscosity or turbulence (Jain *et al.*, 1978) or circulation (Jain *et al.*, 1978; Rao *et al.*, 1997). 'A' can vary from 1/2 (Jain *et al.*, 1978; Gulliver *et al.*, 1986), to 2/3 (Gulliver, 1988; Rao *et al.*, 1997) or 1 (Reddy and Pickford, 1972). Alternately, $(s/d)_c$ may scale with Fr^A at small Fr values and flatten out at greater Fr values (Jiming *et al.*, 2000). Hebaus (1979) and Amphlett (1979) derived a similar trend from the relations developed by Jain *et al.* (1978) using experimental data. Similarly, Markland and Pope (2003) observed a linear increase of $(s/d)_c$ with inlet velocity U_i at low U_i values that flattened out at higher values.

Circulation is imposed using guide vanes in many studies of vortex flow in both cylinder and approach channel intake studies (Toyokura and Akaike, 1970; Daggett and Keulegan, 1974; Jain *et al.*, 1978), because it is found to be necessary to produce a stable vortex (Anwar *et al.*, 1978; Anwar and Amphlett, 1980; Kocabaş and Yıldırım, 2002). The initiation of vortices in the absence of a clear source of circulation is more challenging to predict and has not been studied extensively. Exceptions include (Levi, 1972; Yıldırım and Kocabaş, 1998; Marghzar *et al.*, 1956; Carriveau, 2004, 2006; Carriveau *et al.*, 2009).

Empirical correlations for $(s/d)_c$ as a function of Fr such as those developed by Gordon (1970) continue to be used today to try to predict the critical submergence during the early stages of the design process (Groupe Conseil Lasalle, 2007; Jiming *et al.*, 2000; Tastan and Yıldırım, 2010). However their predictive accuracy is limited by the fact that vortex activity is dependent on the intake geometry (Markland and Pope, 2003; Pennino and Hecker, 1979; Jiming *et al.*, 2000; G. Montilla and Castro, 2004; Yıldırım *et al.*, 2012) as well as the approach velocity distribution (Ansar and Nakato, 2001). For example, the piers that hold the trash racks in place across the intake opening tend to produce vortices in their wake if the flow does not approach them head-on, which decreases the critical submergence compared to a similar intake without piers (Pennino and Hecker, 1979; Gulliver *et al.*, 1986; Jiming *et al.*, 2000; G. Montilla and Castro, 2004). This effect was examined by Hite (1991) and Hite and Mih (1994). In the case of flow in a cylinder, Pavelyev and Shtarev (2005) showed that a small deviation from axisymmetry causes the critical submergence for air core vortex formation to increase. Physical

testing using laboratory-scale models therefore remains a key component in the assessment and optimization process for most large projects (Jiming *et al.*, 2000; Schäfer and Hellman, 2005; Walder and Rutschmann, 2007; Mercier *et al.*, 2008; Nakayama and Hisasue, 2010; Wang *et al.*, 2011) and it is recommended (Quick, 1962b; Hecker, 1981; Blaisdell, 1982; Chang and Prosser, 1987) and common practice to build these physical laboratory-scale models at Froude similitude, such that $\mathrm{Fr_M} = \mathrm{Fr_P}$ (Padmanabhan and Hecker, 1984; Schäfer and Hellman, 2005; Villeneuve *et al.*, 2005). If problematic vortices are observed, the physical model is used to test different devices such as ribs or curtain walls or screens to prevent vortex formation (Sweeney *et al.*, 1982; Gulliver *et al.*, 1986; Schäfer and Hellman, 2005).

The influence of factors such as the molecular viscosity, turbulence, and surface tension do not scale in the same manner as the Froude number, so their influence on the translation of results from laboratory-scale models to the full-scale 'prototype' intake remains a topic of debate despite more than 30 years' research (Heller, 2011). Since water is commonly used in both the laboratory model and prototype, it is not possible to match the Reynolds number ($\mathrm{Re_s} = U_i s/\nu$ or $\mathrm{Re_s} = U_i d/\nu$ or $\mathrm{Re_{ch}} = Q/(s\nu)$) and Weber number ($\mathrm{We} = \rho U_i^2 s/\sigma$) in the lab model to that in the prototype, where ρ, ν and σ are the water density, kinematic viscosity, and the air-water surface tension coefficients, respectively (Schäfer and Hellman, 2005; Wang *et al.*, 2010). Though some authors initially suggested running laboratory models at a discharge greater than that corresponding to Froude similitude (Denny, 1956), this approach has not been taken up as it has been shown to produce excessively strong vortices in the model compared to those occuring in the prototype (G. Montilla and Castro, 2004). Denny (1956) suggested that though Froude similitude may be appropriate for predicting dimple-shaped vortices, the process of bubble detachment from the tip of funnel-shaped vortices might be determined by the local velocity and thus not scale with Froude number over the range of sizes investigated.

Much research has been devoted to determining how Re and We influence the critical condition in reduced-scale models. Most authors agree that the influence of Re decreases asymptotically (Hecker, 1987; Tastan and Yıldırım, 2010) with increasing Re, while some argue that the influence of Re becomes negligible beyond a threshold Re value (Wang *et al.*, 2011) whose proposed value ranges from 4×10^4 to 1.4×10^5 (Anwar, 1983), depending on the geometry,

Froude number, and Re definition. Beyond the uncertainty associated with the actual threshold number, the minimum geometric size required for the physical model to meet these threshold values is sometimes difficult or impossible to meet within economic or spatial constraints for some large projects such as hydropower intakes.

Several authors have examined how vortex activitiy is affected by different geometric configurations (Denny, 1956; Quick, 1962b; Anwar, 1968a; Gulliver *et al.*, 1986; Quick, 1970; Rutschmann *et al.*, 1987; Hite, 1991; Hite and Mih, 1994; Nakayama and Jones, 1998), or different approach flow profiles (de Siervi *et al.*, 1982; Ansar and Nakato, 2001), while others have developed submergence critera using potential flow models that incorporate geometric parameters such as the intake pipe diameter (Yıldırım and Kocabaş, 1998) and shape (Yıldırım, 2004; Yıldırım *et al.*, 2012), wall clearance (Yıldırım *et al.*, 2000; Yıldırım and Kocabaş, 2000; Yıldırım, 2004; Tastan and Yıldırım, 2010; Goel, 2012) and bed permeability (Kocabaş and Ünal, 2010), as well as different flow configurations such as uniform cross-flow (Yıldırım and Kocabaş, 1995), still water in a reservoir (Yıldırım and Kocabaş, 1998), multiple intake pipes (Yıldırım *et al.*, 2011, 2012), or different degrees of approach flow circulation imposed using guide vanes (Kocabaş and Yıldırım, 2002). Recently, several authors have tested statistical methods (Kocabaş *et al.*, 2012) and machine learning techniques such as artificial neural networks (Kocabaş and Ünal, 2010; Kocabaş *et al.*, 2012; Goel, 2012) to predict critical submergence, or nearest-neighbour methods to generate probability maps for risk assessment (Travis and Mays, 2011). These methods use new and existing experimental datasets (Reddy and Pickford, 1972; Rindels and Gulliver, 1983; Ahmad *et al.*, 2008) to train and test the models. Some authors have suggested that CFD might be useful for predicting the larger flow patterns produced by a proposed intake geometry, which could then be used in combination with an analytical vortex model to estimate the vortex characteristics. Ito *et al.* (2010a) estimate the onset of bubble entrainment from a combination of the axial velocity gradient at the free surface and the circulation. Montazerin *et al.* (2001) suggests that the critical submergence could be predicted from the pressure distribution in a fixed lid simulation.

The influence of the Coriolis effect on axially stretched vortices was examined by Shapiro (1962), Binnie (1964) and Trefethen *et al.* (1965) at different latitudes in the Northern (Shapiro,

1962; Binnie, 1964) and Southern hemispheres (Trefethen *et al.*, 1965). When still water was emptied out of a 1.5 m or 1.8 m diameter cylindrical tank through a bottom orifice at a sufficiently low submergence, a counter-clockwise rotating vortex was observed to form most of the time in the Northern hemisphere and a clockwise vortex formed in the southern hemisphere. The authors in all three experiments note that very slight perturbations such as residual velocity from filling or very mild ambient air currents or temperature gradients in the water due to lamps or sunlight perturb this trend. These results indicate that even at the prototype scale, the influence of the Coriolis force on intake vortices is negligible compared to that of approach flow asymmetry and geometry.

2.1.2 Surface tension

Surface tension can significantly reduce the depth of the free surface depression in the lab setting, and Weber number We is often used as a way to estimate whether or not surface tension effects will be significant for a given set of flow conditions. Several authors have studied how We influences the critical condition, hoping to identify a minimum We above which surface tension effects can be neglected (Daggett and Keulegan, 1974; Jain *et al.*, 1978; Anwar and Amphlett, 1980; Anwar, 1983), but the observed trends and conclusions vary signigicantly from author to author. Comparison of results is complicated by the different definitions used: $\mathrm{We}_s = \rho U_i^2 s/\sigma$, and $\mathrm{We}_d = \rho U_i^2 d/\sigma$. Daggett and Keulegan (1974) and Jain *et al.* (1978) report no significant influence of surface tension on air entrainment in their respective tests in cylindrical tanks using fluids of varying surface tension coefficients. The lowest Weber number in Jain *et al.*'s experiment is $\mathrm{We}_d > 120$, while the We range is not documented in Daggett and Keulegan (1974). Similarly, Padmanabhan and Hecker (1984) find no difference in vortex types observed in different pump intake model scales operating at $\mathrm{We}_d > 600$ that would indicate surface tension effects. Möller *et al.* (2012b) observed no influence of surface tension on either the onset of air entrainment or the rate of air entrainment in their experiment operated at $748 < \mathrm{We}_d < 6.2 \times 10^4$. On the other hand, Anwar *et al.* (1978) and Anwar (1983) studying the evolution of vortex intensity at horizontal and vertical intakes in a channel found that surface tension affects results for We_s up to 1.5×10^4 for dimple depressions and up to 4×10^4 for air core vortices. Tastan

and Yıldırım (2010) conclude from their experimental data that the limiting values for We for air entrainment depend on the flow and geometrical conditions and therefore no fixed value can be identified. Odgaard (1986) concludes from a rough theoretical order-of-magnitude analysis that the effect of surface tension on the critical condition for air entrainment should be negligible for $\mathrm{We}_d > 720$.

Other authors have examined how the radial profile of the free surface depression is modified by surface tension by solving the coupled differential equations describing an axisymmetric vortex using the finite-difference method (Andersen *et al.*, 2003, 2006; Yıldırım and Jain, 1981), an approximate series solution (Stepanyants and Yeoh, 2008a), or quadratic approximations of the free surface near the vortex tip (Ito *et al.*, 2010b). Yıldırım and Jain (1981) find that the relative effect of surface tension on tip depth is much more significant for a weak vortex with small circulation than for a strong vortex with larger circulation.

2.1.3 Viscous effects and turbulence

Most authors observe that the critical condition for air entrainment (Daggett and Keulegan, 1974; Jain *et al.*, 1978; Anwar, 1983; Chang and Prosser, 1987) or the discharge coefficient (Zielinksi and Villemonte, 1968) serving as a proxy for vortex activity (Anwar, 1965; Anwar *et al.*, 1978) is less and less sensitive to Re as it increases. This trend leads them to conclude that viscous effects in a reduced-scale model can be neglected if Re for the scale model is greater than a certain cutoff value, ranging from 4×10^4 to 1.4×10^5, depending on the geometry and/or the Froude number, using various definitions of Re (Daggett and Keulegan, 1974; Jain *et al.*, 1978; Anwar, 1983; Padmanabhan and Hecker, 1984; Chang and Prosser, 1987; Tastan and Yıldırım, 2010). Although the data seem fairly convincing that Re's influence asymptotically decreases at higher values, it has not been clearly demonstrated why this occurs. In order to try to understand the observed trends and the processes that determine them, a number of vortex models have been developed of varying complexity. These are discussed in the following section.

2.2 Analytical and semi-analytical vortex models

In order to better understand the processes that govern vortex characteristics it is necessary to examine the flow structure within the vortex and how it is influenced by the surrounding flow. Some key general vortex models are presented here, followed by an overview of relevant models that have been adapted to describe vortices at intakes or in similar configurations. The velocity field in the vortex is described using a local cylindrical coordinate system (r, θ, z) with z pointing along the central axis of the vortex, and with corresponding radial, azimuthal and axial velocities V_r, V_θ and V_z. In the case of free surface vortices, z will be defined pointing down from the free surface.

A vortex can be thought of as a local concentration of vorticity within which streamlines follow a circular, helical, or spiral pattern. Vorticity, a vector quantity defined as $\boldsymbol{\omega}$, locally quantifies the rate of rotation of a fluid particle about its centre of mass. It is defined mathematically as the curl of the velocity vector: $\boldsymbol{\omega} = \boldsymbol{\nabla} \times \boldsymbol{V}$ (Helmholtz, 1867). In physical terms it describes the rotation of a local fluid particle about its center of mass. In viscous fluids, vorticity concentrated in the vortex core gets smeared outward by diffusion, producing a smooth radial profile that resembles a bell curve. Helmholtz formulated several key theorems about vortices and vorticity. He described vorticity using the concept of vortex filaments or tubes, which are bundles of vortex filaments. He postulated that if viscous losses are negligible, then the vortex's angular momentum is conserved and vorticity in the vortex increases in proportion to the axial gradient of the axial velocity component (Helmholtz, 1867). Thomson (1869) reiterated some of these concepts in different forms, and defined the quantity Γ_∞, which he called the circulation. Given that the vorticity is concentrated in the core of the vortex ($r < r_o$), Γ_∞ can be estimated by integrating V_θ along the full circumference of a circle of radius $r \gg r_o$: $\Gamma_\infty = \Gamma(r \gg r_o) = \int_0^{2\pi} V_\theta r d\theta$ (Thomson, 1869).

Rankine (1876) modelled a vortex as a constant-vorticity inner 'forced vortex' region surrounded by a null-vorticity 'free vortex' region of zero vorticity. In most real flows, viscosity smears vorticity radially outwards producing a Gaussian-like profile (Rott, 1958; Rouse, 1963; Saffman, 1992).

Burgers (1948) and Rott (1958) independently developed a vortex model that incorporates both the spreading effect of viscosity and the concentrating effect of axial stretching of the vortex. If the axial velocity V_z in a vortex increases along its axis, the vortex is said to be axially stretched, and its streamlines converge towards the axis ($V_r < 0$). Burgers (1948) and Rott (1958) assume that the radial profiles of V_θ and V_r are constant along z and that the axial velocity V_z is independent of r and increases linearly with z: $V_z(z) = az$, $V_r(r) = -ar/2$, where the gradient a is a constant with units of s^{-1} and the profile of V_r is set to satisfy continuity. Solving the axisymmetric Navier-Stokes equations with these assumptions produces

$$V_\theta(r) = \frac{\Gamma_\infty}{2\pi r}\left[1 - \exp\left(-(r/r_o)^2\right)\right], \tag{2.1}$$

where Γ_∞ is the bulk circulation, assumed to reach a constant value far from the vortex centre. What we will call the characteristic radius r_o is determined by the ratio of viscosity to axial gradient:

$$r_o = 2(\nu/a)^{1/2}, \quad a = \partial V_z/\partial z, \tag{2.2}$$

where ν is the kinematic viscosity of the fluid, $V_z(z) = az$ and $V_r(r) = -ar/2$ to satisfy continuity. The gradient a is a constant with units of s^{-1}. Petitjeans (2003) verified Eqn. 2.2 experimentally in a stretched vortex in the wake of a step, emphasizing the importance of axial stretching in determining the characteristic radius r_o.

Rankine and Burgers's vortex models are starting points for many subsequent vortex models relevant to intake vortices that have been developed using observations and measurements from a wide range of flow configurations including airplane wing-tip vortices (Batchelor, 1964; Moore and Saffman, 1973; Birch *et al.*, 2004; Beninati and Marshall, 2005a; Duraisamy and Iaccarino, 2005), swirling flow in pipes (Muntean *et al.*, 2005b; Petit *et al.*, 2010) swirling flow in a fixed cylinder with a bottom orifice (Anwar, 1965, 1968b; Quick, 1962a; Daggett and Keulegan, 1974; Mory and Yurchenko, 1993; Echavez and McCann, 2002; Andersen, 2002; Kocabaş and Yıldırım, 2002; Pavelyev and Shtarev, 2005; Andersen *et al.*, 2006; Sakai *et al.*, 2008; Bøhling *et al.*, 2010; Ito *et al.*, 2010b), flow in a single rotating cylinder (Huang *et al.*, 2008), flow in cyclones used for separating particles (Vatistas, 1989; Montavon *et al.*, 2000; Bunyawanichakul

et al., 2006; Haque *et al.*, 2006), free surface vortices in nuclear reactor vessels (Ito *et al.*, 2010a), at pump intakes (Rajendran *et al.*, 1999; Rajendran and Patel, 2000; Ansar and Nakato, 2001; Montazerin *et al.*, 2001; Li *et al.*, 2004; Tokyay and Constantinescu, 2006; Chuang and Hsiao, 2011; Tang *et al.*, 2011; Möller *et al.*, 2012b; Zhan *et al.*, 2012), in generic horizontal intakes (Montazerin *et al.*, 2001), hydropower intakes (G. Montilla and Castro, 2004; Li *et al.*, 2008; Nakayama and Hisasue, 2007, 2010), and in specific laboratory configurations aimed at gaining insight into individual vortices in turbulent flow (Petitjeans *et al.*, 1998; Rossi *et al.*, 2004; Beninati and Marshall, 2005a).

The velocity field and flow structure is documented experimentally in water using injected dye (for example Anwar (1983); Hecker (1987); Vatistas (1989); Echavez and McCann (2002); Andersen (2002); Kocabaş and Yıldırım (2002); Schäfer and Hellman (2005); Walder and Rutschmann (2007); Huang *et al.* (2008); Nahas *et al.* (2010)), propeller meters (Quick, 1962a), particle tracking velocimetry (PTV) using particles floating on the free surface (Toyokura and Akaike, 1970; Kiviniemi and Makusa, 2009; Wang *et al.*, 2011), or within the water volume (Anwar, 1968b; Quick, 1962a; de Siervi *et al.*, 1982; Andersen, 2002; Andersen *et al.*, 2006; Huang *et al.*, 2008), particle image velocimetry (PIV) (Rajendran *et al.*, 1999; Rajendran and Patel, 2000; Li *et al.*, 2004; Rossi *et al.*, 2004; Ezure *et al.*, 2008; Huang *et al.*, 2008; Nahas *et al.*, 2010; Nakayama and Hisasue, 2010), acoustic Doppler velocimetry (ADV) (Ansar and Nakato, 2001), and laser Doppler anemometry (LDA) (Hite, 1991; Mory and Yurchenko, 1993; Marghzar *et al.*, 1956). and pressure probes (Birch *et al.*, 2004; Schäfer and Hellman, 2005), or hot-wire anemometry (Beninati and Marshall, 2005a) in air. The profile of the free surface depression produced by free surface vortices is usually recorded directly using video cameras (Andersen *et al.*, 2006; Nakayama and Hisasue, 2010). Earlier studies recorded the depression profile point by point using a surface probe (Julien, 1986), and some authors used the shadow cast by the depression through refraction on the channel bed to extract vortex strength (Berge, 1966; Anwar *et al.*, 1978; Anwar, 1983). Techniques have also been developed to extract the free surface depression from the deformed reflection of patterns projected onto the free surface (Zhang and Su, 2002).

These different studies provide useful insights into the different processes affecting the

vortex characteristics, but variations in flow rate, boundary conditions and geometry complicate the task of identifying the relevant modeling assumptions and processes, while separating out the effect of phenomena that are specific to a given configuration that do not play a role in most intake vortices. One example is the Ekman layer that forms along the flat bed of a cylinder with rotating flow exiting through a bottom orifice (Quick, 1962a; Andersen *et al.*, 2003, 2006; Echavez and McCann, 2002; Huang *et al.*, 2008). Most early detailed velocity studies pertinent to intake vortices were performed on axisymmetric flow in an upright cylinder, which is an easily scaled geometry that produces much more stable vortices than asymmetric geometries (Anwar, 1965, 1969; Daggett and Keulegan, 1974; Mory and Yurchenko, 1993). The Ekman layer is produced by the interaction of the swirling flow with the boundary layer of the radially converging flow along the base of the cylinder. It generates thin concentric layers of alternating upward and downward velocities in the immediate vicinity of the central vortex (Echavez and McCann, 2002). Though data from this configuration can provide insight into the relationship between the azimuthal velocity profile and the free surface depression (for example Andersen *et al.* (2006); Stepanyants and Yeoh (2008a)) or turbulence (Anwar, 1969) for example, caution is required in interpreting the other aspects of the flow, such as the axial velocity profiles.

Several authors since then have emphasized the key role played by axial vortex stretching in concentrating vorticity into coherent vortices at hydropower and pump intakes (Quick, 1970; Carriveau *et al.*, 2009), at airplane engine intakes (Nakayama and Jones, 1998; de Siervi *et al.*, 1982), behind airplane wing-tips (Moore and Saffman, 1973) and in less specific, more generally-applicable laboratory experiments (Petitjeans *et al.*, 1998; Petitjeans, 2003; Rossi *et al.*, 2004).

Odgaard (1986) shows that Burgers's simple model applied to intake vortices can explain how the submergence s of the outlet controls the key process of axial vortex stretching He examines the vortex that forms in a cylindrical tank with imposed circulation and constant outflow through a bottom orifice. He assumes that the axial velocity in the central portion of the tank follows a linear profile from zero at the free surface to U_i at the bottom of the tank, so that $a = U_i/H$, where H is the water depth and U_i is the mean outflow velocity. Odgaard's and subsequent results (Hite and Mih, 1994; Ito *et al.*, 2010b) support the use of Burgers's model for

modelling intake vortices, even if it does not capture their full complexity.

Einstein and Li (1951) propose a relatively simple model in which a Burgers vortex is concentrated in the vortex region, surrounded by an external zone with no axial velocity. This model is adjusted by Bøhling *et al.* (2010) to obtain smooth azimuthal and radial velocity profiles and a continuous axial velocity profile. Numerical and analytical variants of Burgers's model have been proposed, for example by Lewellen (1962), Toyokura and Akaike (1970), Lundgren (1985), Hite and Mih (1994), Miles (1998), Vatistas and Li (1988), Rossi *et al.* (2004), Anh and Hosoda (2005), Stepanyants and Yeoh (2008b), Ito *et al.* (2010b), and Wang *et al.* (2011). Andersen *et al.* (2003, 2006) extends Lundgren's (1985) model to include surface tension. Miles (1998) computes the free surface depression from a Burgers vortex in the case of a mild depression, while Anh and Hosoda (2005) compute the free surface profile for a full air core vortex.

2.3 Turbulence and vortex instability

The interaction of the intake vortices with the turbulent flow that surrounds them has important repercussions for vortex characteristics and their scaling behaviour. Turbulent mixing inside the vortex could enhance radial diffusion of momentum and vorticity (Rouse, 1963), which could produce vortices that are more spread out (with a larger characteristic radius r_o) and thus produce a milder free surface depression for a given bulk circulation Γ_∞. Higher turbulence intensity in the surrounding flow may also prevent vortices from forming or intensifying in certain situations (Padmanabhan and Hecker, 1984; Tastan and Yıldırım, 2010), disrupting otherwise smooth scaling trends of increasing vortex intensity at increasing flow rates. There are also situations where vortex breakdown may be provoked by inherent instability of the vortex or by boundary conditions that are independent of turbulence. These processes are particularly difficult to examine experimentally in intake vortices since they require even higher time and length resolution measurements than mean vortex characteristics such as the $V_\theta(r)$ and $V_z(z)$ profiles.

Much of the relevant research on vortex-turbulence interactions is motivated by interest in the life-span and persistence of wing-tip vortices that trail behind airplanes, which pose a serious hazard to airplanes that follow too closely in their wake (Beninati and Marshall, 2005a,b;

Saffman, 1992). These vortices often include a Gaussian vorticity distribution and an axial flow jet in the core, and include possible interactions between the pair of counter-rotating vortices (Crow, 1970; Jacquin *et al.*, 2005) as in the intake configuration studied in this project, but they are not subjected to axial stretching, which can play a crucial role in stability (Nolan, 2001; Carriveau, 2006; Carriveau *et al.*, 2009). Axial stretching is significant in hurricanes and tornadoes (Levi, 1972; Klimenko, 2007), but thermal effects are significant, and the boundary conditions, driving forces and the scales are different from intake vortices, so once again there is uncertainty as to how directly conclusions from this application regarding vortex-turbulence interactions can be applied to intake vortices.

What follows is an overview of selected work on vortex-turbulence interactions: it does not constitute an exhaustive study of the relevant work on the topic. First, the suppression of turbulence inside the vortex and its effect on radial diffusion in the vortex is discussed, followed by a review of different types of stability analyses that have been performed on different types of vortices subjected to external perturbations or strain fields, with some results that might shed light on observed intake vortex behaviour.

The significant suppression of radial turbulent fluctuations in intake vortices manifests itself most obviously by the formation of a coherent and continuous core of dye along the vortex axis when dye is injected into the core (Anwar, 1983; Berge, 1966; Hecker, 1987; Echavez and McCann, 2002; Carriveau *et al.*, 2009; Rajendran and Patel, 2000; Schäfer and Hellman, 2005; Walder and Rutschmann, 2007), while dye injected outside the core is quickly mixed and diluted by turbulent flow there (Anwar, 1969). The suppression of radial turbulent fluctuations in the vortex core has been studied extensively (White, 1964; Bradshaw, 1973; Beninati and Marshall, 2005a), particularly in trailing wing-tip vortices in turbulent air flow (for example Adams and Gilmore 1972, Spalart 1998 and Jacquin and Pantano 2002). Zeman (1995) and Cotel and Breidenthal (1999) concluded from experimental data that the spreading rate of the vortices in turbulent flow is governed by viscous diffusion, not turbulent diffusion. This characteristic in intake vortices is commonly used by researchers and consulting engineers to detect the presence, persistence and trajectory of the vortices in physical intake models (for example Anwar (1983); Hecker (1987); Schäfer and Hellman (2005); Walder and Rutschmann (2007)). and is used to

categorize the vortex type. Usually, the 'dye core vortex' (Padmanabhan and Hecker, 1984) is the weakest observable vortex type, considered worth examining more closely even if it does not entrain debris or air. Though the clearly defined dye core indicates that the radial component of turbulent mixing is suppressed to a significant degree inside the vortex core, it is possible that enough radial turbulent fluctuations persist to increase the effective diffusivity determining the vortex's characteristic radius. Vladimirov *et al.* (1980) also note that though dye diffusion is a good indicator of turbulence suppression, the mass diffusivity of a turbulent flow is not necessarily equal to its diffusivity of momentum. In certain situations, the flow conditions may be such that the characteristics of turbulent vortices become independent of viscosity effects (Hoffman and Joubert, 1963).

Einstein and Li (1951) suggested using eddy viscosity ν_T to account for the enhanced momentum mixing due to turbulent fluctuations in intake vortices and Anwar (1969) tested different possible distributions of ν_T using measured velocity profiles of a vortex surrounded by turbulent flow in a cylinder, concluding that ν_T could not be constant across the vortex. Following the approach used by Squire (1965) to model the axial growth of a turbulent trailing wing tip vortex, Odgaard (1986) replaced the molecular viscosity ν in the expression for r_o in Burgers's vortex model (Eqn. 2.2) by a effective viscosity $\nu_{\text{eff}} = \nu + \nu_T$, with a constant ν_T accross the vortex equal to $\nu_T = \chi\Gamma_\infty$. Hite and Mih (1994) also use a constant $\nu_{\text{eff}} = \nu + \nu_T$ accross the vortex, except they use $\nu_T = Q/(4\pi d) = 3.5 \times 10^{-3}\text{m}^2\text{s}^{-1}$. Given the measured circulation $\Gamma_\infty = 0.086\text{m}^2\text{s}^{-1}$ in their experiment, this value for ν_T would be equivalent to a much larger value for χ equal to 0.04 in Odgaard's relation for ν_T. Odgaard hypothesized that as turbulence and ν_T in the vortex core grow with increasing intake size (since Γ_∞ increases with increasing intake scale), ν_T would eventually dominate compared to the molecular viscosity ν, effectively rendering the vortex characteristics independent of ν and of Re_s, thus explaining the scaling behaviour observed by many researchers. Using $\nu_{\text{eff}}/\nu > 5$ as a cutoff, Odgaard's model predicts that scale effects associated with molecular viscosity should become negligible for $\text{Re}_s > 1.4 \times 10^5$.

2.3.1 Stability

Linear stability theory is a common mode of analysis to evaluate whether perturbations of turbulent or other origin should persist, grow or decay within a vortex. The steady-state flow solution is subjected to small fluctuations which must also be solutions to the equations of motion. The fluctuations are framed in a normal-mode representation, and the magnitude and sign of the growth rate of the modes of the resulting linear stability equations are examined. In linear analysis, it is assumed that the quadratic fluctuation terms are negligible, which may in some cases predict stability where nonlinear analysis would predict instability (Ash and Khorrami, 1995).

Thomson (1880) used linear stability analysis to show that an inviscid, rigidly rotating columnar vortex without axial flow should be stable to axisymmetric perturbations. Strutt (1917) examined the slightly more general case of inviscid rotating flow without axial flow ($V_z = V_r = 0$) subjected to axisymmetric disturbances and found that a sufficient condition for stability is that the absolute value of the local circulation $rV_\theta(r)$ must increase monotically with r everywhere.

Ash and Khorrami (1995) emphasize that the vortex stability characteristics depend on the vortex velocity field as well as the boundary conditions and the proximity or absence of nearby boundaries, so stability analysis must be performed on a case-by-case basis. They summarize linear stability analyses (where second- and higher-order terms are assumed to be negligible) performed by different authors on inviscid vortices with axial flow, as well as viscous vortices with axial flow. These analyses examine the stability of a Batchelor vortex (Batchelor, 1964), which has a Gaussian axial velocity excess or jet in the vortex centre and gradually spreads radially outward along z since there is no axial stretching. The inviscid results indicate that stability of the Batchelor vortex depends on the the ratio of the local radial gradient of $\Gamma^2(r)$ to the square of the local radial gradient of $V_z(r)$. Ash and Khorrami (1995) assert that instabilities in most rotating flows are inviscid in nature and viscosity was historically assumed to be stabilizing. However they cite some simulation results for trailing vortices that predict viscosity-driven instabilities.

Vortex breakdown can be considered as the result of vortex instability such as those described above, but it can also be provoked by external boundary conditions (Benjamin, 1962)

such as an adverse pressure gradient (Ash and Khorrami, 1995). It remains difficult to determine the conditions under which external turbulence will destabilize or cause vortices to break down (Cotel and Breidenthal, 1999; Beninati and Marshall, 2005b; Jacquin *et al.*, 2005) and studies of different configurations generate conclusions that appear contradictory at times. Cotel and Breidenthal's (1999) work suggests that in the absence of axial flow a vortex is more prone to breaking down under the influence of external turbulence if the Reynolds number of the vortex defined as Γ_∞/ν is high, and that a smaller core radius stabilizes the vortex. On the other hand, Jacquin and Pantano (2002) predict that a vortex with a Gaussian distribution of axial velocity is more resistant to perturbations if the ratio $V_{\theta,\max}/\triangle V_z$ is greater than 1.2, where $\triangle V_z$ is the difference between the peak axial velocity inside the vortex and the axial velocity outside the vortex.

2.4 Computational fluid dynamics

Growing accessiblity and computational power has led to a large volume of research on using Computational Fluid Dynamics (CFD) to model vortices in industrially relevent flows. The main challenges encountered in modelling free surface vortices at hydropower intakes using CFD are associated with computing the level and deformation of the free surface interface and modelling the effect of turbulence interacting with the vortices.

Relevant work that addresses these challenges in combination or individually has been performed with a variety of applications in mind. These include airplane wing-tip vortices (Duraisamy and Iaccarino, 2005) and hydrocyclones (Bunyawanichakul *et al.*, 2006; Haque *et al.*, 2006), as well as vortices in pump intakes (Montazerin *et al.*, 2001; Ansar *et al.*, 2002; Tokyay and Constantinescu, 2006; Chuang and Hsiao, 2011; Tang *et al.*, 2011; Zhan *et al.*, 2012), nuclear reactor vessels (Ito *et al.*, 2010a), hydropower tailrace channels (Cheng *et al.*, 2007), and hydropower intakes (Teklemariam *et al.*, 2002; Yoo *et al.*, 2002; Li *et al.*, 2008; Haque *et al.*, 2006; Nakayama and Hisasue, 2007, 2010; Hisasue and Nakayama, 2011). Some studies examine vortices in simplified geometries such as cylinders with a bottom orifice (Sakai *et al.*, 2008; Bøhling *et al.*, 2010), swirling flow in pipes (Muntean *et al.*, 2005b; Skerlavaj *et al.*, 2010), or

axially stretched flow in the wake of a step (Rossi *et al.*, 2004) designed to help elucidate vortex phenomena in a more general sense. Many CFD simulations of hydropower intakes are aimed at assessing velocity or temperature distributions to facilitate the passage of fish (Haque *et al.*, 2007; Khan *et al.*, 2008).

The wide range of geometric and time scales encountered in the flow also pose a numerical challenge, which is addressed by using special grid-generation strategies or by choosing to model some of the smaller-scale phenomena using an analytical or empirical model (Ito *et al.*, 2010a) instead of resolving them in full detail in the CFD simulation.

2.4.1 Free surface modelling

Different strategies are employed to capture the free surface interface. Many authors bypass the associated challenges and computational expense by modelling the free surface as a fixed, free-slip surface, often referred to as a fixed lid boundary condition (Rajendran *et al.*, 1999; Montazerin *et al.*, 2001; Ansar *et al.*, 2002; Marghzar *et al.*, 1956; Li *et al.*, 2004; Tokyay and Constantinescu, 2005b,a, 2006; Haque *et al.*, 2007; Khan *et al.*, 2008; Li *et al.*, 2008; Sakai *et al.*, 2008; Škerlavaj *et al.*, 2011; Tang *et al.*, 2011). There are several methods for capturing the free surface deformations, but the volume-of-fluid (VOF) method is one most commonly used in the work relevant to this study (Haque *et al.*, 2006; Cheng *et al.*, 2007; Ito *et al.*, 2010a; Chuang and Hsiao, 2011; Zhan *et al.*, 2012). The VOF method models the flow as two-phase flow (air and water in this case), with a more-or-less distinct interface separating the two. The water volume fraction w.v.f., a scalar quantity defined over $0 =< \text{w.v.f.} =< 1$, is initially set to 1.0 in the water phase and 0.0 in the air phase; It is then advected with the flow as the solution evolves, and the interface between the two phases is estimated to be located roughly along the contour of w.v.f. $= 0.5$. (Hirt and Nichols, 1981; Zwart *et al.*, 2007) Nakayama *et al.* (2006) use a height function $H((X,Y)$ that explicitly defines the free surface level for every horizontal coordinate (X,Y) in the domain. In this model, H may only have one value for a given horizontal coordinate (X,Y), so certain phenomena such as the entrainment of air bubbles cannot be modelled (Nakayama *et al.*, 2006). Nakayama and Hisasue (2010) discuss the start-up strategy and boundary conditions required to start the flow solution gradually so as to avoid

generating waves that travel back and forth along the length of the channel. Gridless CFD methods such as smoothed particle hydrodynamics (SPH) lend themselves well to modelling free surface flow, though testing for open channel flow remains limited so far. In SPH, the flow is divided into discrete particles that move through the domain and the flow properties at a given point are obtained by averaging the properties of the neighbouring particles (Monaghan, 2005).

2.4.2 Turbulence modelling

Turbulence is characterized by flow structures and velocity fluctuations with a wide range of length and time scales. The length scale can vary from the characteristic length of the domain down to the so-called Kolmogorov scales, which can be several orders of magnitude smaller than those of the domain and mean flow (Tennekes and Lumley, 1972; Hunt and Morrison, 2000). Due to its chaotic nature, turbulent flow is commonly described using statistical tools (Hunt and Morrison, 2000; Pope, 2000). Turbulence models employ different approaches to 'model' the effect of turbulence on the mean flow as an alternative to simulating the full range of turbulent fluctuations, which is too computationally expensive for the majority of industrial flows (Reynolds, 1976; Rodi, 1993; Ferziger and Peric, 1999). The most significant effect of the velocity fluctuations on the mean flow is to significantly enhance the mixing of mass and momentum, which appears in the Reynolds-Averaged Navier-Stokes (RANS) equations as a 3x3 tensor referred to as the Reynolds stresses, commonly designated using $\overline{u_i' u_j'}$, where u_i' and u_j' are the fluctuating velocity components and the overbar indicates averaging over time. RANS turbulence models employ different strategies to estimate the Reynolds stresses in the RANS equations.

Eddy viscosity models model the effect of turbulence by replacing ν in the Navier-Stokes equations by $\nu_{\text{eff}} = \nu + \nu_{\text{T}}$ where ν_{T} is the eddy viscosity ν_{T} introduced earlier. Many models designated as two-equation eddy-viscosity models have been developed to compute the ν_{T} distribution by solving 2 differential equations in addition to the RANS equations (Menter, 1994). k-ε (Launder and Spalding, 1974), one of the earliest and most widely used, solves a transport for k, the turbulent kinetic energy, and another for ε, the dissipation rate of turbulent kinetic energy; ν_{T} is then computed from k. The $k-\omega$ model solves the transport of ω, the dissipation

rate of kinetic energy k per unit k, instead of ε (Wilcox, 2006). Eddy viscosity models and in particular the k-ε model, were the default until recently in industrial applications and are still frequently used since they are easy to employ and relatively inexpensive in computational terms (Gatski and Rumsey, 2002).

One weakness of eddy-viscosity models is that they assume turbulence is isotropic, which can lead to overestimated diffusion in certain flows. Various corrections and variants to k-ε have been adapted for specific flows to try to correct for this. For example, the strong velocity gradients in rotating flows lead to excessive generation of turbulent kinetic energy without the accompanying turbulence suppression due to streamline curvature (Gatski and Speziale, 1993; Duraisamy and Iaccarino, 2005; Muntean *et al.*, 2005a). Different approaches have been attemped to account for the effect of streamline curvature on the 'effective viscosity' (Pope, 1975), and curvature correction has been implemented in several eddy-viscosity models (Duraisamy and Iaccarino, 2005) to try to account for the suppression of turbulence in rotating flows; these perform with mixed success for helical vortex flow (Montavon *et al.*, 2000; Duraisamy and Iaccarino, 2005; Škerlavaj *et al.*, 2011).

Explicit algebraic stress models incorporate anisotropy of the Reynolds stresses using an algebraic relation (Gatski and Speziale, 1993), while Reynolds stress models (RSM) solve a transport equation for each of the components of the Reynolds stresses, which requires the solution of seven transport equations for the turbulence quantities in their most general form (Hanjalic and Launder, 1976; Durbin, 1993; Warsi, 2006); this is much more complex and computationally expensive. For highly-swirling flow, RSM models seemed to perform better in some cases, with azimuthal velocity profiles that resemble experimental data more closely (Haque *et al.*, 2006; Palau *et al.*, 2007; Montavon *et al.*, 2000), while more accurate results were obtained in other cases with the k-ε model (Bunyawanichakul *et al.*, 2006). In other cases the results are unclear as to which performs better (Muntean *et al.*, 2005b; Škerlavaj *et al.*, 2011).

The large eddy simulation (LES) approach employs an unsteady approach to resolve the larger turbulent eddies present in the flow and spatially filters out the eddies whose size is smaller than a specified geometric and time-scale cutoff (Meneveau and Katz, 2000; Pope, 2004). The effect of the smaller eddies is modelled using an eddy-viscosity approximation. Comparisons

of LES simulations with either RSM (Montavon *et al.*, 2000) or unsteady eddy viscosity model simulations (Tokyay and Constantinescu, 2005b) showed that the LES model captured vortex characteristics more accurately, though at considerable additional expense. Generally, LES seems to capture the vortex characteristics more consistently than any other turbulence modelling approach (Chuang and Hsiao, 2011; Tokyay and Constantinescu, 2006; Nakayama and Hisasue, 2010; Škerlavaj *et al.*, 2011). Muntean *et al.* (2005b) found that laminar simulations of swirling flow in a pipe captured the vortex characteristics just as well as LES at a fraction of the computational cost. Some authors avoid the computational cost and uncertainty associated with turbulence modelling by modelling the flow as inviscid (Ansar *et al.*, 2002; Muntean *et al.*, 2005b) or laminar (Sakai *et al.*, 2008; Ito *et al.*, 2010a) even if the flow outside the vortices is known to be turbulent. But it would appear that LES is necessary in situations where vortices are highly unsteady or interactions with background turbulence are significant.

The interaction of the free surface with turbulence presents additional numerical challenges. Nakayama *et al.* (2006) began by testing their code by comparing a free surface simulation with LES turbulence modelling of turbulent open channel flow to experimental data.

Direct numerical simulation (DNS) of turbulent flows do not constitute examples of turbulence 'modelling', because they simulate the full range of turbulent fluctuations, and hence no modelling of the effect of turbulence on the mean flow is required. DNS remains far too computationally expensive to apply to most industrially-relevant flows but results from DNS simulations provide insight for understanding different aspects of of turbulent flow such as flow separation and reattachment, (Moin and Mahesh, 1998), vortex stability (Jacquin and Pantano, 2002), turbulence in vortices (Duraisamy and Lele, 2006) and the interaction of vortices with external turbulence (Melander and Hussain, 1993; Beninati and Marshall, 2005b).

Chapter 3

Methodology

This chapter describes the methods used to collect and analyse flow data in the physical scale model, as well as the procedure used to perform the simulations. Mean velocity profiles in the upstream portions of the channel are collected using an Acoustic Doppler Velocimeter (ADV), and approximately instantaneous profiles of $V_\theta(r)$ and $V_z(z)$ inside the vortices are measured using Particle Tracking Velocimetry (PTV). A one-dimensional finite-difference code that includes surface tension is written to compute the radial profile of the free surface depression that should be produced by the measured $V_\theta(r)$ profile, to be compared to the the actual profile recorded in the same images as those used for the PTV measurements. The last section describes the procedure developed to run the free surface simulations of the intake flow, including a custom turbulence modelling strategy with an static eddy-viscosity distribution imposed using an analytical function of the geometric location in the domain.

3.1 Test bench

A simplified model of a hydropower intake with piers was constructed with recirculating water from a large underground storage tank that is shared with other test benches in the laboratory. Fig. 3.1 shows section (*a*) and isometric (*b*) views of the full channel and intake.

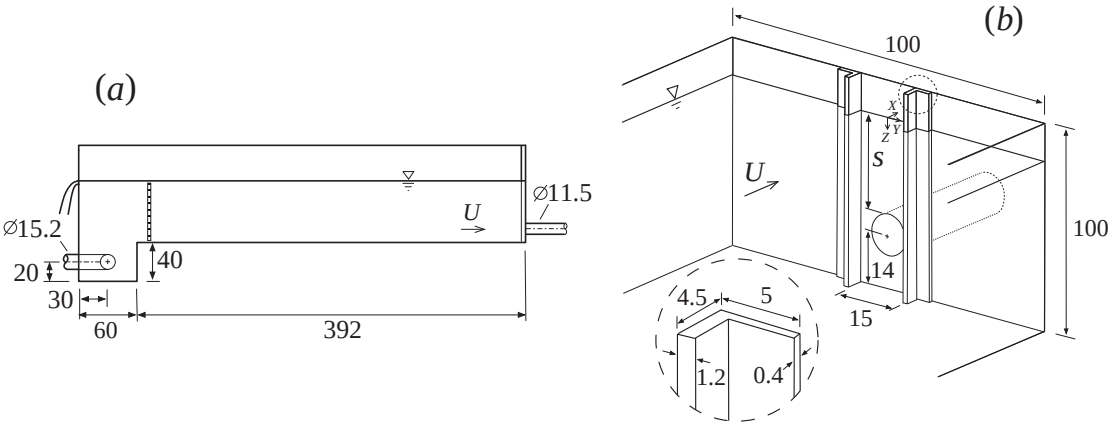

FIGURE 3.1: Vertical section (*a*) and isometric (*b*) views of the laboratory model (dimensions in cm).

The channel has a square 1 by 1 m square cross-section and a 3.9 m long flat bed with tolerances of roughly $\pm$ 3 mm. The first portion of the channel (2.9 m long) is constructed from painted wood. The last meter, including the bed, is contructed out of plexiglass to facilitate measurement and observation of the vortices. Flow enters the depressed reservoir upstream from the channel through a "T"-shaped diffuser with 34 evenly spaced 16 mm diameter holes across the bottom of the span-wise portion of the "T", which is 0.7 m in total length. The diffuser is manufactured by joining two pieces of PVC pipe a 152 mm (6") nominal diameter. The distance from the upstream wall of the reservoir where the diffuser enters to the axis of the cross-piece is 0.3 m (Fig. 3.1*a*). Large eddies produced as the flow exits the diffuser are broken down with a 19 mm (3/4") thick sheet of aluminum honeycomb placed across the full channel just downstream of the upward step from the reservoir to the channel.

At the downstream end, the flow exits the channel through a cylindrical perspex pipe mounted flush with the downstream wall of the channel. The pipe has an inner diameter $d = 115.2 \pm 0.05$ mm, and its axis is located on the channel centerline, 140 ± 2 mm above the bed.

In order to produce vortices that are more stable in time and space (as discussed later in this paragraph), two rectangular cross-section piers are mounted symmetrically about the intake pipe, spaced 150 ± 1 mm apart. The piers have a rectangular cross-section, 12 ± 0.5 mm thick and protruding 45 ± 0.5 mm into the flow; they span the full channel depth (Fig. 3.1(*b*). Each pier produces a pair of relatively stable vortices in its wake, one vortex connected at one end to

the free surface, and one vortex connected at one end to the channel bed, as shown in Fig. 3.2. The other end of both vortices is entrained into the intake pipe. The piers roughly reproduce the piers that hold trash racks across the opening of hydropower intakes, which are often the site of the most problematic vortices in run-of-river laboratory models. The vortices that form in the wake of the pier are much more stable vortices than vortices produced by many other mechanisms, and they also tend to be geometrically confined to the space delimited by the pier and downstream wall. The geometric stability significantly eases measurement with the camera used for the PTV measurements, which has a very shallow depth of field (roughly 20 mm) at the high aperture required to achieve sufficient exposure. The free surface vortices that form in the absence of the piers are extremely transient and move around an area more than 0.3 m across, as noted by other authors in flows without significant generation of localized circulation (Anwar *et al.*, 1978; Hite, 1991). The piers employed here have a rectangular cross-section without the rounded tip commonly employed at intakes so as to remove uncertainty at the simulation stage as to the location on the pier tip where the boundary layer separates. The exact location where the boundary layer separates off streamlined bodies is very sensitive to accurate resolution of the boundary layer, whereas a sharp corner provokes separation at a predictable location (Binnie, 1964; Hite, 1991). Using the less realistic square-tipped piers was judged to be an acceptable price to pay for the benefit of eliminating uncertainty regarding separation, given the many challenges anticipated in simulating the vortex flow.

Only the free surface vortices are studied here because they are more likely than the submerged ones to cause operating problems in the hydropower intake by entraining air or floating debris. The submerged vortices are also minimized or absent in most hydropower intakes, where the inlet opening is roughly aligned with the bottom of the channel. Measurements are taken in the free surface vortex generated by the right-hand pier (as seen looking downstream) because of geometrical symmetry, though temporal asymmetry arises due to the interaction of the two vortices (Crow, 1970).

The water level is stabilized with the help of a 16 mm (5/8 inch) thick square-crested weir cut into the upstream wall of the channel, over which flows a roughly 7 mm deep sheet of water. The water supply into the channel is driven by pumping water up to a small reservoir located

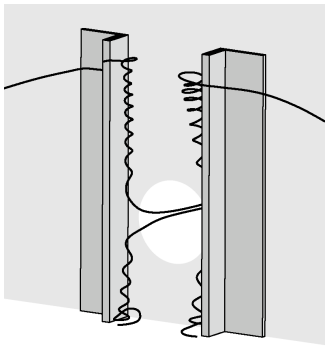

FIGURE 3.2: Flow structure. Free surface and submerged vortices in the wake of the piers.

roughly 4 m above the channel, out of which the water flows at a steady rate over a weir. The flow rate into and out of the channel is controlled using manually adjustable butterfly valves.

To start up the flow in the channel, the outflow valve was first closed while the inflow pump was started for several minutes to begin filling the channel. Then the outflow valve was gradually opened and set to roughly the desired opening. The inflow and outflow rates were then iteratively adjusted until the desired water level and flow rate were achieved, after which a delay of a minimum of 30 to 40 minutes was allowed before flow measurements were taken to ensure that the levels were stable.

The flow rates into and out of the channel are monitored using orifice plates of inner diameter 83 mm and 108 mm, respectively. The tolerance on the outlet flow rate is $\pm$ 0.2 l/s. The variablitity on the inlet flow rate is greater due to variations in the pump rate and depth of the water in the reservoir. The flow over the weir helps to stabilize the level and flow rate through the channel. The industrial context in which the test bench was constructed influenced the tolerances of the geometry and flow rate, which are slightly greater than they might be in a research laboratory setting. The water level at the downstream wall of the channel is measured using a millimeter-graduated printed rule taped to the outside of the plexiglass wall. It is recorded at the beginning and end of each sequence of ADV or PTV measurements. The water level may vary by up to 3 mm from the mean value.

The temperature of the water was measured using a digital thermometer placed in the water near the intake for 10 minutes at the beginnnig of each day of measurements. The temperatures range from 12 to 15 °C over all the measurements. The corresponding water density for pure water is 999.5 $\pm$0.3 kg/m^3 and kinematic viscosity ranges from 1.16 to 1.25 $\times 10^{-6}$ m^2/s (Nakayama and Boucher, 2000).

The surface tension coefficient σ for a clean-water interface at the mean value of these measured temperatures is 0.0739 N/m with less than 1% variation due to temperature variations (Vergaftik *et al.*, 1983). Impurities in the water or floating on the free surface probably produce greater variations in the effective surface tension than temperature variations, but they cannot be directly evaluated since they vary with time. In particular, the convergence of flow towards the vortices leads to an accumulation of fine particles at the tip of the free surface depression produced by the vortex for mild vortices that produce only a mild depression. The free surface was cleared of floating residues and particles periodically between test runs by placing a 15 cm wide, 60 cm tall rigid plate vertically across the channel depth just upstream from the piers for several minutes so that the massive recirculation zone and free surface depression that formed in its wake entrained everything floating on the free surface down into the intake pipe.

Eight combinations of submergence and flowrate are selected to produce a wide range of vortex types under different operating conditions (see Table 3.1). The flow rates range from Q = 6.0 to 18.8 l/s and the relative submergence ranges from s/d = 1.5 to 3.3, where s is the vertical distance from the top of the pipe opening to the free surface. $\mathrm{Re} = U_i s/\nu$, $\mathrm{Fr} = U_i/(gs)^{1/2}$ and $\mathrm{We} = \rho U_i^2 s/\sigma$ are the submergence Reynolds, Froude and Weber numbers respectively. U_i is the mean velocity in the intake pipe and g is the gravitational acceleration. The deepest submergence $s/d = 3.3$ was selected because it constitutes the rough limit beyond which clear coherent vortices cease to form. The goal was to produce a range of vortex types ranging from almost non-existent to air-entraining bubbles but not a full air funnel, since this is the range of vortex intensities that are commonly observed in scale models of hydropower intakes. Different combinations of s/d and Q were selected so that the interaction of processes driven by these two parameters could be examined. At the lowest submergence, the vortices produce a 5 mm-deep depression at the lowest flow rate and regularly entrain air at the strongest flow rate. At the

Case	s/d	Q [l/s]	$\mathrm{Re}_s \times 10^{-4}$	Fr_s	We $\times 10^{-3}$
1	1.5	6.0	2.9	0.22	0.8
2	1.5	9.0	4.1	0.34	1.8
3	1.5	14.6	6.6	0.55	4.7
4	2.4	9.0	2.6	0.17	2.8
5	2.4	18.8	5.4	0.36	12
6	3.4	9.0	1.9	0.10	3.9
7	3.4	14.6	3.1	0.17	10
8	3.4	18.8	4.0	0.21	17

TABLE 3.1: Operating conditions of the measurements

deepest submergence, vortices are very weak and intermittent, and the depression they produce is only discernable from deformed reflections on the free surface.

The range of relative submergences s/d studied here is relatively high compared to typical values in low-head hydropower intakes. This is due in large part to the piers, which are longer in relative terms than typical trash rack piers to produce more stable vortices. The piers studied here would have produced excessively strong (air core) vortices at lower submergences for the same range of flow rates, while lower flow rates would have produced flow that is almost laminar, which is also not realistic.

The channel and inflow diffuser were designed to produce uniform flow across the channel width, but the velocity is somewhat higher on the right side of the channel (looking downstream) than on the left for higher flow rates (Q=0.015 and 0.019 m^3/s). This may be due to a bend in the inlet pipe 0.4 m upstream from the diffuser or to imperfections in the channel construction. The greatest relative velocity differences are found 2 m upstream from the intake at the deepest submergence (s/d = 3.4), just below the free surface. The maximum values for these conditions deviate by 12% and 23% from the mean values 0.06 m/s and 0.038 m/s respectively. The relative velocity variation is much lower (6%) 0.09 m below the free surface for those two extreme cases, while for other conditions it ranges from 1% to 9%. The greater relative asymmetry at the free surface is due to the fact that velocities are particularly small there for deep submergences, so that smaller velocity differences have a greater relative effect. The asymmetry generated at the inflow may also be amplified through an interaction with the rotating flow around the intake

vortices. The asymmetry does not appear to create a marked asymmetry in the strength of the two free surface vortices, except for case s/d=3.3 at Q=9 l/s. At this condition, only one vortex forms at a time, closer to the middle between the two piers, and the counter-clockwise vortex (as viewed from above) formed by separation off the left pier is more frequent.

3.2 Measurements

A global coordinate system (X, Y, Z) is defined with its origin located where the free surface meets the downstream wall of the channel, half-way across the channel width (on the channel centerline), as shown in Fig. 3.1(b). Z points down towards the bed and X points downstream and Y points towards the right when looking downstream. The local vortex coordinate system is located where the vortex meets the free surface, which corresponds approximately to (X, Y, Z) = (-25, 55, 0) mm.

3.2.1 PTV measurements

The literature suggests that Burgers's vortex model describes the velocity field in intake vortices fairly well. Burgers's model allows the $V_\theta(r)$ profile to be quantitatively described using two parameters, r_o and Γ_∞, and hypothesizes that r_o is controlled by the ratio $2(\nu/r_o)^{1/2}$ (Eq. 2.2), where a is the axial stretching $\partial V_z/\partial z$ of the vortex. This relation has been experimentally verified by Petitjeans (2003) for laminar flow in the wake of a step and Odgaard (1986) assumed it to hold true in the vortex produced in a cylinder with bottom orifice, but it has not been verified experimentally in an intake vortex surrounded by turbulent flow. Hite (1991) took measurements of velocity across an intake vortex generated in the wake of a pier, but he used LDA so he could only measure the velocity at one location at a time, obtaining a radial profile averaged over time. Because of this limitation, he measured only the velocity profiles for an air core vortex, which is more stable and migrates less than weaker vortices. Since the air core reaches all the way to the intake and velocities are very high in direct proximity to the air core and so are difficult to measure, it is not possible to determine the vortex characteristic radius from these measurements.

In order to verify the relation $r_o \sim \nu/a$ in the unsteady vortices, V_z and V_θ must be measured at multiple points along r and z within a short enough timeframe $\triangle t_{meas}$ so that it is smaller than the timescale of the the fluctuations in V_θ and V_z linked to changes in vortex characteristics and lateral displacement of the vortex axis. The goal is to obtain enough measurements of $V_\theta(r)$ at different values of r both within the vortex core ($r < r_o$) and outside the core ($r > r_o$) so that the radial location and magnitude of the peak velocity $V_{\theta,\max}$ can be identified, allowing the characteristic radius and bulk circulation of the vortices to be be determined by fitting Burgers's profile Eq. (2.1 to the measured $V_\theta(r)$ profile. PTV is selected to measure the velocities in the vortex because it is non-intrusive and allows a greater number of velocity points to be extracted from a relatively limited number of particles. By assuming the streamlines follow a helical pattern with $V_r \ll V_\theta$, PTV can be used to simultaneously measure the $V_\theta(r)$ and V_z profiles using an experimental setup that is far simpler and less expensive than that required for 3D PIV or PTV measurements. Use of a second or third camera would significantly increase the complexity of setting up and synchronizing the cameras and analyzing the particle trajectories, without a comparable increase in the amount of useful measurement detail for the purpose of the current research goals. The relatively simple setup and analysis procedure for the current single-camera configuration allows measurements to be taken and analyzed more quickly for different operating conditions than a more sophisticated multi-camera setup, and with less room for error and uncertainty. Although deviations from axisymmetry cannot be documented with the current configuration, the relative ease of installation and operation allows wider investigation and documentation of the variations in vortex characteristics that occur with time and across different operating conditions.

The particles employed for the PTV measuremnts must be neutrally buoyant and sufficiently small to be carried with the flow in a passive manner and reach the surrounding flow velocity quickly, but they must also be sufficiently large to be slightly larger than a pixel on the camera images. Pliolite VT is employed for the particles since its mass density (1.003 kg/m^3) is very close to that of water (0.999 kg/m^3) and it can be ground up and sieved to obtain the desired range in particle diameters. roughly 1.5 times the size of one pixel on the film images. One pixel on the film images corresponds to roughly 0.25 mm so particles ranging in size from 0.15 to 0.35 mm are used. The particles are rinsed in diluted dish soap to remove the tiny air bubbles that

otherwise remain attached to the irregular surface, causing the particles to float. After rinsing the particles sink in water, with a terminal velocity of 0.6 to 1.3 mm/s in still 12°C water.

A high number of particles is required within the measurement volume to obtain enough measurement points within the short span of time of the film segment $\triangle t_{\text{meas}}$, so the particles are mixed with a small amount of water and injected directly into the vortex roughly 2 mm below the free surface using a syringe mounted with a short flexible thin-walled tube of 2 mm diameter instead of a needle. The particles are injected downward from just below the free surface, roughly at the edge of the vortex core (at a distance $r \approx r_o$ from the vortex axis), at an angle ranging from 0 to 80 degrees from the vertical. The particles generally enter the flow in a little clump which then diffuses around the vortex as the particles are entrained into different portions of the high-gradient flow. The velocity at the free surface is relatively low (under 5 mm/s) in most cases, so the particles remain in the field of view long enough after injection so that one can wait half a second for the residual injection velocity to decay before beginning particle velocity analysis.

In order to measure the $V_z(z)$ and $V_\theta(r)$ profiles simultaneously, the particle trajectories are filmed from the side through the downstream wall of the channel. From this viewpoint, the particles follow a sinusoidal trajectory, as shown in Fig. 3.3. The flow in the vortex is assumed to be helical with moderate deviation from axisymmetry, and V_r is assumed to be negligible compared to V_θ. Though deviations from axisymmetry are observed in the axial velocity profile in particular, this effect is accounted for by averaging the velocity over the full circumference of the vortex (see Appendix C for further details.) The particle trajectories are recorded through the plexiglass downstream wall of the channel using a digital high-speed Fastec Troubleshooter video camera with manual focus and fixed exposure operating at 50 and 250 frames-per-second with a 240 by 320 pixel field of view.

V_θ reaches its peak value at the limit of the vortex core $r = 1.12r_o$. In order to successfully track the particles at this velocity, a high frame rate is necessary so that the particles take several frames (at least 12) to travel around the circumference of the vortex. Otherwise the particles appear as streaks that are very faint, difficult to identify on the images and even more difficult to track from frame to frame. Based on the highest aximuthal velocities $V_{\theta,\max}$ observed in

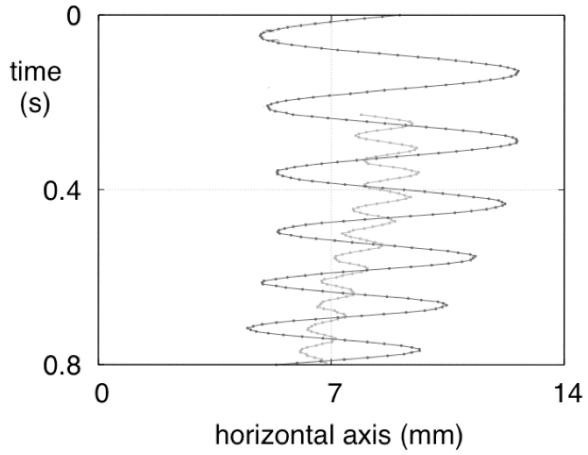

FIGURE 3.3: Sample particle trajectory.

initial measurements for Case 3 (0.4 m/s), a frame rate of 250 frames-per-second is required for the cases with low and medium submergence (Cases 1 to 5). A frame rate of 50 is more appropriate for the deepest submergence cases (Cases 7 to 9) were the weaker vortices have far lower velocities and require much longer film segment lengths ($\triangle t_{\text{meas}}$ = 2 to 5 seconds) to obtain enough data points in the $V_\theta(r)$ profile.

The scale of the recorded images is evaluated before each set of measurements by filming a 1mm x 1mm graduated grid clamped to the pier at the streamwise (X) location where the vortex forms. The scale of the images ranges 0.23 to 0.25 mm/pixel for the different film segments. The particle sizes (0.15 to 0.35 mm) employed therefore correspond to 0.6 to 1.6 pixels in the images.

The high camera frame rate requires extremely strong illumination for the particles to appear in the images. In order to maximize exposure, maximum lens aperture is used, which produces a very shallow depth of field, on the order of 10 to 20 mm. The light from a slide projector is used to illuminate the vortex from the top, with an additional external lens to further focus the light. Some effort was required to find a means to illuminate the particles sufficiently so that they are visible on the images at the high shutter speed. Mirrors are used to control the location and direction of the light beam so that it was shining down on the vortex from a short distance above the free surface. The free surface depression diffracts the light beam so the

projector light was supplemented using a halogen construction lamp set up under the channel shining up through the plexiglass bed. Impurities in the water diffuse the bottom light more as a result of passing through the deep column of water.

The recorded images include both the free surface depression and the top 0.1 m of the particle trajectories through the water. Below that the illumination became dimmer so that it was difficult to track the particles.

3.2.1.1 Image sequence analysis

The goal of the measurements is to obtain simultaneous measurements of $V_\theta(r)$ and $V_z(z)$ over a short period of time that is smaller than the time-scale of fluctuations in vortex characteristics (2-5 seconds). Each $V_\theta(r)$ data point requires that a particle be tracked around the full circumference of the vortex so that the average V_θ and radius r can be extracted. It is therefore necessary to develop a tracking methodology that is capable of tracking particles and producing continuous trajectories over many frames, despite frequent changes in the direction travelled by the particles in the recorded images as well as their shape and pixel intensity as their apparent velocity across the image changes. The film segments selected for analysis range in length from 0.3 to 2 seconds in length, with the longer segments selected for the weaker vortices.

The selected film segments must have enough visible particles that remain visible for a sufficiently long period of time over the desired range of r and z values needed to obtain the axial and radial profiles. The brightest channel (green) of the selected film segments is extracted from the RGB AVI movie files produced by the Troubleshooter and converted to a sequence of grayscale .tiff images using the open source image conversion program ImageMagick. To limit computational memory needs during subsequent tracking, the images are cropped down to the zone of interest where the particles are present.

An existing particle tracking plugin for the image analysis program ImageJ is used to track the particle trajectories. The modified code for the plugin is included in Appendix B, as well as a discussion of the uncertainty of the velocity measurements made using PTV. The results of the PTV measurements are also compared to simple dye-tracking measurements made for 3

of the operating conditions. ImageJ is an open-source image analysis program developed at the National Institutes of Health in the United States; version 1.37 was employed. In its initial form, the trajectories computed by the particle tracker have many breaks at points where the particle velocity changes direction and/or magnitude, so the algorithm is modified for the purpose of this experiment to improve tracking performance and to analyze the trajectory characteristics.

The particle-tracking plugin was developed and optimized by Sbalzarini and Koumoutsakos (2005) to track bacteria in microscope images. The bacteria 'particles' have erratic, jerky trajectories in unpredictable directions, but the size and light intensity of a given particle remains fairly constant along its trajectory. In contrast, the particles tracked here have a smooth vertical velocity that generally increases quite slowly from frame to frame, but the apparent size and light intensity of the particle image varies significantly depending on the particle's horizontal speed across the frame and its location. In cases with very high azimuthal velocities particles appear as short, dimmer streaks when they are moving in the image plane and as brighter round dots when they are moving perpendicular to the image plane. The particles also dim if they pass through a portion of the flow that is less well lit because of light diffraction by the free surface profile. To account for this and improve tracking performance of the plugin, the cost function was modified that evaluates how likely two particles in sequential images are likely to be the same particle that has moved. The new cost function assigns greater weight to the similarity of the vertical (V_z) velocities of the two particles, with moderate emphasis on similarity of their velocity across the image, and much less emphasis on similarity of the light intensity and size of the two particle images.

3.2.1.2 Azimuthal velocity profile $V_\theta(r)$

In order to perform an initial analysis of the computed particle trajectories and to determine if enough $V_\theta(r)$ values can be extracted over a suitable range of radii, $V_\theta(r)$ profiles from the new function are added to the plugin which performs a rough analysis of the particle trajectories that might have the right characteristics to provide useful data about the azimuthal velocity profile. The horizontal axis on the image is referred to here as y. For a particle that is rotating at a roughly constant azimuthal velocity and radius around the vortex, the y-coordinate of its

trajectory follows a sinusoidal curve in time, as shown in 3.3. The vertical velocity is much lower than the azimuthal velocity, it has greater deviation from axisymmetry, and optical effects due to the camera viewing angle make the particles appear to move upward at times, so the shape of the particle coordinate y plotted as a function of the vertical coordinate does not produce a clear sinusoidal path. The new sub-function in the particle-tracking software examines the trajectories computed in the first part of the code to identify the ones that appear to have a sinusoidal path in time and that are long enough (that complete a full turn about the vortex axis) to compute a mean azimuthal velocity and radius. For these trajectories, the code calculates the radius r_j of the trajectory (1/2 the amplitude of the sine wave) and the period τ_j of the sine wave (how long it takes for a particle to complete a turn around the vortex). Assuming that the azimuthal velocity is steady and axisymmetric and that the radial velocity is negligible in comparison, the azimuthal velocity V_θ is given by $V_{\theta,j} = 2\pi r_j/\tau_j$. If a trajectory includes many complete cycles about the vortex, the radius, period, and mean vertical velocity V_z over that cycle are computed and printed for each complete cycle.

The 'useful' computed trajectories and computed r_j and τ_j values are examined for errors in the tracking (for example if the tracking algorithm mistakenly linked the trajectories of two particles that crossed paths) or in the analysis (for example if the vortex axis was moving laterally in time or space, making the trajectory radius more difficult to evaluate).

The trajectory characteristics computed for different film segments are examined to identify short segments that have a sufficient number of $(r_j, V_{\theta,j})$ points over the necessary range of r_j values needed to evaluate the characteristic radius r_o and bulk circulation Γ_∞. Segments must also have a free surface depression that remains relatively constant in depth and location over the span of the segment. The selected segments range in length from 0.1 to 2.4 s for the low and medium submergences and 2.5 to 4.6 s for the deepest submergence.

Continuous trajectories that have completed a full turn about the vortex are much rarer outside the vortex core ($r_j > r_o$) than inside the core, mainly because the azimuthal velocities are lower while the trajectory radius is high, so it takes much longer for a particle to complete a turn around the full circumference $2\pi r_j$. These trajectories also move forward and backward a greater distance from the central plane on which the camera is focused on and where the

peak light intensity occurs, so the particles are more likely to go out of focus and become dim, increasing the chances of a break in the trajectory. The azimuthal velocity inside the core makes a greater contribution to the free surface depression than that outside the core, so the particles were injected closer to the core to ensure that a good resolution was achieved there, contributing to the shortage of complete large-radius trajectories. Given the rarity of complete large-radius trajectories it is necessary in many cases to examine plots of all the computed trajectories to identify possible complete large-radius trajectories that might have been broken into several pieces. Alternatively, or in addition, it may be necessary to estimate the radius and mean V_θ of a large-radius trajectory that only completes a partial cycle around the vortex, using core trajectories to approximate the location of the vortex axis for estimating r. The radius and V_θ of large trajectories therefore has more uncertainty than for the smaller-radius trajectories.

Once enough (r_j, τ_j) points have been computed over radii below r_o, around r_o and above $1.5r_o$ for a given film segment, Burgers's model (2.1) rewritten in terms of the frequency τ^{-1} (using the relation $V_{\theta,j} = 2\pi r_j/\tau_j$)

$$\tau^{-1} = \frac{\Gamma_\infty}{(2\pi r)^2}\left\{1 - \exp\left(-(r/r_o)^2\right)\right\}, \tag{3.1}$$

is fitted to the experimental points (r_j, τ_j^{-1}) by adjusting the parameters Γ_∞ and r_o The inverse of (3.1) is then fitted to (r_j, τ_j), which yields different values for r_o and Γ_∞. Fig. 3.4 shows sample datasets with the curves fitted to τ (top), τ^{-1} (middle), and the corresponding Burgers velocity profile (bottom). Different values are obtained from the two fitting methods because the points at larger radii points are more heavily weighted when fitting the (r_j, τ_j) profile, while points at smaller radii are are more heavily weighted when fitting the (r_j, τ_j^{-1}) profile. Both the mean of the two values and the values themselves are plotted (as error bars). A larger error bar might indicate that the measured velocity points do not fit Burgers's profile as well. For example, the velocity outside the vortex core ($r > 1.5r_o$) might not follow the profile $V_\theta \sim r^{-1}$ proposed by Burgers. There are few data points for $r > 1.5r_o$ so it is not easy to draw conclusions about the exact shape of the profile in this range. It appears as though the velocity might deviate more from axisymmetry at larger radii and/or that the shape of the trajectory strays further from the idealized helical shape assumed in the analysis. The scarcity of data points at large radii is partly

due to the radius at which the particles are initially injected and because the particles generally move inward towards the axis instead of away from it. The trajectories at large radii also require a much longer time to complete a full cycle because V_θ is lower and the distance to be travelled around the circumference is larger (due to the larger radius).

3.2.1.3 Axial velocity profile $V_z(z)$

In order to evaluate the validity of Burgers's relation $r_o = 2(\nu/a)^{1/2}$ (Eq. 2.2), the axial gradient $a = \partial V_z/\partial z$ inside the vortex core near the free surface must be evaluated. The axial velocity V_z of the particles is computed from the vertical displacement travelled by the particles over the time τ required to complete a full cycle (from θ = 0 to 2π) about the vortex axis. a is evaluated by fitting a straight line $V_{z,\text{fit}}(z) = az + b$ through the measured $V_z(z)$ data points using the linear regression algorithm in the open source statistics program 'R' (Crawley, 2012). Fig. 3.5 shows a sample of the measured velocities and curve fit for Case 1. The vertical error bars are calculated from the uncertainty in measuring the vertical displacement and the length of time required to travel that distance. More details are included about the measurement and curve fit uncertainty in Appendix C. A certain amount of scatter is present in the $V_z(z)$ data points even though they are averaged about the vortex axis, as shown in the figures in Appendix C, but a clear slope in the profile is discernable for most of the operating conditions. For Cases 6 to 8, the slope a is so small that the depdence on z is difficult to distinguish from the experimental noise.

b is not assumed to be zero because the measurements begin below the lowest point of the free surface depression, not at $z = 0$, and in several cases $V_z(z)$ experiences a much sharper gradient in velocity in the first few millimeters below the free surface than further below. This sharp gradient right below the free surface coincides with the reorientation of the flow at the free surface from a horizontal direction to a more vertical one as it is entrained into the vortex. It is therefor more appropriate to consider the velocity as starting at a non-zero value just below the free surface for the purpose of evaluating the mean axial gradient experienced by the vortex over the top 10 cm of the flow.

The results and analysis of the PTV measurements are presented in Manuscript 1.

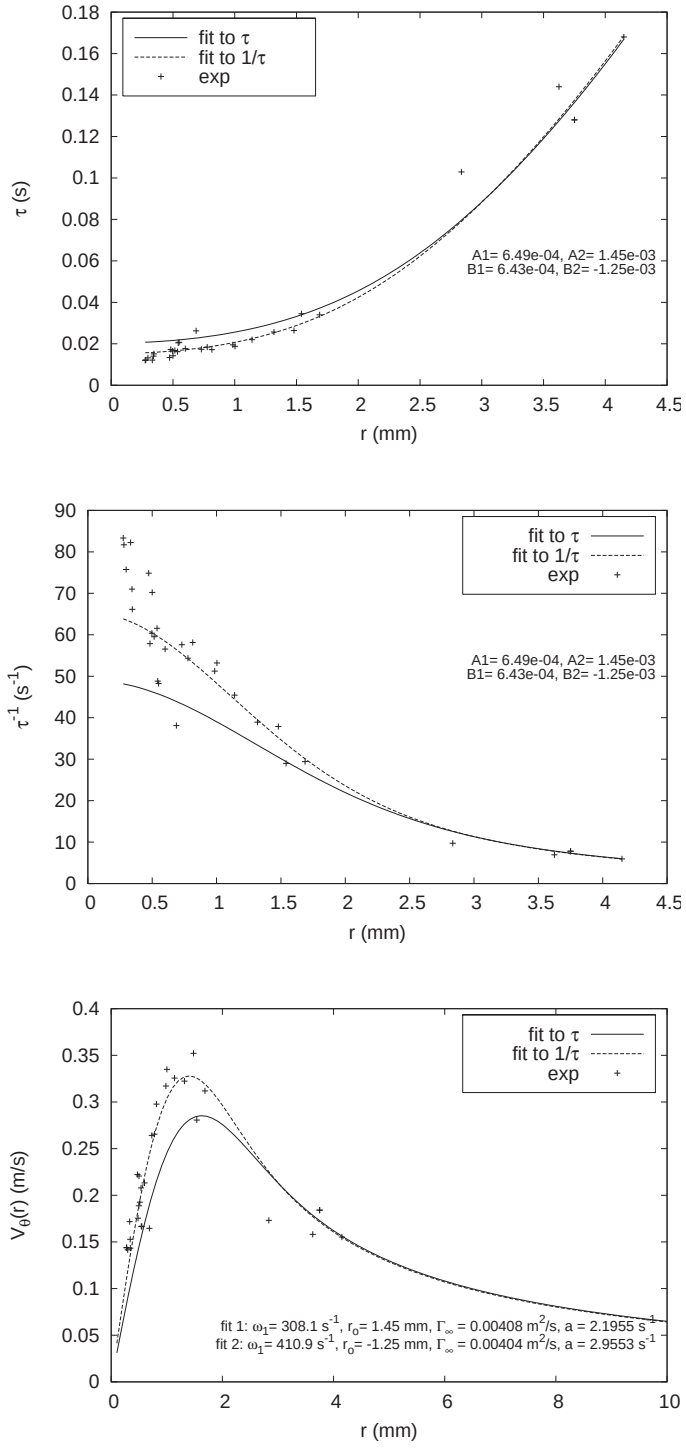

FIGURE 3.4: Sample curve fit to the measured profiles of $\tau_j(r_j)$ (top) and $\tau_j^{-1}(r_j)$ (middle), and the corresponding $V_\theta(r)$ profile (bottom) for Case 3.

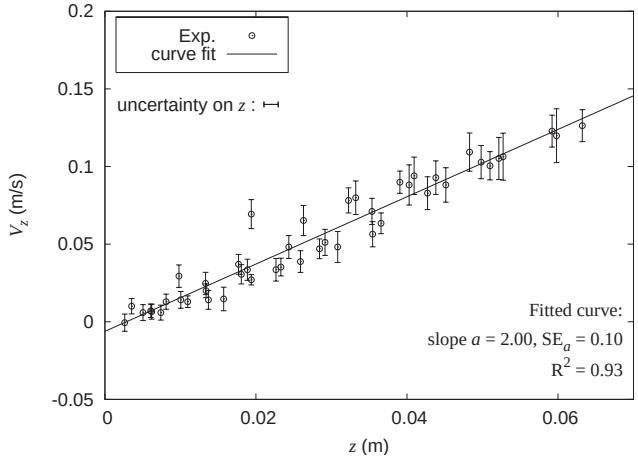

FIGURE 3.5: The profile of $V_z(z)$ measured by PTV. SE_a is the estimated standard error on the linear curve fit and R^2 is its coefficient of determination.

3.2.2 Free surface profile

Practicing engineers commonly use the depth and shape of the free surface depression to assess and categorize vortex intensity, because it can be easily observed in qualitative terms in a laboratory model and because a deeper or steeper depression suggests greater risk of air entrainment. The free surface profile also provides the opportunity to verify that the $V_\theta(r)$ profiles have been measured correctly and that it is appropriate to fit Burgers's model to them. The free surface profile $h_{\sigma,\mathrm{comp}}(r)$ is therefore computed from the $V_\theta(r)$ profiles using a one-dimensional axisymmetric finite-difference calculation and compared to the measured profile $h_{\mathrm{exp}}(r)$. $h_{\sigma,\mathrm{comp}}(r)$ must include the effect of surface tension because it is expected to be significant since r_o of the vortices is comparable to the characteristic length $l_\sigma = \{\sigma/(\rho g)\}^{1/2}$ for the air-water interface. l_σ indicates the scale at which surface tension effects become significant. The Weber number varies from 800 to 17×10^3 for the cases studied here.

The free surface depression is visible in profile at the top of the images from which the particle trajectories are extracted so it can be used as complementary data to verify that the velocities were properly measured and that the fitted model Burgers model is appropriate. The correspondence between the measured velocities and the free surface profile is evaluated by computing the radial profile of the free surface depression that should be produced by the measured azimuthal

velocity profile. The free surface profile is calculated using the one-dimensional equation that describes the equilibrium of forces acting at the free surface, including surface tension

$$h_\sigma(r) = \int_\infty^r \left(\frac{V_\theta(\acute{r})^2}{g\acute{r}} - l_\sigma^2 \kappa(\acute{r}) \right) d\acute{r}, \tag{3.2}$$

(Andersen *et al.*, 2006). This equation does not include the pressure drop associated with the kinetic energy associated with V_z and V_r, which is negligible compared to that of V_θ (Odgaard, 1986). Equation 3.2 is discretized by central-differences. The code is given in Appendix A. A constant value for l_σ of 2.73 mm is used, which corresponds to a clean air-water interface at 15°C. The variations in l_σ associated with the range of experimental temperatures (13 to 15 °C) are negligible compared to those that might be caused by impurities in the water or floating on the free surface.

The mean local curvature $\kappa(r)$ is given by

$$\kappa(r) = -\frac{1}{2} \left\{ \frac{h_r}{r[1+(h_r)^2]^{1/2}} + \frac{h_{rr}}{[1+(h_r)^2]^{3/2}} \right\}, \tag{3.3}$$

where h_r and h_{rr} are the first and second derivatives of h with respect to r respectively (Andersen *et al.*, 2006). The first term on the right is the curvature about the horizontal axis (perpendicular to the page in a 2D section of the profile such as Fig. 3.6 and the second term is the curvature about the vortex's (vertical) axis of rotation. The free surface profile has a positive (concave) horizontal axis curvature at the vortex tip, then some distance beyond $r > r_o$ it passes through an inflection point and the horizontal axis curvature becomes negative (convex). The surface tension force thus pushes the interface upward in the core portion of the vortex and pulls it down very slightly just outside the core.

Since the primary goal is to get a larger view of trends in surface tension effects over a range of shapes and scales rather than to obtain the exact shape of the depression, the free surface profile is computed by directly substituting Burgers's relation for $V_\theta(r)$ from Eq. (2.1) into Eq. (3.2):

$$h_\sigma(r) = \int_\infty^r \left\{ \frac{\Gamma_\infty^2}{4\pi^2 g\acute{r}^3} \left[1 - \exp\left(-(\acute{r}/r_o)^2 \right) \right] - l_\sigma^2 \kappa(\acute{r}) \right\} d\acute{r}, \tag{3.4}$$

This approximation neglects the effect of the free surface depression on the velocity field and indirectly its effect on the depression itself as well. Stepanyants and Yeoh's (2008b) results suggest that this approximation produces a negligible error in $\Delta h/h_{\mathrm{n},0}$ in the case of a mild dimple depression and an error of 26% for an extremely deep, funnel-type depression with a nominal free surface depression slope $\zeta \equiv h_{\mathrm{n},0}/r_o = 110$. $h_{\mathrm{n},0}$ is the maximum depth of the free surface depression without surface tension effects. This is judged to be an acceptable level of error for the purpose of this study.

Equation (3.2) is discretized along r by central differences and an equilibrium profile $h_\sigma(r)$ is computed numerically for the desired r_o and Γ_∞ values. The values for $V_\theta(r)$ and $h(r)$ are computed at the nodes and $h_r(r)$, $h_{rr}(r)$ and $\kappa(r)$ are evaluated at the midsection of each segment (length dr) of the profile. See Appendix A for the code used to perform the calculations. Note that to ease definition in the code, the variable h used to define the free surface level is defined pointing up from a submerged datum instead of pointing downward like h from a nominal undeformed free surface. This may create some confusion in signs in the following discussion, where h is employed.

The boundary conditions for the local free surface slope h_r at $r = r_{\max}$ (outer boundary) and $r = 0$ are difficult to set without generating oscillations in the profile. h_r should tend to 0 for sufficiently large $r_{\max}$, but a small non-zero slope persists at $r = r_{\max}$, which is set to $r_{\max} = 20r_o$. Similarly, the free surface slope h_r at $r = 0$ should be zero due to symmetry, but imposing this as a boundary condition produces oscillations in the free surface depression near the tip. This may be linked to the discretization, since the slope of the first segment from $r = 0$ to $r = dr$ in the discretized profile is not actually zero. The function for κ is also undefined at $r = 0$ (division of h_r by $r = 0$ in the first term on the right-hand side in Eq.(3.3). The value of $h_r(r_{\max})$ is therefore roughly approximated to follow the slope of the neighbouring segments $h_r(r_{\max}) = 2h_r(r_{\max} - dr) - h_r(r_{\max} - 2dr)$. The value of $h(r_{\max})$ remains fixed throughout the simulation. At $r = 0$, h_r is calculated as $h_r(0) = \{h_r(dr) - h(0)\}/dr$ and h_{rr} is calculated as $h_{rr}(0) = \{hr(dr) - h(0)\}/(2dr^2)$. These values are used to estimate the curvature $\kappa(0)$ at $r = 0$ using only the second term on the right-hand side of Eq. (3.3) for lack of a better approximation. Several variations were tested, this one appears to be the most stable. $\kappa(0)$ is used to compute a

smoothed profile of $\kappa(r)$ but it is not directly used to compute $h(0)$. Instead, a somewhat flexible version of the $h_r(0) = 0$ boundary condition is imposed by setting $h(0) = h(dr) + 0.2\{h(2dr) - h(dr)\}$. If the grid is fine enough, the slope $h_r(dr)$ should tend towards zero. This relation pushes $h_r(0)$ towards a smaller slope while preserving a smooth profile.

The profile is computed by first calculating the free surface depression without surface tension $h_{\mathrm{n}}(r)$, and then iteratively correcting the profile to account for the contribution of surface tension $l_\sigma^2\kappa(r)$. The profile is adjusted gradually at each iteration m:

$$h_{m+1}(r) = h_m(r) - \alpha_R \triangle h_m(r), \tag{3.5}$$

where $\triangle h_m = -l_\sigma^2 \kappa_m(r)$ is computed from the local mean curvature $\kappa_m(r)$ of the mean profile $h_m(r)$ computed at the previous timestep and the relaxation factor $\alpha_R < 1$ is set to lower values for deeper depressions where the profile is more susceptible to oscillations. To further stabilize the profile of $h(r)$, it is smoothed between each iteration. The smoothed free surface level $h_{\mathrm{sm}}(r_j)$ at radius r_j is computed from the original value at that node $h(r_j)$ and at neighbouring nodes, $h(r_j + dr)$ and $h(r_j - dr)$ using the relation

$$h_{\mathrm{sm}}(r_j) = 0.5h(r_j) + 0.25\{h(r_j - dr) + h(r_j + dr)\}. \tag{3.6}$$

Similarly, the curvature $\kappa(r_j)$ is smoothed using the relation $\kappa_{\mathrm{sm}}(r_j) = 0.5\kappa(r_j) + 0.25\{\kappa(r_j - dr) + \kappa(r_j + dr)\}$.

Funnel-shaped vortices with a steep slope of the free surface depression have a particularly large peak in the mean curvature $\kappa(0)$ at $r = 0$ in the absence of surface tension. The corresponding and equally large correction $\triangle h(0) = -l_\sigma^2\kappa(0)$ generates oscillations in the free surface profile near the tip if too large a value for α_R is employed. α_R values as low as 0.0008 are used in some cases, requiring more timesteps to reach a converged profile. The calculations require only a few minutes to perform even in these cases.

The effect of surface tension on the free surface profile is a highly non-linear one, so an attempt is made to roughly mimic the process through which the free surface profile develops, and different iterative modes for computing the corrected profile are tested to verify that the

iterative solution method does not significantly affect the the final result. One possible mode in which the free surface vortex may form and strengthen, producing a gradually deepening depression, is for the characteristic radius to start from a large value that gradually decreases until it reaches the prescribed final value. This would produces a depression that starts out with a very mild slope and depth and gradually becomes steeper and deeper. An outer computation loop is therefore performed in which the characteristic radius is gradually decreased from a large value $r_{\max}/2$ to the final desired value r_o, over 10 steps (loops), with Γ_∞ maintained constant at the desired value throughout. r_o is decreased in a non-linear fashion so that the corresponding tip depth increases in a quasi-linear way. For each r_o value, an equilibrium profile $h_\sigma(r)$ is computed following the procedure described in the previous paragraph. In order to test the sensitivity of the calculations to this solution method, the same procedure of gradually increasing vortex intensity was tested but with r_o maintained at a constant value and Γ_∞ increased from a low value to the desired value. The final computed profile was identical. Both procedure produces profiles that are very similar to those computed directly at the desired r_o, Γ_∞ combination but they appear less susceptible to oscillations.

Although the boundary conditions imposed at $r = 0$ are somewhat dubious, tests with variations of these conditions and different grid densities produce essentially identical profiles for grids beyond 700 grid points, except for slight variations or oscillations in $h(r)$ in the first few segments neighbouring $r = 0$. Furthermore, $h_r(0)$ is very close to 0 in the final computed profiles, even without explicitly imposing $h_r(0)$ as a boundary condition. Grid densities ranging from 200 to 1400 grid points across the profile (from $r = 0$ to $r_{\max}$ were tested. A 700 point grid is used to compute the profiles for the analysis.

The free surface profile code is first tested using the free surface and velocity profiles measured and computed by Andersen *et al.* (2003) for a moderate funnel of nominal depression slope $\zeta = h_{\mathrm{n},0}/r_o = 15$, and the results compare very well. The code is then tested by computing the free surface depression from the measured velocity profiles in the experiment and comparing the computed tip depth $h_{\sigma,0,\mathrm{comp}}$ to that recorded in the film segments. Fig. 3.6 shows the free surface profiles computed from the velocity profile obtained from the two fitting methods in Fig. 3.4 for the same dataset, compared to the recorded free surface profile (the bright pixels from the

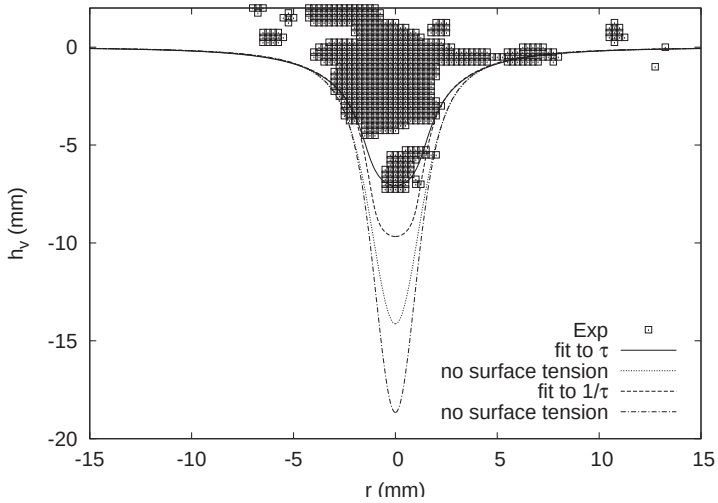

FIGURE 3.6: Computed free surface profile compared to the measured one from a dataset for Case 3.

light reflected off the free surface are plotted here). From the comparison of the computed free surface profiles with the measured ones, it would appear that variations in surface tension due to impurities in the water or on the free surface have a far lesser impact on the free surface depression than do variations in the flow velocity and flow structure that affect the circulation and characteristic radius of the vortices.

3.2.3 ADV measurements

The intake geometry and approach flow have most often been shown by a number of researchers to influence the depth of the free surface depression by comparing trends in the critical submergence (e.g Knauss (1987)). The processes by which they affect vortex formation have been discussed by many authors (Denny, 1956; Quick, 1962b, 1970; Anwar, 1968a; Pennino and Hecker, 1979; de Siervi *et al.*, 1982; Gulliver *et al.*, 1986; Rutschmann *et al.*, 1987; Nakayama and Jones, 1998; Jiming *et al.*, 2000; G. Montilla and Castro, 2004; Carriveau, 2004; Pavelyev and Shtarev, 2005) and several authors have derived expressions that link intake geometry to critical submergence (Odgaard, 1986; Hite and Mih, 1994; Yıldırım *et al.*, 2000). However, few

measurement datasets exist documenting the approach flow velocity field for intakes in combination with detailed measurements of the vortex characteristics, which would allow the processes linking the two to be explicitly examined (Ansar and Nakato, 2001). To examine expressions that link submergence to axial stretching (Odgaard, 1986), ADV measurements of the vertical profile of the mean velocity (U_X, U_Y, U_Z) are taken directly upstream from the intake. This allows the vertical gradient in velocity outside the vortex produced by the intake to be compared with the axial gradient inside the vortex. It also allows the relationship between the streamwise velocity U_X approaching the intake and the bulk circulation of the vortex to be examined. The velocity cannot be measured at the exact location where the vortex forms (at roughly X=-0.025 m, Y=0.07 m) due to the size of the ADV probe, so the velocities are measured slightly further upstream, on the channel centerline at $X = -0.055$ m, $Y = 0$ m. Initial CFD simulation results suggest that this approximation is acceptable since the vertical profiles of U_X and U_Z and $|U|$ at these two locations are very close and, in particular, the vertical gradients near the free surface closely match.

Information about the velocity profiles further upstream from the intake is also desired to evaluate the CFD simulations to determine whether the model setup is appropriate so that the large-scale structure of the flow approaching the intake region is captured sufficiently well. Furthermore, it is desired to establish the magnitude of the spanwise asymmetry observed near the free surface through dye injected into the flow.

A SonTek MicroADV operating at 30 Hz is used to take mean velocity measurements of the approach flow (Morissette, 2009). The Micro-ADV measures the velocity in a roughly cylindrical 1-cm diameter sample volume that is located 5.5 cm away from the tip of the probes. Since the velocities near the free surface are of particular interest, the ADV is oriented horizontally so that velocities can be measured as close as 3 cm from the free surface. The ADV is operated with the probe pointing horizontally towards the wall for all the off-center profiles and pointing towards the right for the centerline profile. The orientation of the ADV is accurate within 3 degrees. The ADV is fixed to a vertical traversing mechanism that is attached to a cross-beam across the top of the channel. The vertical level of the ADV is manually adjusted to the desired height.

First, the vertical profile of mean velocity is measured at X=-0.055 m on the channel centerline ($Y = 0$), just upstream from the piers (which protrude 0.045 m into the flow from the wall), with a vertical spacing of $\triangle Z$= 3 cm. Velocity profiles are then taken on vertical planes across the channel cross-section at X= -2 m and X = -0.2 m. Five vertical velocity profiles are measured, at Y = (-0.46,-0.25, 0.1, 0, 0.1, 0.25, 0.46), at vertical intervals of 0.11 m, on average.

For each vertical profile the measurements are taken first at the point closest to the bed (0.04 m above the bed) and then the ADV is moved upward for the subsequent points. After the ADV is moved to the desired height, there is a delay of 60 seconds before beginning to record the velocities to allow decay of perturbations of the flow due to the ADV movement and of oscillations of the metal rod that holds the ADV. The velocities are then recorded and averaged over 2 minutes, which was judged to be sufficient to average out the bulk of the turbulent fluctuations, based on a few cumulative averaging tests performed in the flow. The velocity sensitivity range is set to $\pm$ 0.1 m/s for most measurements, and increased to $\pm$ 0.3 m/s or $\pm$ 1.0 m/s for profiles where the velocities are greater and peaks rise above this threshhold. See Appendix D for a discussion of the measurement uncertainty for the ADV data.

3.3 CFD simulations

One of the goals of this research is to evaluate whether CFD can predict the characteristics of free surface vortices at hydropower intakes with sufficient accuracy within industrial time and resource constraints to be useful as an aid in the assessment and optimization of proposed intake designs. The commercial CFD software package ANSYS-CFX (version 11) is employed because it is widely used in industry, and in particular is employed by the turbine engineers collaborating on this project. Use of a common simulation tool by the civil engineers and turbine engineers facilitates collaboration between them.

Initial simulations using the fixed lid approximation produced a toroidal recirculation bubble at the vortex/free surface junction point when the vortex became stronger, which appeared to be a product of the constraint imposed by the rigid surface in the absence of a boundary layer. Based on this experience, it was judged necessary to include the free surface deformations in

the simulations. The VOF method implemented in CFX is used to compute and track the free surface interface. The VOF simulations reveal themselves to be extremely sensitive to initial and boundary conditions as well as mesh quality near the free surface, and are generally prone to instability. In order to address these difficulties and develop effective strategies for running the free surface simulations, simulations of three test cases of increasing complexity are peformed before proceeding to simulations of the full intake studied experimentally.

3.3.1 Training test cases

Before beginning simulations on the intake flow, a few simple laminar test cases are used to develop appropriate techniques to run the free surface simulations:

1. subcritical 2D flow over a gradual change in bed elevation,
2. subcritical 2D flow leading into a submerged culvert,
3. three-dimensional flow under a sluice gate with free surface vortices.

The result from the first test case was compared to analytical predictions, and the result from the third case was compared to experimental data (Roth and Hager, 1999). These preliminary simulations helped determine compatible inlet and outlet boundary conditions and initial conditions that would not provoke sloshing or surface waves during startup.

Fig. 3.7 (top) shows the domain definition for the first test case. The water levels at the inlet ($h1 = 0.073$ m) and outlet ($h2 = 0.068$ m) are selected with a mean inflow velocity $U_{m,1}$ of 0.27 m/s so that the channel Froude number is subcritical ($\mathrm{Fr}_{ch,1} = U_m/[gh]^{1/2}$ ranges from 0.32 to 0.36) throughout the domain. This test case helped understand how the inlet and outlet boundary conditions interact for subcritical channel flow. CFX requires that both the velocity and the free surface level be prescribed at an inlet, which over-constrains the flow, since the water level in subcritical flow is controlled by the downstream conditions. When the free surface level imposed at the inlet as a boundary condition does not correspond to that imposed by the downstream conditions, a kink in the free surface develops, as shown on the left in Fig. 3.7(bottom), producing a small velocity surplus or deficit near the free surface. The test case also revealed the

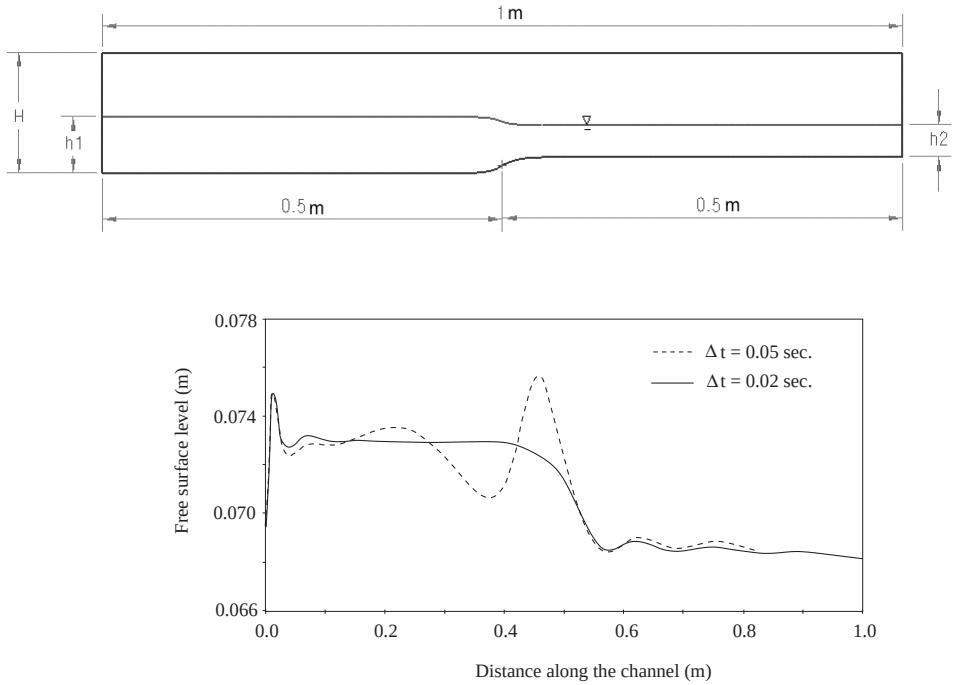

FIGURE 3.7: Test Case 1, change in bed elevation. The domain definition (top) and the free surface profile (bottom) computed with different timesteps.

sensitivity of the free surface simulations to the time-step $\triangle t$ set to iteratively converge towards the steady-state solution using a local time-stepping scheme.

For a timestep $dt = 0.05$ seconds, persistent free surface oscillations were generated at the transition in bed elevation (dashed line in Fig. 3.7), while the bulk of the oscillations decayed when the timestep was reduced to 0.02 seconds (solid line).

Test Case 2 is a horizontal streamise contraction and transition from subcritical open channel flow to pressure (confined) flow, such as occurs in a full culvert, or at a hydropower intake. Fig. 3.8 (left) shows the full domain and computed velocity field with the kink in the free surface (and resulting velocity deficit near the free surface) that occurs at the inlet, as in Test Case 1. The free surface level at the inlet is 0.2 m and the inlet velocity is 0.5 m/s, corresponding to a channel Froude number $\mathrm{Fr}_{\mathrm{ch}} = 0.36$. The homogeneous multiphase solver in CFX computes one velocity field over the entire domain for both the liquid (water) and gas (air) phases of the flow, with the value of the water volume fraction (w.v.f.) determining which portions of

the flow are water (w.v.f. = 1) and air (w.v.f. = 0). The inhomogeneous solver computes two distinct velocity fields for the gas and water phases over the entire domain and is therefore far more computationally costly. The homogeneous solver produces an acceptable solution for the first test case but, in this case, it generates non-physical entrainment of air into the water at the free surface where the water impinges on the dowstream wall and turns downward. The air becomes mixed with the water, producing a recirculating zone with w.v.f. ≈ 0.5, as shown in Fig. 3.8 (center). The only solution that was found to eliminate this entrainment was to compute the flow using the inhomogeneous solver, which produces a distinct air-water interface and no mixing or recirculatoin at the transition point, as shown in Fig. 3.8 (right).

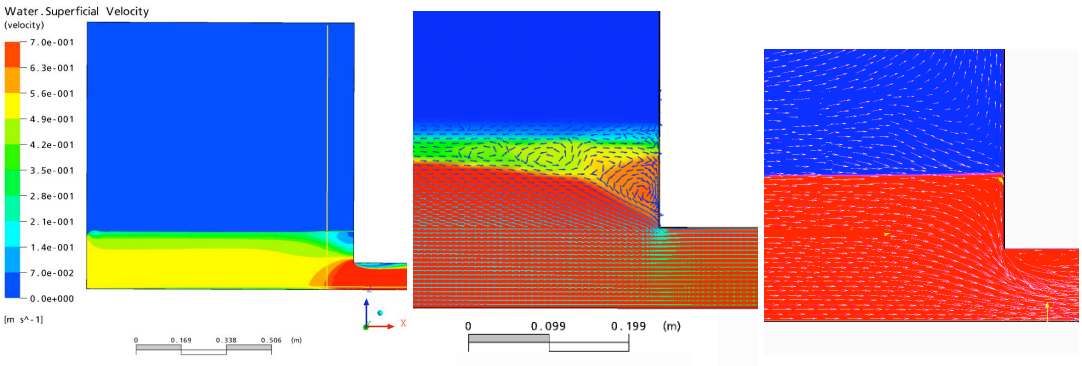

FIGURE 3.8: Test Case 2, full culvert. The full domain with the velocity field computed using the inhomogeneous solver (left). The water volume fraction at the transition zone computed using the homogeneous solver (center) and the inhomogeneous solver (right). Red indicates w.v.f. = 1.0 (water), blue indicates w.v.f. = 0.1 (air) and green, yellow and orange indicate intermediate values (an air-water mixture).

Test Case 3 is a three-dimensional simulation of an experiment performed and documented by Roth and Hager (1999), where flow through a channel encounters a sluice gate, with free surface vortices that form at the junction of the wall and sluice gate. The flow in this case and all subsequent simulations is computed using the inhomogenous solver. Fig. 3.9 on the left shows an isometric view of the flow and geometry, with the computed streamlines on the free surface. Fig. 3.9 in the center shows the magnitude of velocity on a vertical section through the vortex, with superimposed streamlines through the vortex. Fig. 3.9 on the right shows a top view of the vorticity distribution on a horizontal plane just below the free surface, with streamlines shown in black. In this case vorticity from the wall boundary layer accumulates at the sluice and is concentrated through axial stretching by the flow accelerating downwards. The

simulated vortex appears to be weaker than that observed in the experiment, but only the vortex is only described in qualitative terms as a dimple type vortex, so it is difficult to evaluate why the simulated vortex produces a milder free surface deformation. This test case was therefore not pursued further, and simulations of the flow in the simplified intake studied here were started instead.

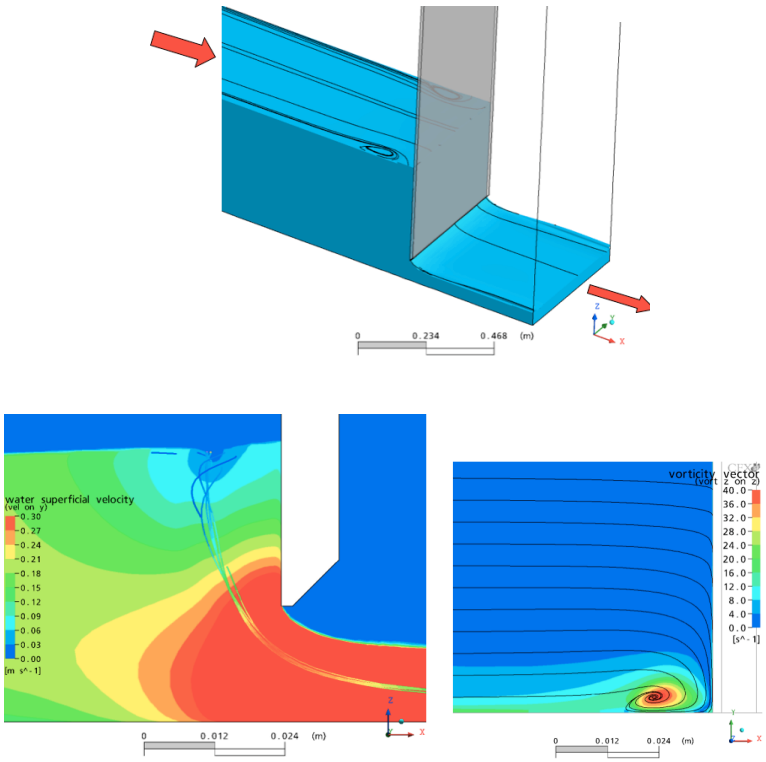

FIGURE 3.9: Test Case 3, sluice gate. The water portion of the domain with the sluice gate and computed streamlines on the free surface (top). The velocity magnitude on a vertical section through the vortex (bottom left). The distribution of the vertical component of vorticity on a horizontal plane below the free surface, with the sluice gate on the right (bottom right).

These test cases helped to identify challenges and develop strategies for performing the free surface simulations. Generally, the free surface simulations are far more challenging and time-consuming to perform than the single-phase (fixed lid) simulations, which converge much more easily and quickly on the same mesh. The multiphase simulations are far less stable, requiring very small timesteps, careful definition of the initial conditions, and repeated adjustment of the

pressure imposed at the outlet to obtain the desired free surface level and flow rate. The challenges described above in modelling the free surface flow are amplified in the three-dimensional intake flow where the third dimension appears to multiply the opportunity for instabilities to occur. The next sections describe the procedure used to set up and run simulations of the simplified intake.

3.3.2 Intake simulations

3.3.2.1 Operating conditions

Simulations are performed of three operating conditions which were documented experimentally, as described above: Cases 3, 5 and 8 as listed in Table 3.1. Engineers assessing a proposed intake must be able to predict the presence of problematic vortices but they also need to be able to accurately predict the absence of problematic vortices. Therefore, two cases with different submergences and flow rates that produce vortices which would be considered problematic are selected (Cases 3 and 5), and one case (Case 8) that produces vortices that are very weak and occasional and would therefore not be considered to be of concern. Case 3 produces very strong vortices that periodically entrain air bubbles, while the vortices in Case 5 are somewhat weaker and do not entrain air. Case 8 produces very weak vortices that do not deform the free surface; they are sporadic and short-lived and they appear to be heavily perturbed by the high turbulence of the surrounding flow.

3.3.2.2 Computational domain and boundary conditions

To avoid generating erroneous velocities near the free surface through approximate inlet conditions, the same geometry and roughly the same boundary conditions were used for the simulations as in the physical test bench, even though it is quite costly to model the full channel length. To minimize the cost of computing the flow in the upstream portions of the channel, a relatively coarse mesh is used there, which required a simplification of the inlet boundary condition. Intead of higher-velocity jets exiting the bottom of the diffuser, the flow in the simulation

enters the domain as a uniform vertical upward velocity averaged across the bottom surface of the reservoir. This approximation has a slight impact on the simulated vertical velocity profile in the upstream portion of the reservoir compared to the measured one, but this effect becomes negligible closer to the intake where acceleration into the intake pipe dominates.

A hydrostatic pressure distribution is imposed at the intake pipe exit and adjusted during the course of the simulation to obtain the desired steady water level and flow rate as head losses evolve due to shear and flow contraction into the pipe during the simulation. A minuscule discharge exits the domain through the slanted vertical exit surface of the overflow weir cut into in the upstream wall of the reservoir, (on the left in Fig. 3.11*b*) roughly 2 mm below the desired water level: the weir was found to be necessary in both the experiment and the simulations to stabilize the water level. The flow rate across this vertical surface is not sensitive to the pressure imposed as a boundary condition there because the flow is supercritical. Atmospheric pressure is thus imposed on both this surface and on the top surface through which air freely enters and exits the domain. All the solid boundaries of the channel are defined as smooth no-slip walls.

3.3.2.3 Computational mesh

The computational mesh fills the portion of the channel were the water flows, as well as a volume above the water level to capture the air phase. Preliminary tests suggest that the VOF model is particularly sensitive to grid structure and orthogonality at the air-water interface, and numerical diffusion generally seems to be less important in structured meshes, so a hexahedral structured mesh is generated using ICEM-CFD. To achieve greater mesh density in the vortices, nested o-grids are generated in the wake of the piers. There are 12 to 19 grid points across the vortex core at the free surface, depending on the vortex location, as shown in Fig. 3.10. In order to produce a sufficiently fine mesh across the air-water interface while minimizing total mesh size, highly stretched cells are generated at the free surface in the upstream portions of the flow. The simulations are started on a coarse mesh and then interpolated onto a finer mesh as the flow develops. The high-resolution grids range in size from 4.1 million elements for Case 3 to 5 million elements for Case 8 with the deepest submergence. Results of the simulations suggest that resolution of the vortices might be slighly improved by further increasing the mesh density,

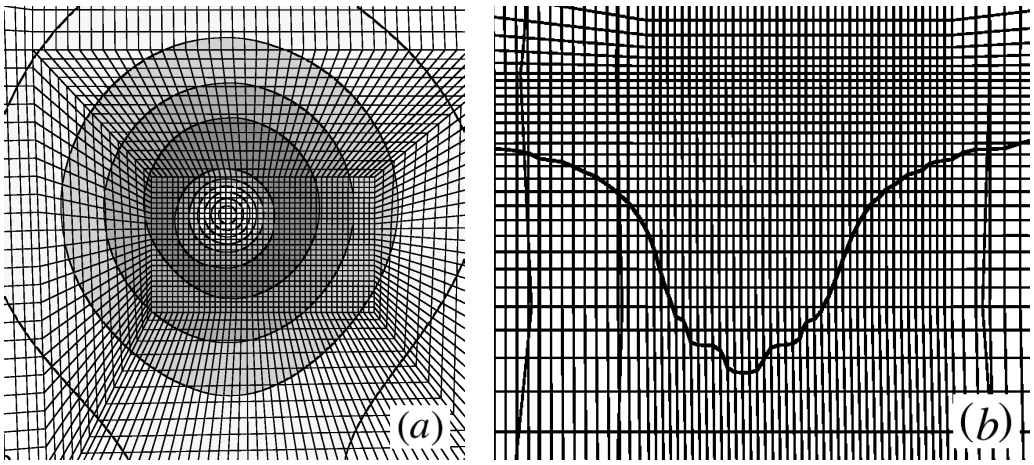

FIGURE 3.10: Plan (*a*) and side (*b*) views of the grid through the vortex, with shading in (*a*) indicating magnitude of V_θ. The free surface profile is indicated by the thick curve in (*b*).

but it would require a substantial increase in the total number of elements and the impact of turbulence modelling on solution accuracy appears to be much more significant and has yet to be suitably resolved (see the following section). Performing a methodical grid sensitivity study at this stage is judged to be premature, given that an effective turbulence modelling strategy has yet to be identified.

3.3.2.4 Turbulence modelling

Initial tests with several Reynolds-Averaged-Navier-Stokes (RANS) turbulence models produced poor results, and LES is judged to be too complex and computationally expensive for the industrial hydraulic optimization context at the current time. Both the k-ε model and the SST model with curvature correction (also an eddy-viscosity model, see Menter, 1994) produced excessively diffuse vortices. When the turbulence model was switched from k-ε to RSM, the vortices initially appeared to become much more intense and concentrated but then instabilities developed at the free surface in upstream portions of the flow (at points 1 and 2 in Fig. 3.11), repeatedly causing the simulation to diverge and fail within a few timesteps of switching to RSM. This may be due to the RSM model being less tolerant of highly stretched grid cells near the free surface in upstream portions of the flow. These highly stretched cells cannot be eliminated without producing an excessively fine mesh with too many cells.

It seems quite clear that the k-ε model predicts vortices that are too diffuse because it overestimates the eddy viscosity in their core. It also appears that relatively high eddy viscosity levels are necessary elsewhere in the domain to stabilize the free surface simulations. In order to test the hypothesis that the excessive radial diffusion of the vortices is caused by the excess eddy viscosity and not by other sources, a custom eddy viscosity distribution is developed, which can be thought of as a variant of the strategy employed by Muntean *et al.* (2005b), Sakai *et al.* (2008) and Ito *et al.* (2010a). An explicitly defined eddy viscosity distribution $\nu_{\mathrm{i}}(X,Y,Z)$ is defined over the computational domain using an analytic expression that is somewhat arbitrarily selected so as to stabilize the upstream flow without inducing diffusion of the vortices.

This approach produces relatively stable solutions without excess amounts of diffusivity in the vortices. $\nu_{\mathrm{i}}(X,Y,Z)$ is set roughly equivalent to the eddy viscosity distribution that is produced by the k-ε simulation, except in the wake of the piers where the vortices form, where ν_{i} is set equal to the molecular viscosity $\nu = 8.9 \times 10^{-6}$ m^2/s. $\nu_{\mathrm{i}} = 120\nu$ in the reservoir and along most of the channel length, and $\nu_{\mathrm{i}} = 10\nu$ in the viscinity of the free surface; this both roughly models the effect of turbulence in the channel and stabilizes the simulation in the free surface region. $\nu_{\mathrm{i}} = 1000\nu$ at the entrance to the pipe where the velocities and shear are very high, with a Gaussian profile that decays radially with increasing distance from the pipe entrance, producing a gradual transition. $\nu_{\mathrm{i}} = 500\nu$ in the rest of the pipe.

3.3.2.5 Simulation procedure

The multiphase simulations are extremely prone to numerical instability, so a multi-pronged and multi-step solution procedure is developed to start the simulations and reach the final result. The procedure includes a specific combination of initial conditions and evolving boundary conditions to start up the flow. One set of solvers and turbulence model is used with smaller timesteps during the early phases of the simulation, and a finer mesh, larger timestep and more accurate solvers and turbulence model are used in the later phases as the flow establishes itself.

The simulations are performed as steady-state simulations with local time-stepping, with a physical timestep of 0.01 seconds at the beginning of the simulations which is gradually increased up to a maximum of 0.06 seconds depending on the stability of the simulation. Due to the length of the channel, an extended period of time is required for changes to propagate from one end of the domain to the other, which translates into thousands of timesteps in this case where small time steps are required to ensure stability.

The flow is initialized at the desired water depth, but it is necessary to start the flow with a negligible velocity along the channel because a fair amount of time is required for the flow to develop and any significant massflow imbalance in the channel generates a local accumulation and increase of the water level, which then travels back and forth along the channel as a low amplitude wave. The low frequency oscillations of the water level caused by these waves decay extremely slowly (over thousands of iterations), causing corresponding oscillations in the flow rate velocities at the intake. The inlet velocity entering the reservoir is therefore started at zero and gradually increased over a hundred timesteps, while the pressure at the outlet of the intake pipe is gradually decreased so that the flow rate out of the channel increses at roughly the same rate.

Numerical instability originates most frequently at locations where the water flow impinges on or turns away from the free surface, which occurs at the points along the channel indicated by numbers 1,2 and 3 in Fig. 3.11. These instabilities are most likely to develop and dominate when the velocity near the free surface is very low. In order to limit their occurance at the beginning of the simulation, a low but non-zero vertical velocity is imposed in the reservoir and a very low streamwise velocity in the channel as initial conditions so that the velocity vectors start out pointing in roughly the right direction.

The homogeneous multiphase solver is used during only the first few hundred timesteps of the simulation because it appears to be less vulnerable to instability linked to velocity vectors that are not aligned with the free surface. The solver is then switched to the inhomogeneous mode before any significant amount of air can be entrained at the downstream end of the reservoir. Small amounts of ‘dissolved’ air are quickly evacuated by the inhomogeneous solver if it is switched on before any accompanying recirculation begins to develop.

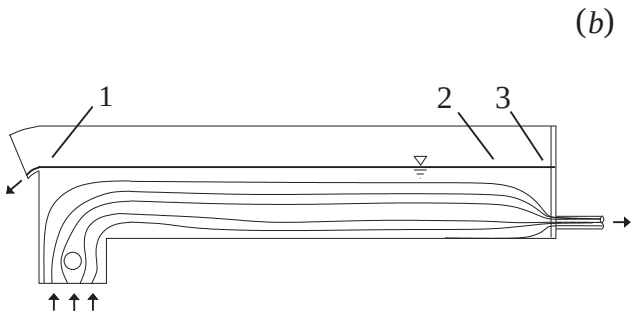

FIGURE 3.11: Computational domain with sensitive free surface flow locations (1,2,3). Flow inflow and outflow are indicated with arrows.

The segregated multiphase solver is also used during the early phases of the simulation and every time the solution is restarted after changing a boundary condition or the mesh because it is much less suceptible these changes than the coupled multiphase solver. The segregated solver computes the velocity field and the volume fraction separately at each time step, while the coupled multiphase solver computes the velocity and interface level simultaneously, in the same matrix (Zwart *et al.*, 2007). The coupled flow solver achieves better and quicker convergence of the massflow equations than the segregated solver once the bulk flow field has been established, and also allows a larger timestep to be used. Any time a boundary condition (such as outflow pressure) or mesh is changed, the solution is started up with the segregated solver for a few hundred timesteps til the flow stabilizes.

For the cases where the imposed eddy viscosity ν_i is used to model turbulence effects, the simulation is started up with the k-ε turbulence model, which is more stable, until the flow in the channel and the vortices has become established. Then the simulation is restarted with the static ν_i distribution using the k-ε solution as an initial condition for the flow field. In the last phase of the simulation, the solution is interpolated onto a finer mesh that has greater resolution where the vortices form.

In order to assess the evolution and stability of the simulation, several flow quantities are monitored during the course of the simulation at different locations in the flow. Variations in the free surface level with time and along the channel length are monitored using the static pressure at different streamwise locations on the bed. The mass flow out the intake pipe and over the weir

are monitored and compared to the mass flow that enters the reservoir to check for mass flow imbalance. The development and intensification of the vortices is roughly monitored through the vertical velocity and vertical component of vorticity ω_z at a point located roughly where the vortex forms a third of the way down from the free surface. The vortex migrates a certain amount so these two values oscillate a fair amount but their mean value over time (particularly V_z) is a useful indicator of the intensification (or breakdown) of the vortex.

Quantities such as the mass flow rate and free surface level continue to evolve after the residuals have flattend out around 10^{-4}. The vortex location and intensity continue to fluctuate, so it is difficult to establish whether or not a stable solution has been reached. In the ν_{i} simulations vortical instabilities with a horizontal axis begin to develop and grow at the upstream limit of the vortex near the free surface, appearing to destabilize the vortex. The instabilities begin to amplify and spread to other parts of the flow, so the simulations are stopped at this point. This instability may be linked to a physical vortex breakdown process but may also be a product of the turbulence model, due to the lack of stabilizing eddy viscosity just outside the vortex core. This outer region is less resistant to instability than the inner core region (Jacquin and Pantano, 2002). In the actual (non-simulated) flow, turbulence is more likely to persist outside the vortex core and may produce a more stable mean azimuthal velocity profile through increased radial diffusion. An unsteady simulation would probably be more appropriate but it was not possible within the time constraints. At the point where the simulations were stopped, oscillations in the mass flow out of the intake pipe were less than 2% of the mean value and oscillations of the free surface level were less than 1% of the total flow depth.

Chapter 4

Free surface intake vortices: Theoretical model and measurements (Manuscript 1)

ABSTRACT

Axially stretched free surface vortices occur at low-head hydropower intakes under specific flow and geometric conditions. Hydropower intakes are defined as having a low head if the difference in water level up- and down-stream from the plant falls in the range of 1 to 5 m, though according to some regulations or categorizations, the upper limit can be as high as 15 m (Hatch Engineering, 2008). When they are sufficiently strong, they can harm performance or cause premature failure of mechanical components. Laboratory-scale experimental models are currently used to assess the risk of vortex formation during the design phase, but uncertainty remains as to how vortex characteristics translate from the laboratory scale to the much larger scale of an actual hydropower plant. This paper proposes a semi-empirical model that roughly predicts how the approach flow and intake geometry determine the key vortex characteristics which are the core radius, bulk circulation and the depth of the free surface depression. The model is developed using detailed velocity measurements of both the approach flow and the

flow inside the vortex in a laboratory-scale physical model, using analytical models and insights drawn from previous work on this and other vortex applications.

4.1 Introduction

Free surface vortices are a common problem directly upstream of low-head hydropower plants and pumping stations. Vortices form in the region approaching the plant in which flow changes from relatively slow moving open channel free surface flow to faster pressure (confined) flow entering the submerged pipe or penstock that leads to the turbines or pumps. The structure that guides the flow through this transition is called the intake, and the vortices are referred to as intake vortices

The phenomenon of intake vortices was studied extensively in the 70s and 80s by researchers seeking to predict vortex characteristics and risk of air entrainment at a given flow rate and submergence. Early efforts relied on scale laboratory experiments (Daggett and Keulegan, 1974; Jain *et al.*, 1978; Pennino and Hecker, 1979; Anwar, 1983) as well as some surveys of vortex activity in full-scale 'prototype' hydropower and pumping intakes (Gordon, 1970; Pennino and Hecker, 1979; Gulliver *et al.*, 1986). Today design engineers use the resulting empirical correlations during the early stages of the design process to estimate the minimum acceptable submergence, which is how close the opening of the intake pipe or penstock may be to the free surface at a given intake velocity before problematic vortices occur (Tastan and Yıldırım, 2010). The predictive accuracy of these correlations is limited by the fact that vortex characteristics such as the characteristic radius, bulk circulation and the tip depth (the total depth of the free surface depression) are very sensitive to the geometry of the intake structure and to the associated velocity distribution. Physical testing using laboratory-scale models therefore remains a key component of the assessment and optimization process for most large projects. though a degree of uncertainty remains when interpreting the results of these tests, because the various forces that control vortex characteristics scale differently.

Many attempts have been made to assess and predict scale effects. Daggett and Keulegan (1974), Jain *et al.* (1978), Anwar (1983), and Tastan and Yıldırım (2010) approach the question empirically, identifying the minimum size of a laboratory model or recommended cut-off values of associated non-dimensional parameters necessary for scale effects to be negligible. These recommended cut-off values vary from author to author (Tastan and Yıldırım, 2010) and may be difficult to meet for large-scale projects such as hydropower intakes within the economic and spatial constraints.

Several analytical models have been developed to model processes such as vorticity generation, diffusion and axial vortex stretching that govern intake vortex characteristics. Vorticity is a vector quantity $\boldsymbol{\omega}$ that locally quantifies the rate of rotation of a fluid particle about its centre of mass. It is defined mathematically as the curl of the velocity vector: $\boldsymbol{\omega} = \boldsymbol{\nabla} \times \boldsymbol{V}$ (Helmholtz, 1867).

The vortex flow is described using a local cylindrical coordinate system (r, θ, z) with z pointing down from the free surface along the central axis of the vortex, and with corresponding radial, azimuthal and axial velocities V_r, V_θ and V_z. If the axial velocity V_z of a vortex increases along its axis, the vortex is said to be axially stretched, and its streamlines converge towards the axis ($V_r < 0$). If viscous losses are negligible, then the vortex's angular momentum is conserved and vorticity in the vortex increases in proportion to the axial gradient (Helmholtz, 1867). In most flows, viscosity tends to smear vorticity radially outwards, leading to a Gaussian-like profile (Rott, 1958).

Burgers (1948) and Rott (1958) independently developed a vortex model in which an equilibrium of axial stretching and viscous diffusion produces a stable vortex with a constant vorticity profile along its axis. They assume that the radial profiles of V_θ and V_r are constant along z and that the axial velocity V_z is independent of r and increases linearly with z: $V_z(z) = az$, $V_r(r) = -ar/2$, where the gradient a is a constant with units of s^{-1} and the profile of V_r is set to satisfy continuity. Solving the axisymmetric Navier–Stokes equations with these assumptions produces

$$V_\theta(r) = \frac{\Gamma_\infty}{2\pi r}\left[1 - \exp\left(-(r/r_o)^2\right)\right], \tag{4.1}$$

where Γ_∞ is the bulk circulation, assumed to reach a constant value far from the vortex centre. What will be hereafter referred to as the characteristic radius r_o is determined by the ratio of viscosity to axial gradient:

$$r_o = 2(\nu/a)^{1/2}, \quad a = \partial V_z/\partial z, \tag{4.2}$$

where ν is the kinematic viscosity of the fluid.

Einstein and Li (1951) applied a modified version of this model to intake vortices (later further adjusted by Bøhling *et al.* (2010)), defining an inner region in which a Burgers vortex is concentrated, surrounded by an external zone with no axial velocity. Odgaard (1986) used Burgers's (1948) model directly to predict critical submergence for an air core vortex in a cylindrical tank with imposed flow rotation, highlighting the link between submergence and the key process of axial stretching (Quick, 1970; Petitjeans, 2003). Odgaard (1986) assumes that the axial velocity in the central portion of the tank follows a linear profile from zero at the free surface to U_i at the bottom of the tank, so that $a = U_i/H$, where H is the water depth and U_i is the mean outflow velocity. Odgaard's and subsequent results (Hite and Mih, 1994; Ito *et al.*, 2010b) support the use of Burgers's model for modelling intake vortices, even if it does not capture their full complexity. Other variants of Burgers's model include Lundgren (1985); Hite and Mih (1994); Miles (1998), Rossi *et al.* (2004), Andersen *et al.* (2006), Stepanyants and Yeoh (2008b), Ito *et al.* (2010b), and Wang *et al.* (2011).

There remains a shortage of detailed measurements of vortices and the flow surrounding them for geometries more closely resembling hydropower intakes, such as those studied by Hite and Mih (1994) and Nakayama and Hisasue (2010). These are required to help adapt models of free surface vortices to specific intakes and to better understand how geometry and intake approach flow influence vortex characteristics (Quick, 1970; Yıldırım *et al.*, 2000; Ansar and Nakato, 2001). Computational fluid dynamics models have potential to help predict the flow field approaching intakes, but they remain expensive and insufficiently validated for modelling the vortices themselves with sufficient accuracy within the time and economic constraints of an hydraulic industrial context.

This paper aims to build on Odgaard's (1986) model by first testing its hypotheses using experimental data collected in a laboratory model and then adapting it to incorporate the influence of the intake geometry. The paper is divided into three parts. The first part presents Burgers's vortex model and some relevant insights from other work regarding axial flow and turbulence. The second part describes the experimental setup and the detailed velocity measurements that were taken to establish the relationship between the geometry, the flow approaching the intake pipe and the characteristics of the vortices that form. The third part uses the measurements to adapt Burgers's vortex model to the specific intake geometry studied in the laboratory.

4.2 Experimental setup

A laboratory-scale experimental model is constructed that reproduces the flow configuration of a simplified low-head hydropower intake with approximately uniform approach flow conditions. As shown in Fig. 4.1, the channel has a square 1 by 1 m cross-section with a 3.9 m long flat bed and a circular 'intake' pipe of inner diameter d = 0.115 m mounted flush into the downstream wall of the channel, with its axis located 0.14 m above the channel bed.

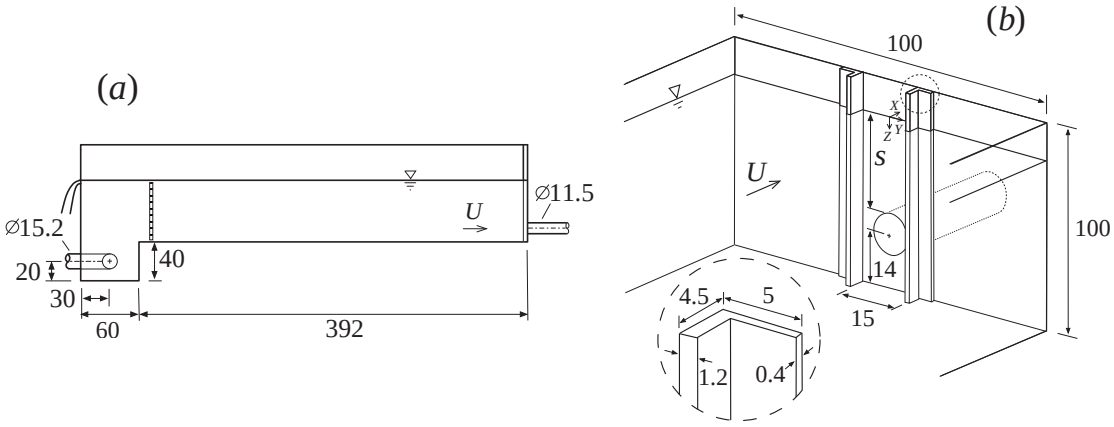

FIGURE 4.1: Vertical section (*a*) and isometric (*b*) views of the laboratory model (dimensions in cm).

Two narrow piers are mounted perpendicular to the downstream wall on each side of the intake pipe. Each pier generates a relatively stable vortex pair in its wake (Hite and Mih, 1994) with one vortex starting at the free surface and one starting from the floor of the tank; both

vortex tails are entrained into the outlet pipe as shown in Fig. 4.2(a). Similar piers are found at hydropower intakes where they hold the trash-racks across the penstock opening. The piers in the experiment protrude further into the flow and are less streamlined. This shape produces more stable vortices and a clearly defined separation zone, thus easing measurements and analysis. Figure 4.2(b) shows a top view schematic of the free surface streamlines in the experiment, with the piers and back wall shown in grey. Only the free surface vortices are examined in this paper since their presence and effects are of greater concern to plant operators. The two piers are spaced k=15 cm apart, symmetrically about the pipe axis; their cross-section is rectangular, 1.2 cm thick and 4.5 cm long and they span the full channel depth (Fig. 4.1(b).

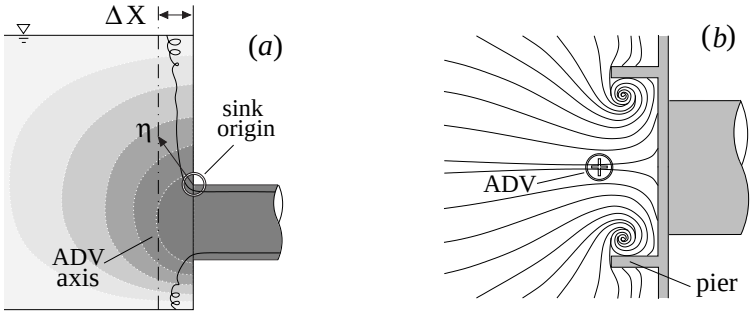

FIGURE 4.2: (a) Schematic side view of the intake approach flow on the vertical plane along the channel centerline, with shading indicating velocity magnitude. The location of the horizontal line sink described by Eq. 4.3 is shown at the top of the intake pipe opening. (b) Top view sketch of streamlines separating off the pier tips.

The water level in the channel is controlled by the back-pressure at the exit of the intake pipe and it is stabilized with a square-crested weir mounted into the upstream wall of the channel. The water is injected into the tank through a T-shaped diffuser submerged in a 60 cm long, 40 cm deep reservoir directly upstream of the channel. Large eddies produced as the flow exits the diffuser are broken down with a 1.9 cm (3/4") thick sheet of aluminum honeycomb placed just downstream of the step from the reservoir to the channel. A global coordinate system (X,Y,Z) is defined with its origin at the free surface, half-way across the downstream wall of the channel. Z points down towards the bed and X points downstream and Y points towards the right when looking downstream.

Eight combinations of submergence and intake velocity are selected to produce a wide range of vortex intensities (see Table 4.1). The intake velocity ranges from U_i=0.58 to 1.80 ms^{-1} and

TABLE 4.1: Operating conditions for the measurements

Case	s/d	U_i (ms^{-1})	Re $\times 10^5$	$\mathrm{Re}_{\mathrm{ch}}$ $\times 10^4$	Fr	We $\times 10^3$
1	1.5	0.58	0.8	2.7	0.4	0.8
2	1.5	0.86	1.2	4.1	0.7	1.8
3	1.5	1.40	2.0	6.7	1.1	4.8
4	2.4	0.86	1.9	2.7	0.5	2.8
5	2.4	1.80	4.1	5.5	1.1	12.4
6	3.3	0.86	2.7	1.9	0.4	3.9
7	3.3	1.40	4.3	3.1	0.7	10.2
8	3.3	1.80	5.6	4.0	0.9	16.9

the relative submergence s/d ranges from 1.5 to 3.3, where $U_i = 4Q/(\pi d^2)$ is the mean velocity in the intake pipe and s is the vertical distance from the free surface to the top of the pipe opening (as shown in Fig. 4.1 *b*). The deepest submergence studied (s/d = 3.3) is the approximate transition point where the vortices become much weaker and more sporadic. $\mathrm{Re} = U_i s/\nu$, $\mathrm{Fr} = U_i/(gs)^{1/2}$ and $\mathrm{We} = \rho U_i^2 s/\sigma$ are the submergence Reynolds, Froude and Weber numbers respectively, and $\mathrm{Re}_{\mathrm{ch}} = Q/(s\nu)$ is the channel Reynolds number. The experiment is operated at temperatures ranging from 12 to 15 °C.

4.2.1 Measurements

Three types of data are collected at each operating condition, which document the flow conditions upstream from the intake and directly in front of it, as well as the velocity field inside the vortex and the free surface depression it produces. These data allow us to clarify how the intake geometry controls the structure of the flow directly in front of it and how it thereby controls the vortex characteristics. The measurements are then used to guide the choice of analytical relations and coefficients used to relate the vortex characteristics to the intake configuration. The data are collected using an acoustic Doppler velocimeter (ADV) and high-speed films recorded at 50 to 250 frames-per-second that simultaneously record the free surface profile and particle trajectories for particle tracking velocimetry (PTV).

4.2.2 ADV measurements

A Sontek Micro-ADV is used to record the larger-scale structure of the flow approaching the intake and to quantify how the velocity fields outside the vortex control the circulation and the characteristic radius of the vortex through axial stretching. Mean velocities U_X, U_Y and U_Z are measured with a sampling frequency of 30 Hz and averaged over two minutes. Coarse measurement grids are taken 2 m and 0.2 m upstream of the intake and a vertical line of more closely-spaced measurements is taken at $X = -55$ mm, directly upstream from the intake pipe on the channel centreline. The $X = -55mm$ profile is referred to hereafter as the intake approach flow. The ADV orientation is accurate within 5° and the signal to noise ratio was above 8 for the majority of the measurements, which is sufficient for mean velocity measurements.

The channel flow is roughly uniform with moderate left-right asymmetry across the channel cross-section that is probably due to a bend in the feeder pipe. The relative asymmetry is amplified at deeper submergences near the free surface where velocities are very low, possibly due to influence of the vortices.

4.2.3 PTV Measurements

An optical method such as PTV is preferred to measure the velocities in the vortices because they are small and easily perturbed. The vortices also fluctuate in intensity and position over time scales of a few seconds. PTV is accessible and allows the velocity to be measured at many points across the vortex over time-scales (0.3 to 2 seconds) that are sufficiently small compared to the vortex time-scale. Vortex stability is assessed from the shape of the free surface depression, which is visible on the particle images, in order to select appropriate film segments.

Velocities are measured in the right vortex by tracking particles (Pliolite VT) that are injected into the vortex just below the free surface and filmed through the outflow wall with a high-speed camera (Fastec Troubleshooter). The particles are injected at the centre of the vortex to get a more clearly defined profile in the vortex core ($r < r_o$), since velocities there have the most significant impact on the free surface depression. The vortex is lit from above and below

to compensate for light refracted by the free surface depression. The particles have diameters ranging from 150 to 350 μm so each particle covers 0.6 to 1.6 pixels in the image. They have a density of 1.003 $\mathrm{kg \cdot m^{-3}}$ and a terminal velocity of 0.6 to 1.3 $\mathrm{mm \cdot s^{-1}}$ in still 12 °C water. The images are recorded at 250 frames per second in order to capture the high aziumthal velocities in the vortex core. For the deepest submergence cases, the azimuthal velocities are much lower so 50 frames per second is more appropriate. The particles are tracked using an open-source particle-tracking code developed by Sbalzarini and Koumoutsakos (2005) that was modified for this experiment to optimize tracking.

4.3 Analysis and discussion

In this section, the vortices observed in the experiment are qualitatively described, followed by a discussion of the procedure used to process and analyze the PTV data to obtain profiles of the azimuthal velocity V_θ and axial velocity V_z. The characteristic radius r_o and the bulk circulation Γ_∞ are extracted from the $V_\theta(r)$ profile using Burgers's vortex model (Eq. 4.1) and the degree of axial stretching a is extracted from $V_z(z0)$. A theoretical model is then developed by combining Burgers's model with simple analytical relations that link the characteristic radius r_o, and the bulk circulation Γ_∞ to the intake approach flow and intake geometry. The analytical relations are adjusted to the particular intake geometry using empirical coefficients fitted to measurements from the experiment. The final model predicts the range of r_o, Γ_∞ and tip depth values that one should expect for a given set of flow conditions for this configuration.

4.3.1 Qualitative description of the vortices

The vortices produced at the lowest submergence are the strongest and most persistent and those formed at the deepest submergence are the weakest and least persistent. The vortices at the low and medium submergences produce a visible depression of the free surface with a tip depth h_0 (maximum depression) ranging from a few millimeters to a deep funnel more than a centimeter deep that periodically entrains air bubbles at the highest intake velocity. The vortices produced

at the deepest submergence (s/d = 3.3) produce such a small depression that it can only be detected from the deformation of reflections on the free surface. At greater flow rates, they rarely last more than a few seconds before dissipating and they require many minutes to form again. They also appear to be more strongly influenced by minor asymmetries in the approach flow. At the lowest flow rate for the deepest submergence, the vortices produce a more coherent and long-lasting dye core; this is probably due to lower background turbulence levels and associated perturbations.

4.3.2 Analysis of PTV measurements

In this section, the PTV data are analyzed to obtain the vortex characteristic radius r_o, axial gradient a, and bulk circulation Γ_∞ for a few vortices measured at each operating condition. The radial profile of the azimuthal velocity $V_\theta(r)$ and the axial profile of the axial velocity $V_z(z)$ are derived for each film segment from the particle trajectories identified by the particle-tracking code, and Burgers's model is fitted to the profiles to extract r_o, a, Γ_∞. The relationship between these quantities and the mean approach flow velocities measured using the ADV are discussed in the next section.

The transverse coordinate of the particles follows a sinusoidal path in time, of amplitude $2r_j$ and period τ_j, which is computed for every complete trajectory cycle j found in the image sequence. Assuming that the azimuthal velocity is steady and axisymmetric and that $V_\theta \gg V_r$, V_θ can be computed as $V_{\theta,j}(r_j) = 2\pi r_j \tau^{-1}$. Burgers's model (Eq. 4.1) can be rewritten in terms of the frequency τ and fitted to the measured velocities by adjusting r_o and Γ_∞. Fitting Burgers's model to plots of (r_j, τ_j) or the inverse (r_j, τ_j^{-1}) yields different values for r_o and Γ_∞ since points at large radii are weighted more heavily when fitting to τ and smaller radius points are weighted more heavily for τ^{-1}. The mean of the two values obtained from each fitting approach is indicated in the graphs of the measured r_o and Γ_∞ values (Figs. 4.3 to 4.5), by the points, while the two fitted values are indicated by the extremities of the error bars. A greater difference between the two values obtained suggests greater deviation from Burgers's profile. Figure 4.3 shows the 18 radial profiles of azimuthal velocity $V_\theta(r/r_o)/V_{\theta,\max}$ that were measured for the eight operating conditions, with Burgers's profile (Eq. 4.1) plotted as a solid line. The data

points measured outside the vortex core ($r_j > r_o$) tend to stray further from the model profile, possibly due to the non-axisymmetric geometry or greater turbulence there.

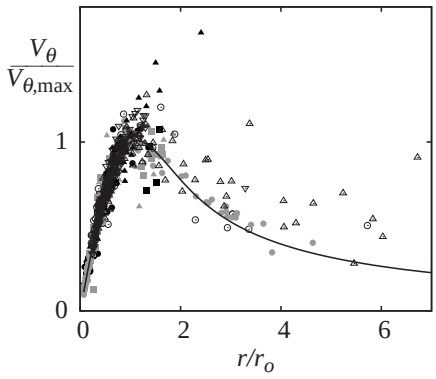

FIGURE 4.3: The radial profiles of V_θ measured using PTV for the eight operating conditions. ($\triangledown, \triangle, \odot, \boxdot$), measured values at intake velocities U_i=(0.59, 0.86, 1.4, 1.8) ms^{-1} respectively with shade (○, ●, ●) indicating the relative submergence s/d=(1.5, 2.4, 3.3) respectively; ——, Burgers's profile (Eq. 4.1) fitted to the data.

The axial velocity V_z is computed by averaging the vertical displacement travelled by the particles as they travel a full cycle around the circumference of the vortex, because V_z fluctuates significantly as the particles complete each circuit around the vortex. These fluctuations are due to deviation from axisymmetry as well as to optical effects caused by the viewing angle of the camera. (These effects are discussed at greater length in Appendix C). Deviation of the V_z field from axisymmetry may be due to the presence of the wall or pier, curvature of the vortex, or long-wave oscillations travelling along its axis (Crow, 1970; Jacquin and Pantano, 2002).

The mean slope $a = \partial V_z/\partial z$ is obtained by fitting a straight line through the measured $V_z(z)$ values. The slopes of the non-dimensionalized profiles obtained in this manner seem quite consistent for each submergence over different flow rates, despite considerable scatter of the individual velocity points (see Fig. 4.4*b*). A few profiles that cover the full vortex length are obtained by tracking TiO_2 powder 'dye' injected into the vortex core from the free surface to the intake pipe for three conditions (the highest flow rates at each submergence level). These profiles are consistent with those obtained using PTV and appear in Fig. 4.4(*b*) as well.

4.3.3 Axial flow gradients and the vortex characteristic radius

This section demonstrates how the characteristic radius r_o can be predicted from the gradients of the flow outside the vortex. First, r_o is shown to be quite well predicted by the ratio of the molecular viscosity ν to the axial gradient of the axial velocity $a = \partial V_z/\partial z$ inside the vortex near the free surface. Next, the axial gradient a inside the vortex is shown to be driven by the vertical gradient of the intake approach velocity $\partial|U|/\partial Z$ outside the vortex. Finally, the non-dimensional intake approach velocity $|U|/U_i$ for all the operating conditions can be written as a simple analytical function of the non-dimensional distance η/d to the top of the inlet, with two empirical coefficients that account for the specific geometry of the intake. In order to present the resulting vortex model in a more logical sequence, these three elements are presented below in the reverse order: from the structure of the intake approach flow to the flow inside the vortex to the characteristic radius.

First, the intake approach flow is examined. For the purpose of evaluating mean vertical gradients, we find that the flow bracketed by the piers can be sufficiently well described as a slice of two-dimensional flow into a horizontal line sink, as has been employed by other authors such as Bøhling *et al.* (2010) and Yıldırım *et al.* (2000). In this case we locate the horizontal sink at the upper edge of the intake opening, as shown in Fig. 4.2(a). Accordingly, the flow is described by

$$\frac{|U|_{\text{fit}}(\eta)}{U_i} = \frac{\mathrm{c}_1 d}{4k}\left(\frac{d}{\eta} - \mathrm{c}_2\right). \tag{4.3}$$

$|U| = (U_X^2 + U_Y^2 + U_Z^2)^{1/2}$ and η is the total distance from the top of the inlet opening to each measurement point, so that $\eta = [(s-Z)^2 + (\triangle X)^2]^{1/2}$ (see Fig. 4.2a). $\triangle X = 55$ mm is the horizontal distance from the ADV measurement line to the downstream wall of the channel. The non-dimensional coefficients c_1= 0.8 and c_2=0.28 are adjusted to produce the best fit to the non-dimensionalized approach velocities $|U|/U_i$ measured by ADV. As shown in Figure 4.4(a), the measured approach velocities (indicated by points) collapse onto a single line which corresponds to the relation given by Eq. (4.3). for $|U|_{\text{fit}}/U_i$ (shown by the solid curve). The upper boundary formed by the free surface causes the flow to deviate from that into a pure line sink. At the deepest submergence, the approach velocity approaches zero at the free surface and

begins to recirculate slightly about a horizontal axis formed by the line where the free surface meets the downstream wall. The point $\eta/d = c_2 = 0.28$ where the line crosses the graph's vertical axis in Figure 4.4(a) roughly corresponds to the point where recirculation begins to occur at the free surface for the deepest submergence.

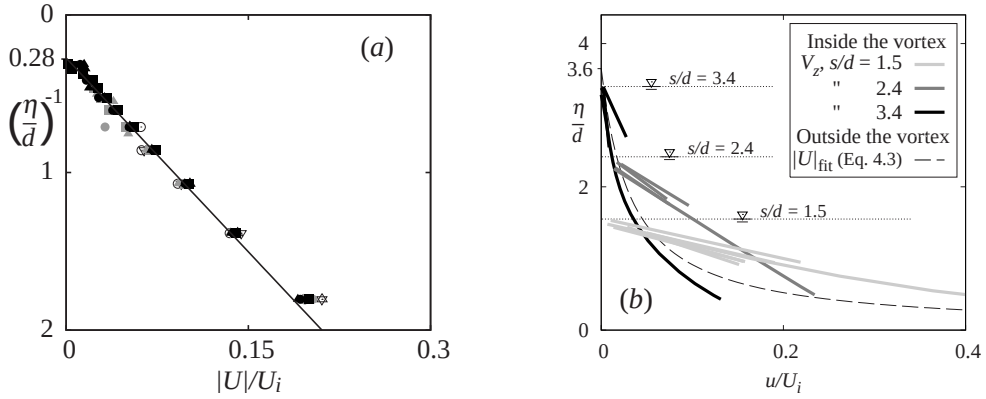

FIGURE 4.4: (a) The mean magnitude of velocity $|U|/U_i$ outside the vortex. ——, the sink flow $|U|_{\text{fit}}$ (Eq. 4.3); ($\triangledown, \triangle, \odot, \boxdot$), ADV measurements, see Fig. 4.3 caption for the key. (b) Velocity measured inside and outside the vortex (V_z and $|U|$, respectively).

Next, we examine the link between the intake approach flow (outside the vortex) and the axial flow inside the vortex. Although the vortex is not perfectly vertical along its full length, it is close enough to vertical near the free surface, which is the zone of interest. As shown in Fig. 4.4(b), the measurements reveal that the mean gradient of the axial flow V_z inside the vortex is driven by the mean vertical gradient of the velocity outside the vortex. However it tends towards a more linear profile for the low and medium submergences, producing much higher axial velocities and gradients near the free surface inside the vortex than outside it. The thick solid lines in Fig. 4.4(b) show the axial velocity V_z/U_i measured inside the vortex, while the dashed line shows $|U|_{\text{fit}}/U_i$, as defined in Eq. (4.3). The location of the free surface is indicated for each submergence; moving upward on the graph to larger values of η/d indicates a greater vertical distance from the intake pipe.

The central jet of higher V_z following a linear axial profile resembles the axial velocity field produced by Rossi *et al.*'s (2004) analytical/numerical model and the simulation results of Bøhling *et al.* (2010). It is possible that the linear axial profile of V_z forms inside the vortex

because it is more stable than a non-linear one. Pressure may play a role in pushing the axial profile of V_z from a non-linear one towards a linear one: the tighter vortex produced by the steeper axial gradient near the intake opening should produce a greater pressure local drop due to centripetal acceleration in the vortex that could drive greater axial velocity from the weaker gradient zone near the free surface to the stronger gradient region closer to the intake pipe. V_z appears to stay closer to the velocity $|U|$ outside the vortex for the deepest submergence, developing a linear profile only under some conditions. The effect of the pressure gradient may be too weak under these conditions to push the axial velocity towards a more linear one. Alternatively, the linear axial profile may not have time to form if the vortices have a shorter lifespan, or a weak gradient $\partial V_z/\partial z$, (Nolan, 2001) or weak circulation (Jacquin and Pantano, 2002) are insufficient to stabilize the vortices in the presence of the radial gradient in V_z.

The axial gradient of V_z near the free surface is significant because it determines the characteristic radius r_o of the vortex in combination with the molecular viscosity ν. As shown in Figure 4.5(a), r_o extracted from the measured azimuthal velocity profile (Fig. 4.3) is well predicted by Burgers's model $r_o = 2(\nu/a)^{1/2}$, with $a = \partial V_z/\partial z$ extracted from the same particle trajectories as r_o. The horizontal error bars indicate the standard error of the linear curve fit on a (see Appendix C) and the vertical error bars indicate the difference between the r_o values obtained by fitting Burgers's profile to $\{r, \tau\}$ or to $\{r, \tau^{-1}\}$ (see section 4.3.2 above). Previous authors proposed using an effective turbulent viscosity ν_{eff} to predict r_o (Odgaard, 1986; Hite and Mih, 1994), but here the molecular ν predicts r_o in a case with surrounding turbulent flow quite well, as it did in the laminar case studied by Petitjeans (2003). It supports the hypothesis that radial turbulent mixing is suppressed inside the vortex by the flow rotation as has been extensively documented in airplane wing tip vortices and other applications (Spalart, 1998; Jacquin and Pantano, 2002), where the spreading rate of vortices in turbulent flow has been shown to be governed by viscous diffusion, not turbulent diffusion (Cotel and Breidenthal, 1999). It would appear that turbulence is suppressed to a significant degree within intake vortices as well, given that dye injected into the vortex produces a clearly delimited dye core (Anwar, 1983; Hecker, 1987; Schäfer and Hellman, 2005), but it is possible that a sufficient level of turbulence persists to influence diffusion and hence r_o. This question is discussed further in (Suerich-Gulick *et al.*, 2013c).

Greater scatter and deviation from the predicted value of r_o is observed for the deep submergence (black data points), where r_o is more sensitive to variations in a and where the slope of $V_z(z)$ is very small and difficult to distinguish from the azimuthal oscillations. It is much more difficult to assess the stability of these shorter-lived vortices since they don't deform the free surface enough to be visible from the side, so these vortices may not have reached the equilibrium state assumed in Burgers's model, and a may vary considerably with time for a given operating condition as the vortex forms, strengthens and weakens.

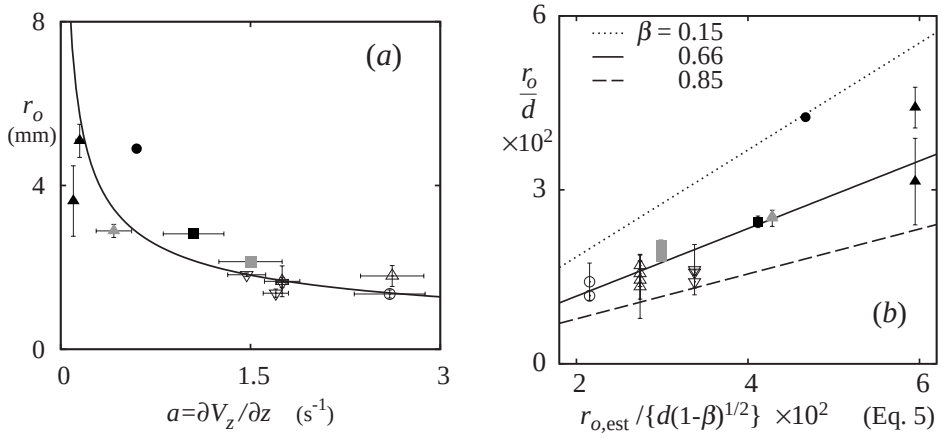

FIGURE 4.5: (*a*) Dependence of the measured characteristic radius r_o on the axial velocity gradient $\partial V_z/\partial z$ measured inside the vortex near the free surface. ——, r_o estimated from Eq. (4.2) using the measured axial gradient a; ($\triangledown,\triangle,\odot,\boxdot$), PTV measurements, see Fig. 4.3 caption for the key. (*b*) Dependence of r_o on the geometry and flow conditions. (·····, ——, --), r_o estimated from Eq. (4.5).

We have established that r_o is controlled by ν and $\partial V_z/\partial z$ and that the profile $V_z(z)$ is driven by the intake approach velocity. r_o can therefore now be predicted as a function of the submergence s/d and the intake velocity U_i. Given the uncertainty as to how much $V_z(z)$ will tend towards a more linear profile, a range of values for r_o is predicted instead of a fixed value. We assume that the axial velocity V_z inside the vortex matches the magnitude of velocity $|U|$ outside the vortex at the free surface and at a distance $z = \beta s$ below the free surface, following a linear profile between the two points. The non-dimensional coefficient β, ranging from 0 to 0.85, indicates how far the linear profile extends below the free surface. $\beta = 0.66$ indicates that the linear profile extends 2/3 of the distance from the free surface to the top of the intake pipe and $\beta = 0$ would indicate that V_z matches the $|U|$ profile along the full length of the vortex. $|U|_{\text{fit}}$ is estimated using Eq. (4.3) with $\eta \approx s$ at the free surface and $\eta \approx (1-\beta)s$ at $z = \beta s$,

producing

$$a_{\text{est}} = \frac{c_1 U_i d^2}{4ks^2(1-\beta)}. \tag{4.4}$$

The resulting characteristic radius $r_{o,\text{est}}$ is obtained by substituting a_{est} into Eq. (4.2):

$$r_{o,\text{est}} = \frac{4s}{d}\left[\frac{\nu k(1-\beta)}{c_1 U_i}\right]^{1/2}. \tag{4.5}$$

When $V_z(z)$ follows the outside profile $|U|(Z)$ over most of the vortex length (corresponding to a smaller value of β), then the axial gradient $a = \partial V_z/\partial z$ at the free surface is weaker, producing a larger characteristic radius r_o for a given U_i and s/d. If a linear profile forms over a greater proportion of the flow (larger β), then a greater a at the free surface will produce a smaller characteristic radius. Figure 4.5(b) compares the values of r_o/d measured in the experiment to the envelope of values estimated from Eq. (4.5) using different values of β (0.15,0.66,0.85). The solid line $\beta = 0.66$ roughly corresponds to the profiles observed in Fig. 4.4(b) for $s/d = 2.4$ and some cases of $s/d = 1.5$. $\beta = 0.15$ (dotted line) and $\beta = 0.85$ (dashed line) roughly bracket the measured values that lie above and below this mean, respectively.

In this graph and the next, all the measurements for a given operating condition are vertically aligned, so the significant variability of r_o within one operating condition is clearly visible. Once again the measured values of r_o for the deep submergence (black points), stray furthest from the mean value in Fig. 4.5(b). It is likely that some of this variability is due to variations in the axial velocity profile inside the vortex,

4.3.4 Bulk circulation Γ_∞

The bulk circulation Γ_∞ is controlled by the interaction of the channel flow with the intake geometry, as vorticity generated upstream or near the intake becomes concentrated into a vortex above the intake pipe through axial stretching (Quick, 1970; Hite, 1991). Γ_∞ is estimated by integrating V_θ along the full circumference of a circle of radius $r \gg r_o$ (Thomson, 1869) since the bulk of vorticity is concentrated in $r < r_o$: $\Gamma_\infty = \Gamma(r \gg r_o) = \int_0^{2\pi} V_\theta r d\theta$. The two free surface vortices are roughly confined to the wake of the pier here in all but one case, so the

integral is computed along a circle of diameter l_p inscribed inside the region delimited by the pier and the downstream wall (Hite, 1991) (see Fig. 4.2*b*). The azimuthal velocity on this circle should be proportional to the mean horizontal free surface velocity measured directly in front of the intake (Anwar, 1968a), which is roughly equal to $|U|_{\text{fit}}$ at $\eta = s$, since $U_Z = 0$ at the free surface. Γ_∞ is therefore estimated as $\pi l_p |U|_{\text{fit},\eta=s}$. As was the case for r_o, there are significant variations in Γ_∞ at each operating condition, so we estimate a range of values for Γ_∞ instead of a fixed value:

$$\Gamma_{\infty,\text{est}} = \frac{\text{c}_3\text{c}_1 d U_i \pi l_p}{4k}\left(\frac{d}{\text{c}_4 s} - \text{c}_2\right), \tag{4.6}$$

where the coefficients c_3 and c_4 are fitted to the measured data. $\text{c}_3 = 0.33$ and c_4 takes two values, 1.0 and 0.6 which give the lower ($\Gamma_{\infty,\min}$) and upper ($\Gamma_{\infty,\max}$) estimated values of Γ_∞, respectively. The resulting range of values is indicated by the grey boxes in Fig. 4.6(*a*), while the points show the measured values. The error bars indicate the variation between the Γ_∞ values obtained by fitting Burgers's profile to $\{r, \tau\}$ or to $\{r, \tau^{-1}\}$ (see section 4.3.2 above).

Setting c_4 to 0.6 instead of 1.0 is roughly equivalent to estimating the circulation from the approach velocity $|U|$ a third of the way down from the free surface instead of directly at the free surface. This suggests that the stronger approach velocity below the free surface may be strengthening the vortex to a greater Γ_∞ value under certain conditions, for example if the vortex lasts longer. It also appears that the magnitude of the variations in Γ_∞ might scale with the channel Reynolds number Re_{ch}, as shown in Fig. 4.6(*b*). The upper limit on the variations is roughly given by

$$\Gamma_{\infty,\max} - \Gamma_{\infty,\min} \approx \text{c}_5 \nu \text{Re}_{\text{ch}}, \tag{4.7}$$

where $\text{c}_5 = 0.06$ is fitted to the measured data. Perhaps the greater turbulence levels at greater Reynolds numbers produce greater temporal fluctuations in the free surface velocity, generating greater circulation at certain moments.

In all cases except for case 6 ($U_i = 0.86, s/d = 3.3$), the mean intensity of the two free surface vortices appears to be roughly equal when averaged over time. In case 6, the mean approach velocity at the free surface was so weak that the flow structure was qualitatively different from

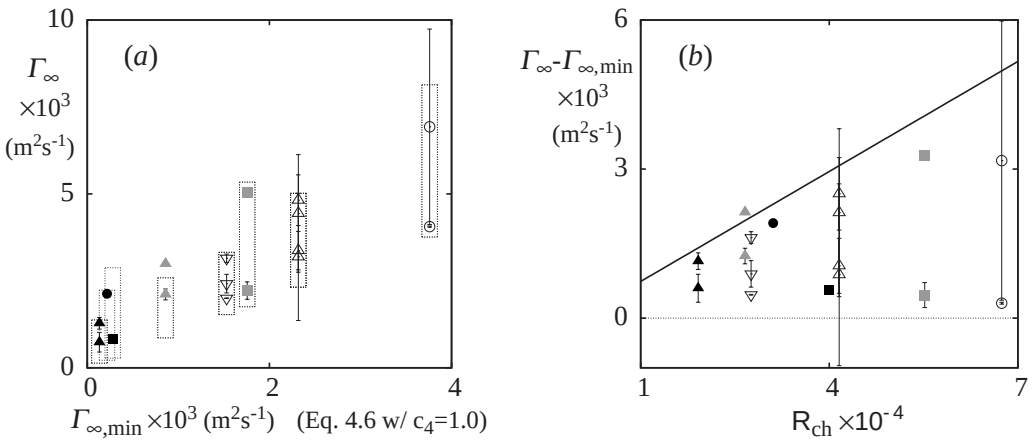

FIGURE 4.6: The bulk circulation Γ_∞. (*a*) Comparison of measured to estimated values: ($\triangledown,\triangle,\odot,\boxdot$), measured values, see Fig. 4.3 caption for the key; $\square$, estimated range (Eq. 4.6); (*b*) Variation in measured Γ_∞ as a function of $\mathrm{Re_{ch}}$: ——, estimated upper limit (Eq. 4.7).

the other cases and only one vortex formed at any given time, halfway between the two piers. The data points for this case are not included in Fig. 4.6.

4.3.5 Free surface depression

The centripetal acceleration V_θ^2/r in the vortex generates a pressure drop in its centre and hence a depression of the free surface whose magnitude is determined by the equilibrium of the forces exerted by gravity, centripetal acceleration, and surface tension. Neglecting surface tension, which is left to a subsequent paper (Suerich-Gulick *et al.*, 2013c), an analytical relation for the tip depth h_0 is obtained by substituting Burgers's profile (Eq. 4.1) for $V_\theta(r)$:

$$h_0 = \int_\infty^0 \left(\frac{V_\theta(\acute{r})^2}{g\acute{r}} \right) d\acute{r} = \frac{0.17\Gamma_\infty^2}{\pi^2 r_o^2 g}, \tag{4.8}$$

where h_0 is the distance from the nominal (undeformed) free surface down to the lowest point of the free surface depression caused by the vortex, and g is the gravitational acceleration.

The tip depth $h_{0,\mathrm{comp}}$ that corresponds to the V_θ profiles measured in the experiment is computed by substituting the measured values of Γ_∞ and r_o into Eq. (4.8). It is compared in Fig. 4.7(*a*) to the actual measured tip depth $h_{0,\mathrm{exp}}$ recorded in the same film segments as the particle trajectories used to measure the velocities, allowing us to evaluate if the velocities were

properly measured and if Burgers's model is appropriate. The solid line in Fig. 4.7(a) indicates exact agreement between $h_{0,\mathrm{comp}}$ and $h_{0,\mathrm{exp}}$ and the horizontal error bars show the spread in r_o and Γ_∞ values obtained from the two fitting methods (section 4.3.2), while the symbols indicate their mean. The $h_{0,\mathrm{comp}}$ values follow the same trend as $h_{0,\mathrm{exp}}$, but the former are larger because they are computed without surface tension, which significantly reduces the total depression in the experiment.

Alternatively the expressions for Γ_∞ (Eq. 4.6) and r_o (Eq. 4.5) developed above can be substituted into Burgers's relation (Eq. 4.1) for $V_\theta(r)$, producing an estimated tip depth $h_{0,\mathrm{est}}$ in terms of the intake conditions and geometry:

$$\frac{h_{0,\mathrm{est}}}{d} = \frac{0.17\Gamma_\infty^2}{\pi^2 d r_o^2 g} = \frac{\mathrm{c}_6 \mathrm{c}_3^2 \mathrm{c}_1^3}{(1-\beta)}\ \mathrm{ReFr}^2 \left(\frac{d}{k}\right)^3 \left(\frac{l_p}{s}\right)^2 \left(\frac{d}{\mathrm{c}_4 s} - \mathrm{c}_2\right)^2, \tag{4.9}$$

where $\mathrm{c}_6 = 6.6 \times 10^{-4}$ is determined by the integration and $\mathrm{ReFr}^2 = U_i^3/(\nu g)$.

The estimated range of $h_{0,\mathrm{est}}/d$ compares fairly well to the measured values $h_{0,\mathrm{exp}}/d$, as shown in Fig. 4.7(b). The symbols indicate the measured values and the gray boxes indicate the values estimated using Eq. (4.9) with ($\mathrm{c}_4 = 1.0, \beta = 0.15$) for the minima, ($\mathrm{c}_4 = 0.66, \beta = 0.75$) for the mid-range values, and ($\mathrm{c}_4 = 0.6, \beta = 0.85$) for the maxima. There is much greater scatter in this graph, due to the variations in r_o and Γ_∞ discussed above.

4.4 Summary and conclusions

Detailed measurements in a laboratory-scale physical model of a simplified intake with piers are used to adapt Burgers's vortex model to include the influence of geometry and the approach flow velocity profile on vortex characteristics. Approach flow and vortex characteristics recorded at eight combinations of intake velocity U_i and relative submergence s/d allow quantitative relations for the vortex's characteristic radius r_o, bulk circulation Γ_∞ and tip depth h_0 to be developed in terms of U_i and s/d.

First, a simplified sink model is formulated to describe the flow directly in front of the intake. Then a quantitative relation is established between the velocity profile directly in front

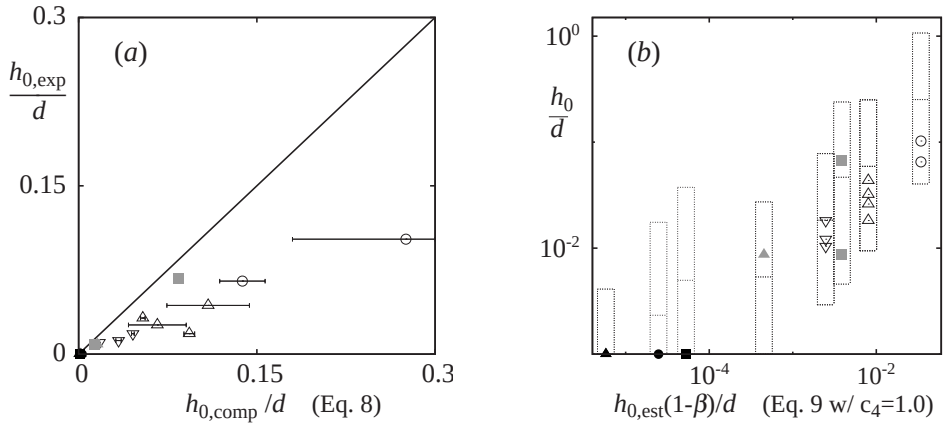

FIGURE 4.7: (*a*) Free surface depression. Correspondence between the measured tip depth $h_{0,exp}$ and the tip depth $h_{0,comp}$ computed from the measured $V_\theta(r)$ profile ($\triangledown, \triangle, \odot, \boxdot$), measured values (see Fig. 4.3 caption for the key); ——, exact correspondence. (*b*) The measured tip depth and the predicted limiting values estimated from the geometry and flow conditions (Eq. 4.9). ⌸, range of estimated values.

of the intake and the axial velocity profile $V_z(z)$ inside the vortex, highlighting the role of the intake approach flow in driving axial vortex stretching. The measurements strongly suggest that radial turbulent diffusion is effectively suppressed in the vortex core, in agreement with observations in wing tip vortices. The sink model is also used to develop a relationship between Γ_∞ and U_i and s/d.

It is difficult to predict how much $V_z(z)$ will stray from the non-linear profile of the flow outside the vortex towards the more linear one observed inside the vortex and to explain the significant variations in Γ_∞ observed for a given operating condition. Due to observed variations in the axial profile $V_z(z)$ and Γ_∞, expected ranges for r_o, Γ_∞ and h_0 are estimated as a function of U_i and s/d instead of fixed values. These analytical relations are used in a subsequent paper (Suerich-Gulick *et al.*, 2013c) to propose and discuss quantitative relations for translating vortex characteristics observed in a laboratory-scale model to the prototype scale based on the scaling behaviour of surface tension, viscosity and turbulence.

Logical Bridge 1

Manuscript 1 employed velocity and free surface profile measurements carried out in the physical laboratory-scale model to adapt Burgers's vortex model to include the influence of geometry and approach flow conditions on vortex characteristics. Manuscript 2 extrapolates from the adapted model to estimate how vortex characteristics observed at the laboratory scale should translate to the prototype scale. The results suggest that the scale effect due to viscosity, indicated by the lack of similarity of the Reynolds numbers because water is used as the fluid in both the laboratory and the prototype, might be very significant. The scale effect due surface tension, indicated by the lack of similarity of the Weber number, appears to be much less important. Processes that might modify this prediction are discussed, including the possible transition from viscosity- to turbulence-driven diffusion in the vortex core.

Chapter 5

Free surface intake vortices: Scale effects due to surface tension and viscosity (Manuscript 2)

ABSTRACT

In a previous paper, the free surface vortices that form at a simplified hydropower intake were studied in a laboratory model (Suerich-Gulick *et al.*, 2013d). Measurements of the velocity profiles and vortex characteristics were used to develop a simple analytical model that relates the vortex characteristics to the intake geometry and operating conditions. This paper explores the influence of surface tension, viscosity and turbulence on vortex characteristics in order to quantify how they affect the translation of results from the laboratory to the full prototype scale. A numerical model of the free surface profile produced by a Burgers (1948) vortex reveals that both the profile shape and scale influence the impact of surface tension. Extrapolation from the analytical vortex model indicates that effects due to viscosity could be substantially greater than those due to surface tension, but variations in the axial velocity profile and turbulent diffusion in the vortex could significantly modify this result.

5.1 Introduction

Free surface vortices are a common problem upstream from hydropower intakes and it is common practice for engineers to use laboratory-scale physical models to assess and optimize proposed intake designs to maximize flow uniformity and steadiness at the turbines and minimize the occurrence and intensity of vortices. This work aims to increase understanding of the processes that influence key vortex characteristics and to develop quantitative methods by which engineers can estimate the magnitude of scale effects when translating observations from laboratory-scale models to the full-scale prototype. In Part I of this paper (Suerich-Gulick *et al.*, 2013d), we used measurements in a physical model of a simplified intake to develop a semi-empirical analytical model based on Burgers's (1948) vortex model that predicts the vortex's characteristic radius r_o, bulk circulation Γ_∞ and tip depth h_0 (maximum depth of the free surface depression produced by the vortex) in terms of the intake velocity U_i and relative intake submergence s/d, where s is the submergence of the intake pipe and d is its inner diameter (see Fig. 5.1). First we examine how surface tension acts on the free surface depression by performing a parametric study of the surface depression produced by a Burgers's vortex using a finite-difference model with and without surface tension. Two distinct types of free surface shape are identified: the dimple, which is a mild depression, and the funnel, which is a deeper depression with a steeper free surface slope and a large peak in surface curvature at the tip. It is found that the impact and scaling behaviour of surface tension on these two profile shapes is qualitatively different. We use the results of the calculations to produce a correction factor that can be used to estimate the magnitude of the change in tip depth caused by surface tension for a given free surface depression scale and shape. Then we extrapolate from the results obtained in Suerich-Gulick *et al.* (2013d) to estimate how the vortex characteristics observed in a physical laboratory-scale model might translate to the full-scale intake, discussing how this prediction compares to previous work and how turbulence might influence the results.

5.2 Scale effects

It is widely recognized that the dominant parameter influencing vortex intensity is the Froude number, defined as $\mathrm{Fr_s} = U_i/(gd)^{1/2}$ or $\mathrm{Fr_s} = U_i/(gs)^{1/2}$, where g is the gravitational acceleration (Quick, 1962b; Jain *et al.*, 1978; Anwar, 1983; Chang and Prosser, 1987), though the exact dependence on Froude number varies with the intake configuration and geometry (Knauss, 1987). It is therefore common practice to build laboratory-scale models to Froude similitude such that $\mathrm{Fr_M} = \mathrm{Fr_P}$, where $\mathrm{Fr_M}$ and $\mathrm{Fr_P}$ are the laboratory model and prototype values, respectively (Quick, 1962b; Chang and Prosser, 1987). However since water is used in the laboratory model, it is impossible to match the Weber ($\mathrm{We} = \rho U_i^2 s/\sigma$), Reynolds ($\mathrm{Re}_s = U_i s/\nu$) and Froude numbers simultaneously, where ρ, ν and σ are the water density, kinematic viscosity, and the air-water surface tension coefficients, respectively. Work continues today to determine how the Reynolds and Weber numbers of reduced-scale models of hydropower and pumping station intakes operating at Froude similitude influence the characteristics and behaviour of free surface vortices observed therein (Tastan and Yıldırım, 2010).

5.2.1 Surface tension

Many authors have studied the influence of viscosity and surface tension by experimentally examining how the critical condition varies with the Reynolds and Weber numbers. The critical condition is most commonly defined as the operating condition at which air entrainment begins to occur, which is often identified as the point where the tip of the free surface depression just reaches the intake pipe (Daggett and Keulegan, 1974; Jain *et al.*, 1978; Anwar, 1983; Odgaard, 1986; Gulliver, 1988; Hite and Mih, 1994; Möller *et al.*, 2012b). The critical condition may also be defined as the point where 'weak' or mild-depression vortices become 'strong' vortices with a noticeable or funnel-shaped depression (Anwar, 1983). A vortex whose depression forms a long narrow funnel that reaches far below the free surface is commonly referred to as an air core vortex.

Surface tension can significantly reduce the depth of the free surface depression in the lab setting, and the Weber number is often used to try to determine if surface tension effects will

be significant. Several authors have studied how We influences the critical condition, seeking to identify a minimum value above which surface tension effects can be neglected (Daggett and Keulegan, 1974; Jain *et al.*, 1978; Anwar and Amphlett, 1980; Anwar, 1983), but the observed trends and conclusions vary significantly from author to author. Comparison of results is complicated by the different definitions used: $\mathrm{We}_s = \rho U_i^2 s/\sigma$, and $\mathrm{We}_d = \rho U_i^2 d/\sigma$. Daggett and Keulegan (1974) (undocumented We) and Jain *et al.* (1978) ($\mathrm{We}_d > 120$) report no significant influence of surface tension on air entrainment in their respective tests in cylindrical tanks using fluids of varying surface tension coefficients, nor do Möller *et al.* (2012b) in their study of air entrainment in a horizontal intake with $\mathrm{We}_d > 748$. Similarly, Padmanabhan and Hecker (1984) find no difference in observed vortex types that would indicate surface tension effects in comparisons of different pump intake model scales operating at $\mathrm{We}_d > 600$. On the other hand, Anwar (1983) finds that surface tension affected vortex intensity for We_s up to 1.5×10^4 for dimple depressions and up to 4×10^4 for air core vortices in horizontal and vertical intakes in a channel. Tastan and Yıldırım (2010) conclude from their experimental results that the limiting values for We_d for air entrainment depend on the flow and geometrical conditions and therefore no fixed value can be identified. Odgaard (1986) concludes from a rough theoretical order-of-magnitude analysis that the effect of surface tension on the critical condition for air entrainment should be negligible for $\mathrm{We}_d > 720$.

Other authors examine how the radial profile of the free surface depression is modified by surface tension by solving the coupled differential equations describing an axisymmetric vortex using the finite-difference method (Andersen *et al.*, 2006; Yıldırım and Jain, 1981), an approximate series solution (Stepanyants and Yeoh, 2008a), or quadratic approximations of the free surface near the vortex tip (Ito *et al.*, 2010b). Yıldırım and Jain (1981) find that the relative effect of surface tension on tip depth is much more significant for a weak vortex with small circulation than for a strong vortex with larger circulation.

5.2.2 Viscous effects and turbulence

Most authors observe that the critical condition for air entrainment (Daggett and Keulegan, 1974; Jain *et al.*, 1978; Anwar, 1983; Chang and Prosser, 1987) becomes less and less sensitive to Re

as Re increases, leading them to conclude that viscous effects in a reduced-scale model can be neglected if Re for the scale model is greater than a certain cutoff value, ranging from 4×10^4 to 1.4×10^5, depending on the geometry and/or the Froude number, using various definitions of Re (Daggett and Keulegan, 1974; Jain *et al.*, 1978; Anwar, 1983; Padmanabhan and Hecker, 1984; Chang and Prosser, 1987; Tastan and Yıldırım, 2010). This paper uses the definitions $\mathrm{Re}_s = U_i s/\nu$ and $\mathrm{Re}_d = U_i d/\nu$.

Although the data seem fairly convincing that Re's influence asymptotically decreases at higher values, it is not entirely clear why this occurs and data that would allow possible explanations to be tested are lacking. Furthermore, economic or spatial constraints sometimes make it difficult to respect the suggested cutoff guidelines, especially for hydropower intakes, which tend to have larger dimensions and often require the inclusion of significant upstream stretches of the river reach in the reduced-scale model in order to properly capture the approach flow conditions. So the question remains as to how one can account for scale effects when one is unsure whether the reduced-scale model is sufficiently large.

Odgaard (1986) explores possible explanations for these observed trends with the help of Burgers's (1948) vortex model, which assumes that the radial profiles of the azimuthal $V_\theta(r)$ and radial $V_r(r)$ velocities are constant along the vortex axis z and that the axial velocity $V_z(z)$ is independent of r and varies linearly with z:

$$V_\theta(r) = \frac{\Gamma_\infty}{2\pi r}(1 - \exp((r/r_o)^2)) \tag{5.1}$$

$$V_z(z) = az, \qquad V_r(r) = -ar/2, \tag{5.2}$$

$$r_o = 2(\nu/a)^{1/2}, \qquad a = \partial V_z/\partial z, \tag{5.3}$$

where r, θ, z are the radial, azimuthal and axial cylindrical coordinates with z aligned with the vortex axis pointing down from the free surface, and V_r, V_θ, V_z are the corresponding velocities. The gradient a is a constant with units s^{-1}, Γ_∞ (units $\mathrm{m}^2\mathrm{s}^{-1}$) is the bulk circulation of the vortex, and ν (units $\mathrm{m}^2\mathrm{s}^{-1}$) is the kinematic viscosity of the fluid. Burgers's model is based on the hypothesis that a stable vortex with a constant vorticity and $V_\theta(r)$ profile along the vortex

axis is produced by an equilibrium of axial stretching $\partial V_z/\partial z$ and radial viscous diffusion. Detailed measurements of the velocity field of a free surface intake vortex suggest that the model captures the basic vortex structure quite well (Suerich-Gulick *et al.*, 2013d) even if some subtle discrepancies exist.

Odgaard (1986) suggests that at larger scales, turbulence enhances the effective viscosity in the vortex. He replaces ν in Burgers's expression for r_o (Eq. 5.3) , by $\nu_{\text{eff}} = \nu + \nu_{\text{T}}$, where ν_{T} is the eddy diffusivity, which models the enhanced momentum mixing caused by turbulence, and which Odgaard assumes to be equal to $\chi\Gamma_\infty$, following Squire (1965). With the non-dimensional constant χ set to 6×10^{-5}, Odgaard's (1986) model predicts Jain *et al.*'s (1978) critical submergence measurements quite well (Gulliver, 1988). The proposal that ν_{eff} increases with Γ_∞ would appear to contradict past results that radial turbulent fluctuations are suppressed by flow rotation (Bradshaw, 1973; Spalart, 1998; Jacquin and Pantano, 2002) and that the spreading rate in the case of wing tip vortices is governed by viscous diffusion rather than by turbulent mixing (Zeman, 1995). However the critical condition $(h = s_{\text{c}})$ implies here that Γ_∞/ν scales roughly with $(s_{\text{c}}/d)\text{Re}_{\text{s}}^{1/2}$, so Odgaard's relation would produce an increasing ν_{eff}/ν at larger Re_{s} values, producing a gradual decrease in the overall influence of ν on the critical submergence as ν_{eff} becomes significantly larger than ν. Setting $\nu/\nu_{\text{eff}} < 0.2$ as a cutoff, Odgaard obtains from his model that scale effects associated with molecular viscosity should become negligible for $\text{Re}_{\text{s}} > 1.4\times10^5$. Hite and Mih (1994) employ an eddy diffusivity that scales directly with the flow rate, setting $\nu_{\text{T}} = Q/(4\pi d)$, which equals $3.5\times10^{-3}\,\text{m}^2\text{s}^{-1}$ in their case. Given the measured circulation $\Gamma_\infty = 0.086\,\text{m}^2\text{s}^{-1}$ in their experiment, this would correspond to $\chi = 0.04$ in Odgaard's relation for ν_{T}, two orders of magnitude greater than Odgaard's value.

Although it seems quite clear from our measurements (Suerich-Gulick *et al.*, 2013d) that eddy diffusivity is effectively suppressed in the vortices under the operating conditions examined here, it is possible that at larger scales and Re_{s} values, turbulence in the vortex core might be less completely suppressed, leading to a non-negligible and gradually increasing eddy diffusivity added to the effect of molecular viscosity. The value for χ suggested by Odgaard (1986) is small enough that in the range of values of Γ_∞ $(< 0.01\,\text{m}^2\text{s}^{-1})$ measured in our experiment, the corresponding value for ν_{T} would reach a maximum of $6\times10^{-7}\text{m}^2\text{s}^{-1}$, half the molecular

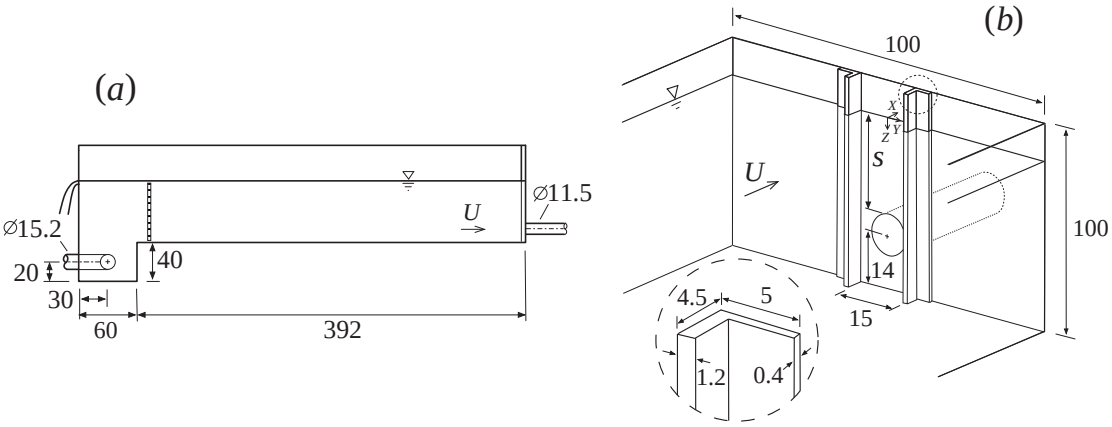

FIGURE 5.1: Vertical section (*a*) and isometric (*b*) views of the laboratory model (dimensions in cm)

viscosity. According to Eq. (5.3), this would produce a 22% increase in the core radius r_o, which is not significantly greater than the experimental variation observed in Fig. 5(*a*) of Suerich-Gulick *et al.* (2013d).

5.3 Method

5.3.1 Experiment

A laboratory-scale model of a simplified low-head hydropower intake is constructed with two tall pier-like plates mounted perpendicular to the downstream wall of the channel, one on each side of the intake opening, as shown in Fig. 5.1. Each pier produces two vortices in its wake: a submerged vortex with one end connected to the channel bed, and a free surface vortex with one end connected at the free surface. The other end of each vortex is drawn into the intake pipe. We study a range of vortex intensities, ranging from an imperceptible dimple to a funnel vortex that regularly entrains air bubbles. The details of the experimental setup and the eight operating conditions studied are described in Suerich-Gulick *et al.* (2013d).

A high-speed video camera is used to simultaneously record the particle trajectories of the free surface vortex produced by the right pier (defined looking downstream) and the profile of

the free surface depression it produces. The profiles of $V_\theta(r)$ and $V_z(z)$ are then computed using particle tracking velocimetry (PTV) and Burgers's profile (Eq. 5.1) is fitted to the measured profiles. The results are presented and discussed in Suerich-Gulick *et al.* (2013d). In this paper, we numerically compute the free surface depression that should be produced by the measured velocity profile $V_\theta(r)$ including surface tension, and we compare it to the actual free surface depression recorded at the same time as the velocity. Once we have ascertained in this manner that the numerical model predicts the free surface depression with sufficient accuracy, we perform a parametric study using the numerical model to gain insight into the relative impact of surface tension for different shapes and scales of the free surface depression.

5.3.2 Free surface profile computations

At small scales, surface tension can significantly reduce the depth of the free surface depression produced by the vortex. This effect is highly nonlinear since it both modifies and is controlled by the local curvature of the free surface. We examine the scaling behaviour of surface tension by numerically computing the depression profile $h(r)$ with (h_σ) and without (h_n) surface tension over a wide range of vortex intensities produced by different combinations of Γ_∞ and r_o. The evolution of the relative difference $\delta \equiv \Delta h/h_{\mathrm{n},0}$ between the profile tip depths is examined, where $\Delta h \equiv h_{\mathrm{n},0} - h_{\sigma,0}$ (Yıldırım and Jain, 1981).

The free surface profile is controlled by the equilibrium of the forces exerted by gravity, centripetal acceleration and surface tension. Following Andersen *et al.* (2006), Stepanyants and Yeoh (2008a) and Ito *et al.* (2010b), we use Laplace's model that surface tension reduces the pressure across the air-water interface by $l_\sigma^2\kappa(r)$, where $\kappa(r)$ is the local mean curvature of the air-water interface and $l_\sigma^2 = \sigma/(\rho g)$ is the squared characteristic length of the air-water interface. The resulting radial profile of the depression $h_\sigma(r)$ is given by

$$h_\sigma(r) = \int_\infty^r \left(\frac{V_\theta(\acute{r})^2}{g\acute{r}} - l_\sigma^2 \kappa(\acute{r}) \right) d\acute{r}, \tag{5.4}$$

(Andersen *et al.*, 2006). A constant value for l_σ of 2.73 mm is used here, which corresponds to a clean air-water interface at 15°C. The variations in l_σ associated with the range of experimental

temperatures (13 to 15 °C) are negligible compared to those that might be caused by impurities in the water or floating on the free surface. The kinematic energy associated with V_z and V_r would slightly increase the depth of the depression, but this contribution is negligible compared to that of V_θ (Odgaard, 1986).

The mean local curvature $\kappa(r)$ is given by

$$\kappa(r) = -\frac{1}{2}\left\{\frac{h_r}{r[1+(h_r)^2]^{1/2}} + \frac{h_{rr}}{[1+(h_r)^2]^{3/2}}\right\}, \tag{5.5}$$

where h_r and h_{rr} are the first and second derivatives of h with respect to r respectively (Andersen *et al.*, 2006). The first term on the right is the curvature about the horizontal axis (perpendicular to the page in a 2D section of the profile such as Fig. 5.4*a*) and the second term is the curvature about the vortex's (vertical) axis of rotation. The free surface profile has a positive (concave) horizontal axis curvature at the vortex tip, then some distance beyond $r > r_o$ it passes through an inflection point and the horizontal axis curvature becomes negative (convex). The surface tension force thus pushes the interface upward in the core portion of the vortex and pulls it down very slightly just outside the core.

Since our primary goal is to get a larger view of trends in surface tension effects over a range of shapes and scales rather than to obtain the exact shape of the depression, the free surface profile is computed by directly substituting Burgers's relation for $V_\theta(r)$ from Eq. (5.1) into Eq. (5.4):

$$h_\sigma(r) = \int_\infty^r \left\{\frac{\Gamma_\infty^2}{4\pi^2 g\acute{r}^3}\left[1-\exp\left(-(\acute{r}/r_o)^2\right)\right]^2 - l_\sigma^2\kappa(\acute{r})\right\} d\acute{r}, \tag{5.6}$$

This approximation neglects the effect of the free surface depression on the velocity field and hence indirectly on the depression itself as well. Stepanyants and Yeoh's (2008b) results suggest that this approximation produces a negligible error in $\Delta h/h_{\mathrm{n},0}$ in the case of a mild dimple depression and an error of 26% for an extremely deep, funnel-type depression with a nominal free surface depression slope $\zeta \equiv h_{\mathrm{n},0}/r_o = 110$. This is judged to be an acceptable level of error for the purpose of this study.

Equation (5.6) is discretized along r by central differences and an equilibrium profile $h_\sigma(r)$ is computed numerically for the given r_o and Γ_∞ by gradually decreasing r_o from a large value (which produces a very shallow depression) to the desired r_o. A large relaxation factor and smoothing of the computed curvature $\kappa(r)$ between each iteration is required for certain cases such as deep funnel vortices (with a nominal free surface slope greater than 10), in order to suppress oscillations generated by the steep peak in curvature at $r = 0$.

5.4 Analysis and discussion

5.4.1 Surface tension effects

The free surface profile code is first tested using the free surface and velocity profiles measured and computed by Andersen *et al.* (2006) for a moderate funnel of nominal depression slope $\zeta = 15$ and the results compare very well. The code is then tested by computing the free surface depression from the measured velocity profiles in our experiment, where surface tension effects are significant, and comparing the computed tip depth $h_{0,\text{comp}}$ to that recorded in the film segments.

Figure 5.2(a) shows each measured tip depth $h_{0,\text{exp}}$ compared to the tip depth $h_{0,\text{comp}}$ computed using Eq. (5.6) with Γ_∞ and r_o obtained by fitting Burgers's profile (Eq. 5.1) to the measured $V_\theta(r)$ profiles. The horizontal error bars show the spread between the two values of $h_{\sigma,0}$ computed from $r_o and \Gamma_\infty$ obtained from the two fitting methods, and the symbols show the mean. Although the spread is somewhat large for some points, the agreement is close enough to indicate that both the method used to measure the azimuthal velocities and Burgers's model used to describe the measured profiles are suffiently accurate to predict the free surface depression from the velocity measurements.

The code is then used to compute the free surface depression with and without surface tension produced by Burgers's vortices with a range of Γ_∞ and r_o values. As shown in Fig. 5.3(b), the results reveal that the relative surface tension effect $\Delta h/h_{\text{n},0}$ scales very differently depending on the shape of the depression, which is quantified here using the nominal depression slope ζ.

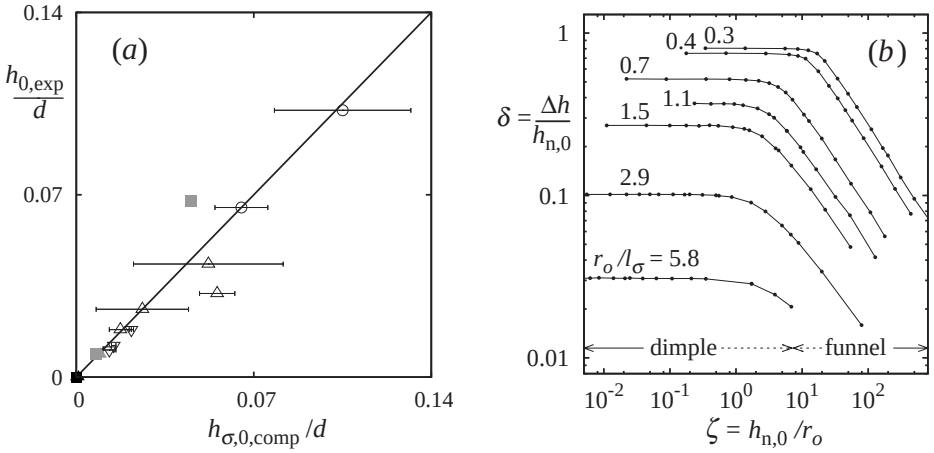

FIGURE 5.2: (*a*) Correspondence between the measured tip depth $h_{0,\mathrm{exp}}$ and the tip depth $h_{0,\mathrm{comp}}$ computed from the measured $V_\theta(r)$ profile: ($\triangledown, \triangle, \odot, \boxdot$), measured values at intake velocities U_i=(0.59, 0.86, 1.4, 1.8) ms^{-1} respectively with shade (○, ●, ●) indicating the relative submergence s/d=(1.5, 2.4, 3.3) respectively; ——, exact correspondance. (*b*) Relative surface tension effect $\Delta h/h_{\mathrm{n},0}$ as a function of the scale r_o/l_σ and depression slope ζ; ——, lines of constant r_o/l_σ.

The transition between the dimple and funnel modes occurs around $1 < \zeta < 10$, depending on the scale. For dimple-shaped depressions corresponding to $\zeta \lessapprox$ 1-10, $\Delta h/h_{\mathrm{n},0}$ becomes independent of ζ, while for funnel-shaped depressions ($\zeta \gtrapprox$ 1-10), $\Delta h/h_{\mathrm{n},0}$ varies with both the scale and shape ζ. Furthermore, the data show that for a given scale r_o/l_σ, the relative surface tension effect $\Delta h/h_{\mathrm{n},0}$ is much more significant in a dimple than in a funnel vortex, as obtained by Yıldırım and Jain (1981).

Figure 5.3(*a*) shows that once the limiting dimple shape is reached (towards the upper right of the graph), $\Delta h/h_{\mathrm{n},0}$ converges to a unique function f_σ for the different Γ_∞ values that depends only on the scale r_o/l_σ:

$$f_\sigma(r_o/l_\sigma) = \left[\exp(-0.44(r_o/l_\sigma)^2) + 1.9(r_o/l_\sigma)^{1.6}\right]^{-1}, \tag{5.7}$$

which at large scales ($r_o/l_\sigma \gtrapprox 3$) tends towards a straight line $\Delta h/h_{\mathrm{n},0} \sim (r_o/l_\sigma)^{-1.8}$. Conversely, when $\Delta h/h_{\mathrm{n},0}$ is plotted in Fig. 5.3(*b*) as a function of the product $(r_o/l_\sigma)^2\zeta = r_o h_{\mathrm{n},0}/l_\sigma^2$, the curves collapse at large values (corresponding to the funnel shape) to a straight line of slope $\Delta h/h_{\mathrm{n},0} \sim (r_o h_{\mathrm{n},0}/l_\sigma^2)^{-0.6}$.

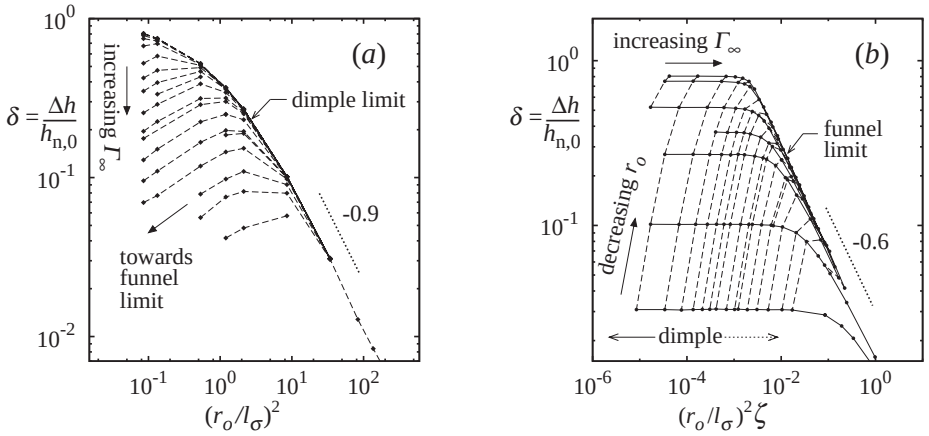

FIGURE 5.3: Relative surface tension effect $\Delta h/h_{n,0}$ as a function of (*a*) scale and (*b*) the combined scale and slope: ----, lines of constant Γ_∞; ——, lines of constant r_o/l_σ.

These trends can be compared to the scaling behaviour of the local curvature $\kappa_{n,0}$ of the free surface at $r = 0$ in the absence of surface tension (Eq. 5.5) in the limits $\zeta \ll 1$ (dimple) and $\zeta \gg 1$ (funnel). If r is assumed to scale with r_o, h_r with ζ and h_{rr} with $h_{n,0}/r_o^2$, then Eq. (5.5) produces $\kappa_{n,0} \sim h_{n,0}/r_o^2$ for the dimple and $\kappa_{n,0} \sim r_o^{-1}$ for the funnel. If it is further estimated that $\Delta h/h_{n,0} \sim \kappa_{n,0} l_\sigma^2/h_{n,0}$, this produces the scaling behaviour $\Delta h/h_{n,0} \sim (l_\sigma/r_o)^2$ for the dimple and $\Delta h/h_{n,0} \sim l_\sigma^2/(r_o h_{n,0})$ for the funnel (the relation used by Odgaard (1986) in his analysis). So the same essential scaling behaviour is produced by the computations and the theoretical analysis, except that the slopes of the computed trends (-1.8 and -0.6 for the dimple and funnel respectively) are weaker than those (-2 and -1) produced by the rough theoretical analysis. Stepanyants and Yeoh (2008a) also obtain $\Delta h/h_{n,0} \sim r_o^{-2}$ for the dimple. The difference between our numerical result and that of Stepanyants and Yeoh (2008b) might be due to simplifications in the velocity profile model used here, or to the different solution methods, since Stepanyants and Yeoh use a series solution with analytical functions to approximate the shape of the tip instead of computing a discretized profile. However it seems quite possible that the difference in slopes between our computed trend and the present theoretical analysis is due to physics rather than numerical error, since the theoretical analysis does not capture the non-linearity of the process by which surface tension changes the shape of the free surface depression, which in turn affects the magnitude of the surface tension and so forth.

To understand these trends, we examine how the computed shape of the free surface depression is modified by surface tension and how that effect depends on the initial shape and scale of the depression. Comparison of the profiles in Fig. 5.4(a) computed with surface tension (dashed and dotted lines) and without (solid line) shows that surface tension acts differently on different regions of the profile depending on the shape of the depression. Within a given scale (r_o/l_σ=0.3) there is a much stronger relative reduction of the depression $h_\sigma/h_{\mathrm{n},0}$ for the dimple vortices ($\zeta \lessapprox 20$) than for the funnel vortices ($\zeta \gtrapprox 20$). Surface tension acts strongly over a much larger radius in the dimple vortex (up to $r/r_o \approx 2$) than in the funnel vortex where the effect is restricted to an inner region $r/r_o \lessapprox 0.5$ that shrinks as the funnel gets deeper. In the funnel vortices, surface tension appears to essentially clip off the tip of the depression, thereby significantly diminishing the spike in curvature at the tip that characterizes funnel vortices. This can be seen in Fig. 5.4(b), which shows the curvature profiles $\kappa_\sigma(r/r_o)$ that correspond to the free surface profiles in Fig. 5.4(a). In the absence of surface tension (solid line), $r_o\kappa$ for ζ=350 reaches a peak of 510 at $r = 0$. Figure 5.4(c) shows that surface tension has much less effect at a larger scale ($r_o/l_\sigma = 1.5$) in both the dimple ($\zeta \lessapprox 5$ here) and funnel vortices. The profiles for the two lowest values of ζ in Figs. 5.4(a) and (c) coincide, indicating that the dimple shape limit has been reached, where $\Delta h/h_{\mathrm{n},0}$ becomes independent of ζ.

These results clearly demonstrate that surface tension effects do not scale in the same way for dimple vortices and funnel vortices. This qualitative difference in behaviour might partly explain the variability in recommendations found in the literature for the minimum laboratory model size required to avoid surface tension effects. The results also strongly suggest that empirical surface tension scaling laws derived by studying the onset of air entrainment (ie. deep funnel vortices) must not be directly employed to interpret vortex observations in reduced scale models of hydropower plants, where spatial constraints are such that only dimple vortices are commonly observed.

5.4.2 Scale effects associated with viscosity and turbulence

In Eq.(9) of Suerich-Gulick *et al.* (2013d), the range of expected tip depths $h_{\mathrm{n},0,\mathrm{est}}$ for a specific geometry was estimated as a function of the intake velocity U_i and relative submergence s/d.

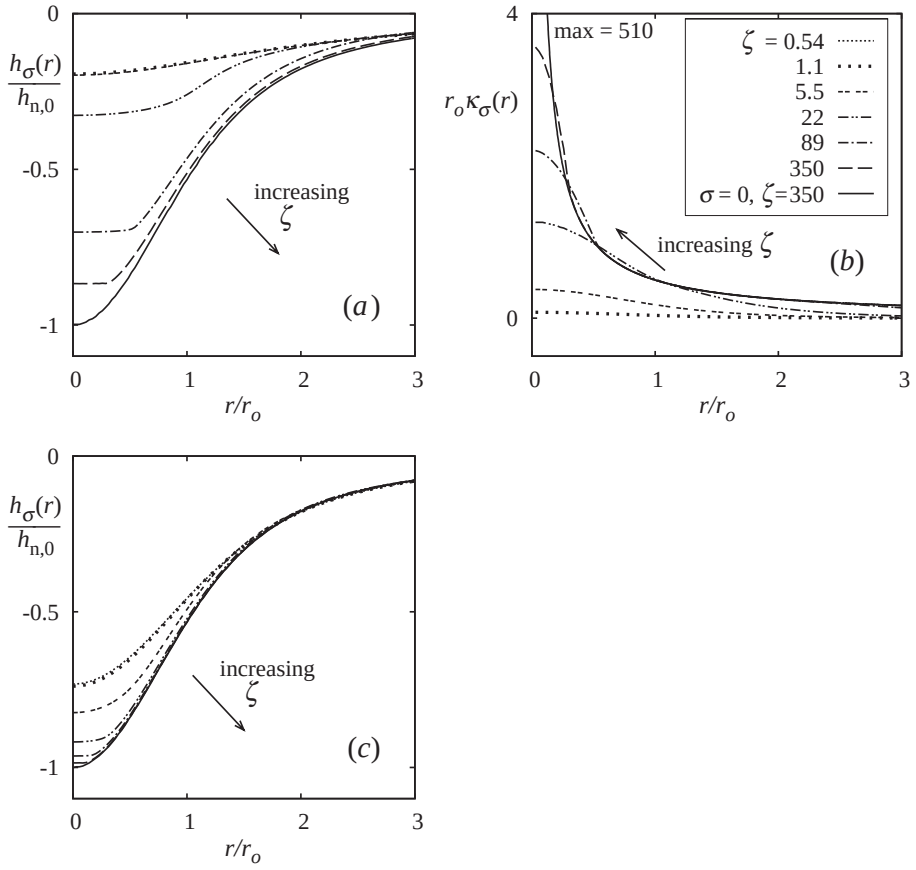

FIGURE 5.4: (*a* and *c*) Free surface profiles $h_\sigma(r)/h_{n,0}$ with surface tension for different depression slopes ζ at two scales, r_o/l_σ=0.3 (*a*) and r_o/l_σ=1.5 (*c*). (*b*) Profiles of the free surface curvature $r_o\kappa_\sigma(r)$ for r_o/l_σ=0.3.

We obtain $h_{0,\text{est}}$ including surface tension by adding the surface tension correction function f_σ (Eq. 5.7):

$$\frac{h_{0,\text{est}}}{d} = \frac{c_0(1-f_\sigma)}{(1-\beta)}\,\text{Re}_s\text{Fr}_s^2\left(\frac{d}{k}\right)^3\left(\frac{l_p}{s}\right)^2\left(\frac{d}{c_4 s}-c_2\right)^2, \tag{5.8}$$

with the non-dimensional coefficients $c_0 = 3.7\times10^{-5}$ and $c_2 = 0.28$. c_4 has two values, 1.0 and 0.6, corresponding to low and high values of Γ_∞, respectively. l_p is the length of each pier, k is the distance between the piers, and $\text{Re}_s\text{Fr}_s^2 = \text{Re}_s\text{Fr}_s^2 = U_i^3/(\nu g)$. This expression is valid for all the conditions examined, regardless of vortex shape, except that f_σ (Eq. 5.7) is valid only for dimple-type depressions and will overestimate the surface tension effect for funnel- and transition-type depressions. For a more accurate correction for these latter shapes, $\Delta h/h_{n,0}$ can be read off Fig. 5.2(*b*) for a given ζ and r_o/l_σ and substituted for f_σ in Eq. (5.8).

Figure 5.5(a) shows the range of values $h_{0,\mathrm{est}}$ estimated from Eq. (5.8) compared to the measured values. Surface tension has a minimal impact compared to the variability associated with variations in r_o and Γ_∞. The predicted range of $h_{0,\mathrm{est}}$ values is shown by the boxes: the upper limit is obtained with $\mathrm{c}_4 = 0.6$ and $\beta = 0.15$ and the lower limit is obtained with $\mathrm{c}_4 = 1.0$ and $\beta = 0.85$. Possible causes of Γ_∞ variability include as-yet poorly understood strengthening processes within the vortex, and turbulent fluctuations in the surrounding flow. Variability in r_o would appear to be mainly due here to variations in the shape of the $V_z(z)$ profile in the upper portion of the flow, ranging between a more linear ($V_z(z) \sim z$) and a more non-linear one ($V_z(z) \sim (h-z)^{-1}$). This effect is indicated in Eq. (5.8) by the parameter β. As discussed in Suerich-Gulick *et al.* (2013d), β indicates over how long a distance $V_z(z)$ follows a linear profile, where $0 \leq \beta \lessapprox (1 - 0.5d/s)$ is a proportion of the distance s from the free surface to the top of the inlet. $\beta = 0$ indicates that $V_z(z)$ inside the vortex follows the non-linear profile of the flow outside the vortex, while larger values of β indicate that $V_z(z)$ follows a linear profile in z from the free surface over a greater distance, producing a steeper slope in $V_z(z)$ at the free surface. In the experiment, β is observed to fall in the range $0.15 \leq \beta \leq 0.85$ (Suerich-Gulick *et al.*, 2013d). Turbulence in the vortex core might also produce variations in r_o by enhancing the effective radial diffusivity in Eq. (5.3).

In order to compare Eq. (5.8) to other results, it is reformulated in terms of the critical relative submergence s'_c for air entrainment, where the tip of the vortex depression reaches the top of the outlet so that $h_{\sigma,0}|_{\mathrm{crit}} = s$. Substituting $s'_{\mathrm{c}} \equiv (s/d)|_{\mathrm{crit}}$ for $h_{\sigma,0}/d$ in Eq. (5.8) and isolating terms in s'_{c} produces

$$\frac{s'^5_{\mathrm{c}}}{(\mathrm{c}_4^{-1} - \mathrm{c}_2 s'_{\mathrm{c}})^2} = \frac{\mathrm{c}_0(1-f_\sigma)}{(1-\beta)} \left(\frac{dl_p^2}{k^3}\right) \mathrm{Re_s Fr_s^2}. \tag{5.9}$$

As shown in Fig. 5.5(b), this relation predicts that s'_{c} scales roughly as $s'_{\mathrm{c}} \sim A\mathrm{Re_s^{1/6}Fr_s^{1/3}}$ at smaller values of $\mathrm{Re_s^{1/2}Fr_s}$, with $A^2 = \mathrm{c}_0(1-f_\sigma)(1-\beta)^{-1}(dl_p^2/k^3)$. It then flattens out at larger values, becoming less sensitive to $\mathrm{Re_s^{1/2}Fr_s}$ at deeper submergences. The two curves are produced by the two values of c_4 (0.6 and 1), and they have a singularity at $s'_{\mathrm{c}} = 6.0$ and 1.7, respectively. The shift to a milder slope at larger $\mathrm{Fr_s}$ reproduces trends observed in vertical

intakes by Tastan and Yıldırım (2010) and in horizontal intakes by Jiming *et al.* (2000), both using physical models. It differs from the trends with a constant slope on a log-log scale found by other researchers. Gulliver (1988) observed $s'_c \sim \mathrm{Fr}_\mathrm{s}^{2/3}$ in experiments with vertical intakes, and Rao *et al.* (1997) derived the same relation from Yıldırım and Kocabaş's (1995) analysis of lateral intakes in crossflow or at the end of a channel. Jain *et al.* (1978) observed $s'_c \sim \mathrm{Fr}_\mathrm{s}^{0.5} N_{\Gamma *}^{0.42} K^{-1}$ and Odgaard (1986) analytically derived $s'_\mathrm{c} \sim N_{\Gamma *}^{1/2} \mathrm{Re}_d^{1/4} \mathrm{Fr}_\mathrm{s}^{1/2}$, both for flow in a cylinder, where $N_{\Gamma *} = \Gamma_\infty s/Q$ is the non-dimensional circulation and K is a viscous correction factor.

The decreased sensitivity to $\mathrm{Fr_s}$ predicted by Eq. (5.9) at greater $\mathrm{Fr_s}$ values is due to the non-linear $V_z(z)$ profile that roughly follows $V_z/U_i \sim d/(s-z)$, as opposed to the linear profile $V_z/U_i = z/s$ assumed by Odgaard (1986). The non-linear profile has a much milder gradient $\partial V_z/\partial z$ at the free surface at large submergences, which produces more diffuse and thus weaker vortices, requiring a greater relative increase in $\mathrm{Fr_s}$ to produce an air core than at lower submergences. The linear profile assumed by Odgaard (1986) in his model might explain why it tends to overpredict s'_c compared to observations (Jain *et al.*, 1978) at larger s'_c values in several configurations (Gulliver, 1988). It should also be noted that Γ_∞ is dependent on U_i, s/d and the relative pier length l_p/d in the current experiment, whereas it is imposed using adjustable guide vanes in the experiments considered by Odgaard (1986) and Jain *et al.* (1978), which should affect the corresponding scaling relations.

Eq. (5.8) can also be used to evaluate how the characteristics of a free surface vortex in a laboratory-scale model operated at Froude similitude would translate to a much larger prototype intake with the same geometry with a geometric scaling ratio $\alpha = \ell_\mathrm{P}/\ell_\mathrm{M}$, where ℓ_M and ℓ_P are the characteristic lengths in the laboratory model and the prototype respectively. Neglecting surface tension $(1 - f_\sigma)$ and assuming the model and prototype are geometrically identical so that (d/k), (d/s), and (l_p/k) are identical in both the model and prototype, Eq. (5.8) becomes

$$h' \equiv \frac{h_{\mathrm{n},0}}{d} \sim \frac{\mathrm{c}_0}{(1-\beta)} \left(\frac{d}{\mathrm{c}_4 s} - \mathrm{c}_2 \right)^2 \mathrm{Fr}_s^2 \mathrm{Re}_s. \tag{5.10}$$

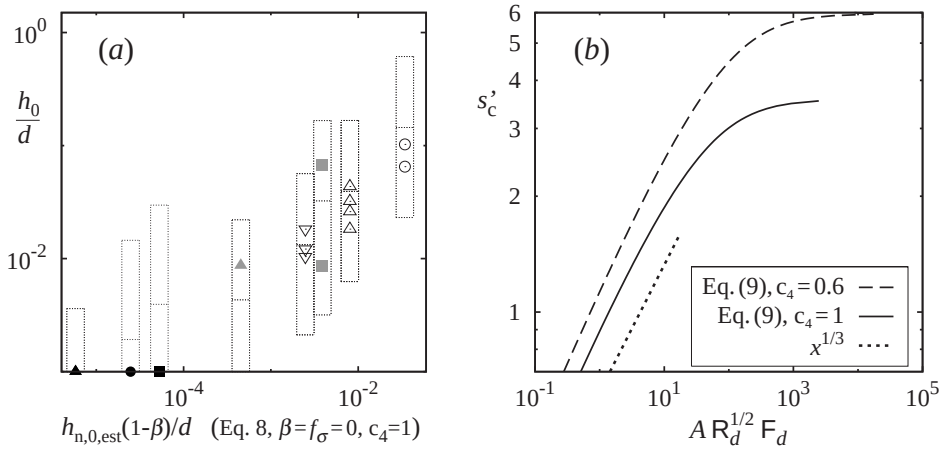

FIGURE 5.5: (*a*) The measured tip depth compared to the range estimated with surface tension from the geometry and flow conditions; ($\bigtriangledown, \bigtriangleup, \odot, \boxdot$), measured values, see the Fig. 5.2 caption for the key to the operating conditions; ⌸, range of values estimated using (Eq. 5.8), with r_o in f_σ (Eq. 5.7) estimated using $\beta = 0$. (*b*) The predicted scaling behaviour of the critical submergence s_c'.

Since $\mathrm{Fr_M} = \mathrm{Fr_P}$, the ratio of the outflow velocities $U_{i,\mathrm{P}}/U_{i,\mathrm{M}} = \alpha^{1/2}$, and because water is usually employed in the laboratory model, $\nu_\mathrm{M} = \nu_\mathrm{P}$ and the prototype-to-model ratio of the Reynolds numbers is $\mathrm{Re_P}/\mathrm{Re_M} = \alpha^{3/2}$. If it is further assumed that the velocity profiles outside and inside the vortex follow the same shape in the model and prototype so that $\{[d/(\mathrm{c}_4 s)] - \mathrm{c}_2\}$ and $(1-\beta)$ are identical in the model and prototype, we obtain

$$\frac{h'_\mathrm{P}}{h'_\mathrm{M}} = \frac{\mathrm{Re_P}}{\mathrm{Re_M}} = \alpha^{3/2}. \tag{5.11}$$

This indicates that the vortex depression h'_P produced in the prototype would be significantly greater in relative terms than that h'_M produced in the laboratory model if the scaling ratio α is large – scaling ratios of 20 are common and can reach as high as 200 in some cases (Hecker, 1981). This large effect is caused by the fact that the vicosity of the fluid is identical in both model and prototype while circulation increases with intake size and is thus larger in the prototype. It suggests that the magnitude of scale effects due to viscosity could be much larger than those due to surface tension. Though this result provides insight into how viscous diffusion and axial stretching affect the scaling behaviour of the vortices, it should be interpreted with caution, given the significant assumptions involved in its derivation and the high success rate

of laboratory-scale modelling for predicting prototype vortex activity in the past (Hecker, 1981; G. Montilla and Castro, 2004). To begin with, the laboratory and prototype intakes could have different axial profiles $V_z(z)$, producing $\beta_M \neq \beta_P$, and/or slightly different flow structures outside the vortex, whereas they are assumed to be identical. If turbulent diffusion enhances the effective viscosity controlling r_o at larger scales and/or higher flow rates as suggested by Einstein and Li (1951), Anwar (1969) and Odgaard (1986), this would reduce the value of $h_{\sigma,0}$ at larger scales. In order to properly assess this possibility, it would be necessary to make simultaneous measurements of the $V_z(z)$ and $V_\theta(r)$ profiles such as those performed in Suerich-Gulick *et al.* (2013d), but at larger scales and Re values.

Increased turbulence in the surrounding flow might also modify scaling behaviour at higher Re values by preventing vortices from forming or intensifying, as observed by Padmanabhan and Hecker (1984) and Tastan and Yıldırım (2010). Work on the interaction of external turbulence with the trailing vortices produced in the wake of airplane wings indicates that its impact depends on the length- and time-scale characteristics of both the background turbulence and of the central vortex of interest (Zeman, 1995; Jacquin and Pantano, 2002; Beninati and Marshall, 2005b). Further transient measurements and analyses of axially stretched free surface vortices in turbulent flow will be needed to shed light on how intake vortices strengthen, stabilize and break down and how turbulence intervenes in these processes (Huang *et al.*, 2008; Kimura *et al.*, 2008; Nakayama and Hisasue, 2010; Trivellato, 2010).

5.5 Summary and conclusions

Scale effects associated with surface tension, viscosity and turbulence were examined in a free surface vortex upstream from a hydropower intake. First, the effect of surface tension was examined by computing the free surface profiles produced with and without surface tension by a Burgers's (1948) vortex, revealing that both the shape and the scale of the free surface profile determine how surface tension will modify the shape and total depth of the depression. The trends produced by the calculations were used to formulate a correction factor that can be used to correct for surface tension effects in a laboratory-scale vortex. The tip depth of the depression

was then predicted for a specific intake geometry and set of operating conditions using the vortex model developed in a previous paper (Suerich-Gulick *et al.*, 2013d) with the addition of surface tension. The predictions compare fairly well with the measured values, considering the scatter in the measured data. Finally, the vortex model was used to estimate how vortices observed in a laboratory-scale model might translate to the prototype scale. Uncertainties associated with the scaling of the flow structure and perturbations and enhanced diffusion caused by turbulence were discussed, with suggestions as to how greater light could be shed on these processes.

Logical Bridge 2

The aim of this thesis is to produce useful guidelines for hydraulic engineers practicing in industry; thus Manuscript 3 interprets the results described in Manuscripts 1 and 2 in terms that are relevant and accessible to them. Flow structures and patterns that are familiar and readily observable in physical models are interpreted in terms of processes such as axial stretching. Accessible measurement and analysis techniques are proposed to extract quantitative data from these models to help assess how the approach flow is influencing vortex characteristics. Finally, the manuscript discusses how the measured velocity fields in the vortex can be linked to properties like the shape of the free surface depression the vortices produce and their ability to entrain floating particles. These properties are commonly used to categorize vortices in the industrial context.

Chapter 6

The Characteristics of free surface vortices at low-head hydropower intakes (Manuscript 3)

ABSTRACT

Tools for engineers who assess and optimize hydropower intakes are provided to help them measure and quantify the characteristics of free surface vortices (characteristic radius, bulk circulation, tip depth, debris entrainment) that form at the intakes. Accessible methods are proposed for measuring and modelling vortex characteristics and the processes that affect their generation and strength. Common mechanisms that produce and strengthen the vortices (flow separation, shear, asymmetric approach flow) are discussed. An analytical model, based on Burgers's vortex model and laboratory measurements, is described that incorporates the effect of the approach flow and intake geometry on vortex characteristics. Simple measurement techniques (acoustic Doppler velocimetry and surface particle velocimetry) are presented by which the flow and vortex characteristics can be documented, allowing the model to be adjusted to the particularities of the specific intake under consideration. The analytical model is then used to

make estimates about how vortex characteristics might translate from a laboratory-scale physical model to the full-size prototype intake.

6.1 Introduction

Vortices occur in a wide range of scales, in natural and man-made systems, in fluids such as air and water. They are a fundamental component of turbulence. Free surface vortices are sometimes observed near the intake of hydroelectric plants, with one end connected to the free surface and the other entering the inlet. Their occurrence is problematic because they can entrain air or debris or lead to unsteady or non-uniform flow at the turbines. Their impact ranges from simply reducing the power output of the plant to causing premature degradation of mechanical components. Free surface vortices occur most commonly at lower head run-of-river plants where they are most likely to be harmful due to the limited distance between the inlet and the turbines and to the often limited flow-aligning devices. There is great diversity in the layout of run-of-river plants; Fig. 6.1 shows sample schematic plan and side section views. Free surface vortices have on occasion been observed at high head plants with large reservoirs under very specific conditions.

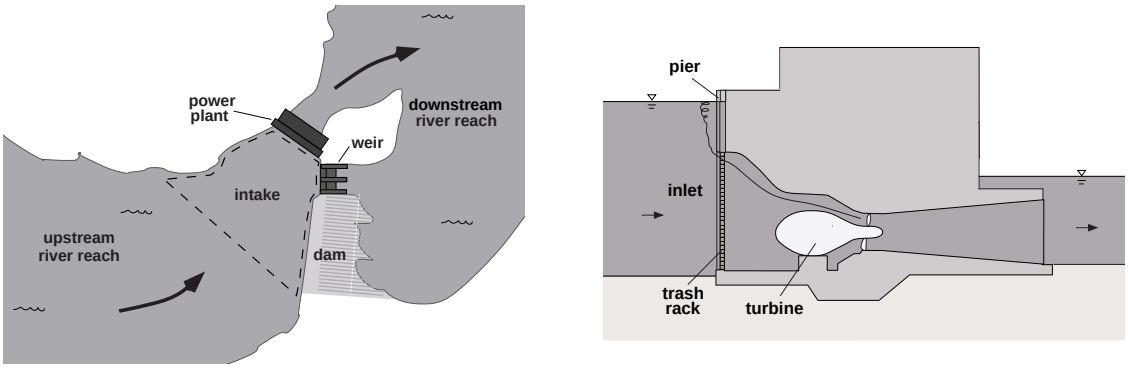

FIGURE 6.1: Plan (right) and section (left) views of sample run-of-river hydropower installations.

This work aims to help practicing engineers assess and interpret vortex activity in physical scale models of intakes to help reduce the risk of problematic vortices forming in the full-scale, 'prototype' intake. We begin by discussing the processes that contribute to the generation

of free surface vortices at intakes and present a relatively simple analytical model that was developed using measurements made in a simplified intake lab model. The model links vortex characteristics to the geometry and flow conditions and it is presented in such a manner that it can be adapted by the reader to other intakes using data that can be collected with relatively accessible measurement devices.

We discuss the implications of the analytical model in terms of vortex characteristics that are observable and relevant to intake designers and plant operators, such as the shape of the free surface depression and the ability of the vortex to entrain floating debris. Finally, the analytical model is used to estimate how the characteristics of a vortex observed in a laboratory model would appear in the prototype intake. Scale effects due to surface tension as well as viscosity are predicted in quantitative terms and the implications and limitations of these predictions are discussed.

6.2 Mechanisms controlling vortex strength

Although in practice vortices are complex and unsteady, much can be grasped about how they are generated and what determines their intensity from a relatively simple analytical vortex model. In this section, Burgers's vortex model is presented. A description of the different ways in which vorticity can be generated at an intake follows. The concentration of vorticity into a vortex of greater intensity by axial stretching is also discussed.

A vortex can be thought of as a local concentration of vorticity within which streamlines follow a circular, helical, or spiral pattern. Vorticity is a vector quantity defined mathematically as the curl of the velocity field: $\boldsymbol{\omega} = \boldsymbol{\nabla} \times \boldsymbol{V}$ (Saffman, 1992). In physical terms it describes the rotation of a local fluid particle about its center of mass. In viscous fluids, vorticity concentrated in the vortex core gets smeared outward by diffusion, producing a smooth radial profile that resembles a bell curve. In free surface intake vortices, the diffusion's spreading effect is counteracted by the concentrating effect of axial vortex stretching that is driven by the flow accelerating down towards the intake's inlet. Burgers's model describes a steady vortex produced by a state of equilibrium between these two processes.

6.2.1 Burgers's vortex model

Burgers's vortex model assumes that the flow is axisymmetric, that the radial velocity depends only on the radial distance r from the vortex axis and that the axial velocity varies linearly and only as a function of the axial coordinate z: $V_r(r) = -ar/2$, $V_z(z) = az$ (Burgers, 1948). The gradient a, a constant with units of s^{-1}, indicates the rate of axial stretching that the vortex is subjected to: $a = \partial V_z/\partial z$, where the z-axis is defined pointing downward from the free surface. The profile of V_r is defined so that continuity is satisfied. Solving the axisymmetric Navier–Stokes equations with these prescribed velocity profiles produces an azimuthal velocity $V_\theta(r)$ field that depends only on the radial coordinate and is constant along the vortex axis z:

$$V_\theta(r) = \frac{\Gamma_\infty}{2\pi r}\left(1 - \exp(-(r/r_o)^2)\right), \tag{6.1}$$

where Γ_∞ is the bulk circulation of the vortex, and r_o is the characteristic radius of the vortex. In Burgers's model, r_o is controlled by the ratio of the molecular viscosity ν (units m^2/s) to the axial gradient a:

$$r_o = 2(\nu/a)^{1/2}. \tag{6.2}$$

This relation shows that a stronger axial gradient a causes the vortex to contract into a tighter vortex with a smaller characteristic radius, while increased viscosity causes the vortex to spread outward.

The bulk circulation can be obtained by integrating the axial vorticity ω_z across the entire vortex cross-sectional area $\mathbf{A}$: $\Gamma_\infty = \int_\mathbf{A} \omega_z d\mathbf{A}$, or by performing a line integral of the azimuthal velocity V_θ along the full circumference of the circle C that encloses the vortex: $\Gamma_\infty = \oint_\mathbf{C} \mathbf{V} \cdot d\mathbf{C}$. The second approach is easiest to compute from experimental data since it is difficult to measure vorticity directly. Setting $r = 4r_o$ as the upper limit of the integration is sufficient to measure the bulk circulation within reasonable accuracy since the bulk of vorticity is concentrated within the vortex core ($r < r_o$) and drops off to a negligible amount beyond $r > 3r_o$.

Burgers's model captures the flow inside the vortex quite well, but it is not directly compatible with the flow field outside the vortex, which at most intakes is not axisymmetric or linearly

varying along the vortex axis. In this paper, we extract axial stretching and circulation estimates from velocity measurements and a rough potential flow model of the flow approaching the intake and then substitute these values into Burger's model to estimate the vortex characteristics.

6.2.2 Vorticity generation and axial stretching leading to vortex formation

This section describes common scenarios in which vorticity is generated at the intake or upstream in the intake channel. If the vorticity is advected to the proximity of the submerged inlet, the vertical flow acceleration driven by the inlet axially stretches the vorticity and produces a vortex.

Vorticity can be generated in a shear layer, such as in the boundary layer along the intake channel's lateral walls where a moment imbalance is produced by the retarding force of the wall on the flow. High velocity flow entering the channel from the river reach can also generate a shear layer between high and low velocity flow, producing vortices. Vorticity can also be generated by flow separation. If the channel narrows or widens too quickly, recirculating flow may develop in the low pressure region of the wake or in the stagnation zone (Quick, 1962b; Gulliver *et al.*, 1986). Similarly, the piers used to hold trash racks across intake openings can obstruct the flow and produce vortices in their wake (see Fig. 6.2*a*) (Jiming *et al.*, 2000). Piers often generate problematic vortices because they are located directly adjacent to the intake opening and span the full depth of the intake, so they strengthen the vortices along their whole length.

Vorticity generated a considerable distance upstream may be advected with the flow as mild, harmless vortices until they reach a point above the intake opening where they becomes concentrated into strong and problematic ones. For example, vortices may be generated at the point where flow is diverted laterally from a river into the intake channel (see Fig. 6.2*b*). Alternatively, flow may enter the intake channel with a lateral velocity at the free surface, creating a helical flow pattern across the channel cross-section whose lateral velocity component could initiate or strengthen vortices at the piers (see Fig. 6.3).

At some intakes, vortices may occur only under very specific and rare circumstances. In multi-turbine installations for example, vortices may occur when one or more turbines is not

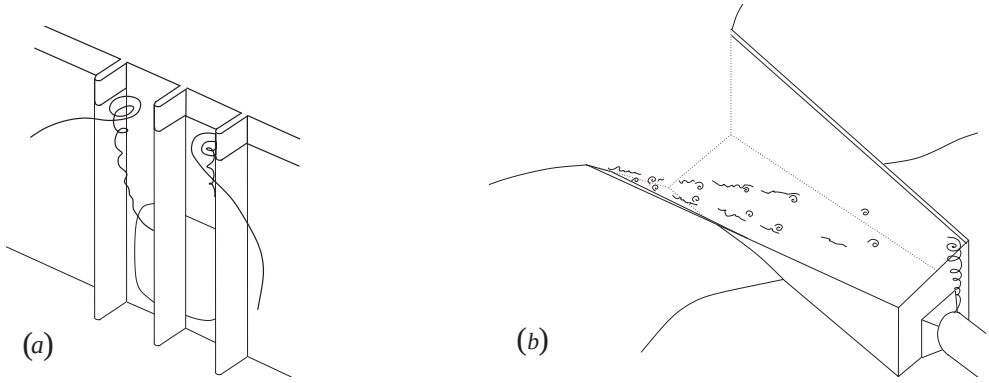

FIGURE 6.2: (*a*) Generation of vortices in the wake of piers. (*b*) Upstream generation and advection of vortices in a wake produced at the junction of the river reach and intake channel.

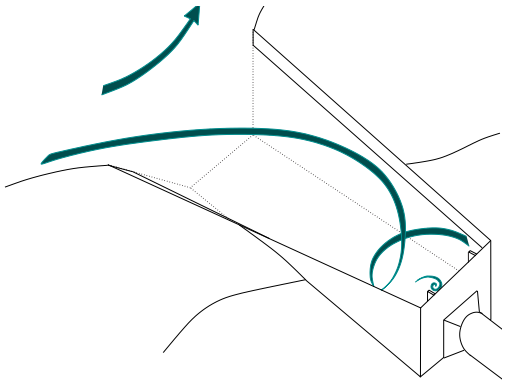

FIGURE 6.3: Large-scale helical flow pattern driven by river flow at the the intake channel entrance.

in full operation, producing skewed flow towards the inlets of those turbines that are. Less predictable conditions can include wind, non-uniform ice buildup or floating debris that can modify the flow pattern to produce vortices.

Finally, turbulence in the river flow can play a significant role in either providing the seeds for problematic vortices or in breaking them down before they become strong enough to cause harm. Turbulence can initiate vortex breakdown by exciting instabilities inherent to the vortex or by stripping vorticity from the primary vortex through the action of secondary ones. Unfortunately turbulence is complex and difficult to characterize so it is difficult to document how it interacts with coherent vortices in any given situation.

6.3 Assessing vortex risk

During the design phase of an intake, engineers use different methods to evaluate the risk that free surface vortices will form over the proposed range of operating conditions. If there appears to be a significant risk, they will attempt to modify the intake within the technical and economic constraints of the project.

As a starting point, vortex risk can be roughly assessed by mapping the proposed submergence-flow rate combinations onto a graph of past studies of vortex activity in intakes with similar configurations, such as Fig. 6.4, adapted from Fig. 3 of Gulliver *et al.* (1986). The filled dots in the figure show operating conditions for horizontal intakes where problematic vortices did form, and empty circles show conditions where they did not. The x's show the data points from the experiment described later in this paper, which was operated at greater relative intake velocities and submergences, which in combination with the piers produce stable vortices and thus ease measurements. The dashed line shows the rough limit between the 'safe' and 'dangerous' conditions, estimated by Gulliver *et al.*. This approach can give a rough idea of vortex risk, but it cannot fully account for particular conditions at a given intake, such as flow asymmetry or geometry, that can significantly influence vortex formation.

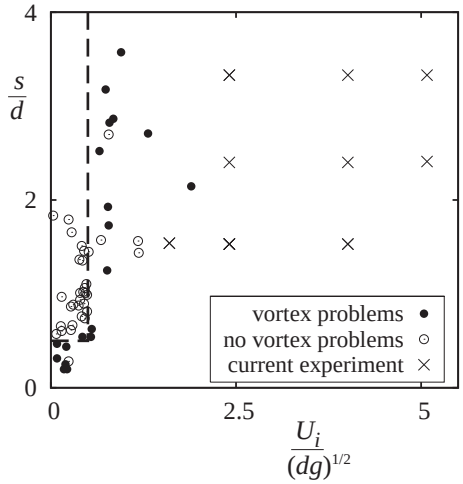

FIGURE 6.4: Vortex risk vs submergence and intake Froude number, adapted from Gulliver *et al.* (1986). — —: limit between 'safe' and 'unsafe' zones.

More rigorous evaluation of vortex risk is achieved by constructing a physical scale model of the proposed intake and visually inspecting the flow for vortices. Physical models are expensive to build but they allow the engineers to acquire a good sense of how the flow and intake geometry interact to produce flow asymmetries or vortices. Physical models can also be relatively easily modified to evaluate and compare alternative designs. There are however many challenges to evaluating vortex activity in a physical model.

The scaling factor between the prototype and laboratory model for hydropower intakes can range from 1:20 up to as large as 1:200 (Hecker, 1981). At large scaling ratios, the free surface depression produced by vortices in the model can be almost imperceptible. Direct observation of the free surface depression is particularly difficult if the model walls are opaque, in which case the free surface only be observed from above. In this situation, the presence of vortices can be detected by watching for the deformation of reflections on the free surface. The vortices tend to be small compared to the intake, and highly transient in time and place. They sometimes appear and become visible a short distance from the intake and slowly intensify as they approach it. They may then attain a stable intensity and location for several seconds and then dissipate, suddenly or gradually. Once a vortex is detected in a lab-scale physical model, the standard practice is to inject dye into its core to evaluate its coherence and stability or persistence. Engineers usually categorize and record vortices in terms of qualitative characteristics such as the coherence of the dye core and the vortex's ability to entrain floating particles (Hecker, 1987; Walder and Rutschmann, 2007; Mercier *et al.*, 2008; Kiviniemi and Makusa, 2009; Taghvaei *et al.*, 2012).

The transient nature of the vortices significantly adds to the challenge of documenting and identifying trends in vortex activity. Turbulence can further complicate the task. At relatively low turbulence levels, vortex intensity tends to increase when the flow rate increases. However, when turbulence also increases significantly with increased flow rate, vortex activity may decrease at higher flow rates, suggesting that the turbulence is preventing vortices from forming or intensifying (Padmanabhan and Hecker, 1984; Tastan and Yıldırım, 2010).

6.4 Quantitative vortex assessment in a physical lab-scale model

The goal of this paper is to provide tools that will allow engineers to quantitatively assess the characteristics of vortices in physical laboratory models using simple and accessible measurement devices or techniques. It also aims to help engineers estimate how these characteristics will translate to the prototype scale. To achieve this, detailed velocity measurements are taken in a simplified physical lab-scale model of an intake, documenting both the approach flow and vortex characteristics such as the characteristic radius r_o and bulk circulation Γ_∞. The measurements are then combined with Burgers's vortex model to produce an analytical model that links the measured vortex characteristics with the approach flow and geometry of the intake.

The analytical model is first used as a guide for estimating the characteristic radius of the vortex from velocity measurements of the approach flow made with an Acoustic Doppler Velocimeter (ADV), and for roughly measuring the bulk circulation using a relatively simple surface particle-tracking technique. In the following section, the analytical model is used to estimate and discuss how vortex characteristics observed in a laboratory scale physical model should scale up to the prototype scale.

6.4.1 Experimental setup

The physical model in which the measurements are made has a 3.9 m long channel, a square 1 by 1 m cross-section and a circular pipe of inner diameter d = 11.5 cm mounted flush into the downstream wall of the channel, with its axis located 0.14 m above the channel bed. The geometry is described in more detail in Suerich-Gulick *et al.* (2013d). Two tall narrow plates are mounted perpendicular to the downstream wall on each side of the outlet opening. These plates produce a more stable vortex by provoking flow separation; they are spaced k=15 cm apart, symmetrically about the pipe axis, and they span the full channel depth. They are referred to as piers in the rest of this paper since they act in the same way as the piers that hold trash racks across the penstock opening at hydropower intakes. Each pier generates a relatively stable vortex pair in its wake: one vortex that starts at the free surface and one that starts from the floor of the tank. Both vortex tails are entrained into the inlet pipe, but we focus on the free

surface vortices in this paper because these are more likely to cause problems by entraining air or floating debris. In most hydropower intakes, the submerged vortices are minimized or absent because the inlet opening is roughly aligned with the bottom of the channel. Only the right-hand free surface vortex is measured (as seen looking downstream) because of geometrical symmetry. Minor mean asymmetry arises due to asymmetry of the supply pipe and temporal asymmetry arises due to the interaction of the two vortices. A global coordinate system (X,Y,Z) with corresponding velocities (U_X,U_Y,U_Z) is defined to refer to the geometry and flow outside the vortex. Its origin is located at the free surface, half-way across the downstream wall of the channel. Z points down towards the bed and X points downstream. A local coordinate system (r,θ,z) with corresponding velocities (V_r,V_θ,V_z) is defined at the vortex axis with z pointing down from the free surface.

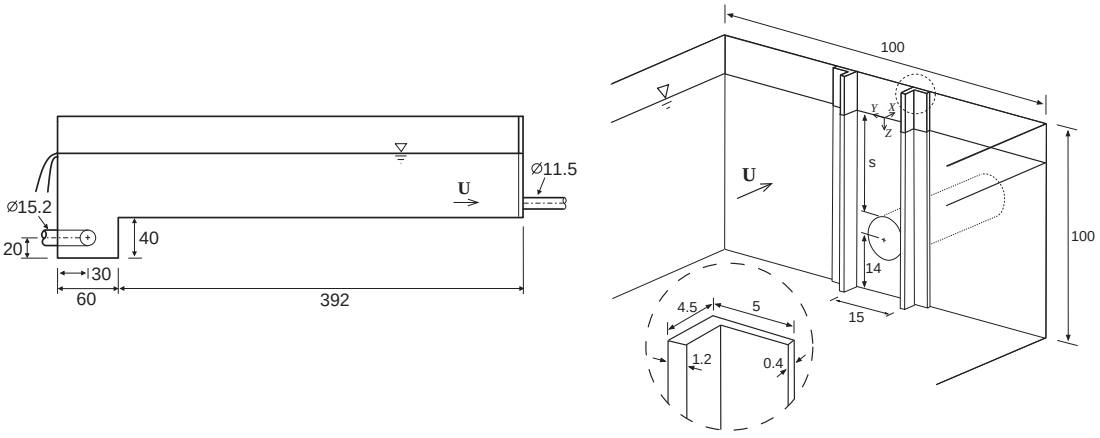

FIGURE 6.5: Vertical section (left) and isometric (right) views of the simplified laboratory model (dimensions in cm).

6.4.2 Estimating the characteristic radius from the approach flow

The characteristic radius r_o is a key determinant of vortex intensity that is also quite difficult to measure directly. However it is possible to estimate r_o from the vertical gradient of the approach flow velocity $\partial|U|/\partial Z$ directly in front of the inlet. This section describes how mean flow velocity measurements made in the simplified intake lab model can be used to calculate r_o (Suerich-Gulick *et al.*, 2013d). The calculations can be adapted to other geometries and configurations.

The magnitude of velocity $|U|$ for the approach flow is measured using an ADV along a vertical line located at the channel centerline ($Y = 0$), $\triangle X$ = 5.5 cm upstream from the inlet pipe. It is found that the bulk flow between the piers in the upper portion of the channel behaves like potential flow drawn into a horizontal line sink along Y located at the upper edge ($Z = s$ of the inlet opening (Yıldırım *et al.*, 2000). (See Fig. 6.6(a) for a schematic section of the flow.) The non-dimensional velocity $|U|/U_i$ thus collapses onto a single curve for all eight flow conditions studied, which makes it possible in the next section to establish relations for r_o and Γ_∞ in terms of the mean inlet velocity U_i and relative submergence s/d:

$$\frac{|U|_{\text{fit}}(\eta)}{U_i} = \frac{c_1 d}{4k}\left(\frac{d}{\eta} - c_2\right), \tag{6.3}$$

where $|U| = (U_X^2 + U_Y^2 + U_Z^2)^{1/2}$, $U_i = 4Q/(\pi d^2)$, and η is the total distance from the top of the inlet opening to each measurement point (as shown in Fig. 6.6a), so that $\eta = \sqrt{(s-Z)^2 + (\triangle X)^2}$. Q is the flow rate through the intake pipe (units m^3/s). The non-dimensional coefficients c_1= 0.8 and c_2=0.28 are selected to produce the best fit. This best fit curve $|U|_{\text{fit}}/U_i$ is plotted as a dashed line in Fig. 6.6(b).

The deepest submergence level $s/d = 3.4$ is selected as the upper limit of operating conditions for study in the experiment because vortex activity becomes much more sporadic above that level. This transition point in vortex activity occurs when the vertical profile of approach flow velocity approaches zero at the free surface, indicating that a small degree of recirculation about the horizontal axis starts to occur where the free surface meets the intake wall. Since there appears to be a qualitative shift in flow structure at the $s/d = 3.4$ submergence, some caution should be used in applying trends observed at lower submergences to predict behavior at submergences equal to or greater than this.

Once the velocity profile of the approach flow has been established, it can be used to estimate the characteristic radius r_o. The measurements show that the mean slope of the axial velocity profile $V_z(z)$ inside the vortex is driven by the velocity profile $|U|(Z)$ outside the vortex over the same vertical section of flow (see Fig. 6.6(b). For a majority of the operating conditions, V_z follows a linear profile in η over a significant portion of the upper flow instead of growing as η^{-1} as does $|U|$. The pressure gradient within the vortex possibly acts to equalize the axial V_z

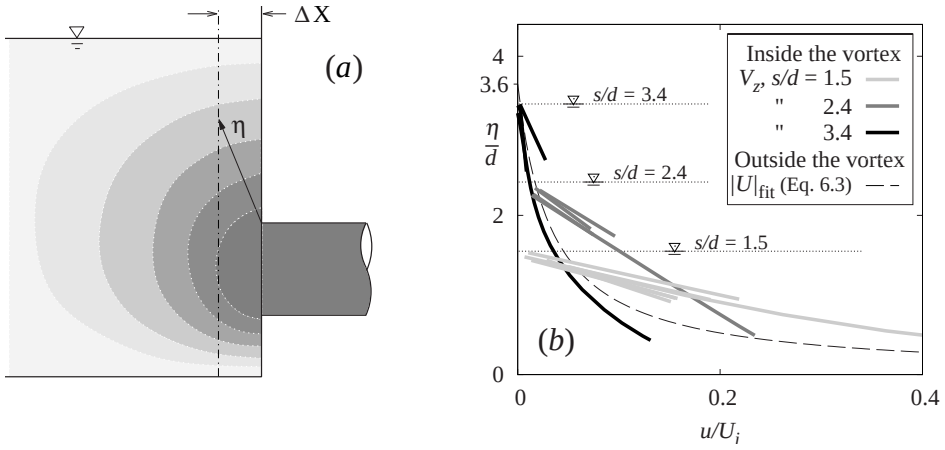

FIGURE 6.6: Side-view section of the lab intake, with $|U|$ indicated by shading (*a*). —·—, the ADV measurement axis. Velocity measured inside and outside the vortex (V_z and $|U|$, respectively).

gradient so that it tends towards the linear profile $V_z = az$, with a slope a that is roughly equal to the mean of $|U|$ over the same section. Closer to the inlet pipe, the gradient or absolute value of $|U|$ must be too strong for the linearization to occur.

The distance over which the linear V_z profile forms varies with operating conditions in a way that is difficult to predict from the available data, so instead of predicting a single value for the axial slope a, a range of values is estimated, within which it should fall. If no linearization occurs, then the axial velocity gradient at the free surface inside the vortex should roughly match $|U|$ outside the vortex. If linearization occurs over a proportion β of the submergence s, then it is estimated that $V_z(z)$ will follow a straight line from $V_z = |U|_{\eta \approx s}$ at the free surface to $V_z = |U|_{\eta \approx (1-\beta s)}$ a distance of roughly βs below the free surface, closer to the inlet pipe. The resulting gradient is

$$a_{\text{est}} = \frac{c_1 U_i d^2}{4ks^2(1-\beta)}, \tag{6.4}$$

where $0 < \beta < 0.8$, and $\beta = 0$ corresponds to no linearization. This estimate can be compared to that obtained directly from the vertical gradient of the measured $|U|$ profiles at the free surface (for $\beta = 0$) or over the top portion of the flow (for $\beta \neq 0$).

Once the axial velocity gradient has been estimated, the characteristic radius r_o can be calculated using Eqn. (6.2):

$$r_{o,\text{est}} = \frac{4s}{d}\left(\frac{\nu k(1-\beta)}{\mathrm{c}_1 U_i}\right)^{1/2}. \tag{6.5}$$

6.4.3 Bulk circulation

The bulk circulation Γ_∞ can be measured in the physical model at the free surface using surface particle tracking or it can be roughly estimated from the measured magnitude of the approach velocity at the free surface.

Surface particle tracking is achieved by placing floating particles on the free surface near the vortex and watching how fast they rotate around the vortex once they are entrained into its domain of influence. If the velocities are very high, it may be necessary to film the particles or take still photos at a low shutter speed and measure the angle spanned by the particle streaks over the time lapse of the image. If a particle completes N full rotations every second around a circular path of radius r_i about of the vortex, then the circulation at that radius r_i is roughly $\Gamma(r_i) = 4\pi^2 r_i^2 N$. Ideally, several measurements of Γ_∞ should be taken for a given operating condition since it is common for there to be significant variation in the circulation for a given vortex and from vortex to vortex.

In order to gain insight into scaling behavior, we want to relate the observed circulation to the operating condition parameters U_i and s/d. Normally, the circulation should roughly scale with the product of the approach velocity at the free surface $|U|_{\text{fs}}$ near where the vortices form and a length scale l that determines the zone in which the circulation may establish itself. These quantities are fairly easy to establish for the intake model considered here, because the vortices are generated by an obvious mechanism (separation off the pier tip) and in a clearly defined zone (the space between the piers). Measurements of the bulk circulation around the vortex reveal that it scales quite well with $|U|_{\text{fs}}\pi l_p$, where l_p=1.2 cm is the length of the pier. Using Eqn. (6.3) with $\eta = s$ for $|U|_{\text{fs}}$, this relation yields

$$\Gamma_{\infty,\text{est}} \approx \frac{\mathrm{c}_3\mathrm{c}_1 d U_i \pi l_p}{4k}(\mathrm{c}_4 d/s - \mathrm{c}_2), \tag{6.6}$$

where the coefficients $c_3 = 0.33$ with $c_4 = 1.0$ fit the lower limit of the measured values for Γ_∞, and the upper limit of the measured values is given by $c_3 = 0.33$ with $c_4 = 1.8$.

6.4.4 Free surface depression

The pressure drop due to centripetal acceleration causes the water level to drop in the vortex's center. The radial profile of the free surface depression for a given azimuthal velocity profile $V_\theta(r)$ can be computed by the following relation with sufficient accuracy if the axial and radial velocities near the free surface are small compared to V_θ:

$$h(r) = \int_\infty^r \left(\frac{V_\theta(r')^2}{gr'} - l_\sigma^2 \kappa(r') \right) dr', \tag{6.7}$$

where $h(r)$ is the vertical distance from the undeformed free surface level to that of the deformed free surface, and r is the distance from the vortex axis. $\kappa(r)$ is the local mean curvature of the air-water interface, $l_\sigma = \sqrt{\sigma/(\rho g)}$ is the characteristic length of the air-water interface, and σ is the surface tension coefficient (Andersen *et al.*, 2006). A constant value of l_σ=2.73 mm is used here, which corresponds to a clean air-water interface at 15°C. The first term on the right-hand side represents the centripetal acceleration that reduces the pressure inside the vortex, pulling the free surface interface downward. The second term represents the upward force exerted by surface tension. The mean free surface curvature $\kappa(r)$ is given by

$$\kappa(r) = -\frac{1}{2} \left[\frac{h_r}{r[1+(h_r)^2]^{1/2}} + \frac{h_{rr}}{[1+(h_r)^2]^{3/2}} \right], \tag{6.8}$$

where h_r and h_{rr} are the first and second derivatives of h with respect to r respectively. The first term on the right is the curvature about the horizontal axis and the second is the curvature about the vortex's (vertical) axis of rotation.

In order to evaluate if a vortex will cause operation problems, two quantities are important: the overall shape of the free surface depression and its maximum depth $h_0 \equiv h(0)$, which will be referred to hereafter as the tip depth. The nominal slope h_0/r_o of the free surface depression will be used as a representative quantity of the vortex shape. In order to compute the slope

and tip depth, the expressions for Γ_∞ and r_o (Eqns. 6.6 and 6.5 respectively) are substituted into Burgers's profile for $V_\theta(r)$ (Eqn. 6.1), which is substituted into the equation for the free surface profile (Eqn. 6.7). Since the resulting equation is non-linear in $h(r)$, an approximate solution for the tip depth is computed. First, the first term in the integral of equation (Eqn. 6.7) is integrated from $r = \infty$ to $r = 0$, which gives the relative tip depth $h_{\mathrm{n},0}/d$ without surface tension effects:

$$h' \equiv \frac{h_{\mathrm{n},0}}{d} = \frac{\mathrm{c}_5 \mathrm{c}_3^2 \mathrm{c}_1^3}{(1-\beta)}\ \mathrm{ReFr}^2 \left(\frac{d}{k}\right)^3 \left(\frac{l_p}{s}\right)^2 (\mathrm{c}_4 d/s - \mathrm{c}_2)^2, \tag{6.9}$$

where $\mathrm{c}_5 = 6.6 \times 10^{-4}$ is determined by the integration, and the Froude and Reynolds numbers Fr and Re are defined in terms of the submergence $\mathrm{Fr} = U_i/(sg)^{1/2}$ and $\mathrm{Re} = U_i s/\nu$ so that $\mathrm{ReFr}^2 = U_i^3/(g\nu)$.

The nominal slope $h_{\mathrm{n},0}/r_o$ is determined by Eqns. (6.9) and (6.5):

$$\frac{h_{\mathrm{n},0}}{r_o} = \frac{\mathrm{c}_5 \mathrm{c}_3^2 \mathrm{c}_1^{7/2} d^5 l_p^2}{(1-\beta)^{3/2}(sk)^{7/2}} \mathrm{Re}^{1/2}\mathrm{Fr}^2(\mathrm{c}_4 d/s - \mathrm{c}_2)^2 \tag{6.10}$$

r_o and $h_{\mathrm{n},0}/r_o$ are then used to obtain the surface tension correction factor $f_\sigma = \Delta h/h_{\mathrm{n},0}$ from Fig. 6.7*(*a), where Δh is the difference between the tip depth with and without surface tension. The tip depth with surface tension $h_{\sigma,0}$ is given by: $h_{\sigma,0} = h_{\mathrm{n},0}(1 - f_\sigma)$. Surface tension changes the shape of the depression as well as its tip depth, but its effect on shape is generally small enough that it does not change the magnitude of the relative surface tension effect to a significant degree.

Figure 6.7(*a*) is a compilation of the results of finite difference simulations of the effect of surface tension on the free surface depression produced by a Burgers's vortex for a wide range of vortex scales r_o/l_σ and shapes $r_o/h_{\mathrm{n},0}$ (Suerich-Gulick *et al.*, 2013c). It reveals that the relative surface tension effect is significant at scales comparable to l_σ, but negligible for $r_o/l_\sigma > 5$. The effect is also much greater for dimple-shaped depressions ($h_{\mathrm{n},0}/r_o \lesssim 1$) than for funnel-shaped depressions ($h_{\mathrm{n},0}/r_o \gtrsim 5$), which are shown in Fig. 6.7(*b*). This result is relevant because many past laboratory studies have focused on scale effects in air core vortices (a subset of funnel-type vortices) whereas the vortices observed in physical scale models of large hydropower projects tend to produce dimple-shaped depressions.

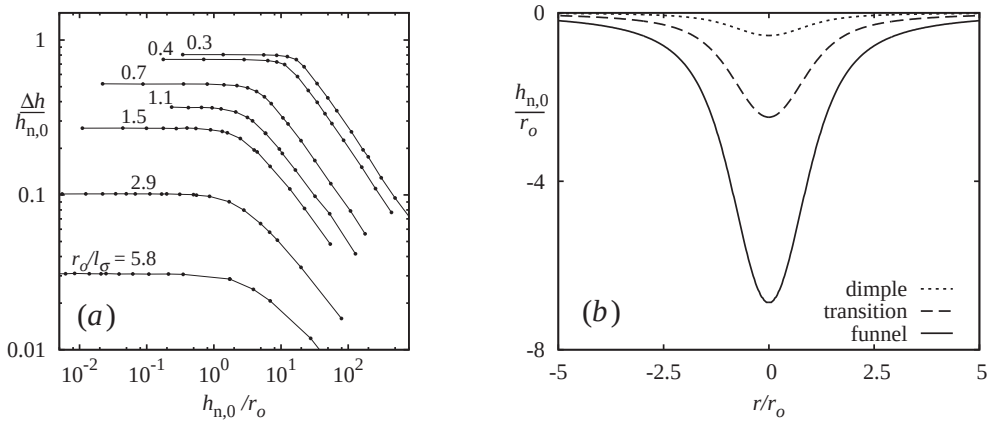

FIGURE 6.7: Relative surface tension effect $\Delta h/h_{n,0}$ as a function of the scale and shape of the depression (*a*). The different depression shapes (*b*): dimple, transition and funnel ($h_{n,0}/r_o$= 0.5,2.5 and 6.8, respectively).

6.4.5 Particle entrainment

Engineers commonly study the ability of free surface vortices to entrain floating particles in physical laboratory models as a means of qualitatively assessing their strength (Hecker, 1987; Walder and Rutschmann, 2007; Mercier *et al.*, 2008; Kiviniemi and Makusa, 2009; Taghvaei *et al.*, 2012), but little research has focused on quantifying the processes that control this phenomenon. Entrained debris or floating ice can become caught in the trash rack and accumulate there, increasing head losses and/or frequency of plant shut downs to clear the trash racks; if it passes through the trash rack, it can damage mechanical components. In order to understand what controls entrainment and predict its scaling behaviour, entrainment trends are examined in the physical laboratory model described above. The relevant forces are discussed and estimated for the different operating conditions and their relative magnitude is compared to the observations.

Plastic granules with a density of ρ_i = 916 kg/m^3 equal to that of ice are placed on the free surface and observed to see if they are entrained by the vortex down from the free surface and into the inlet pipe. The particles are roughly cylindrical in shape and of equal length and diameter ℓ_{part}, ranging from 1 to 5 mm. In this size range, smaller particles are experimentally observed to be more easily entrained than larger ones. Since the relative importance of

surface tension is greater for smaller particles, and since surface tension would work against entrainment, this result suggests that surface tension is not the critical factor in determining if entrainment occurs. The critical particle size $\ell_{\text{part,c}}$ is the the size of the largest particles that are regularly entrained. Predictably, stronger vortices are able to entrain larger particles. This translates to larger critical particle sizes $\ell_{\text{part,c}}$ for the operating conditions with greater flowrates U_i and lower submergences s/d, as shown in table 6.1 (Morissette, 2009).

	U_i [m/s]			
s/d	0.63	0.94	1.5	2.0
1.5	5	>5	>5	-
2.4	-	1	-	5
3.4	-	<1	<1	1

TABLE 6.1: Maximum size $\ell_{\text{part,c}}$ (in mm) of particles entrained at each operating condition.

The magnitude of forces acting on a particle located at the center of the vortex just below the free surface is examined. The critical particle size $\ell_{\text{part,c}}$ is estimated as the size at which the forces pulling the particle downward begin to surpass the upward forces keeping it afloat. Once the particle is no longer in contact with the free surface, the only force acting upward on the vortex is buoyancy F_{b}, while the forces pulling it downward are drag F_{d} and an additional pressure force F_{p} due to axial gradients in the azimuthal velocity.

We find that the critical particle diameters $\ell_{\text{part,c}}$ observed in the experiment are quite well predicted by the balance of the buoyancy force F_{b} and the pressure force F_{p}. The magnitude of F_{d} is much smaller in most cases and does not appear to be a good predictor. Buoyancy F_{b} is the difference between the weight of the particle pulling it downward and the hydrostatic pressure gradient, producing a net upward force, $F_{\text{b}} = A_{\text{cs}}\ell_{\text{part}}g(\rho_{\text{w}} - \rho_{\text{i}})$, where A_{cs} is the cross-sectional area of the particle ($A_{\text{cs}} = \pi\ell_{\text{part}}^2/4$) and ρ_{w} and ρ_{i} are the water and particle density, respectively. The drag force F_{d} is due to the friction and form drag produced by water flowing down past the particle. $F_{\text{d}} = 0.5\text{C}_{\text{d}}A_{\text{cs}}V_z^2$, where C_{d} is a coefficient of drag, assumed to be roughly equal to 1.1. As soon as there is a slight depression of the free surface, V_z does not start at zero just below the free surface, but rather at some larger value that appears to be roughly proportional to $0.1V_{\theta,\text{max}}$, where $V_{\theta,\text{max}} = 0.1\Gamma_\infty/r_o$ is the peak azimuthal velocity.

The azimuthal velocity V_θ is large enough that any axial gradient of its magnitude should produce a negative pressure gradient along the vortex axis that would produce an additional downward force acting on the particle that could be significant. However it is difficult to estimate its magnitude right near the free surface due to the complexity of the flow there, particularly in the presence of a particle. After examining different combinations and estimates of F_d and F_p, we find that $\ell_\mathrm{part,c}$ is best predicted by the balance of buoyancy and a bulk estimate of downward force $F_\mathrm{p} = 0.5\rho_\mathrm{w} A_\mathrm{cs} V^2_{\theta,\mathrm{max}}$ where $V_{\theta,\mathrm{max}}$ is estimated using the mean of the low and high estimated values for Γ_∞ (Eqn. 6.6) and $\beta = 0.8$ in Eqn. (6.5) for r_o.

F_b scales with ℓ^3_part while F_p scales with ℓ^2_part, so F_b is proportionally smaller than F_p for small particle sizes and greater for larger particle sizes. The critical particle length $\ell_\mathrm{part,c}$ is given by the point where F_b becomes equal to F_p, $F_\mathrm{p}/F_\mathrm{b} = 1$:

$$\frac{\ell_\mathrm{part,c}}{d} = \frac{0.5\rho_\mathrm{w} V^2_{\theta,\mathrm{max}}}{\triangle\rho g d} = \frac{\mathrm{c}_6 \mathrm{c}_1^3 \mathrm{c}_3^3 \pi^2}{(1-\beta)} \mathrm{ReFr}^2 \left(\frac{\rho}{\triangle\rho}\right) \left(\frac{d}{k}\right)^3 \left(\frac{l_p}{s}\right)^2 \left(\frac{(1+\mathrm{c}_4)d}{2s} - \mathrm{c}_2\right)^2, \quad (6.11)$$

where $\mathrm{c}_6 = 2 \times 10^{-5}$ comes out of the calculation and $\triangle\rho = \rho_\mathrm{w} - \rho_\mathrm{i}$. As shown in Fig. 6.8, the observed and predicted values for $\ell_\mathrm{part,c}$ are greater at larger values of inlet velocity U_i and smaller values of s/d.

In summary, the vortex characteristics in the lab-scale model can be estimated from the intake velocity U_i and relative submergence s/d using the relations developed above: r_o can be estimated using Eqn. (6.5), Γ_∞ from Eqn. (6.6), $h_{\mathrm{n},0}/d$ from Eqn. (6.9), the shape $h_{\mathrm{n},0}/r_o$ from Eqn. (6.10), and the critical particle diameter $\ell_\mathrm{part,c}$ from Eqn. (6.11).

6.4.6 Scale effects

Empirical data about how free surface vortices affect turbine performance is limited, and translation of vortex characteristics from the laboratory to the prototype scale is insufficiently understood. This double uncertainty makes it quite difficult for engineers to determine if a vortex is truly 'problematic' when it is observed in a lab-scale physical model. The second source of uncertainty is addressed in this section.

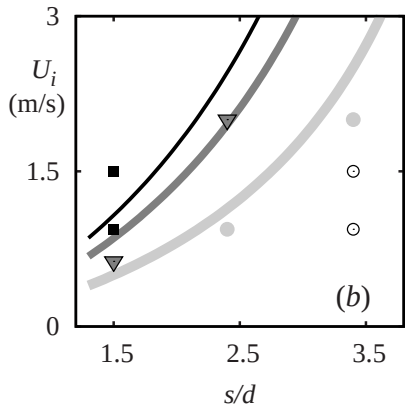

FIGURE 6.8: Predicted (lines) and observed (points) values of $\ell_{\text{part,c}}$. (, ,), isocontours of $\ell_{\text{part,c}}$ = (1,5,10) mm respectively predicted by Eqn. (6.11). (○, ●, ▼, ■), $\ell_{\text{part,c}}$ = (<1,1,5,>5) mm respectively observed in the experiment.

Past researchers have focused primarily on the magnitude of the free surface depression when trying to evaluate the effect of scale on vortex 'strength', because the threat of air entrainment by the vortices is the least ambiguous (Daggett and Keulegan, 1974; Anwar, 1983; Möller *et al.*, 2012a). Daggett and Keulegan (1974) and Anwar (1983) found that the critical parameters in the laboratory model became less sensitive to the Reynolds number for $\text{Re} \gtrsim 4 \times 10^4$ or 1×10^5, respectively. Similarly, Anwar (1983) found that surface tension effects were less sensitive to the Weber number $\text{We} = \rho U_i^2 s/\sigma$ for $\text{We} > 1.5 \times 10^4$ or 4×10^4 if the vortex was a dimple or an air core, respectively.

Here, we start from the premise that scale effects are unavoidable (Hecker, 1987). The analytical model described in the previous sections is used to try to estimate how vortex characteristics observed in a lab-scale physical model might appear in a prototype-scale intake. It is assumed that the geometry of the lab- and prototype-scale intakes is identical, with a scaling factor α, meaning that $d_P = \alpha d_M$, where d_P and d_M represent a specific characteristic length (such as the inlet diameter) in the prototype and the laboratory model respectively. It is further assumed that the lab-scale model is operated according to Froude similitude $\text{Fr}_M = \text{Fr}_P$, which produces a ratio of the prototype and lab-scale Reynolds numbers $\text{Re}_P/\text{Re}_M = \alpha^{3/2}$. The resulting ratio of relative tip depths is $h'_P/h'_M = \alpha^{3/2}$ if $\beta_P = \beta_M$. (The non-dimensional critical particle length $\ell_{\text{part,c}}/d$ would scale by $\alpha^{3/2}$ as well). This indicates that the relative tip depth

in a prototype intake would be 460 times as large as that in the laboratory model if the latter was constructed at a 1:60 scale. A few caveats are discussed below, including factors that might reduce the predicted scale effect.

First, it is useful to recall that the free surface depression observed in lab-scale models tends to be extremely small and often barely discernible, usually less than a millimeter, corresponding to $h/d \sim 0.005$ if $d \approx 0.1$, for example. So a relative depression that is 460 times larger than that could be possible, though it would represent a sizeable depression. There are also several factors that might reduce the actual scaling factor $\alpha^{3/2}$. The flow structure might be largely the same in the laboratory and prototype intakes while certain specific processes scale differently. The degree of linearization (indicated by β) that occurs at the prototype scale might be smaller (or greater) than in the model, in which case $h'_P/h'_M \sim (\mathrm{Re}_P/\mathrm{Re}_M)(1-\beta_M)/(1-\beta_P)$. If $\beta_M > \beta_P$, then h'_P/h'_M will be proportionally smaller.

Secondly, turbulent diffusion was found in the experiment to be effectively suppressed in the vortex so that the effective viscosity determining the core radius is equal to the molecular viscosity. In the prototype intake, turbulence might be stronger and/or might not be suppressed to the same extent inside the vortex (Odgaard, 1986; Hite and Mih, 1994). In this case, the effective viscosity ν_{eff} in the prototype vortex could easily be one or two orders of magnitude greater than that in the model vortex, resulting in a smaller 'effective' prototype Reynolds number, a larger characteristic radius, and a smaller relative tip depth. Finally, greater turbulence at the prototype scale might prevent certain vortices from forming that occur in the laboratory-scale intake in the absence of significant turbulent perturbation.

It is useful to compare the magnitude of scale effects due to surface tension versus scale effects associated with viscosity. The total tip depth of a vortex with a characteristic radius of 1 mm will be reduced to a fifth of its depth without surface tension in the worst case scenario (a dimple-shaped vortex), or to half of its depth if it is a funnel-shaped vortex. This compares to a ratio $h'_M/h'_P = 460$ in relative tip depths due to viscous effects for a laboratory model built to 1:60 scale (if our assumptions are correct).

When evaluating the risk of air entrainment by the vortex, it is perhaps more pertinent to consider how the shape or slope $h_{n,0}/r_o$ of the depression will scale, since a strong free surface slope is necessary to achieve air entrainment (Andersen *et al.*, 2006). Given that $h_{n,0}/r_o \sim \mathrm{Re}^{1/2}$ (see Eqn. 6.10), the ratio of the nominal free surface slope in the prototype compared to that in the model should scale with $\alpha^{3/4}$ if ν and β are identical in the lab-scale model and prototype. Returning to the example of the laboratory model constructed to 1:60 scale, this relation predicts that a vortex with a mild nominal slope 0.1 in the scale model would translate to a vortex with a surface slope of 2.2 in the prototype, which falls in the dimple or transition range at most scales.

6.5 Summary and conclusions

Using measurements in a laboratory-scale intake model and Burgers's vortex model, an analytical model was developed that relates key vortex parameters such as the characteristic radius and the bulk circulation to the intake geometry and approach flow conditions. The analytical model was used to estimate how vortices observed in a lab-scale physical model constructed to 1:α scale would appear in the full-scale prototype. In particular, the scaling behaviour of tip depth, vortex shape and debris entrainment properties were examined.

The analytical model predicts that the ratio of the prototype to lab-scale relative tip depths and non-dimensionalized critical particle diameter should be proportional to $\alpha^{3/2}$ and that the ratio of the nominal free surface slopes should be proportional to $\alpha^{3/4}$. The limitations of these predictions are discussed, as well as factors that could affect the scaling ratios for these quantities. The magnitude of scale effects linked to viscosity are compared to those due to surface tension, demonstrating that effects due to viscosity may often be significantly greater.

Future work is required to understand how turbulence affects the vortex characteristics, their stability, and their scaling behaviour. More in-depth examination of the linearization of the axial velocity is also needed to improve prediction of vortex intensity. Finally, a more detailed study of particle entrainment and the velocities just below the free surface would help clarify the different processes controlling entrainment and hence its scaling behaviour.

Logical Bridge 3

Manuscripts 1 and 2 provided a greater understanding of the processes by which the approach flow velocity field influences vortex characteristics. Manuscript 3 draws on insights gleaned from the experimental work to set up CFD simulations of the intake, in particular to determine an appropriate turbulence modelling strategy, and to set initial conditions and boundary conditions for the free surface simulation. Results from the previous manuscripts are also used to evaluate the accuracy of the solutions and to estimate some vortex characteristics that are poorly predicted in the simulation but can be approximated from the computed mean velocity field of the approach flow.

Chapter 7

Computational fluid dynamics modelling strategies for predicting free surface vortices at hydropower intakes (Manuscript 4)

ABSTRACT

The paper examines strategies for using computational fluid dynamics (CFD) to predict free surface vortices at hydropower intakes within the constraints of a consulting firm in the hydraulic engineering industry, with a focus on modelling of the free surface deformations and turbulence effects. A rough turbulence modelling strategy is tested in which a static eddy viscosity distribution is imposed across the domain using an analytical function that stabilizes the simulation in the upstream and free surface portions of the flow without the excess turbulence in the vortices which is typical of standard eddy viscosity models. The results demonstrate that the suppression of turbulence in the simulated vortices is necessary to predict the vortex characteristic radius reasonably well and to capture the enhanced axial velocity jet that is observed

experimentally in the vortex. The paper concludes with some techniques that could be used to estimate vortex characteristics such as the bulk circulation, characteristic radius, tip depth, and depression shape from a coarse simulation that only roughly captures the vortex structure.

7.1 Introduction

Free surface vortices are problematic when they form at low-head hydropower intakes because they can entrain air or floating debris down to the turbines or affect the uniformity of the flow and thus harm performance. Intakes have traditionally been assessed and optimized using physical laboratory-scale models but there is growing interest in predicting vortex activity at intakes using computational fluid dynamics (CFD) modelling, with the hope that it could one day be competitive both in terms of economic costs, accuracy and the time required to obtain suitable results.

This work examines how effectively a widely used commercial CFD software package might be used to predict the intensity of free surface vortices at hydropower intakes within the constraints of a typical industrial intake optimization process. ANSYS-CFX is tested using detailed measurements of the approach flow and vortex characteristics that were made in a laboratory-scale model of a simplified intake over a range of operating conditions and vortex intensities (Suerich-Gulick *et al.*, 2013d). Faced with the limitations of simpler two-equation eddy viscosity models and the inaccessibility of higher order turbulence models such as LES, a rough approximation of the vortex-turbulence interaction is tested using a static eddy viscosity distribution that is imposed over the domain using an analytical function. The results obtained with the imposed eddy viscosity model are compared to experimental measurements and to the results of a standard k-ε simulation. Burgers's (1948) vortex model is used to analyse the results and to suggest how the characteristic radius r_o, the tip depth h_0 and the nominal depression slope ζ could be estimated from simulations.

7.1.1 Burgers's vortex model

Burger's simple vortex model is commonly used to describe axially stretched vortices. The model is helpful to understand how axial stretching and radial diffusion control vortex strength (Burgers, 1948). The flow in the vortex is described using a cylindrical coordinate system (r, θ, z) with corresponding velocity $\boldsymbol{V} = (V_r, V_\theta, V_z)$ and vorticity vector $\boldsymbol{\omega} = (\omega_r, \omega_\theta, \omega_z)$, where $\boldsymbol{\omega} = \bigtriangledown \times \boldsymbol{V}$. In the current flow configuration, z is defined pointing down from the undeformed free surface. The vortex is described in terms of the bulk circulation Γ_∞ around the vortex, and the characteristic radius r_o:

$$V_\theta(r) = \frac{\Gamma_\infty}{2\pi r}(1 - \exp\left(-(r/r_o)^2\right) \tag{7.1}$$

$$V_z(z) = az, \qquad V_r(r) = -ar/2, \tag{7.2}$$

$$r_o = 2(\nu/a)^{1/2}, \qquad a = \partial V_z/\partial z, \tag{7.3}$$

Γ_∞ indicates the amount of flow rotation around the vortex, which can be computed by integrating $\int_C rV_\theta \mathrm{d}C$ around a curve C of radius $r \gg r_o$ that encircles the vortex, where r_o defines the radius of the zone that contains the majority of the vorticity. The peak azimuthal velocity $V_{\theta,\max} = 0.1\Gamma_\infty/r_o$ occurs at $r/r_o = 1.12$.

Eq. (7.3) describes how r_o is determined by the balance of axial stretching $\partial V_z/\partial z$ concentrating the vorticity radially inward, and viscous diffusion spreading vorticity outward. Some authors have suggested that turbulent fluctuations in the vortex core may increase momentum transfer there, proposing that a greater effective viscosity ν_{eff} be substituted for ν in Eq. (7.3), where $\nu_{\text{eff}} = \nu + \nu_{\text{T}}$ and ν_{T} is an eddy viscosity used to model the increased momentum transfer produced by turbulence (Anwar, 1969; Odgaard, 1986; Hite and Mih, 1994). Though vortex scaling behaviour observed in past intake studies suggests that ν_{T} might become significant at larger scales (Suerich-Gulick *et al.*, 2013c), this hypothesis has not been been explicitly tested experimentally in intake-relevant conditions. Measurements in the intake considered here indicate that r_o is well predicted by Eq. (7.3) using the molecular viscosity ν and the measured gradient $\partial V_z/\partial z$, strongly suggesting that radial turbulent fluctuations are suppressed by flow

rotation in the vortex core under the studied flow conditions (Suerich-Gulick *et al.*, 2013d). This phenomenon has been extensively documented in other vortex and swirling flow configurations (for example Bradshaw, 1973).

7.1.2 Context and challenges

Increasing accessibility of high-performance computing facilities has generated a boom in CFD-modelling in a wide range of industrial contexts in the past decade or two. In order to be competitive with traditional physical laboratory-scale testing, CFD must produce suitable results within time-frames and financial budgets that are comparable with or lower than those required for the construction and operation of a physical model (Haque *et al.*, 2007). Physical models of hydropower intakes can commonly be constructed within two or three weeks of obtaining the complete intake geometry definition, and subsequently, different flow configurations and geometry variants can be tested within a few hours or a few days, depending on the magnitude of the geometry modification. Though CFD holds the promise of financial advantage over physical modelling, high-resolution CFD remains fairly expensive once computing facilities, highly-skilled engineering wages and licensing costs are accounted for. Though computing costs are rapidly decreasing, commercial CFD licensing costs remain substantial, especially for industrial cases that require multi-processor computations. This has led many CFD-reliant companies to invest time and money into exploring open source CFD software (for example, Petit *et al.*, 2010).

The interaction of vortices with both turbulence and the air-water interface figures among the key challenges involved in modelling free surface vortices at hydropower intakes using CFD. Since the vortices are typically much smaller than the intake, it is also challenging to produce a computational mesh of reasonable size that has a sufficiently fine resolution in the vortex and free surface region while also encompassing a sufficiently large region of the intake to account for the influence of approach flow and geometry. Insight can be drawn from past CFD work on airplane wing-tip vortices (Duraisamy and Iaccarino, 2005), swirling flow in pipes (Muntean *et al.*, 2005b; Skerlavaj *et al.*, 2010), cylinders with a bottom orifice (Sakai *et al.*, 2008; Bøhling *et al.*, 2010), hydrocyclones (Bunyawanichakul *et al.*, 2006; Haque *et al.*, 2006), as well as

vortices in pump intakes (Montazerin *et al.*, 2001; Tokyay and Constantinescu, 2006; Chuang and Hsiao, 2011; Tang *et al.*, 2011; Zhan *et al.*, 2012), nuclear reactors (Ito *et al.*, 2010a) and hydropower intakes (Teklemariam *et al.*, 2002; Li *et al.*, 2008; Nakayama and Hisasue, 2010).

Different strategies are employed to capture the free surface interface. Some model the free surface as a fixed, free-slip surface, commonly referred to as a fixed lid boundary condition (Montazerin *et al.*, 2001; Tokyay and Constantinescu, 2006; Haque *et al.*, 2007; Li *et al.*, 2008; Sakai *et al.*, 2008; Škerlavaj *et al.*, 2011; Tang *et al.*, 2011), while methods such as single-value height functions (Nakayama and Hisasue, 2010) or the Volume-of-Fluid (VOF) method (Hirt and Nichols, 1981; Haque *et al.*, 2006; Ito *et al.*, 2010a; Chuang and Hsiao, 2011; Zhan *et al.*, 2012), allow the deformations of the free surface to be captured but increase computational expense and complexity. The VOF method computes the transport of a scalar volume fraction set to 1 in water and 0 in the air and defines the interface at the location where the volume fraction passes from from 0 to 1 (Hirt and Nichols, 1981).

Turbulence modelling presents another substantial challenge. The flow approaching the intake is usually turbulent, while flow rotation in the vortices tends to suppress turbulence in their core. This effect is not captured by standard eddy-viscosity models such as k-ε, so they overestimate eddy viscosity in the vortex core. This produces overly diffuse vortices (Duraisamy and Iaccarino, 2005; Muntean *et al.*, 2005a). Variants of eddy-viscosity models with curvature correction perform with mixed success (Montavon *et al.*, 2000; Duraisamy and Iaccarino, 2005; Škerlavaj *et al.*, 2011), as do more complex and therefore computationally expensive models such as Reynolds Stress models (RSM) (Montavon *et al.*, 2000; Muntean *et al.*, 2005b; Bunyawanichakul *et al.*, 2006; Haque *et al.*, 2006; Škerlavaj *et al.*, 2011). This persistent uncertainty coupled with the cost of higher-order turbulence models has led some authors to approximate the flow as inviscid (Muntean *et al.*, 2005b) or laminar (Sakai *et al.*, 2008; Ito *et al.*, 2010a) even if the flow outside the vortices is turbulent. Large Eddy Simulations (LES) seem to capture the vortex characteristics more consistently (Chuang and Hsiao, 2011; Tokyay and Constantinescu, 2006; Nakayama and Hisasue, 2010; Škerlavaj *et al.*, 2011), though in some simple cases laminar simulations may capture the vortex characteristics just as well (Muntean *et al.*, 2005b) at

a fraction of the computational cost. In situations where vortices are highly unsteady or interactions with background turbulence are significant, a higher order model such as LES may be necessary.

This paper examines how the strategy of modelling the vortices as laminar employed by Sakai *et al.* (2008) and Ito *et al.* (2010a) for fixed-lid simulations might be applied to simulations of free surface vortices at hydropower intakes that include low Froude number channel flow with deformations of the free surface captured using the VOF method. Initial tests revealed that the VOF model causes significant additional numerical instability, so eddy viscosity must be imposed in the upstream and outflow portions of the domain in order to stabilize the simulation.

7.2 Problem definition

Fig. 7.1 shows the geometry of the simplified intake that was studied in a physical laboratory model (Suerich-Gulick *et al.*, 2013d) and is simulated here using CFD. The intake is composed of a circular intake pipe mounted into the downstream vertical wall of a rectangular-sectioned channel. The intake pipe opening is bracketed by piers, each of of which produces a pair of vortices in its wake. Two submerged vortices connect to the channel bed, and two free surface vortices connect to the free surface (see Fig. 7.3*a*). This work focuses on the two free surface vortices, since they tend to be of greater concern to engineers as they risk entraining air down to the turbine. Submerged vortices are often a greater problem at pumping intakes than at hydropower intakes because the hydropower intake opening is often aligned with the bottom of the channel, which is not the case here due to the simplified circular cross-section of the intake pipe.

The channel is 3.9 m long and preceded by a 0.4 m deep reservoir with a T-shaped diffuser with holes along the bottom of the cross piece through which the water is injected into the reservoir. The piers have a rectangular cross-section, they protrude l_p=4.5 cm into the flow, and are spaced 15 cm apart, symmetrically about the intake pipe. The intake pipe has a diameter d=11.5 cm and its axis is located 14 cm above the channel bed, aligned with the symmetry plane that divides the channel in half along its length. The origin of the global coordinate system (X,Y,Z) is defined at the intersection of this symmetry plane and the junction of the free surface

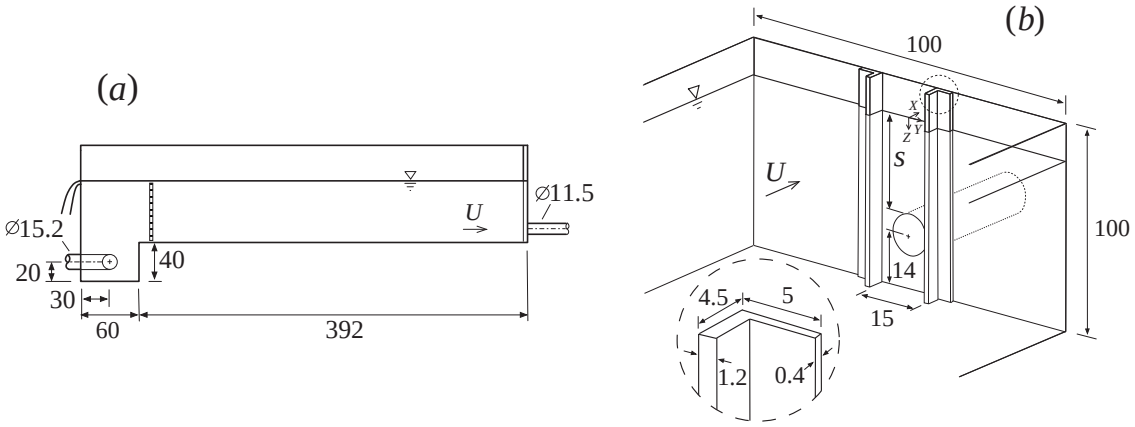

FIGURE 7.1: Vertical section (*a*) and isometric (*b*) views of the laboratory model (dimensions in cm).

TABLE 7.1: Test case conditions and observed vortex characteristics

	Operating condition					Observed vortex	
	H	Q	Re	$\mathrm{Re_{ch}}$	Fr	type	h_0
			$\times 10^{-5}$	$\times 10^{-4}$			
Case	(m)	($\mathrm{ls^{-1}}$)					(mm)
1	0.374	14.6	2.0	6.7	1.1	entrains air	7-12
2	0.475	18.8	4.1	5.5	1.1	deep dimple	1-8
3	0.577	18.8	5.6	4.0	0.9	dye core	0

and the downstream wall of the channel. X points downstream along the channel length and Z points downward from the free surface.

Three operating conditions studied experimentally with different combinations of water level H and flow rate Q are modelled using CFD to evaluate how well it captures the vortex characteristics (see Table 7.1). The tip depth h_0 refers to the maximum depth of the free surface depression produced by the vortex. Case 1 produces very strong vortices that frequently entrain air bubbles, while the vortices in Case 2 are somewhat weaker and do not entrain air. Case 3 produces very weak vortices that do not deform the free surface; they are sporadic and short-lived and they appear to be heavily perturbed by the high turbulence of the surrounding flow.

7.3 Method

This section describes how the simulations are performed, including different strategies that were tested and adapted to achieve results at a reasonable computational cost. The simulations are set up, performed, and post-processed using version 11 of the commercial CFD software package ANSYS-CFX. The free surface is captured using VOF, and a steady-state solver with local time-stepping. Simulations are computed first using the k-ε turbulence model and then a custom eddy viscosity distribution that is defined for this study to roughly model the stabilizing effect of turbulence in the upstream portions of the flow without producing excess diffusion in the vortices.

7.3.1 Computational domain and mesh

The computational domain is essentially identical to the physical model, with additional elements above the water level to capture the air phase in the simulations. A hexahedral structured mesh is generated using ICEM-CFD, with nested o-grids in the wake of the piers so that there are 12 to 19 grid points across the vortex core at the free surface depending on the vortex location (Fig. 7.2). The mesh includes highly stretched elements at the free surface in the upstream portions of the flow in order to produce a sufficiently fine grid across the air-water interface while minimizing total mesh size. The simulations are started on a coarse mesh and then switched to finer meshes as the simulation progresses. The high-resolution meshes range in size from 4.1 million elements for Case 1 to 5 million elements for Case 3. Summary grid sensitivity studies were performed but any further increase in mesh density would appear to produce negligible improvement compared to the error that persists linked to turbulence modelling (see section 7.3.4 below).

7.3.2 Boundary conditions

Flow into the reservoir is simplified in the CFD model by imposing a uniform vertical inflow velocity across the bottom surface of the reservoir (Fig. 7.3*b*). A hydrostatic pressure distribution

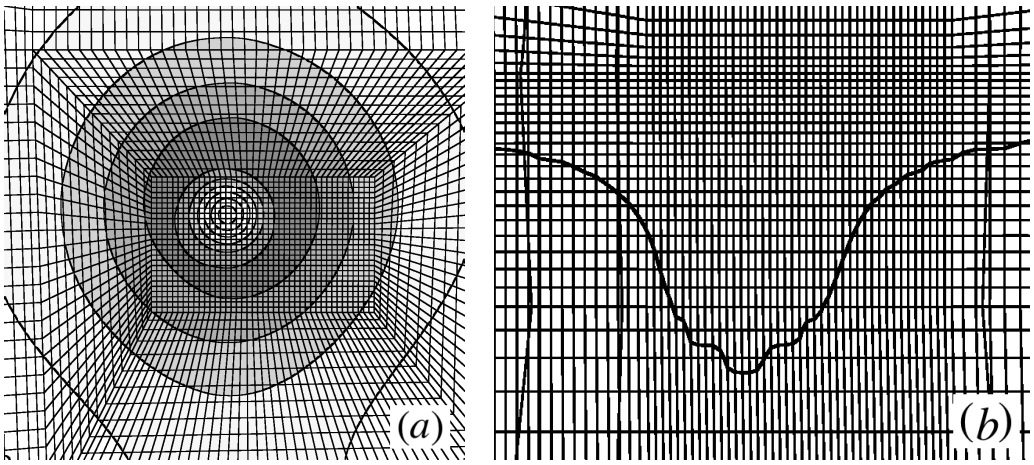

FIGURE 7.2: *a*) Plan (*b*) and side (*b*) views of the grid through the vortex, with shading in (*a*) indicating magnitude of V_θ. The free surface profile is indicated by the thick curve in (*b*).

is imposed at the intake pipe exit and adjusted during the course of the simulation to obtain the desired steady water level and flow rate as head losses evolve due to shear and flow contraction into the pipe during the simulation. A very small discharge exits the domain through the slanted vertical exit surface above the overflow weir cut into the upstream wall of the reservoir (on the left in Fig. 7.3*b*). The level of the weir is roughly 2 mm below the desired water level: it is necessary in both the experiment and the simulations to stabilize the water level. The flow rate across the weir outflow surface is not sensitive to the pressure imposed as a boundary condition there because the flow across it is supercritical. Atmospheric pressure is thus imposed on both this surface and on the top surface of the domain through which air freely enters and exits. All the solid boundaries of the channel are defined as smooth no-slip walls.

7.3.3 Free surface modelling

Initial tests using the fixed lid approximation produced a non-physical toroidal recirculation bubble at the vortex/free surface junction point when the vortex strengthened. It was therefore judged necessary to model free surface deformations in the simulations despite the additional computational cost and complexity. The segregated VOF multiphase solver is used during startup and transition phases (when a boundary condition, the turbulence model or the mesh is

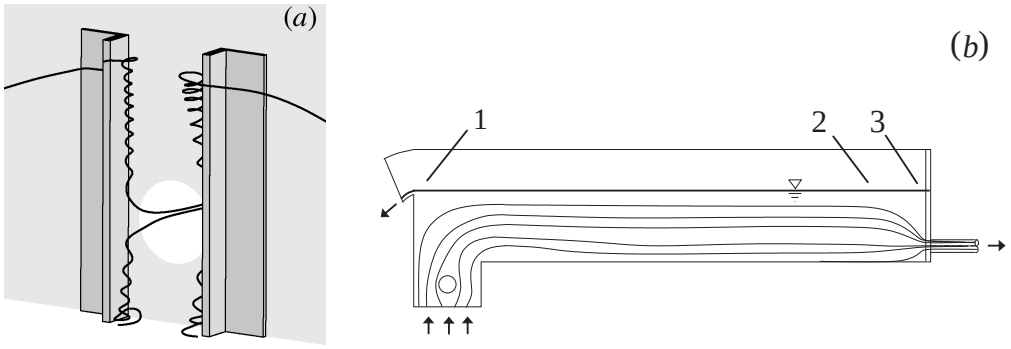

FIGURE 7.3: (*a*) Free surface and submerged vortices in the wake of the piers. (*b*) Computational domain sensitive free surface flow locations (1,2,3). Inflow and outflow boundaries are indicated by arrows.

changed) and the coupled multiphase solver is used at other times. The segregated solver computes the velocity field and the volume fraction separately at each time step, while the coupled multiphase solver computes the velocity and interface level simultaneously, in the same matrix (Zwart *et al.*, 2007). Though more prone to instability, the coupled flow solver produces better convergence of the mass flow than the segregated solver. The use of a continuous function in VOF to capture the discrete air-water interface appears to be a source of numerical instability, particularly during the start-up phase of simulations such as these where the channel Froude number $\mathrm{Fr}_{\mathrm{ch}}$ is very low. $\mathrm{Fr}_{\mathrm{ch}}$ ranges from 0.007 to 0.02 in the measured conditions, with $\mathrm{Fr}_{\mathrm{ch}} = U_{\mathrm{m}}/(Hg)^{1/2}$, where U_{m} is the mean velocity in the channel). Numerical instability originates most frequently at points where the flow impinges on or turns away from the free surface, as indicated by numbers 1,2 and 3 in Fig. 7.3(*b*).

7.3.4 Turbulence modelling

This section briefly describes the challenges encountered while testing different turbulence models and describes the custom imposed eddy viscosity ν_{i} model developed and tested in this study. Initial tests performed with Reynolds-Averaged Navier-Stokes (RANS) turbulence models produced poor results : both the eddy-vicosity models k-ε and SST with curvature correction (Menter, 1994) produced excessively diffuse vortices. When simulations started with k-ε are switched to the RSM model, the vortices initially intensify and become more concentrated but

then instabilities developed at the free surface in upstream portions of the flow (at points 1 and 2 in Fig. 7.3), repeatedly causing the simulation to diverge and fail within a few timesteps of switching to RSM. This may be provoked by an intolerance of the RSM model to the highly stretched grid elements found near the free surface in upstream portions of the flow. The aspect ratio of these elements cannot be reduced without producing an excessively large mesh. LES is judged to be too computationally expensive for the industrial hydraulic optimization context, so a simplified custom turbulence modelling strategy is developed.

The strategy is a variant of that employed by Muntean *et al.* (2005b); Sakai *et al.* (2008); Ito *et al.* (2010a): a static eddy viscosity distribution $\nu_{\mathrm{i}}(X,Y,Z)$ is explicitly defined over the computational domain using an analytical expression, with higher eddy viscosity in the upstream and free surface portions of the flow and lower eddy viscosity in the region where the vortices form. The approach produces relatively stable solutions with minimal excess diffusion of the vortices. $\nu_{\mathrm{i}}(X,Y,Z)$ is set roughly equivalent to the eddy viscosity distribution that was produced by the k-ε simulation, except in the wake of the piers where the vortices form. There, ν_{i} is set equal to the molecular viscosity $\nu = 8.9 \times 10^{-6}$ m/s^2. $\nu_{\mathrm{i}} = 120\nu$ in the reservoir and along most of the channel length, and $\nu_{\mathrm{i}} = 10\nu$ in the viscinity of the free surface: this both roughly models the effect of turbulence in the channel and stabilizes the simulation near the free surface. At the entrance to the intake pipe where the velocities and shear are very high, ν_{i} is set to a with a radial Gaussian profile with a peak value $\nu_{\mathrm{i}} = 1000\nu$ at the center of the opening producing gradual decay with increasing distance from the entrance. $\nu_{\mathrm{i}} = 500\nu$ in the rest of the pipe.

In order to avoid numerical instability while the velocity field establishes itself, the simulations are started with the k-ε turbulence model on a coarse mesh with a very small physical timestep (0.01 s). As the flow field develops, the timestep is increased to 0.06 s, the solution is interpolated onto a finer mesh to and the turbulence model is switched to the custom ν_{i} model.

Quantities such as the mass flow rate and free surface level continue to evolve after the residuals have flattend out around 10^{-4}. The vortex location and intensity continue to fluctuate, so it is difficult to establish if a stable solution has been reached. As the vortex strengthens in the ν_{i} simulation, vortical instabilities with a horizontal axis begin to develop and grow at the upstream limit of the vortex near the free surface, appearing to destabilize the vortex. The

instabilities begin to amplify and spread to other parts of the flow, so the simulations are stopped at this point. These instabilities may be linked to a physical vortex breakdown process but may also be a product of the turbulence model, due to the lack of stabilizing eddy viscosity just outside the vortex core. This outer region is less resistant to instability than the inner core region (Jacquin and Pantano, 2002). In the actual (non-simulated) flow, turbulence is more likely to persist outside the vortex core and may produce a more stable mean azimuthal velocity profile through increased radial diffusion. An unsteady simulation would probably be more appropriate but it was not possible within the time constraints. At the point where the simulations are stopped, oscillations in the mass flow out of the intake pipe are less than 2% of the mean value and oscillations of the free surface level were less than 1% of the total flow depth.

7.4 Results and discussion

Both the ν_i and k-ε solutions capture the larger structure of the approach flow fairly well. Figs. 7.4(*a-c*) compare the ν_i results for Case 2 to vertical and spanwise profiles of the mean streamwise velocity U_X measured by ADV (Suerich-Gulick *et al.*, 2013d). The profiles are evaluated at distances X = -17d, -1.7d and -0.5d upstream from the intake opening. The simulated profile at $X = -17d$ is uniform across the channel width (Fig. 7.4*a*). It slightly underestimates the velocity near the free surface ($Z/s = 0.1$) and overestimates it closer to the bed ($Z/s = 1.3$), which can also be seen in Fig. 7.4(*c*). Closer to the intake at $X = -1.7d$ (Fig. 7.4*b*), oscillations develop in the simulated profile at the free surface, where the velocities are weaker. These oscillations are much greater in the ν_i solution than in the k-ε solution (not shown), where the eddy viscosity damps out instabilities. The flow acceleration into the intake pipe is well captured at $X/d = -0.5$ just in front of the piers, but again, oscillations are visible closer to the free surface (Fig. 7.4*c*).

The velocity fields $V_\theta(r)$ and $V_z(z)$ inside the vortex differ significantly between the k-ε and ν_i solutions, as shown in Figs. 7.5(*a-f*). The vortex axis ($r = 0$) for the $V_\theta(r)$ profiles is identified as the point of local minimum pressure. The vortex simulated using the k-ε turbulence model is far too diffuse, with a characteristic radius r_o that is 4 to 5 times greater than the experimental

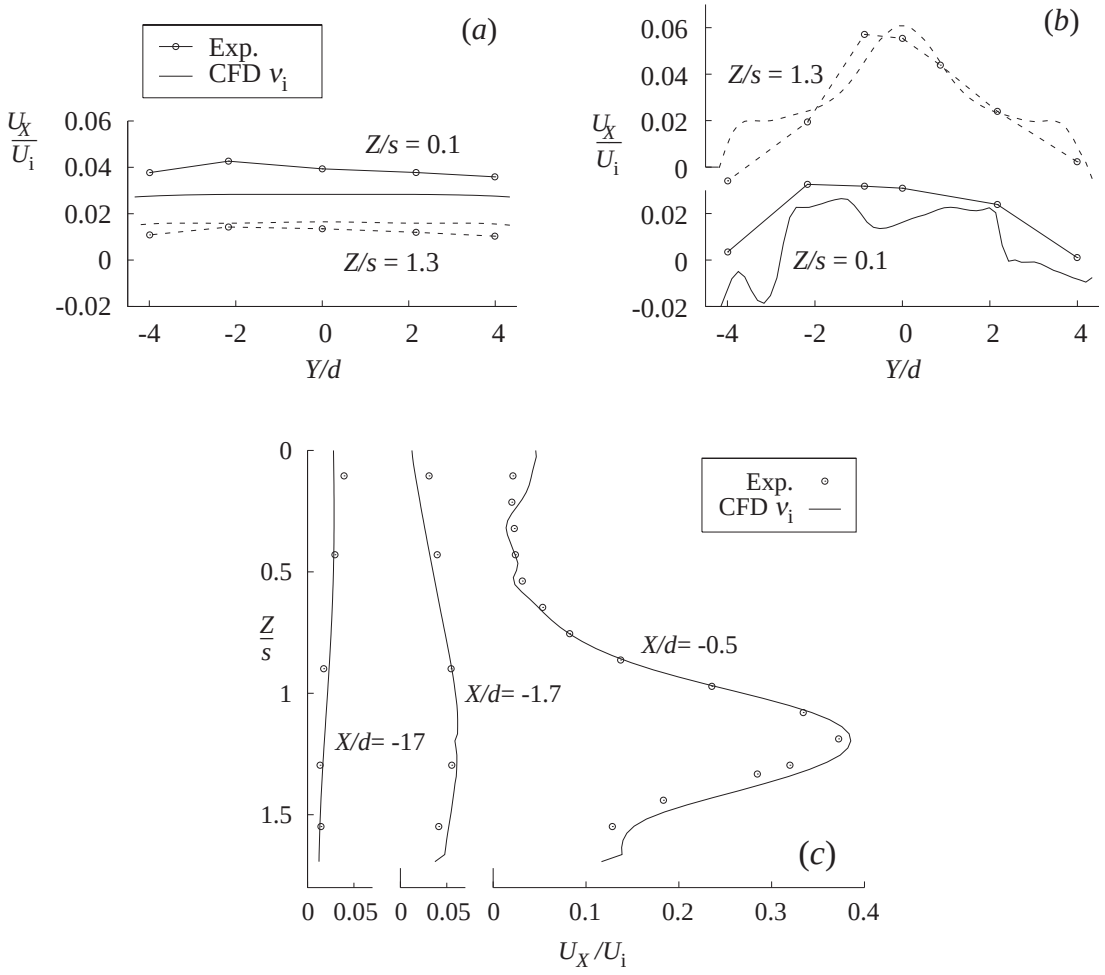

FIGURE 7.4: Profiles of streamwise velocity U_X measured by ADV at different stations along the channel for Case 2, compared to those obtained from the ν_t CFD simulation. (*a,b*): Spanwise profiles at (*a*) $X/d = -17$ and (*b*) $X/d = -1.7$. (*c*): vertical profiles at $Y = 0$.

value. The ν_t solution predicts r_o more closely but it still overestimates it compared to the measured values. The bulk circulation Γ_∞ is roughly twice the measured value in both the k-ε and ν_t solutions (as summarized in Fig. 7.9*b*). The overestimate of Γ_∞ might be due to improper simulation of the separation off the pier tip. It is also possible that the greater streamwise velocities further from the free surface (and closer to the intake pipe) have more time to drive the circulation to higher values at the free surface in the quasi-steady simulations than in the more transient vortices in the physical model.

The profiles of $V_z(z)$ in Figs. 7.5(*a-c*) show that the degree of axial stretching is properly captured in the ν_i simulations, which suggests that that the overestimate in r_o is due to excessive diffusion. This excess diffusion is probably a combination of numerical diffusion and ν_i from the tail end of the Gaussian distribution centered on the intake pipe plus the baseline level $\nu_i = \nu$.

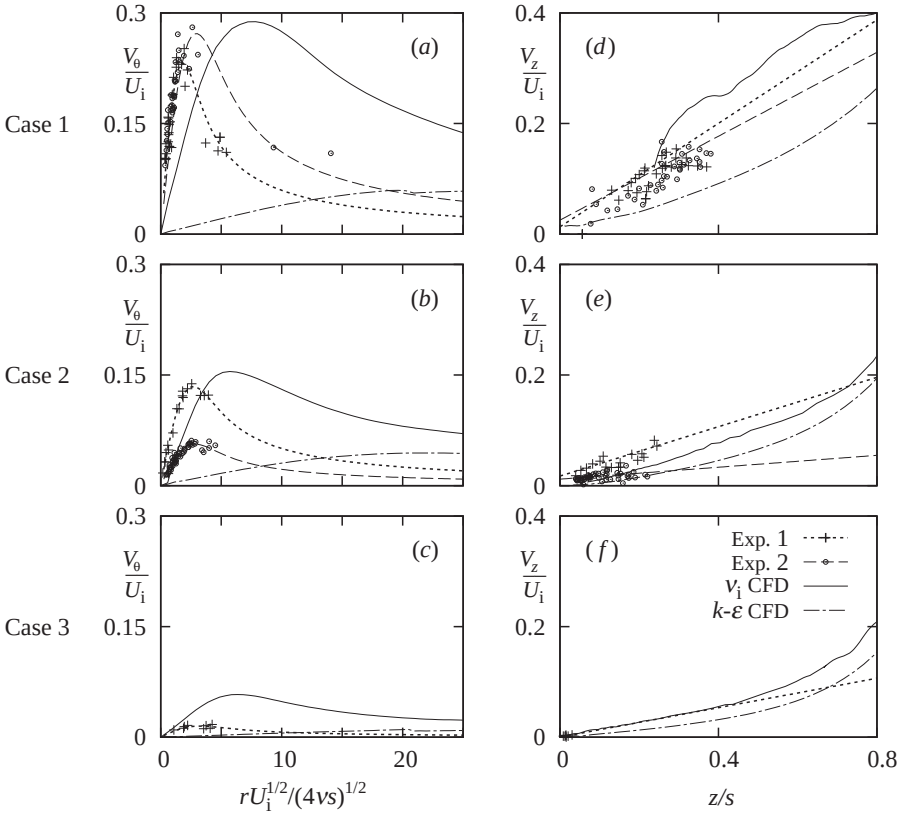

FIGURE 7.5: Comparison of the measured vortex velocity profiles to the CFD results obtained with imposed ν_i and k-ε for Cases 1 (*a,d*), 2 (*b,e*), and 3 (*c,f*). (*a-c*): $V_\theta(r)$ with Eq. (7.1) fitted to the measured data; (*d-f*): $V_z(z)$ with a straight line fitted to the measured data.

The axial velocity is much greater inside the vortex than outside the vortex in the ν_i solutions (Fig. 7.6 on the left, in agreement with the experimental measurements. Fig. 7.6 on the right shows that axial stretching of the vortex is driven by the vertical velocity gradient of the approach flow (U_Z, solid line with circles) just outside the vortex, measured at $X/d = -0.5$. The '+' data points show the measured axial velocity $V_z(z)$ profile inside the vortex from the first PTV

measurement sample ('Exp. 1' in Fig. 7.5), clearly indicating that the velocity inside the vortex is much greater than directly upstream from it. The figure also shows that the ν_{i} simulation successfully predicts the development of this enhanced axial velocity jet (solid line), though its magnitude appears to be somewhat underestimated. The k-ε solution (dash-dot line) does not capture the jet, so it produces a $V_z(z)$ profile inside the vortex that matches the profile $U_Z(Z)$ outside the vortex. The U_Z deficit near the free surface in the ν_{i} simulation (dotted line) appears to be a product of the rotational instabilities beginning to form upstream from the vortex.

Fig. 7.7 shows that the jet-like radial profile of $V_z(r)$ is not axisymmetric in the ν_{i} simulations and evolves along the axis of the vortex. This manifests itself as oscillations when $V_z(z)$ is plotted along the trajectory of a streamline that travels around the vortex. Similar oscillations that cannot be entirely attributed to measurement error are observed in the experiment. These oscillations are much weaker or non-existent in the k-ε solution. In the stronger vortices that produce a depression of the free surface (Cases 1 and 2), $V_z \approx 0$ at $r = 0$ just below the free surface ($z = 2.4$ cm), surrounded by an annulus of higher V_z. This higher-velocity annulus gradually converges into a single peak. However the location of the peak does not coincide with the vortex axis as defined by the local minimum pressure or the center of curvature of the streamlines, as shown in Fig. 7.7 for Case 2. The location of the V_z peak rotates around the axis somewhat, but it remains on the side of the vortex closest to the pier and downstream wall, probably because of acceleration of the flow due to the local constriction. In Case 3 where no free surface depression is generated, no V_z annulus forms and the peak V_z remains roughly at the axis when it forms (not shown).

The ν_{i} results overestimate r_o but they overestimate Γ_∞ to a greater degree, so that the corresponding free surface depression is deeper than the measured ones, as shown in Fig. 7.8. The ν_{i} 'CFD' curve is obtained from a vertical section through the 0.5 iso-contour of the volume fraction. $h_{\sigma,\mathrm{comp}}$ and $h_{\mathrm{n,comp}}$ are computed using Eq. (7.4) defined below, with Burgers's velocity profile (Eq. 7.1) fitted to the simulated $V_\theta(r)$ profile.

$$h_\sigma(r) = \int_\infty^r \left(\frac{V_\theta(\acute{r})^2}{g\acute{r}} - l_\sigma^2 \kappa(\acute{r}) \right) d\acute{r}, \tag{7.4}$$

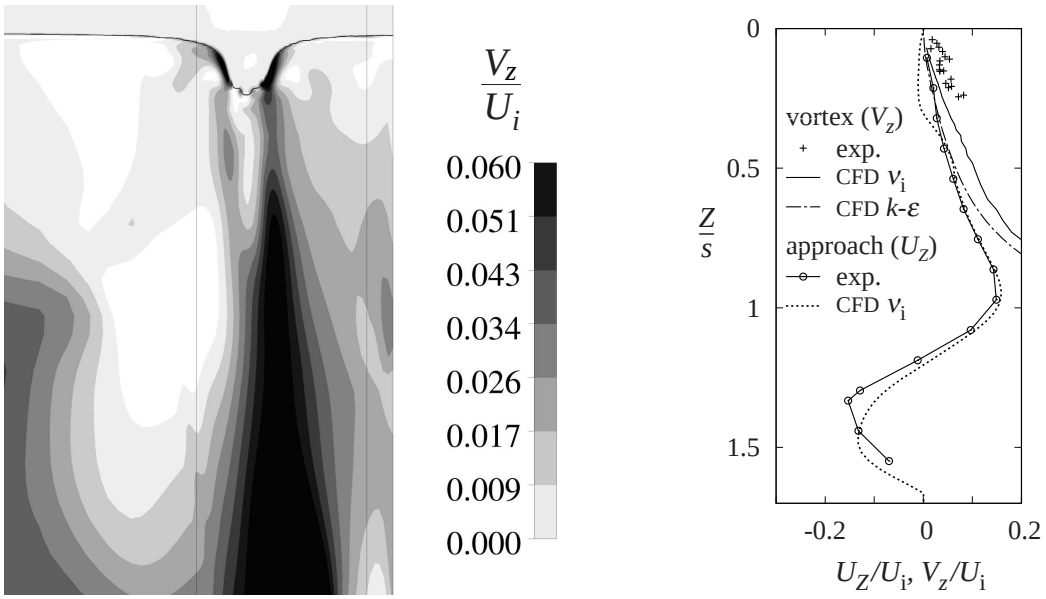

FIGURE 7.6: Profiles of the vertical/axial velocity outside (U_Z) and inside (V_z) the vortex for Case 2. Simulated V_z/U_i from the ν_i solution on a vertical plane normal to Y cutting through the vortex (left). Comparison of the measured and simulated vertical profiles of U_Z/Ui and V_z/U_i (right). U_Z is measured at $X/d = -0.5$.

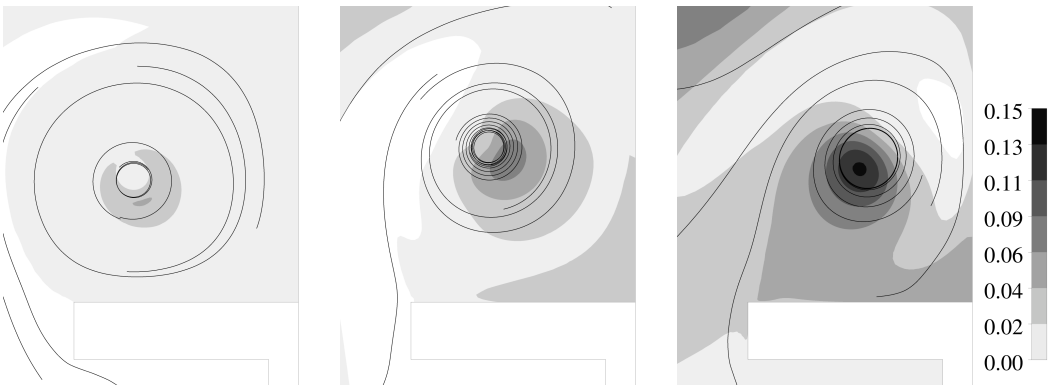

FIGURE 7.7: Distribution of V_z/U_i from the ν_i solution for Case 2 on horizontal planes located at $Z/s = (0.1, 0.3, 0.5)$ respectively, from left to right. The pier appears in section as a horizontal white rectangle at the bottom right of the images.

where $l_\sigma = 2.73$ mm is the characteristic surface tension length for a clean air-water interface at 15°C, and $\kappa(r)$ is the local mean curvature of the free surface (Andersen *et al.*, 2006). See Suerich-Gulick *et al.* (2013c) for more details on the free surface profile computations. Surface tension is neglected in $h_{\mathrm{n,comp}}$ as well as in the CFD simulations. The profile computed by the VOF model matches the $h_{\mathrm{n,comp}}$ profile quite well, and the effect of surface tension indicated by the difference between $h_{\sigma,\mathrm{comp}}$ and $h_{\mathrm{n,comp}}$, is quite small compared to the error due to the $V_\theta(r)$ profile.

The values for the simulated tip depth h_0 and Γ_∞, r_o obtained by fitting Burgers's profile to the simulated $V_\theta(r)$ profile are compared in Fig. 7.9 to the measured values (triangles) obtained for the 8 operating conditions studied in the experiment (Suerich-Gulick *et al.*, 2013d). Both the ν_{i} and k-ε solutions overestimate Γ_∞ and r_o, but the k-ε solution overestimates r_o by such a large degree that it tends to underpredict $h_{\sigma,0}$ while the ν_{i} solution overpredicts $h_{\sigma,0}$ by a fairly large margin.

7.4.1 Estimating expected vortex characteristics

The CFD solutions can be used to roughly predict the expected range of vortex characteristics, even when the simulations don't capture the vortex velocity field exactly. In a low resolution simulation, Γ_∞ and r_o can be roughly estimated from the flow field and used to compute the corresponding depression tip depth h_0 and shape (ζ). Γ_∞ is captured as well or better in the k-ε simulation than in the ν_{i} simulation in this particular configuration. Γ_∞ can be extracted from the solution by fitting Burgers's profile to $V_\theta(r)$ or by integrating rV_θ around a circle with $r > r_o$. In the k-ε simulations, the full Burger's profile does not form because r_o is too large, so Γ_∞ is estimated using $\Gamma_\infty = 2\pi r V_{XY}$ at $r \approx 0.024$ m, where the flow encounters the downstream wall of the channel. V_{XY} is the horizontal component of velocity.

The range of values for the axial gradient of axial velocity $a = \partial V_z/\partial z$ near the free surface can be estimated in a few ways. $V_z(z)$ is clearly driven by the axial profile of velocity outside the vortex |U|(Z) (Suerich-Gulick *et al.*, 2013d), but it is difficult to predict the extent to which $V_z(z)$ will follow a linear profile within the bounds set by |U|(Z).

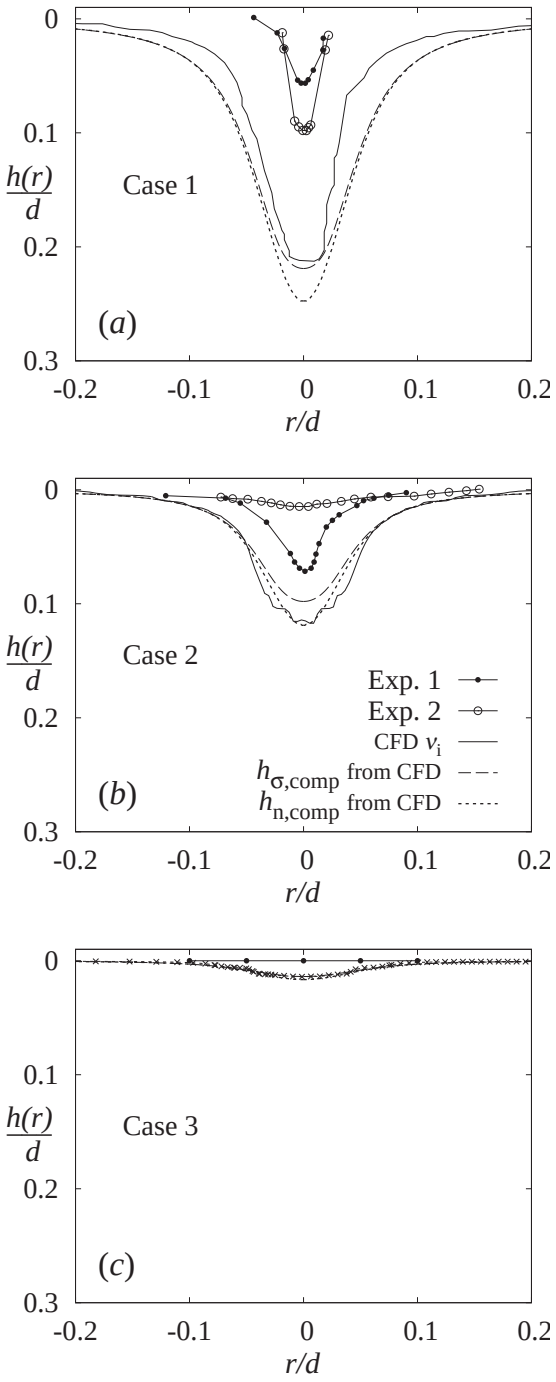

FIGURE 7.8: Free surface profiles obtained from the CFD simulations and measured in the experiment. $h_{\sigma,\mathrm{comp}}$ and $h_{\mathrm{n,comp}}$ are computed using Eq. (7.4) using Burgers's velocity profile (Eq. 7.1) fitted to the simulated $V_\theta(r)$ profile obtained with ν_i.

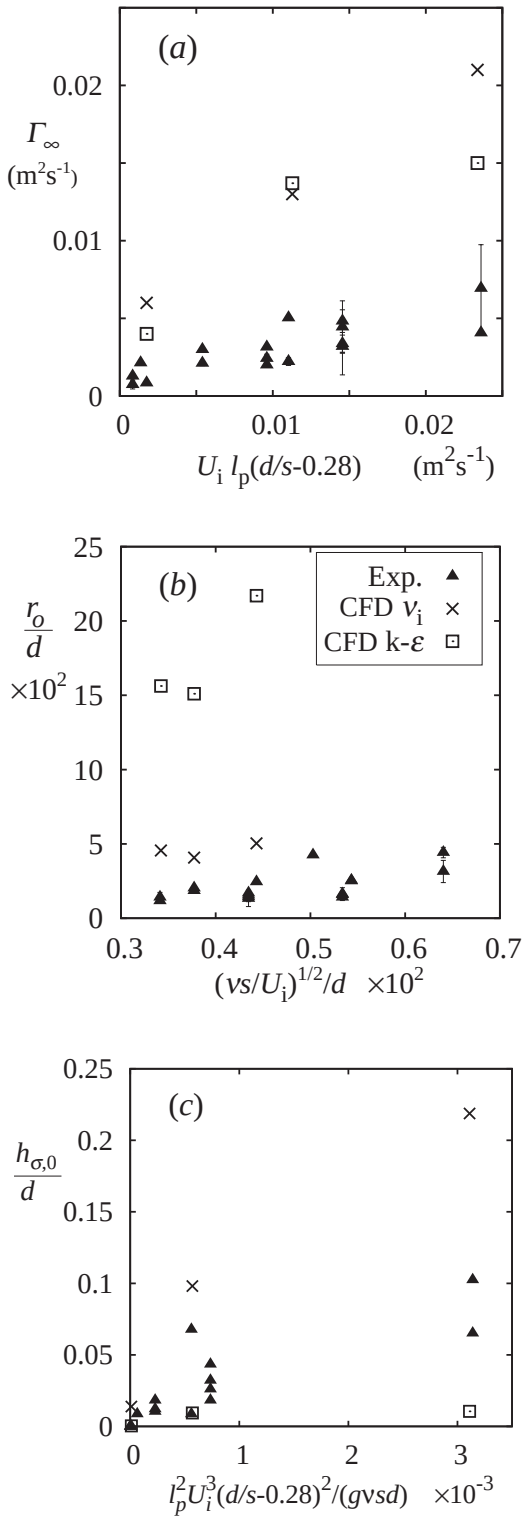

FIGURE 7.9: Comparison of the measured vs. simulated vortex characteristics. (*a*): bulk circulation Γ_∞ (*b*): characteristic radius r_o (*c*): tip depth $h_{\sigma,0}$. The key appears in (*b*).

The degree of linearization of $V_z(z)$ appears to be relatively well captured in the ν_i simulations, at least within the limits of the experimental variability, so a can be extracted from $V_z(z)$ over the portion of the flow near the free surface, from z = 0 to 0.3 s. In a simulation where the vortex is too diffuse, either due to a coarse mesh or excessive eddy diffusivity, the more linear $V_z(z)$ profile inside the vortex will likely not form to the same degree observed in experiments. In that case, a rougher estimate of the range of a can be obtained by examining the slope that would occur if $V_z(z)$ *did* followed a more linear profile, such that

$$a_{\text{est}} = \frac{\{U_Z(\beta s) - U_Z(0)\}}{\beta s}, \tag{7.5}$$

where βs indicates how far the linear profile extends from the free surface. β is observed to fall in the range $0.15 < \beta < 0.85$ in the experiment (Suerich-Gulick *et al.*, 2013d), so these values can be used as limits for the estimated range of β in Eq. (7.5). The corresponding values of r_o can be computed by substituting a into Eq. (7.3). The peak azimuthal velocity $V_{\theta,\max} = 0.1\Gamma_\infty/r_o$ and the tip depth $h_{n,0}$ (the depression at r=0 neglecting surface tension effects) can then be computed using

$$h_{n,0} = \frac{0.17\Gamma_\infty^2}{\pi^2 r_o^2 g}, \tag{7.6}$$

(Suerich-Gulick *et al.*, 2013d), from which the nominal depression slope $\zeta = h_{n,0}/r_o$ can also be computed. Surface tension effects in a laboratory-scale model can be accounted for using the surface tension correction factor f_σ, which equals

$$f_\sigma(r_o/l_\sigma) = \left[\exp(-0.44(r_o/l_\sigma)^2) + 1.9(r_o/l_\sigma)^{1.6}\right]^{-1} \tag{7.7}$$

for dimple vortices or can be read off Fig. 2(*b*) in (Suerich-Gulick *et al.*, 2013b) for funnels and transition-shaped depressions.

Predicting the mean characteristics r_o, Γ_∞, h_o and ζ of the vortex with simulations remains a challenge. There also remains uncertainty as to which vortices observed in laboratory models should be interpreted as 'problematic' and likely to cause problems at the prototype scale. Some of this uncertainty is linked to lingering questions about how vortex characteristics observed in the laboratory will translate to the prototype scale due to scale effects linked to surface tension,

viscosity and turbulence, as discussed in Suerich-Gulick *et al.* (2013c,b). There is also some ambiguity about what characteristics at the prototype scale would make a vortex sufficiently problematic to warrant significant additional expenditures to optimize the intake to eliminate the vortex or reduce its intensity. For example, the impact of a persistent vortex that does not entrain air but occasionally entrains debris has not been methodically evaluated, nor has the associated financial cost in production losses due to head losses or additional maintenance required.

Most vortices that occur at hydropower intakes are extremely transient. The transient nature of the vortices further complicates the analysis and comparison of simulated vortices with experimental vortices. A RANS simulation (even an unsteady one) averages the fluctuating velocities over a wide range of the time and length-scales, so it is likely to predict vortices that are more stable and persistent than those observed in the laboratory model. Since persistence of a vortex in the lab is sometimes used to gauge the danger posed by a vortex, the exaggerated persistence in the CFD simulations could lead one to mistakenly assess a simulated vortex as more problematic than it would be in the laboratory. On the other hand, the vortex intensity obtained by averaging the accurately predicted unsteady velocity field over time will be lower than that in an instantaneous field taken at peak vortex intensity (Nakayama and Hisasue, 2010).

Added to these constraints and numerical challenges, a number of uncertainties confront both physical and numerical modellers about the exact conditions under which an intake will operate. Data about upstream flow asymmetry or turbulence may be limited or absent, possibly requiring additional modelling with two-dimensional or quasi-three-dimensional numerical models to estimate. Other occasional or unpredictable phenomena such as wind and ice and debris accumulation at the free surface can significantly affect velocities at the free surface, but they are generally neglected due to their sporadic nature. All of these factors influence the modelling goals for this work, since they limit the degree of accuracy or certainty that can be realistically expected within an industrial hydraulic context when seeking to predict vortex activity.

7.5 Summary and conclusions

This paper examined the challenges associated with capturing the free surface deformations and modelling turbulence effects in axially-stretched free surface vortices that form in low Froude number flow at a simplified hydropower intake. It was found that careful definition of boundary conditions and a gradual start-up of the flow is required to avoid numerical and physical instabilities. The results clearly demonstrate the need for a turbulence modelling strategy that effectively suppresses turbulence in the vortex core in order to prevent excessive radial diffusion of vorticity and to allow the more linear profile of axial velocity to develop along the vortex axis. The characteristic radius of the simulated vortices with the imposed ν_{i} strategy is still greater than in the measured vortices, and the circulation is significantly overestimated as well, indicating that a more refined turbulence modelling strategy is required to capture the vortex characteristics more accurately. However the analysis indicates that results of the simulation can still be useful to estimate a range of expected vortex characteristics.

The results of this study demonstrate the need for a more sophisticated turbulence modelling strategy to capture the vortex characteristics more accurately. It was also observed that the free surface deformations must be simulated once excess diffusion is suppressed and the simulated vortex intensifies as a result. Until more robust and accurate free surface and turbulence modelling strategies become available and/or accessible, it might be more realistic in an industrial context to perform initial assessments of an intake using the fixed lid approximation with a basic turbulence model such as k-ε. The results could be used to get a rough idea of the bulk circulation Γ_∞ and to estimate a range of values for the characteristic radius using Eqs. (7.3) and (7.5) as described. From these values, the tip depth h_0 and nominal depression slope $\zeta = h_{\mathrm{n},0}/r_o$ could be estimated using Eqs. (7.6) and (7.7).

Chapter 8

Conclusion

8.1 Summary, conclusions and future work

Axially stretched free surface vortices in a simplified low-head hydropower intake with piers were examined through velocity and free surface profile measurements in a physical laboratory-scale model, a relatively simple analytical vortex model and CFD simulations with a custom eddy-viscosity distribution.

The analysis focused particularly on how intake submergence with vertical acceleration of the flow towards the intake opening drives axial stretching of the vortex and thus determines the characteristic radius of the vortex. This and other processes by which the intake geometry and approach flow conditions control vortex characteristics were incorporated into an adapted analytical vortex model that related vortex characteristics to the intake submergence and intake velocity. The analytical model was then used to estimate how vortex characteristics observed in a laboratory model might translate to the prototype scale. Uncertainty related to transition from viscosity-driven to turbulence-driven diffusion in the vortex core was discussed, and the CFD simulations further emphasized the crucial role played by the interaction of turbulence with the vortices.

Chapter 4 (Manuscript 1) described the velocity and free surface profile measurements taken at eight operating conditions in the physical scale model, corresponding to different combinations of of intake velocity U_i and relative submergence s/d. The measurements were used to adapt Burgers's vortex model so as to incorporate the influence of geometry and the approach flow velocity profile on vortex characteristics. This adapted model allows quantitative relations for the vortex's characteristic radius r_o, bulk circulation Γ_∞ and tip depth h_0 to be developed in terms of U_i and s/d. A simplified sink model was formulated to describe the flow directly in front of the intake. Then a quantitative relation was established between the velocity profile directly in front of the intake and the axial velocity profile $V_z(z)$ inside the vortex, highlighting the role of the intake approach flow in driving axial vortex stretching. r_o was well predicted by the ratio of molecular viscosity ν to the axial gradient $a = \partial V_z/\partial z$ strongly suggesting that radial turbulent diffusion is effectively suppressed in the vortex core, in agreement with observations in wing tip vortices. Though $V_z(z)$ was driven by the non-linear vertical profile |U|(Z) of the intake flow outside the vortex, it was found to stray towards a more linear profile, the extent of which varied from case to case and even from vortex to vortex for a given operating condition. Variations in the shape of $V_z(z)$ as well as in the magnitude of the measured circulation Γ_∞ made it more appropriate to offer estimated ranges of expected values for r_o,Γ_∞ and h_0 as functions of U_i and s/d instead of fixed values.

In Chapter 5 (Manuscript 2), scale effects associated with surface tension, viscosity and turbulence were examined. First, the effect of surface tension was examined by computing the free surface profiles produced with and without surface tension by a Burgers's (1948) vortex, revealing that both the shape and the scale of the free surface profile determine how surface tension will modify the shape and total depth of the depression. The trends produced by the calculations were used to formulate a correction factor that can be used to correct for surface tension effects in a laboratory-scale vortex. The tip depth of the depression was then predicted for a specific intake geometry and set of operating conditions using the vortex model developed in Chapter 4 with the addition of surface tension. The predictions compare fairly well with the measured values, considering the scatter in the measured data. Finally, the vortex model was used to estimate how vortices observed in a laboratory-scale model constructed to a 1:α scale might translate in the full-scale prototype. Uncertainties associated with the scaling of the flow

structure and perturbations and enhanced diffusion caused by turbulence were discussed, with suggestions as to how greater light could be shed on these processes. The analytical model predicts that the ratio of the prototype to lab-scale relative tip depths and non-dimensionalized critical particle diameter should be proportional to $\alpha^{3/2}$ and that the ratio of the nominal free surface slopes should be proportional to $\alpha^{3/4}$. Comparison of the magnitude of scale effects linked to viscosity with those due to surface tension suggests that effects due to viscosity may often be significantly greater. The limitations of these predictions are discussed, as well as factors that could affect the scaling ratios for these quantities.

Chapter 6 (Manuscript 3) interpreted the results and conclusions from chapters 4 and 5 to provide guidance to practicing engineers for interpreting the properties of vortices they observe in physical scale models and to extract quantitative information about processes through which the intake flow structure may be controlling vortex characteristics. In addition to the scaling behaviour of the free surface tip depth and shape, the processes that determine debris entrainment were also examined. A rough estimate of the scaling behaviour for particle entrainment was derived. The ratio of prototype to laboratory model values for the non-dimensionalized critical particle diameter should be proportional to $\alpha^{3/2}$.

Chapter 7 discussed the challenges associated with reproducing experimentally observed free surface deformations and turbulence in CFD simulations of the intake flow. It was found that careful definition of boundary conditions and a gradual start-up of the flow are required to avoid numerical and physical instabilities in low-Froude number open channel flow. A custom eddy viscosity distribution ν_i was imposed using a static analytical function to stabilize the upstream portions of the flow without the excess diffusion of the vortices that is typical of standard eddy viscosity models. The characteristic radius obtained with this custom model was much closer to the measured value than that obtained with the k-ε turbulence model, and the more concentrated vortices permitted the more linear profile of axial velocity to develop inside the vortex along its axis, as suggested by the measurements. The circulation in both the ν_i and k-ε simulations is significantly overestimated, indicating that a more refined turbulence modelling strategy is required to capture the vortex characteristics more accurately.

The results of the numerical simulations clearly demonstrate the need for a turbulence model to suppress turbulence in the vortex core in order to approach the correct r_o values and correct axial velocity distribution. These results also highlight the important role played by eddy viscosity in stabilizing the flow solution in the upstream portions of the flow, in the viscinity of the free surface, and possibly directly outside the vortex core as well. The paper ends by discussing how results of simulations similar to these or somewhat more simplified could be used to estimate a range of expected vortex characteristics.

The results of this thesis suggest that further investigation into the interaction of turbulence with vortices (both inside the core and outside them) is needed if the scaling behaviour of vortices is to be estimated with greater confidence or if prototype-scale vortices are to be predicted using CFD. The conditions that determine the extent of the more linear $V_z(z)$ profile inside the vortex also merit further research, since these conditions determine the degree of axial stretching experienced by the vortex near the free surface. More extensive studies relating air and debris entrainment properties of laboratory-scale vortices to the vortex characteristics studied here would help both with scaling estimates for these properties and for evaluating the potential 'severity' of vortices in simulations. It goes without saying that detailed measurements of vortex characteristics in a full-scale intake compared with laboratory-scale observations or with simulations would provide insight into both entrainment and general scaling laws. However, the occurrence of vortices in operational intakes tends to be relatively rare and often unpredictable. This adds the logistical challenge of accessing the intake at the appropriate moment to the technical challenge of taking measurements in a full-scale intake.

8.2 Publications arising from thesis work

8.2.1 Conference papers

Suerich-Gulick, F., Gaskin, S.J., Braune, A., Parkinson, É., Villeneuve, M. (2005). Free surface simulation of hydraulic turbine intakes, *23rd CADFEM Users' Meeting*, Bonn, Germany.

Suerich-Gulick, F., Gaskin, S.J., Parkinson, É., Villeneuve, M. (2007). Numerical simulation of a free surface vortex formed in the wake of a pier at a hydropower intake, *Proceedings of the 32nd Conference of the IAHR*, Venice, Italy.

Suerich-Gulick, F., Gaskin, S.J., Parkinson, É., Villeneuve, M., Holder, G. (2006). Experimental and numerical analysis of free surface vortices at a hydropower intake, *Proceedings of the 7th International Conference on Hydroscience and Engineering*, Philadelphia, PA.

Suerich-Gulick, F., Gaskin, S.J., Villeneuve, M., Parkinson É. (2013) Engineering approach to predicting free surface vortices at low-head hydro-power intakes. *2013 IAHR Congress*, September 2013, Chengdu, China.

Suerich-Gulick, F., Gaskin, S.J., Villeneuve, M. (2007). Impact of geometry on free surface vortices in a scale model of a hydropower intake, *Proceedings of the 5th Hydraulic Measurement and Experimental Methods Conference*, Lake Placid, NY.

Villeneuve, M., Suerich-Gulick, F., Gaskin, S.J., Parkinson, É., Grunder, R. (2005). Optimization of intake flow conditions for compact axial turbines, *Hydro 2005*, Villach, Austria.

8.2.2 Manuscripts submitted for journal publication

Suerich-Gulick, F., Gaskin, S.J., Villeneuve, M., Parkinson, É. (2013b). Assessing the characteristics of free surface vortices at low-head hydropower intakes. *Manuscript submitted for publication to the Journal of Hydraulic Engineering of the ASCE.*

Suerich-Gulick, F., Gaskin, S.J., Villeneuve, M., Parkinson, É. (2013c). Free surface intake vortices: Scale effects due to surface tension and viscosity. *Manuscript submitted to the Journal of Hydraulic Research of the IAHR.*

Suerich-Gulick, F., Gaskin, S.J., Villeneuve, M., Parkinson, É. (2013d). Free surface intake vortices: Theoretical model and measurements. *Manuscript submitted to the Journal of Hydraulic Research of the IAHR.*

8.2.3 Manuscript in preparation to submit to a journal

Suerich-Gulick, F., Gaskin, S.J., Parkinson, É., Villeneuve, M. (2013a). Computational fluid dynamics modelling strategies for predicting free surface vortices at hydropower intakes.

Appendix A

Free surface profile computation source code

This is the annotated C++ source code that was used to compute the free surface profile. Following the code is a sample input parameter file 'param.txt'

A.1 Source code

```
#include <stdio.h>
#include <string.h>
#include <math.h>
#define EPS 1.0e-8
#define PI 3.1416

#define MAXBINS 2100
//MAXBINS is the maximum number of segments
```

```
int main() {

  int i,j,k;
  int iter;
  char line[300];

// set number of divisions and total range
//-------------------------------------------------
  int nrings = 700; // number of sections over which we integrate
//int nrings = 1400; // for higher grid resolution tests
  double rinf = 0.01; // upperlimit of r  (=rmax)
  double hinf = 0.004; // water level at rinf
  double A1 = 0.2;
     // A1 = GammaInfty/(2pi) : bulk circulation/(2pi)
  double A2 = 0.003; //  A2 = ro (characteristic radius)
  double sigma = 0.07349;   //=72 dynes/cm  =  0.072 N/m
  double density = 998.0;  // water density
  double l2 = sigma/(9.812*density);
      // l_sigma = sqrt(l2) = 2.7395 mm
      // this is charact. length for surface tension
  double h0ppnosig; // curvature at tip without surftension
  printf("#l2= %lf \n", l2);

// convergence control
// -------------------
   int itermax0 = 2000;
   double alpha0 = 0.001;  // alpha is the relaxation
   int ttotal0 = 60;

// open output file
//-----------------
  FILE *fm;
  if(( fm = fopen("./h.dat","w")) == 0 ) {
    printf("cannot open output file.\n");
    return(0);
  }
  printf("#opened output file\n");
```

```
// open input file with parameters
//-------------------------------
  FILE *fp2;
  if(( fp2 = fopen("./params.txt","r")) == 0 ) {
    printf("cannot open input parameter file.\n");
    return(0);
  }
  printf("#opened input file\n");

// first line of params.txt is comments
// second line is fit params
//--------------------------
  fgets(line,100,fp2);  // line 1
  if( fgets(line,100,fp2) ) {    // line 2
    sscanf(line,"%lf   %lf ",&A1, &A2);
    fprintf(fm,"#Gamma/2pi= %g  ro= %g  sigma= %g \n", A1, A2, sigma);
    fprintf(fm,"#l2= %lf \n", l2);
  } else {
    return(0);
  }

  fgets(line,100,fp2);  // line 3: comment line

// fourth line is fit params
//--------------------------
  if( fgets(line,100,fp2) ) {   // line 4
    sscanf(line,"%lf %lf ",&rinf, &hinf);
    fprintf(fm,"#rinf= %f  hinf= %f \n", rinf, hinf);
  } else {
    printf("#can't read rinf and hinf \n");
    return(0);
  }

  fgets(line,100,fp2);  // comment line, line 5

// sixth line is converg control
```

```
//------------------------------
  if( fgets(line,100,fp2) ) { // line 6
    sscanf(line,"%d %lf %d",&itermax0, &alpha0, &ttotal0);
    fprintf(fm,"#itermax0= %d  alpha0= %f ttotal0=%d \n", itermax0,
       alpha0, ttotal0);
  } else {
    printf("#can't read itermax0 and alpha0 \n");
    return(0);
  }

// Close the input file
//---------------------
  fclose(fp2);

// Recompute rinf
// --------------
   rinf = 20.0*A2;
   double rr = (0.005/rinf )*(double)nrings;
   int rcutoff= (int) rr;
// printf("#rcutoff= %4d  %6g \n", rcutoff, rr);

// open output converg file
//-------------------------
  FILE *fc;
  if(( fc = fopen("./converg.dat","w")) == 0 ) {
    printf("cannot open output file.\n");
    return(0);
  }
  printf("#opened output converg file\n");

  FILE *fall;
  if(( fall = fopen("./hall.dat","w")) == 0 ) {
    printf("cannot open fall file.\n");
    return(0);
  }
  printf("#opened fall file\n");
```

```
// nrings cannot be greater than MAXBINS
//-------------------------------------
  if( nrings > MAXBINS ) nrings = MAXBINS;

  double dr = rinf / (double) nrings;
  printf("#r0 = %g, dr = %g\n", A2,dr);
  fprintf(fm,"#dr = %g\n", dr);

// note that r=rinf happens at i=0 (outer limit)
// r=0  happens at i=nrings
//================================
  double fsdep[MAXBINS]; // drop in free surface level due to velocity
  double delfs; // drop in level across segment dr due to velocity

  double h[MAXBINS]; // final free surface level
  double hsmooth[MAXBINS]; // smoothed free surface profile
  double hsmooth2[MAXBINS]; // smoothed free surface profile
  double hold[MAXBINS]; // free surface level from previous step
  double hnew[MAXBINS]; // new free surface level before relax
  double r[MAXBINS]; // radius at node i
  double vth[MAXBINS]; // velocity at node i
  double hp[MAXBINS]; // h':  first derivative of h wrt r
  double hpp[MAXBINS]; // h": second derivative of h wrt r
  double R1[MAXBINS]; // first radius of curvature
  double R2[MAXBINS]; // second radius of curvature
  double K[MAXBINS]; // mean curvature

// set the boundary conditions
//-----------------------------------
  r[0] = rinf;
  h[0] = hinf;
  hold[0] = hinf;
  r[nrings] = 0.0;
  vth[nrings] = 0.0;

//I'm going to do a transient solution
//-----------------------------------
```

```
  int t=0;
  int ttotal = ttotal0; // total number of time steps
  double time=(double)t / (double) ttotal;
  double rot = rinf; // this is the transient value of ro (A2)
  double hrinf=rinf/2.0;
     // hrinf=half of rinf so there isn't such a big slope at rinf
  double bsq = pow((hrinf/A2),2.0);
  double t0=1/(bsq-1);
  double aa=1/(hrinf*sqrt(t0));

  fprintf(fc,"# iter   r       h       hp\
     l2K      ch  hnew-hold index \n");
  printf("#t r0 \n");
  for( t=0 ; t <= ttotal ; t++ ) {
    time=(double)t / (double) ttotal;
    rot=1/(aa*sqrt(time+t0));
    if( t%2==0 ) printf("%lf  %lf\n", time, rot);

//  first, compute the free surface depression
//  due to velocity (V^2) only
//  ----------------------------------------
    for( i=0 ; i <= nrings ; i++ ) {
       r[i] = rinf - dr*(double)i;
       double rmid = r[i] + dr/2.0;
       vth[i] = (A1/rmid)*(1.0 - exp(-pow(rmid/rot,2.0)));
       delfs = vth[i]*vth[i]*dr/(rmid*9.812);
       fsdep[i] = fsdep[i-1] + delfs;
       if( t==0) h[i] = hinf - fsdep[i];
    }
    if( t==0) h0ppnosig = (h[nrings-1]-h[nrings])/dr;

  // Copy to hsmooth for subsequent smoothing
  // ---------------------------------------
     for( i=0; i<= nrings; i++ ) {
       hsmooth[i] = h[i];
     }
```

```
  // special conditions at r=0
  // =========================

  // Now calculate surface tension effects
  // First calculate the first and second derivatives
  // -----------------------------------------------
     hp[0] = EPS;
     R1[0] = 1.0e7;
     R2[0] = 1.0e7;
     K[0] = EPS;

//   Do several interations of the free surface calculation
//   ------------------------------------------------------
     double change = 0.0;
     int index=0;
     int itermax=itermax0;
     if( time>0.7) itermax= itermax0+500;

//   do extra iterations on the last timestep, which
//   is the final value of ro
//   -------------------------------------------------
     if( t==ttotal) itermax=itermax0+3000;
     fprintf(fc, "\n\n");
     int converg = 0;
     for( iter = 0; iter < itermax; iter++ ) {
       if(converg==1) break;

//     First derivative of the segment just outwards from node i
//     use central difference
//     Compute it from the *smoothed* h(r) profile
//     ------------------------------------------------------------
       for( i=1; i<nrings; i++ ) {
         hp[i] = (hsmooth[i-1] - hsmooth[i+1] )/ (2.0*dr);
         if( fabs(hp[i]) < EPS ) hp[i] = EPS;
       }

//     Second derivative at node i
```

```
//     ----------------------------
       for( i=1; i< nrings; i++ ) {
//       central difference
//       ------------------------
         hpp[i] = (hsmooth[i-1] - 2*hsmooth[i]
                 + hsmooth[i+1] )/(2*dr* dr);

         if( fabs(hpp[i]) < EPS ) hpp[i] = EPS;
       }

//     Special case at r=0
//     --------------------
       hp[nrings] = (hsmooth[nrings-1]-hsmooth[nrings])/(dr);
//      //  really it should be 0 but it's never exactly zero

//     central difference
       hpp[nrings] = (hsmooth[nrings-1]-hsmooth[nrings])/(dr*dr);

//     Special case at r=rinf
//     ----------------------
       double m = (hp[1] - hp[2])/ dr;
       hp[0] = hp[1]+ m*dr;
       double n = (hpp[1] - hpp[2])/ dr;
       hpp[0] = (-hsmooth[0]+hsmooth[1])/(2*dr*dr);

//     Now calculate the radii of curvature
//     and the corrected free surface profile
//     ----------------------------
       for( i=0; i<= nrings; i++ ) {
         hold[i] = h[i];
         double cc = 1.0+ hp[i]*hp[i];
         R1[i] = r[i]*sqrt(cc)/hp[i];
         R2[i] = cc*sqrt(cc)/hpp[i];

//       Special case at r=0
//       -------------------
         if( i== nrings ) {
```

```
//          R1 at r=0 has a spike/ is undefined
//          -----------------------------------
            K[i] = 1.0/R2[i];
          } else {
              K[i] = 0.5*(1.0/R1[i] + 1.0/R2[i]);
                // standard definition
          }
        }
//      Smooth the computed curvature  profile
//      --------------------------------------
        for( i=1; i< (nrings-1); i++ ) {    //ksmooth
            K[i] = 0.5* K[i]+ 0.25 *( K[i-1]+ K[i+1]);
        }

//      Print the starting ro value r0
//      ------------------------------
        if( iter== (itermax-1)) fprintf(fall,"#r0 = %8g\n", rot );
        change=0.0;
        index=0;
        double hnom;
        double alpha = alpha0;

//      Now correct the free surface profile
//      by subtracting the surfTension effect (l2*K) from
//      the velocity contribution fsdep
//      -----------------------------------------------
        for( i=1; i< nrings; i++ ) {
          hnew[i] = hinf - fsdep[i] + l2*K[i];  // this is ok

//        Apply relaxation
//        ----------------
          h[i] = (1.0-alpha)*hold[i] + alpha*hnew[i];
          double dh = fabs( hnew[i] -hold[i]);
          if( dh > change && i<nrings ) {
            change = dh;
            index=i;
          }
```

```
      }

//    BC at r=0 to make the tip smooth
//    --------------------------------
      m = h[nrings-2]-h[nrings-1];
      h[nrings] = h[nrings-1] - 0.2*m;

//    Do a smoothing on h for calculating hp
//    -only do smoothing on first 1/5th of iterations
//    ---------------------------------------
      int dosmooth=1;
      int rcut = 0;
      if( time>0.2*ttotal) dosmooth=0;
      if( dosmooth) {
        for( i=1; i< nrings-rcut; i++ ) {
          hsmooth[i] = 0.25 *( h[i-1]+ h[i+1]) + 0.5*h[i];
        }
      } else {
//      Copy h to hsmooth directly
//      -------------------------
        for( i=0; i<=nrings; i++ ) {
          hsmooth[i] = h[i];
        }
      }

//    h at r_inf stays constant
//    **but the value is set by hinf-fsdep
//     h[0] = hinf - fsdep[0];
//    ----------------------------------
      hsmooth[0] = h[0];
      hsmooth[nrings] = 1.0*h[nrings] + 0.0*h[nrings-1];


//    Do a second smoothing
//    only for very fine grids (nrings >1000)
//    ---------------------------------------
      dosmooth=1;
```

```
       if( time>0.1*ttotal && iter > 0.3*itermax) dosmooth=0;
       if( time>0.2*ttotal) dosmooth=0;
       if( nrings > 1000 && dosmooth)  {
         for( i=0; i<= nrings; i++ ) {
           hsmooth2[i] = hsmooth[i];
         }

         for( i=1; i< nrings-rcut; i++ ) {
           hsmooth2[i] = 0.5 *( hsmooth[i-1]+ hsmooth2[i+1]);
         }
         for( i=1; i< nrings; i++ ) {
           hsmooth[i] = hsmooth2[i];
         }
       }

//     output to converg  and hall files
//     ---------------------------------
       if( iter%10==0) fprintf(fc,"%d  %.4lf %8lf  \
%8g %8g  %8g %8g %d\n",
          iter, r[nrings-10], h[nrings-10], hp[nrings-10],
          l2*K[nrings - 20], change,
          hold[nrings-2]-hnew[nrings-2], index );

//     Check for convergence
//     ---------------------
       hnom= fabs(fsdep[nrings]);
       if(hnom < 1.0e-6 ) hnom=1.0e-6;
       if( iter > 100 ) {
         if( change/hnom < 0.0001 || change < 1.0e-7) {
//         fprintf(fc, "#Inner loop  converged----------\n");
           converg=1;
         }
       }
       converg=0;
       if( iter<4  ) {
         fprintf(fall,"# r[i] h[i] hnos[i] hnew R1  R2  K \n" );
         fprintf(fall,"# 1     2    3      4     5  6   7  \n" );
```

```
        fprintf(fall,"# iter = %4d\n", iter );
        for( i=nrings; i>=0; i-- ) {
          fprintf(fall,"%7g %7g %7g %7g %7g %8g %8g \n",
                   r[i], h[i], hinf-fsdep[i],hnew[i],
                   R1[i], R2[i], K[i] );

        }
        fprintf(fall,"\n\n");
      }
    }
  } // this it the outer time loop

  printf("\n");

//Print the output data
//----------------------
//  fprintf(fm,"#r    h    vth    R1    R2    l2K     fsdep \n");

// for testing
// -----------
  fprintf(fm,"#r           h     dy/dx      d2ydx2        R1       R2\
        hnos       l2K\n");
  fprintf(fm,"#1           2      3          4            5        6\
          7         8  \n");
  for( i=nrings ; i>=0 ; i-- ) {
    fprintf(fm,"%.6f %10.5e %8.2e %8.2e %8.2e %8.2e %8.2e %10.5e\n",
     r[i], h[i]-hinf, hp[i], hpp[i], R1[i], R2[i], 0.0-fsdep[i],
     l2*K[i]);
  }
//Close the output files
//----------------------
  fclose(fc);
  fclose(fall);
  fclose(fm);
  printf("#closed the output files\n");

// Find the output information for the summary file
```

```
// ---------------------------------- ------------
  int ro_index= 0;
  for( i=0 ; i<nrings; i++ ) {
    if( r[i] >A2 ) ro_index=i;
  }
  if( ro_index==0) printf("error finding ro_index .\n");

  double h0sig=h[nrings];
       // depression at center with surf tension
  double h0nosig=hinf-fsdep[nrings];
       // depression at center without  surf tension
  double h1sig=h[ro_index];  // depression at r0
  double h1nosig=hinf - fsdep[ro_index];
      // depression at r0 without surf tension
  double h0ppsig= (h[nrings-1]-h[nrings])/dr;
      // curvature at tip with surftension
  double K0=K[nrings]; // mean curvature at tip with surftension
  double Vo=vth[ro_index];  // velocity at r0

// open output summary file
//-------------------------
  FILE *fsum;
  if(( fsum = fopen("./sum.dat","a")) == 0 ) {
    printf("cannot open summary file.\n");
    return(0);
  }
  printf("#opened summary file\n");
    fprintf(fsum,"c  %5.2f %7.2f %9.3e %12.6e %12.6e %10.4e %9.3e\
  %8.2e %8.2e %8.2e\n",
                A1*1000,A2*1000, Vo*Vo/9.812,
                hinf-h0nosig, hinf-h0sig,
                hinf-h1nosig, hinf-h1sig,
                h0ppnosig,h0ppsig,K0 );

  fclose(fsum);
  printf("#closed summary file\n");
```

```
  return(0);
}
```

A.2 Sample input file ‘params.txt’

```
#A1  A2
0.00064 0.025
#rinf hinf
0.02  1.0
#itermax0 alpha0 ttotal0
100 0.05 20
```

Appendix B

Particle-tracking algorithm and source code

This appendix briefly describes the algorithm of the particle-tracking code ParticleTracker used to identify and track the particles in the recorded film segments. ParticleTracker is a plugin for the open-source image analysis software ImageJ, written in java (Sbalzarini and Koumoutsakos, 2005). First, the different steps of the algorithm are described, including changes or additions I made. In the last section of this appendix, four excerpts of the code are given, which include all the portions of the code that were modified by myself. Frank Suerich-Gulick for the purpose of the experiment. The starting version was version 1.5 (September 2006), written by Guy Levi. Additions or changes made to the code by myself are preceded by a comment line such as "modified by Frank, –start and –end".

An analysis of the uncertainty in the measured velocity profiles obtained from the particle-tracking is included in Appendix C. The analysis also includes a comparison of the axial velocity profiles $V_z(z)$ measured using the PTV method with the axial profile measured by tracking TiO_2 injected into the vortex at the free surface.

B.1 Algorithm description and modifications

The particle-tracking algorithm proceeds in three steps:

1. Identify the particles
2. Link the particles to form continuous, multi-frame trajectories

3. Analyze and output the characteristics (r_o, τ) of the identified particle trajectories

Each of these steps is described briefly in the next subsections, with explanations of the modifications or additions I made to the code. Variable names used in the code are typset in the description using `typewriter` script.

B.1.1 Particle identification

In this step, the algorithm dentifies all the particles in each frame of the film segment. For each frame, the coordinates (`x,y`) of each particle identified in that frame are stored into a list of objects of type `Particle`. The definition of the `Particle` object is given in Excerpt 1. and later printed to the detailed output file. The coordinates are given in pixels.

For the films clips analyzed here, `x` in the ParticleTracker code is the vertical distance from the top of the image, located a short distance from the free surface. The direction and orientation of x corresponds to those of the z axis in my analysis. The origin of `x` is located a certain distance from the free surface because the top portion of the image is removed before the PTV analysis so as to avoid portions of the free surface being identified as "particles". `y` in the code is the horizontal axis of the images - it is aligned with my global axis Y (see Fig. 3.1*b*), but points in the opposite direction (-Y).

This portion of the algorithm was not modified by myself. The method used to identify the particles and determine their location is described and discussed in (Sbalzarini and Koumoutsakos, 2005).

B.1.2 Particle linking

In this step, the particles identified and stored in the previous step are linked to each other from frame to frame. This task is performed by the function `linkParticles()`, which is included in Excerpt 2.

The decision to link particle `i` from frame `fr-1` to particle `j` in frame `fr` is made based on the "`cost[i][j]`" of linking the two particles. The cost of linking two given particles is an estimate of how likely we believe it is that the two particles are the same particle having undergone a displacement from frame `fr-1` to frame `fr`. The original algorithm was developed for tracking images of bacteria in microscopic images. These bacteria "particles" do not move out of the plane of the image so their apparent size and brighteness do not change much, but their velocities are erratic and do not follow a predictable trajectory. Therefore the original cost function was

based on how similar the two candidate particles were in terms of particle size and brightness. In contrast, my particles have a relatively predictable trajectory, especially in terms of the axial velocity V_z, which is referred to as `vx` in the code. `vx` should change only very slightly from frame to frame. In addition, the particles move in and out of the plane of optimal focus and have variable speeds across the image, so their apparent size and shape may change significantly from frame to frame. Therefore, I modified the cost function to reflect this, attribution less importance to constancy of the particles' geometric caracteristics and greater importance to their velocity from frame to frame. In order to compare the velocity of the particles from frame to frame, I had to store this information in the object `Particle`. The velocities `vx` and `vy` are therefor computed and stored for each particle at each frame as the linking step proceeds from frame to frame. The modified definition of the `Particle` object is given in Excerpt 1.

The algorithm also includes an option whereby the user can select a link 'range' (`linkrange`) greater than 1 so that a particle that "reappears" after disappearing from several intermediate frames can still be linked to a particle that was present 2 or more frames earlier. This increases the chances of producing long, unbroken trajectories, though it also increases the frequency of erroneous linking of particles that should not be linked (that are in fact distinct particles whose paths come close to one another). This occasional mis-linking of particles is difficult to prevent within the code, but erroneous links in the trajectories be easily identified and corrected by examining plots of the trajectories. I did not modify this aspect of the algorithm, though I used its functionality: I used a link range of 2, which means that a trajectory may be linked across a one-frame gap in which no appropriate particle for linking is identified.

B.1.3 Trajectory analysis and output

After the particles have been linked into trajectories, the code prints an output file listing all the linked trajectories. For each trajectory, the coordinates and characterists of the particle at each frame of the trajectory is printed. Function `getTrajectoriesInfo()` (listed in Excerpt 3) assembles this info for output. The original algorithm printed the size and intensity of the particles at each frame, since these were relevant for the bacteria-tracking application. In my application, the velocity is most important, so I modified the algorithm to output this information. I also output the information about the change in direction (angle) of the particle velocity from frame to frame.

I also wrote a new function, `getTrajectoryStats()` (listed in Excerpt 4), that performs an initial analysis of the recorded trajectories to try to identify good candidates for extracting $V_\theta(r)$ values. These trajectories must follow an oscillatory path and complete at least a full cycle (equivalent to θ =0 to 2π). The function estimates the radius r and period τ from such trajectory segments and outputs this information to a summary file. It also prints out the vertical displacement and start- and end-frames for the analyzed trajectory segments for the purpose of calculating $V_z(z)$. The output of this function is used to perform an initial rough assessment of the trajectories but each trajectory identified by `getTrajectoryStats()` and the computed trajectory

statistics are examined to check for faulty linking or erroneous identification of trajectories as appropriate for extraction of r and τ.

B.2 Code excerpts

B.2.1 Excerpt 1

```
// ======= Excerpt 1 ====================================
        /**
         * Defines a particle that holds all the relevant info for it.
         * A particle is detected in an image or given as input in test file
    mode
         *              X and Y coordinates are not
         *              in the usual graph coordinates sense but in the image
     sense;
         *              (0,0) is the upper left corner
         *      x is vertical top to bottom
         *      y is horizontal left to right//
           //  Frank: in my case x is the experimental z direction
           //  and y is horizontal coordinate
         */
        public class Particle {

                float x, y;                                          // the
    originally given coordinates - to be refined
                float original_x , original_y;  // the originally given
    coordinates - not to be changed
                int frame;                                                  //
    the number of the frame this particle belonges to (can be 0)
                boolean special;                                     // a flag
    that is used while detecting and linking particles
                int[] next;                                          // array that
     holds in position i the particle number in frame i

            // that this particle is linked to

                /* only relevant to particles detected in images */
                float m0, m2;                                        // zero and
    second order intensity moment
                float score;                                         // non-
    particle discrimination score

// Frank velocities
                float vx, vy;
                float vx_avg ;  // store the average velocity of the last 2
    timesteps
                boolean vgood;   // set to 1 when there's a velocity stored
```

```
                float costm, costa;  // the angle and magnitude costs
                boolean vcgood;  // set to 1 when there's a velocity cost
    and vx_avg computed

                float costd;  // displacement cost
//

                /* only relevant to particles given as input */
                String[] all_params;                    // all params that
    relate to this particle,

            // 1st 2 should be x and y respectfully

                /**
                 * constructor.
                 * @param x - original x coordinates
                 * @param y - original y coordinates
                 * @param frame_num - the number of the frame this particle
    belonges to
                 */
                public Particle (float x, float y, int frame_num) {
                        this.x = x;
                        this.original_x = x;
                        this.y = y;
                        this.original_y = y;
                        this.special = true;
                        this.frame = frame_num;
                        this.next = new int[linkrange];

// Frank
                        this.vx = 0.0F;
                        this.vy = 0.0F;
                        this.vx_avg = 0.0F;
                        this.vgood = false;
                        this.costa = -1.0F;
                        this.costm = -1.0F;
                        this.vcgood = false;
                        this.costd = -1.0F;

                }

                /**
                 * constructor for particles created from text files.
                 * @param x - original x coordinates
                 * @param y - original y coordinates
                 * @param frame_num - the number of the frame this particle
    is in
                 * @param params - all params that relate to this particle,
    first 2 should be x and y respectfully
                 */
                public Particle (float x, float y, int frame_num, String[]
    params) {
                        this.x = x;
                        this.original_x = x;
                        this.y = y;
```

```
                        this.original_y = y;
                        this.all_params = params;
                        this.special = true;
                        this.frame = frame_num;
                        this.next = new int[linkrange];
                        this.score = 0.0F;
                        this.m0 = 0.0F;
                        this.m2 = 0.0F;
// Frank
                        this.vx = 0.0F;
                        this.vy = 0.0F;
                        this.vx_avg = 0.0F;
                        this.vgood = false;

                        this.costa = -1.0F;
                        this.costm = -1.0F;
                        this.vcgood = false;
                        this.costd = -1.0F;
//
                }

                /* (non-Javadoc)
                 * @see java.lang.Object#toString()
                 */
                public String toString() {
                        return toStringBuffer().toString();
                }

                /**
                 * The method <code>toString()</code> calls this method
                 * <br>Generates (in real time) a "ready to print" <code>
    StringBuffer</code> with information
                 * about this Particle:
                 * <ul>
                 * <li> frame
                 * <li> x
                 * <li> y
                 * <li> m0
                 * <li> m2
                 * <li> score
                 * </ul>
                 * For text files mode - just prints all the information
    given for the particles
                 * @return a StringBuffer with this infomation
                 */
                public StringBuffer toStringBuffer() {

                        // I work with StringBuffer since its faster than
    String
                        // At the end convert to String and return
                        StringBuffer sb = new StringBuffer();
                        StringBuffer sp = new StringBuffer("  ");

                        // format the number to look nice in print (same
    number of digits)
```

```
                        NumberFormat nf = NumberFormat.getInstance(Locale.
    ENGLISH);
                        nf.setMinimumIntegerDigits(2);  // Frank added this
                        nf.setMaximumFractionDigits(3);  //Frank was 6
                        nf.setMinimumFractionDigits(3);  //Frank was 6
                        sb.append(this.frame);
                        if (text_files_mode) {
                                nf.setMinimumIntegerDigits(2);  // Frank
    added this
                                nf.setMaximumFractionDigits(3);  //Frank was
    6
                                nf.setMinimumFractionDigits(3);  //Frank was
    6
                                for (int i = 0; i<all_params.length; i++) {
                                        sb.append(sp);
                                        sb.append(nf.format(Float.parseFloat(
    all_params[i])));
                                }
//                              Frank
//              sb.append(nf.format(this.score));

                        } else {
                                sb.append(sp);
                                sb.append(nf.format(this.x));
                                sb.append(sp);
                                sb.append(nf.format(this.y));
                                sb.append(sp);
                                sb.append(nf.format(this.m0));
                                sb.append(sp);
                                sb.append(nf.format(this.m2));
                                sb.append(sp);
//                              sb.append("\n");
                        }
                        // Frank's information about velocities
                        sb.append("  ");
                        sb.append(nf.format(this.vx));
                        sb.append("  ");
                        sb.append(nf.format(this.vy));
                        sb.append("  ");
            if( this.vcgood ) {
              sb.append(nf.format(this.vx_avg));
              sb.append("  ");
              sb.append(nf.format(this.costm));
              sb.append("  ");
              sb.append(nf.format(this.costa));
            } else {
                 sb.append( "00.00 00.00 00.00");
            }
            sb.append("  ");
            sb.append(nf.format(this.costd));
                        sb.append("\n");
                        return sb;
                }
        }
```

```
%%% ========== END of Excerpt 1 ==============================
```

B.2.2 Excerpt 2

```
%% =========Excerpt 2 ===================================
        /**
         * Second phase of the algorithm -
         * <br>Identifies points corresponding to the
         * same physical particle in subsequent frames and
         *links the positions into trajectories
         * <br>The length of the particles next array
         *   will be reset here according to the current linkrange
         * <br>Adapted from Ingo Oppermann implementation
         */
        private void linkParticles() {

        int m, i, j, k, nop, nop_next, n;
        int ok, prev, prev_s, x = 0, y = 0, curr_linkrange;
        int[] g;
        double min, z, max_cost;
        double[] cost;
        double vxn, vyn, dotp;
        double cost_angle = 10.0, cost_mag = 10.0, cost_disp = 10.0;
        double epsilon = 1.0;
        Particle[] p1, p2;

        // set the length of the particles next array according to the
    linkrange
        // it is done now since link range can be modified after first run
        for (int fr = 0; fr<frames.length; fr++) {
                for (int pr = 0; pr<frames[fr].particles.length; pr++) {
                        frames[fr].particles[pr].next = new int[linkrange];
                }
        }
        curr_linkrange = this.linkrange;

        /* If the linkrange is too big, set it the right value */
        if(frames_number < (curr_linkrange + 1))
                curr_linkrange = frames_number - 1;

//Frank
//      max_cost = this.displacement * this.displacement;
        max_cost = 3.0 + epsilon;

//loop on frames
        for(m = 0; m < frames_number - curr_linkrange; m++) {
                nop = frames[m].particles.length;

//loop on particles in this frame m
                for(i = 0; i < nop; i++) {
                        frames[m].particles[i].special = false;
                        for(n = 0; n < this.linkrange; n++)
```

```
                                frames[m].particles[i].next[n] = -1;
                }

//do the linking process for the next n frames to be linked to

                for(n = 0; n < curr_linkrange; n++) {

// Frank               max_cost = (double)(n + 1) * this.displacement
                               * (double)(n + 1) * this.displacement;
                         max_cost = (double)(n + 1) * 3.0 + epsilon;

                         nop_next = frames[m + (n + 1)].particles.length;

                         /* Set up the cost matrix */
                         cost = new double[(nop + 1) * (nop_next + 1)];

                         /* Set up the relation matrix */
                         g = new int[(nop + 1) * (nop_next + 1)];

                         /* Set g to zero */
                         for (i = 0; i< g.length; i++) g[i] = 0;

                         p1 = frames[m].particles;
                         p2 = frames[m + (n + 1)].particles;

                         /* Fill in the costs */
                         for(i = 0; i < nop; i++) {

// loop on j particles in next frame

                                 for(j = 0; j < nop_next; j++) {

   // Frank changed
   //                                    cost[coord(i, j, nop_next + 1)] =
   //                                    (p1[i].x - p2[j].x)*(p1[i].x - p2[j].
    x) +
   //                                    (p1[i].y - p2[j].y)*(p1[i].y - p2[j].
    y) +
   //                                    (p1[i].m0 - p2[j].m0)*(p1[i].m0 - p2[
    j].m0) +
   //                                    (p1[i].m2 - p2[j].m2)*(p1[i].m2 - p2[
    j].m2);
   //  Frank comment: note dy here is dz in experiment
   // it would be nice to include changes in dz (velocity) as a cost too..
   //  note: contribution of m2 should be negligible because
   //        particles change shape depending location along  sine wave

// ********New code by Frank starts here**************
//     compute cost based on velocity in last timestep, only if there is info
     in p1[i]
                                           vxn = (double) (p2[j].x - p1[i].x)
    ;
                                           vyn = (double) (p2[j].y - p1[i].y)
    ;
```

```
                                        double magnew = Math.sqrt(vxn*vxn
    + vyn*vyn);
                        cost_disp = magnew / (float)(displacement);
                        cost_mag = 1.0;
                        cost_angle = 1.0;

// if velocity info is stored for previous frame, calculate the velocity
    costs for this pair
                        if( p1[i].vgood == true) {
// old velocities
                                double vxo = (double) p1[i].vx;
                                double vyo = (double) p1[i].vy;
                                dotp = vxn * vxo + vyn * vyo;

                                double magold = Math.sqrt(vxo*vxo + vyo*vyo
    );
                                magnew = Math.max( magnew, 0.1);
                                magold = Math.max( magold, 0.1);

        // calculate non-dimensional angle, magnitude and displacement
                //scale them so they're on the order of 1
                                if( (magnew*magold) > 0.001) {
                                        cost_angle = 1.0 - dotp / (magnew *
     magold);
                                } else {
                                        cost_angle = 0.0;
                                }
                                cost_mag = Math.abs(magnew - magold);
                                if( (magnew+magold) > 0.001) {
                                        cost_mag =  cost_mag / (magnew+
    magold);
        //                                      can't be bigger than
    0.5
                                } else {
                                        cost_mag = 0.0;
                                }
                                // calculate mag cost based solely on vx
                                //(this is the Z velocity)
                                vxo = Math.max(vxo,0.001);
                                                double vxavg = 0.5*(
    vxo + vxn);
                                                if( p1[i].vcgood ) {
                                                        vxavg = (
    double) p1[i].vx_avg;
                                                        vxo = vxavg;
      // this is a test
                                                }
                                double costvz = Math.abs((vxn - vxo)/(vxavg
    ));
                                if( Math.abs(vxo) > 1.0 && Math.abs(vxn) >
    1.0 && costvz > 2.0) {
                                        cost_mag = Math.min(3.0, costvz);
                                }
                                else if( Math.abs(vxo) < 0.5 && Math.abs(
    vxn) > 2.0 )  {
```

```
                                        cost_mag = Math.min(3.0, costvz);
                                    }
                                    else if(costvz > 3.0  && Math.abs(vxn)> 1.2
     ) cost_mag = costvz;

//                                  else if( Math.abs(vxo) < 1.0 || Math.abs(
    vxn) > 2.0 )  {
//                                              cost_mag = Math.min(4.0,
    costvz);
//                                    }


        // add this for corners
                                    if( magold < 1.0 && magnew < 1.0 ) {
                                      cost_angle = Math.min(cost_angle,0.5);
                                    }
                               }

//  Total cost is the sum of these three costs
                        cost[coord(i, j, nop_next + 1)] = cost_angle +
    cost_mag + cost_disp;
 //                                  cost[coord(i, j, nop_next + 1)] =
    cost_disp;

                    //                  1.0*(p1[i].x - p2[j].x)*(p1[i].x - p2
    [j].x) +
                    //                  0.4*(p1[i].y - p2[j].y)*(p1[i].y - p2
    [j].y) +
                    //                  0.2*(p1[i].m0 - p2[j].m0)*(p1[i].m0 -
     p2[j].m0);
                                }
                            }
// ********New code by Frank ends here**************

// cost of linking a particle to a dummy is max_cost
                        for(i = 0; i < nop + 1; i++)
                                cost[coord(i, nop_next, nop_next + 1)] =
    0.75*max_cost;
                        for(j = 0; j < nop_next + 1; j++)
                                cost[coord(nop, j, nop_next + 1)] = 0.75*
    max_cost;
// cost of linking 2 dummies is 0.0
                        cost[coord(nop, nop_next, nop_next + 1)] = 0.0;

                        /* Initialize the relation matrix */
                        for(i = 0; i < nop; i++) { // Loop over the x-axis
                                min = max_cost;
                                prev = 0;
                                for(j = 0; j < nop_next; j++) { // Loop over
    the y-axis
                                        /* Let's see if we can use this
    coordinate */
                                        ok = 1;
                                        for(k = 0; k < nop + 1; k++) {
```

```
                                                if(g[coord(k, j, nop_next +
    1)] == 1) {
                                                        ok = 0;
                                                        break;
                                                }
                                        }
                                        if(ok == 0) // No, we can't. Try the
    next column
                                                continue;

                                        /* This coordinate is OK */
                                        if(cost[coord(i, j, nop_next + 1)] <
    min) {
                                                min = cost[coord(i, j,
    nop_next + 1)];
// reset previously found lowest cost particle relation slot to 0
                                                g[coord(i, prev, nop_next +
    1)] = 0;
// set newest found lowest cost particle relation slot to 1, j is now the '
    prev' lowest cost particle
                                                prev = j;
                                                g[coord(i, prev, nop_next +
    1)] = 1;
                                        }
                                }

                                /* Check if we have a dummy particle */

// this means no particle was found that had a cost lower than max_cost

                                if(min == max_cost) {
//the last lowest cost particle wasn't low enough, reset g to 0

                                        g[coord(i, prev, nop_next + 1)] = 0;
// nop_next must be the last slot in the list of particles in the next frame
                                        g[coord(i, nop_next, nop_next + 1)] =
     1;
                                }
                        }

                        /* Look for columns that are zero */
  //are all particles in next frame unallocated?
                        for(j = 0; j < nop_next; j++) {
                                ok = 1;
                                for(i = 0; i < nop + 1; i++) {
                                        if(g[coord(i, j, nop_next + 1)] == 1)
                                                ok = 0;       // no
                                }

                                if(ok == 1)
                                        g[coord(nop, j, nop_next + 1)] = 1;
// we've greated a dummy particle in frame j
                        }

                        /* The relation matrix is initilized */
```

```
                        /* Now the relation matrix needs to be optimized */
                        min = -1.0;
                        while(min < 0.0) {
                                min = 0.0;
                                prev = 0;
                                prev_s = 0;
                                for(i = 0; i < nop + 1; i++) {
                                        for(j = 0; j < nop_next + 1; j++) {
                                                if(i == nop && j == nop_next)
                    // we're at the end of the loop
                                                        continue;

                                                if(g[coord(i, j, nop_next +
    1)] == 0 &&
                                                cost[coord(i, j, nop_next +
    1)] <= max_cost) {
  // it's an acceptable link but not the cheapest
                                                        /* Calculate the
    reduced cost */

                                                        // Look along the x-
    axis, including
                                                        // the dummy
    particles
// check if there are other particles in frame i that connect to this
    particle in frame j
                                                        for(k = 0; k < nop +
    1; k++) {
                                                          if(g[coord(k, j,
    nop_next + 1)]
                                                              == 1) {
                                                                    x = k
    ;
                                                                    break
    ;
                                                          }
                                                        }

                                                        // Look along the y-
    axis, including
                                                        // the dummy
    particles
                                                        for(k = 0; k <
    nop_next + 1; k++) {
                                                           if(g[coord(i, k,
    nop_next + 1)]
                                                              == 1) {
                                                                y = k;
                                                                break;
                                                           }
                                                        }
                                                        /* z is the reduced
    cost */
// this is just for the dummy particles: the only potential
```

```
// 'cheap' particles are dummy particles
                                                        if(j == nop_next)
                                                                x = nop;
      // we're at the end of the j loop

                                                        if(i == nop)
                                                                y = nop_next;

                                                        double a =
                                                            cost[coord(i, j,
    nop_next + 1)];
                                                        double b =
                                                            cost[coord(x, y,
    nop_next + 1)];
                                                        double c = cost[coord
    (i, y, nop_next + 1)];
                                                        double d = cost[coord
    (x, j, nop_next + 1)];

                                                        z = cost[coord(i, j,
    nop_next + 1)] +
                                                        cost[coord(x, y,
    nop_next + 1)] -
                                                        cost[coord(i, y,
    nop_next + 1)] -
                                                        cost[coord(x, j,
    nop_next + 1)];
                                                        if(z > -1.0e-10)
                                                                z = 0.0;
                                                        if(z < min) {
                                                                min = z;
                                                                prev = coord(

    i, j, nop_next + 1);
                                                                prev_s =
    coord(x, y, nop_next + 1);
                                                        }
                                                    }
                                                }
                                        }

                                        if(min < 0.0) {
                                                g[prev] = 1;
                                                g[prev_s] = 1;
                                                g[coord(prev / (nop_next + 1), prev_s
     % (nop_next + 1), nop_next + 1)] = 0;
                                                g[coord(prev_s / (nop_next + 1), prev
     % (nop_next + 1), nop_next + 1)] = 0;
                                        }
                                }

                                /* After optimization, the particles needs to be
    linked */
                                for(i = 0; i < nop; i++) {
                                        for(j = 0; j < nop_next; j++) {
```

```
                                        if(g[coord(i, j, nop_next + 1)] == 1)
     {
                                                p1[i].next[n] = j;

// *********Frank new code addition starts here ***************
//Frank: compute velocity
                          p2[j].vx = p2[j].x - p1[i].x;
                          p2[j].vy = p2[j].y - p1[i].y;
                          p2[j].vgood = true;

// Frank: calculate the velocity costs
                          if( p1[i].vgood == true) {
                             vxn = (double) (p2[j].x - p1[i].x);
                             vyn = (double) (p2[j].y - p1[i].y);
// velocities from previous timestep
                             double vxo = (double) p1[i].vx;
                             double vyo = (double) p1[i].vy;
                             double magnew = Math.sqrt(vxn*vxn + vyn*vyn);
                             double magold = Math.sqrt(vxo*vxo + vyo*vyo);
                             dotp = vxn * vxo + vyn * vyo;

// calculate non-dimensional angle, magnitude and displacement
  //scale them so they're on the order of 1

                             if( (magnew*magold) > 0.001) {
                                   cost_angle = 1.0 - dotp / (magnew * magold)
    ;
                             } else {
                                   cost_angle = -1.0;
                             }
                         //get the old average vx_avg if you can
                                              double vxavg = 0.5*(vxo +
    vxn);
                                          if( p1[i].vcgood ) {
                                                   vxavg = (double) p1[i
    ].vx_avg;
                                                   vxo = vxavg;  //this
    is a test
                                              }
                                          cost_mag = Math.abs(magnew -
    magold);
                            if( (magnew+magold) > 0.001) {
                                 cost_mag =  cost_mag / (magnew+magold);
//                               can't be bigger than 0.5
                            } else {
                                   cost_mag = -1.0;
                            }

                            // calculate mag cost based solely on vx
                               //(this is the Z velocity)
                            vxo = Math.max(vxo,0.001);
                            double costvz = Math.abs((vxn - vxo)/(vxavg));
                                if( Math.abs(vxo) > 1.0 && Math.abs(vxn) > 1.0
     && costvz > 2.0) {
                                        cost_mag = Math.min(3.0, costvz);
```

```
                                }
                                else if( Math.abs(vxo) < 0.5 && Math.abs(vxn)
    > 2.0 )  {
                                        cost_mag = Math.min(3.0, costvz);
                                }
                                else if(costvz > 3.0  && Math.abs(vxn)> 1.2 )
    cost_mag = costvz;

                            cost_disp = magnew / (float)(displacement);

                            p1[i].costa = (float) cost_angle;
                            p1[i].costm = (float) cost_mag;
                            p1[i].costd = (float) cost_disp;
// compute the average vx for the last 2 timesteps
                            p2[j].vcgood = true;
                            p2[j].vx_avg = (float) (0.5*(vxo+vxn));
                          }
// *********Frank new code addition ends here ***************

                       }
                                 }
                             }
                 }

                 if(m == (frames_number - curr_linkrange - 1) &&
    curr_linkrange > 1)
                        curr_linkrange--;
         }

         /* At the last frame all trajectories end */
         for(i = 0; i < frames[frames_number - 1].particles.length; i++) {
                 frames[frames_number - 1].particles[i].special = false;
                 for(n = 0; n < this.linkrange; n++)
                         frames[frames_number - 1].particles[i].next[n] = -1;
         }
     }

         /**
          * Generates <code>Trajectory</code> objects according to the
    infoamtion
          * avalible in each MyFrame and Particle.
          * <br>Populates the <code>all_traj</code> Vector.
          */

// ============End of Excerpt 2 =====================
```

B.2.3 Excerpt 3

```
// ============Beginning of Excerpt 3 =====================

         /**
```

```
         * Generates (in real time) a "ready to print" report with all
    trajectories info.
         * <br>For each Trajectory:
         * <ul>
         * <li> Its serial number
         * <li> All frames of this trajectory with infomation about the
    particle in each frame
         * </ul>
         * @return a <code>StringBuffer</code> that holds this information
         */
        private StringBuffer getTrajectoriesInfo() {

//****** Frank added this ******
                StringBuffer traj_info = new StringBuffer("## Trajectories:\n
    ");
                traj_info.append("##\t 1st column: frame number\n");
                traj_info.append("##\t 2nd column: x coordinate top-down\n");
                traj_info.append("##\t 3rd column: y coordinate left-right\n
    ");
//              if (text_files_mode) {
//                      traj_info.append("##\t next columns: other
    information provided for each particle in the given order\n");
//              } else {
                        traj_info.append("##\t 4th column: zero-order
    intensity moment m0\n");
                        traj_info.append("##\t 5th column: second-order
    intensity moment m2\n");
                        traj_info.append("##\t 6th column: vx from previous
    timestep\n");
                        traj_info.append("##\t 7th column: vy from previous
    timestep\n");
                        traj_info.append("##\t 8th column: cost_mag for the
    next  timestep\n");
                        traj_info.append("##\t 9th column: cost_angle for the
     next timestep\n");
                        traj_info.append("##\t 10th column: cost of
    displacement for the next timestep\n");
//              }
                traj_info.append("\n");
//****** End Frank addition *************************
                int minTrajLen = 8;
                int trajCounter = 0;  // use this to locally identify
    trajectory numbers
                Iterator iter = all_traj.iterator();
                while (iter.hasNext()) {
                        Trajectory curr_traj = (Trajectory)iter.next();

// Frank Commented this out
//                      if( curr_traj.length < minTrajLen) continue;
                        traj_info.append("\n## Trajectory " + curr_traj.
    serial_number +"\n");
                        traj_info.append(curr_traj.toStringBuffer());
                        trajCounter++;
                }
```

```
                return traj_info;
        }
// ================ End of Excerpt 3 =================
```

B.2.4 Excerpt 4

```
// ================ Excerpt 4  New function written by Frank
    ==================
//
//   New function getTrajectoryStats() written by Frank.
//   This function analyses the computed trajectories
//   and evaluates r and tau (period) of each trajectory
//   that looks like it follows a sinusoidal curve
//   The function is called in ResultsWindow using the call
//      write2File(sd.getDirectory(),stats_file.toString(),
    getTrajectoryStats().toString());
//

        private StringBuffer getTrajectoryStats() {

                //Save a gnuplot script file for each trajectory
                /* show save file user dialog with default file name 'frame'
    */
                int noGnuscript = 0;
                //StringBuffer outputDir = new StringBuffer();
                SaveDialog sd = new SaveDialog("Write Gnuplot scripts", IJ.
    getDirectory("image"), "g", "");
                //outputDir.append("/gnuplot/");
                // if user cancelled the save dialog
                //if (sd.getDirectory() == null || sd.getFileName() == null)
    noGnuscript = 1;

                StringBuffer traj_info = new StringBuffer("## Trajectory
    stats:\n");
                traj_info.append("#==================\n");
                traj_info.append("#t   ff    mean     r         hp       t0
         t2     z0        z2     std/r  m   file\n");
                traj_info.append("#1   2       3      4          5        6
          7     8          9      10    11   12\n");

                int minTrajLen = 6;
                int fileCounter = 0;  // use this to locally identify
    gnuscript files
                Iterator iter = all_traj.iterator();
                double eps = 0.01;
                int trajLen; // length of the trajectory
            //      int ti, tn; //first and last frame of trajectory
                double mean, r, alpha, hp;  //statistics for this trajectory
    section
                int c0, c1, c2=-1; // indices of frames where trajectory
    crosses mean line
                            //   index of first frame after sign changes
```

```
            int firstframe;
            //int firstGoodIndex = 0; // set to 1 if it looks like the
first frame is bad
            double t0, t1, t2; // time where trajectory crosses mean line
            double r0, r1; // radii for first and second sections
            double hp0; // half periods
            double hp1;
            boolean r0IsNeg = true; // sign of first section past c0
            int newTraj = 1; // set to 0 when we're relooping on an old
trajectory
            int startingIndex = 0; // the first frame we'll look at for
this trajectory section
            boolean firstTraj= true;
            Trajectory curr_traj = (Trajectory)iter.next();
            int sectionLen = -1; // length of the treajectory section
length we're considering
            int lastIndex = -1; //index of the last frame in the
trajectory

            while (iter.hasNext()) {
                    if(fileCounter > 66 ) {
                            traj_info.append("#stopped at traj " +
curr_traj.serial_number+"\n");
                            return traj_info;
                    }
                    if(newTraj == 1) {
                            if( !firstTraj) {
                                    curr_traj = (Trajectory)iter.next();
                            }
                            startingIndex = 0;
                            sectionLen = curr_traj.existing_particles.
length;
                    } else {
                            //continuing on an old trajectory
                            //startingIndex = c2 - 1; // set starting
index at the end of the last section
                            sectionLen = curr_traj.existing_particles.
length - startingIndex;
                    }
                    firstTraj = false;
                    trajLen = curr_traj.existing_particles.length;

                    if( sectionLen < minTrajLen) {
                            newTraj =1;
                            continue;
                    }
                    c0 = -1;
                    c1 = -1;
                    c2 = -1;
                    r0 = 1;
                    r1 = 1;
                    firstframe = curr_traj.existing_particles[0].frame;
                    lastIndex = startingIndex + sectionLen;
                    // check if we should start from index 1 instead of 0
                    if( Math.abs(curr_traj.existing_particles[1].vx)
```

```
                        > 0.5 && startingIndex == 0 ) {
                              startingIndex = 1;
                              sectionLen = sectionLen -1;
                        }
                        //calculate the mean (core line)
                        mean = 0.0;
                        for (int i = startingIndex; i< lastIndex; i++) {
                                mean = mean + (double) curr_traj.
existing_particles[i].y;
                        }
                        mean = mean / (double)sectionLen;

                        //check if i should do a curve fit
                        boolean doCurveFit = false;
                        //little test to see if i can do a curve fit -check
how many cycles there are
                        boolean pos = (curr_traj.existing_particles[
startingIndex+1].vy > 0.0F);
                        int nCycles = 0;
                        int newStartingIndex = startingIndex;
                        double vymax = 0.0;
                        int lastCorner =startingIndex; // index of last time
we turned a corner
                        double r_approx = 0.0;
                        int nr = 0;
                        double y_last = 0.0;
                        for (int i = startingIndex+1; i< lastIndex; i++) {
                                vymax = Math.max(vymax,
                                   Math.abs((double)curr_traj.
existing_particles[i].vy));
                                double vy = (double) curr_traj.
existing_particles[i].vy;
                                if( (vy < -0.2 && pos) || (vy > 0.2 && !pos )
) {
                                        if(nCycles == 0 ) {
                                                y_last = curr_traj.
existing_particles[i].y;
                                        }
                                        if(nCycles == 1 ) newStartingIndex =
i;
                                        if( i>startingIndex+1 && i-lastCorner
 > 1 ) {
                                          if(nCycles > 0){
                                            r_approx = r_approx
                                            + 0.5*Math.abs(curr_traj.
existing_particles[i].y
                                            - y_last);
                                            nr++;
                                          }
                                          y_last = curr_traj.
existing_particles[i].y;
                                          nCycles++;
                                          pos = !pos;
                                        }
                                }
```

```
                        }
                        if( nr > 0){
                                r_approx = r_approx/(double)nr;
                        }
                        if( nCycles < 2 || vymax <0.2) {
                                newTraj =1;
                                continue;
                        }
                        if( nCycles > 2 ) {
                                doCurveFit = true;
                                int remove = newStartingIndex - startingIndex
;
                                if(sectionLen-remove > 5) {
                                        sectionLen = sectionLen - remove;
                                        startingIndex = newStartingIndex;
                                }
                        }
                        double [] trajy = new double[sectionLen];
                        double [] time = new double[sectionLen];
                        for (int i = 0; i< sectionLen; i++) {
                                trajy[i] = curr_traj.existing_particles[i+
startingIndex].y
                                                - mean;
                                time[i] = (double)
                                   curr_traj.existing_particles[i+
startingIndex].frame;
                        }
                        double [] cory = new double[curr_traj.
existing_particles.length];
                        for(int i = 0; i< curr_traj.existing_particles.length
; i++)
                                cory[i] = 0.0;

                        if( doCurveFit) {
                                GMatrix data = new GMatrix(1,sectionLen, time
);
                                GVector values = new GVector(trajy,sectionLen
);
                                Kernel kernel = new PolynomialKernel(1);
                                //Kernel kernel = new GaussianKernel(3.0);
                                //Kernel kernel2 = new LinearKernel(KERNEL);
                                double lambda = 0.01;
                                //LinearKernel kernel2 = LinearKernal;
                                Representer representer = Regression.solve(
data, values, kernel, lambda);
                                GVector predictedValues = Matrices.mapCols(
representer, data);

                                // copy to a vector with the same indices as
rlocal
                                for(int i = startingIndex; i< lastIndex; i++)
                                   cory[i] = predictedValues.getElement(i-
startingIndex);
                         }
                         //write the data points to a file
```

```
                        StringBuffer fit = new StringBuffer("#t y \n");
                        for(int i = startingIndex; i< lastIndex; i++)
                           fit.append(time[i-startingIndex]+" "+ cory[i]+"\n
    ");

                        //calculate the slope
                        double y1, y2, x1,x2;
                        x1 = time[0];
                        x2 = time[lastIndex-startingIndex-1];
                        y1 = cory[startingIndex];
                        y2 = cory[lastIndex-1];
                        double m = (y2-y1)/(x2-x1);
                        double b = y2 - m*x2;
                        //predictedValues.sub(values);
                        //double cost = predictedValues.normSquared();


                       // calculate the coreline shape without the mean (aa)
//                     double[] cory = new double[curr_traj.
    existing_particles.length];
//                     mean = aa;
//                     for (int i = 0; i< curr_traj.existing_particles.
    length; i++) {
//                             double x = curr_traj.existing_particles[i].x;
//                             cory[i] = bb*x +cc*x*x + dd*x*x*x;
//                     }

                       // calculate the characteristics first with the core
    line function,
                       // then a second time with a corrected estimate of
    the mean
                       double[] rlocal = new double[curr_traj.
    existing_particles.length];
                       for (int i = startingIndex; i< lastIndex; i++) rlocal
    [i] = 0.0;
                       //start calculating
                       for( int loop = 0; loop < 4; loop++) {
                               //calculate the local radius
                               double rmax = 0.0;
                               double rmin = 0.0;
                               double rmean = 0.0;
                               for (int i = startingIndex; i< lastIndex; i
    ++) {
//                                     rlocal[i] =
                                       (double) curr_traj.
    existing_particles[i].y - mean;
                                     rlocal[i] =
                                       (double) curr_traj.
    existing_particles[i].y
                                             - cory[i] - mean ;
                                     rmax = Math.max(rlocal[i],rmax);
                                     rmin = Math.min(rlocal[i],rmin);
                                     rmean = rmean+rlocal[i];
                               }
                               rmean = rmean/(lastIndex-startingIndex);
```

```
//                              check to make sure mean is passing through
    the trajectory

/*                              if(Math.abs(rmean) < 20.0){
                                        double possible_offset = rmean;
                                        mean = mean + possible_offset;
                                        //recalculate rlocal
                                         *
*/                              //check for a straight line trajectory
                                if( (rmax - rmin) < 0.8) {
                                        newTraj = 1;
                                        break;
                                }

                                //find c0
                                c0 = -1;
                                c1 = -1;
                                c2 = -1;
                                boolean rIsNeg = true; // r is negative
                                r0IsNeg = true;
                            if(rlocal[startingIndex] > 0.0) rIsNeg = false;
                            if(Math.abs(rlocal[startingIndex]) < 0.0 ) c0 =
    startingIndex;
                                for (int i = startingIndex; i< lastIndex; i
    ++) {
                                    if( (rIsNeg && rlocal[i] > 0.0)
                                        || (!(rIsNeg) && rlocal[i] < 0.0 )){
                                          if( c0 < 0) {
                                                  c0 = i;
                                                  rIsNeg = !rIsNeg;
                                                  r0IsNeg = rIsNeg;
                                               // sign of first section after
     c0
                                          } else if( c1 < 0) {
                                                  c1 = i;
                                                  rIsNeg = !rIsNeg;
                                                  if( (c1-c0) < 1) {
                                                          c2 = -1;
                                                          break;
                                                  // NOTE: this might waste
    some trajectories
                                                  }
                                          } else {
                                                  c2  = i;
                                                  if( (c2-c1) < 1) {
                                                          c2 = -1;  // bad
    trajectory
                                                  // NOTE: this might waste
    some trajectories
                                                  }
                                                  break;
                                          }
                                    }
                                }
                                if( c2 < 0 ) {
```

```
                                        newTraj = 1;
                                        break;  // trajectory didn't cross
over core enough times
                                }
                                // Now find the radii in c0-c1 and c1-c2
sections
                                r0 = 0.0;
                                r1 = 0.0;

                                //calculate signed values for r0 and r1
                                for (int i = c0; i< c1; i++) {
                                        if( r0IsNeg) {
                                                r0 = Math.min(r0,rlocal[i]);
                                        }else{
                                                r0 = Math.max(r0,rlocal[i]);
                                        }
                                }
                                for (int i = c1; i< c2; i++) {
                                        if( r0IsNeg) {
                                                r1 = Math.max(r1,rlocal[i]);
                                        }else{
                                                r1 = Math.min(r1,rlocal[i]);
                                        }
                                }
                                //france
                                //if(mean > 0.0)break;
                                // calculate the corrected mean
                                double offset = 0.5*(r0+r1);
                                if( Math.abs( offset) < eps ) break;  //we've
 zeroed in on the mean
                                mean = mean + offset;
                        }
                        if(c2 < 0) {
                                newTraj = 1;
                                continue; //go to the next trajectory
                        }
                        //calculate t0, t2, z0 and z2
                        double toffset;// y1, y2;
                        double z0 = (double) curr_traj.existing_particles[c0
].x;
                        double z2 = (double) curr_traj.existing_particles[c2
].x;
                        double dt = 1.0;
                        //t0 & z0
                        t0 = (double) curr_traj.existing_particles[c0].frame
- (double)firstframe;
                        t1 = (double) curr_traj.existing_particles[c1].frame
- (double)firstframe;
                        t2 = (double) curr_traj.existing_particles[c2].frame
- (double)firstframe;
                        if( c0 > 0 &&  Math.abs(rlocal[c0]) > eps ) {
                                dt = (double) (curr_traj.existing_particles[
c0].frame - curr_traj.existing_particles[c0-1].frame);
                                toffset = 0.0;
                                y1 = Math.abs(rlocal[c0-1]);
```

```
                                y2 =  Math.abs(rlocal[c0]);
                                if( (y1+y2) > 0.001) toffset = y1/(y1+y2);
                                t0 = (t0-dt) + dt*toffset;
                        // z0
                                double dz = (double) (curr_traj.
existing_particles[c0].x
                                                - curr_traj.
existing_particles[c0-1].x);
                                double zoffset = toffset*dz;
                                z0 = (double)(curr_traj.existing_particles[c0
-1].x) + zoffset;
                        }
                        // t1 -- z1 isn't necessary
                        if( Math.abs(rlocal[c1]) > eps ) {
                                dt = (double) (curr_traj.existing_particles[
c1].frame - curr_traj.existing_particles[c1-1].frame);
                                toffset = 0.0;
                                y1 = Math.abs(rlocal[c1-1]);
                                y2 = Math.abs(rlocal[c1]);
                                if( (y1+y2) > 0.001) toffset = y1/(y1+y2);
                                t1 =  (t1-dt) + dt*toffset;
                                // z2
                        }
                        //t2
                        if( Math.abs(rlocal[c2]) > eps ) {
                                dt = (double) (curr_traj.existing_particles[
c2].frame - curr_traj.existing_particles[c2-1].frame);
                                toffset = 0.0;
                                y1 = Math.abs(rlocal[c2-1]);
                                y2 = Math.abs(rlocal[c2]);
                                if( (y1+y2) > 0.001) toffset = y1/(y1+y2);
                                t2 = (t2-dt) + dt*toffset;
                                // z2
                                double dz = (double) (curr_traj.
existing_particles[c2].x
                                                - curr_traj.
existing_particles[c2-1].x);
                                double zoffset = toffset*dz;
                                z2 = (double)(curr_traj.existing_particles[c2
-1].x) + zoffset;
                        }
                        //compute r and r_error
                        r = 0.5*(Math.abs(r0)+Math.abs(r1));
                        double rerror = 0.5*(Math.abs(r0-r) + Math.abs(r1-r))
;
                        if( r < 0.0001) r = 0.001;
                        rerror = rerror/r;
                        //compute period and period error
                        hp0 = (t1 - t0);
                        hp1 = (t2 - t1);
                        hp = 0.5*(t2-t0);
                        double hperror = 0.5*(Math.abs(hp0-hp) + Math.abs(hp1
-hp));
                        if( hp < 0.0001) hp = 0.001;
                        hperror = hperror/hp;
```

```
                        alpha = 1.0/hp;
                        //calculate the standard deviation
                        double stddev = 0.0;
                        int n = 0;
                        double factor = 1.0;
                        if( r0IsNeg ) factor = -1.0;
                        for (int i = c0; i< (c2+1); i++) {
                          n++;
//                        double fx = mean + factor*r*Math.sin(alpha*Math.PI
    *((double)i-t0));
                          double fx = mean + cory[i] + factor*r*Math.sin(
    alpha*Math.PI*((double)i-t0));
//                        double diff = (double) curr_traj.existing_particles
    [i].y -cory[i] - fx;
                          double diff = (double) curr_traj.existing_particles
    [i].y -fx;
                          stddev = stddev + diff*diff;
                        }
                        if(n>1) stddev = Math.sqrt(stddev/ (double)(n-1) );
                        if(r>0.0001) stddev = stddev / r;
                        if(stddev > 1.0 || r < 0.5) { // this section was bad
     but maybe there's something better
                                newTraj = 0;
                                if( c1-c0 > 1){
                                        startingIndex = c1 -1;
                                } else {
                                        startingIndex = c1;
                                }
                                continue;
                        }
                        if(stddev > 0.2)traj_info.append("#");


                        //Output

                        NumberFormat ffi = new java.text.DecimalFormat("000")
    ;
                        //NumberFormat ffis = new java.text.DecimalFormat
    ("000");
                    NumberFormat ffd = new java.text.DecimalFormat
    ("0000.00;-000.00");
                    NumberFormat ffds = new java.text.DecimalFormat
    ("00.00;-0.00");
                        traj_info.append(ffi.format(curr_traj.serial_number)
    + " ");
                        traj_info.append(ffi.format(firstframe) + "  ");
                        traj_info.append(ffd.format(mean) +"  ");
                        traj_info.append(ffd.format(r) +"  ");
                        traj_info.append(ffd.format(hp) +"  ");
                        traj_info.append(ffd.format(t0+(double)firstframe) +"
      ");
                        traj_info.append(ffd.format(t2+(double)firstframe) +"
      ");
                        traj_info.append(ffd.format(z0) +"  ");
                        traj_info.append(ffd.format(z2) +"  ");
```

```
                    traj_info.append(ffds.format(stddev) +"  ");
                    traj_info.append(ffds.format(m) +"  ");
                    traj_info.append(ffi.format(fileCounter)+"  ");
                    traj_info.append("\n");


                    //Write the information to a gnuplot script to plot
the actual trajectory
                    //and the fitted sin curve and the mean.
                    StringBuffer gnuscript = new StringBuffer("#
Trajectory ");
                    gnuscript.append( ffi.format(curr_traj.serial_number)
+"\n");
                    gnuscript.append("a = "+ ffi.format(curr_traj.
serial_number)+"\n");
                    gnuscript.append("mean = "+ffd.format(mean) +"; ");
                    gnuscript.append("r = "+ ffd.format(r) +"; ");
                    gnuscript.append("hp = "+ ffd.format(hp) +"; ");
                    gnuscript.append("t0 = " + ffd.format(t0+(double)
firstframe) +"\n");
                    gnuscript.append("alpha = " + (1.0/hp) +"\n");
                    gnuscript.append("fact = " + ffd.format(factor) +"\n
");
                    gnuscript.append("m = " + m +";");
                    gnuscript.append("b = " + b +"\n");
                    /*
                    gnuscript.append("aa = " + aa +";");
                    gnuscript.append("bb = " + bb +";");
                    gnuscript.append("cc = " + cc +";");
                    gnuscript.append("dd = " + dd +";\n");
                    */
                    gnuscript.append("f(x)= mean+fact*r*sin(alpha*pi*(x-
t0))\n");
                    gnuscript.append("c(x)= m*x+b\n");
                    gnuscript.append("plot 'tt' u 1:3 i a w lp t 'exp " +
 curr_traj.serial_number+ "',");
                    gnuscript.append(" f(x) w l t '"+curr_traj.
serial_number+ " fit stdev/r=" + ffd.format(stddev)+"', mean \n");
                    //gnuscript.append("plot 'tt' u 1:3 i a w lp, 'f"+ffi
.format(fileCounter)+ "' u 1:($2+mean) w l \n");
                    gnuscript.append("plot 'tt' u 1:3 i a w lp, c(x)+mean
 w l \n");
                    gnuscript.append("plot 'tt' u 1:($3-c($1)-mean)  i a
w lp, f(x)-mean w l t 'fit' \n");
                    gnuscript.append("#plot 'tt' u 1:($3-c($1)) i a w lp,
 f(x) w l t 'fit'\n");
                    if (!write2File(sd.getDirectory(), "g" + ffi.format(
fileCounter),gnuscript.toString())) {
                            // upon any problam savingto file return;
                            return traj_info;
                    } else {
                            //write2File(sd.getDirectory(), "f" + ffi.
format(fileCounter),fit.toString());
                            fileCounter++;
```

```
//                                This traj was good, let's see if we can
    continue on the same trajectory
                                newTraj = 0;
                                if(c2-c1>1 ) {
                                        startingIndex = c2 -1;
                                } else {
                                        startingIndex = c2;
                                }
                        }
                }

                return traj_info;
        }

% ============End of Excerpt 4 ========================
```

Appendix C

PTV Measurements

This chapter documents the results of the PTV measurements that were made to record the azimuthal and axial velocity profiles in the vortex. First, an analysis of possible sources of measurement error is presented in order to estimate the uncertainty of the results. Possible sources of error include uncertainty about the exact location of the free surface, resolution limitations of the film images in time and space, and possible error in the measured vertical displacement of the particles due to parallax effects linked to the viewing angle of the camera compared to the trajectory of the particles. The scatter of the data points about the fitted curve also generates uncertainty in the estimated slope of the fitted curve. The magnitude of the error that might be produced by these uncertainties is estimated and included when possible in the subsequent graphs documenting the results.

These graphs include the recorded PTV data for $V_\theta(r), V_z(z)$ with the parameters a, r_o and Γ_∞ obtained from curve fits to the measured data. The profile of the free surface depression computed from these measured parameters is compared to the profile recorded simultaneously with the particle trajectories in the film segments.

C.1 Analysis of measurement uncertainty

The scale of the recorded images from which the particle locations are extracted is determined by filming a millimeter-graduated grid placed in the water at the location where the vortices form. The scale is computed from the number of pixels that cover 1 cm. The scale ranges from 0.23 to 0.25 ± 0.003 mm/pixel depending on the operating condition and day that the measurements were taken.

The pixel resolution controls the minimum particle size that can be consistently identified on the images by the particle-tracking algorithm (Sbalzarini and Koumoutsakos, 2005). It also affects the resolution at which the particle location can be determined. If we assume the particle location cannot be consistently determined below the resolution of one pixel, this signifies that the minimum velocity resolution that can be computed from the films is 0.058 m/s for the films recorded at 250 frames-per-second, and 0.012 m/s for the films recorded at 50 frames-per-second.

Sbalzarini and Koumoutsakos (2005) report that the particle-tracking algorithm is capable of identifying the particle location at a sub-pixel resolution, the accuracy of which depends on the signal-to-noise (SNR) ratio of the particle intensity vs. background noise in the images. The images employed here include some particles that are slightly smaller than those employed by Sbalzarini and Koumoutsakos (2005) to determine sub-pixel resolution, and the intensity of each particle (and hence its SNR) varies significantly along its trajectory depending on its distance from the in-focus plane, its degree of illumination and its velocity across the plane of the image. It is therefore difficult to evaluate the sub-pixel accuracy of the particle locations computed by the particle-tracking algorithm. For some of the film segments, the distribution of the axial velocity V_z computed from the frame-to-frame displacement of the particles shows clear peaks at velocities corresponding to 0, 1 and 2 pixels/frame, suggesting that sub-pixel location resolution is not consistently achieved.

The pixel resolution does not place a significant constraint on the computed azimuthal velocity $V_\theta(r)$ profiles because the characteristic radius of the vortices is greater than 3 pixels in size, and V_θ is computed from the time (multiple frames) it takes for a particle to travel the full circumference (of its trajectory of radius r) around the vortex.

The camera is located quite close to the vortex (approximately 0.24 m from the vertical axis around which the particles travel), producing a parallax effect. The camera is placed so that its horizontal line of sight is aligned with the free surface, i.e. so that it is not looking at the free surface from above or below. The viewing angle causes a vertical displacement in the lower portion of the image frame (80 mm below the free surface) to appear slightly (roughly 5%) shorter than at the free surface. This is verified using the recorded millimeter grid. The measured vs. exact magnitude of the displacement along the vortex axis might also be slightly affected by the fact that the vortex axis is not perfectly vertical as assumed, but may bend towards the intake opening slightly. The degree of bending near the free surface should not exceed 15°, which would produce an error of less than 5% in the measured vertical displacement, which is much less important compated to variations in V_z.

The measured V_z is affected to a much more significant degree by the contribution of the azimuthal velocity V_θ, which can increase or decrease the perceived V_z by up to $0.3V_\theta$ when the particle trajectory is viewed from slightly above or below. (the viewing angle θ_p is estimated to reach a maximum of 18° at the bottom of the image). This effect causes an 'artificial' oscillation in the measured V_z that interacts with 'true' oscillations in V_z due to the fact that the velocity

profile deviates from axisymmetry. The deviation from axisymmetry in both the V_θ and V_z profiles makes it difficult to correct for the contribution of V_θ to the perceived V_z. However, if an average value of V_z is computed by measuring the vertical distance (and corresponding time) travelled by a particle that travels one complete cycle around the circumference around the vortex, the contribution of V_θ should cancel out. That is the strategy employed here. If the axis of the vortex moves or bends towards the camera, the displacement ΔX in the stream-wise direction (perpendicular to the vertical plane on which the scaling grid was located) combined with the parallax effect would make the z coordinate of a particle appear to be slightly higher (closer to the free surface), by an amount roughly equal to $\Delta X \sin(\theta_p)$. The lateral displacement ΔY due to bending or displacement of the vortex axis in the span-wise (Y) direction appears in the film images and is found to have a maximum value of roughly 7 mm. Assuming that the upper limit of the magnitude of the bending or displacement in the streamwise direction is comparable to that in the span-wise direction, this corresponds to an uncertainty in the measured z of ± 1.1 mm. An error bar of total length 1.1 mm is plotted at the top of the graphs to give an idea of its magnitude.

Since V_z is computed from the ratio of the displacement $[\Delta z]_T$ over the time-span $[\Delta t]_T$ of the trajectory segment, the relative error $\delta V_z/V_z$ of the axial velocity is computed from the sum of the squared relative errors in the measured displacement and time-span, $\delta z/[\Delta z]_T$ and $\delta t/[\Delta t]_T$, respectively:

$$\frac{\delta V_z}{V_z} = \left\{ \left(\frac{\delta z}{[\Delta z]_T} \right)^2 + \left(\frac{\delta t}{[\Delta t]_T} \right)^2 \right\}^{1/2} . \tag{C.1}$$

The upper limit on the uncertainty of z is estimated as $\delta z = 4$ pixels ≈ 1 mm, and on t as $\delta t = 1$ frame, which is equal to 0.004 s or 0.02 s depending on the frame-rate. The size of the error bars on V_z varies depending on the length of the trajectory segment. A longer segment with produce a smaller error bar. In some cases, the cycle-averaged V_z varies a fair degree along the length of a multi-cycle trajectory, and the plotted V_z values used for the curve fit are averaged over multiple cycles. Averaging over multiple cycles reduces the scatter in the graphs and reduces the estimated uncertainty (error bars) on V_z; it may however also conceal deviations from the assumed linear profile in z.

The axial gradient $a = \partial Vz/\partial z$ is obtained by fitting the linear function $V_z(z) = az + b$ to the values of $V_z(z)$ extracted from the film segment using the open-source statistical software package R (Crawley, 2012). a is the slope of the line and is also the value of the axial gradient in Eq. 2.2 in Burgers's model. b is the intercept of the line (the value of V_z at z=0). The exact location of the free surface (the location of $z = 0$) on the film images is slightly difficult to ascertain since the camera sight line is not always exactly aligned with the free surface. There may therefore be a bias in the measured z values (and hence in b), however the quantity of interest, a, is unaffected by this bias.

The uncertainty of the curve fit and the variability of the data about the fitted value for a are evaluated using the standard error (SE_a) and the R^2 value. The standard error SE_a is the standard deviation of the sampling distribution about the fitted value (Crawley, 2012). The magnitude of

the standard error on the slope SE_a gives an idea of the precision of the estimate of the slope a; its inverse is a measure of its reliability. SE_a is given by the relation

$$\mathrm{SE}_a = \left(\frac{s_e^2}{\mathrm{SSX}} \right)^{1/2}, \tag{C.2}$$

where s_e^2 is the variance on the error

$$s_e^2 = \frac{\Sigma (V_z - V_{z,p})^2}{n-2}, \tag{C.3}$$

and SSX is the corrected sum of squares of the explanatory variable z, which is the sum of squares of the deviation from the mean z_m of z:

$$\mathrm{SSX} = \Sigma (z - z_m)^2. \tag{C.4}$$

V_z is the measured velocity, $V_{z,p} = az + b$ is the value predicted by the curve fit, z_m is the mean of all the measured z values in the sample, and n is the number of samples.

The standard error SE_a estimated for the slope a is used to set the half-width of the error bars on a in Figure 4.5(a) comparing a to r_o.

The R^2 value gives the fraction of the total variation in V_z that is explained by variation in z. A value of R^2 close to 0 indicates that none of the variation in V_z can be explained by varation in z, and a value R^2 close to 1 indicates that the variation in V_z can be entirely explained by variation in z. R^2 is defined as:

$$R^2 = \frac{\mathrm{SSY} - \mathrm{SSE}}{\mathrm{SSY}}, \tag{C.5}$$

where SSY is the corrected sum of squares of the deviation of the dependent variable V_z from its mean $V_{z,m}$

$$\mathrm{SSY} = \Sigma (V_z - V_{z,m})^2, \tag{C.6}$$

and SSE is the unexplained scatter of the dependent variable V_z:

$$\mathrm{SSE} = \Sigma (V_z - V_{z,p})^2. \tag{C.7}$$

C.1.1 PTV measurement duplicates

To estimate the reliability of the PTV measurements and analysis, five film segments are evaluated for one operating condition (Case 1). The relative variability of the results of the analysis compared to the variation produced by different operating conditions can be seen in Figure C.1 below: the solid dots show the 5 data points for Case 1, and the $\times$'s show the data points for the other cases. Figure C.1(a) shows the relationship between the values of r_o and a measured by

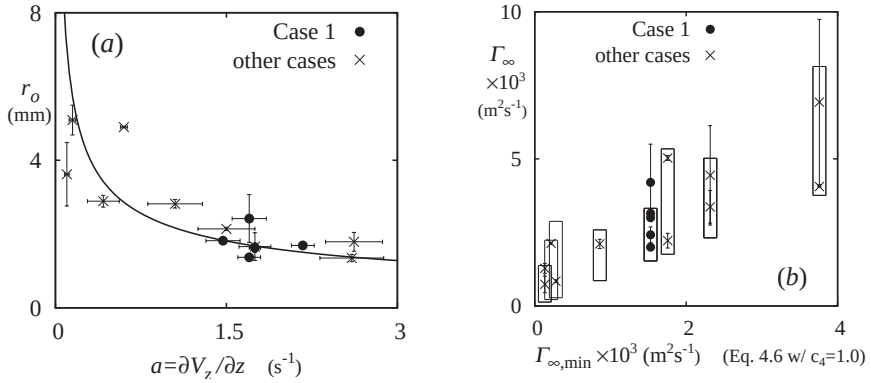

FIGURE C.1: Duplicate PTV measurements of r_o and Γ_∞ for Case 1.

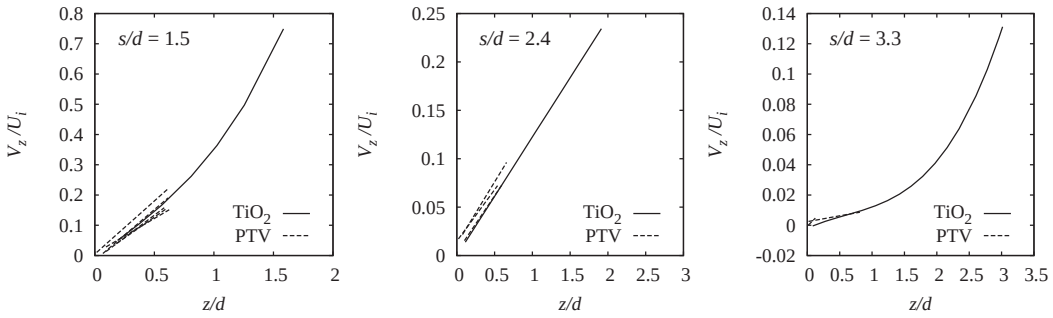

FIGURE C.2: Comparison of particle-tracking and dye (TiO_2) tracking measurements.

PTV and Figure C.1(*b*) shows the bulk circulation Γ_∞ measured by PTV as a function of $\Gamma_{\infty,\text{est}}$ estimated using Eq. 4.6 in Chapter 4.

C.1.2 Dye-tracking measurements

A few measurements of $V_z(z)$ profiles were also made by injecting white TiO_2 dye (fine TiO_2 powder mixed in water) into the vortex at the free surface for 3 operating conditions, one at each submergence level. The dye forms a clear dye core whose lower limit (or dye front) is easily identified as it progresses along the vortex axis, away from the free surface. This dye core can be filmed from further away and at a lower frame-rate than the particles, so $V_z(z)$ can be measured over a greater vertical depth, from the free surface almost all the way to the intake pipe. The location of the dye front z_f is tracked with time t and a polynomial function is fitted to the plot of z_f vs. t. $V_z(z)$ is estimated from the derivative of this function with respect to time. As shown in Figure C.2, the slope of the resulting profiles near the free surface roughly coincides with that of the shorter profiles measured using PTV near the free surface, providing reassurance that the PTV analysis and curve-fitting approach are accurate.

C.2 PTV results

The following pages show the measured PTV data with the curve fits and the calculated and measured free surface depression. 'exp a*r' indicates the name of the film segment from which the data was extracted. 'f_o' indicates the first frame of the film segment employed to extract the trajectories for this set of graphs. $\triangle t$ indicates the total length (time-span) of the film segment.

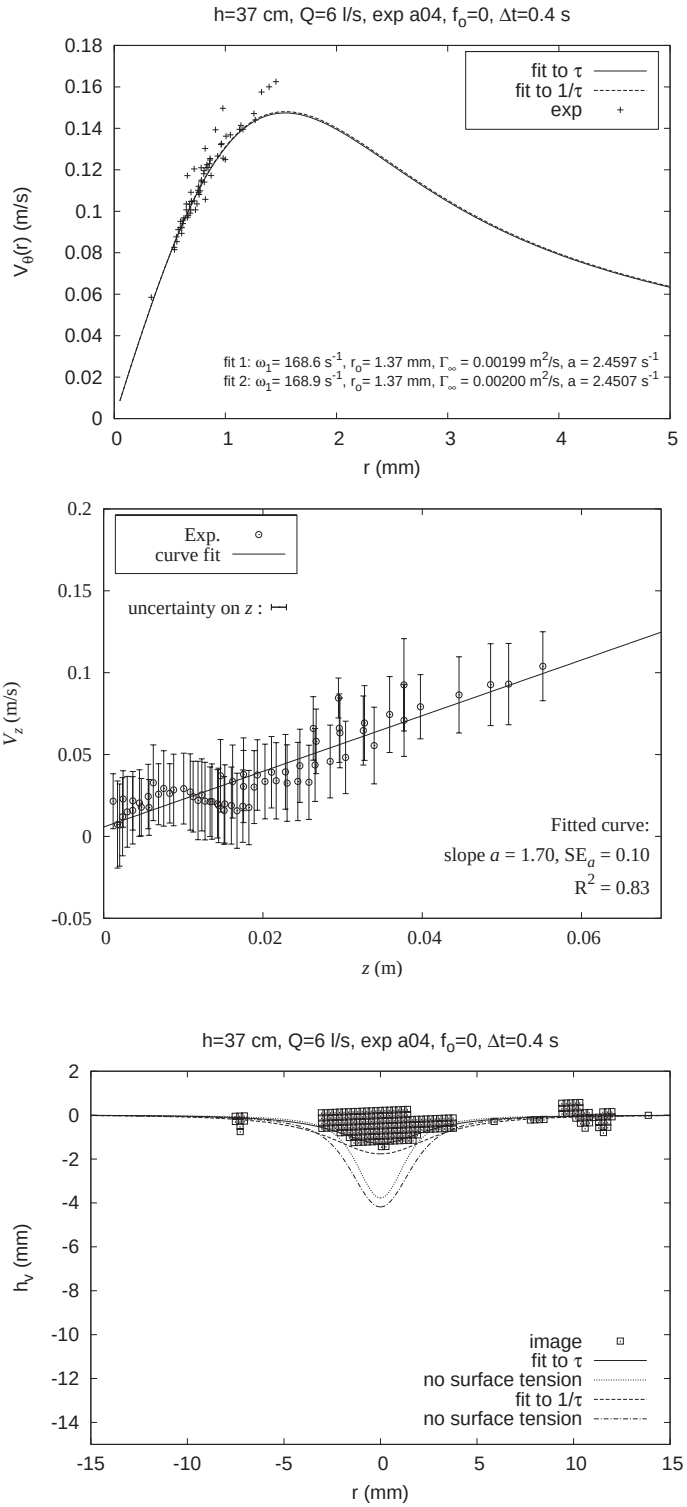

FIGURE C.3: Case 1, Film segment 1: PTV data for $V_\theta(r), V_z(z)$ with curve fits and corresponding computed free surface profile compared to the recorded one.

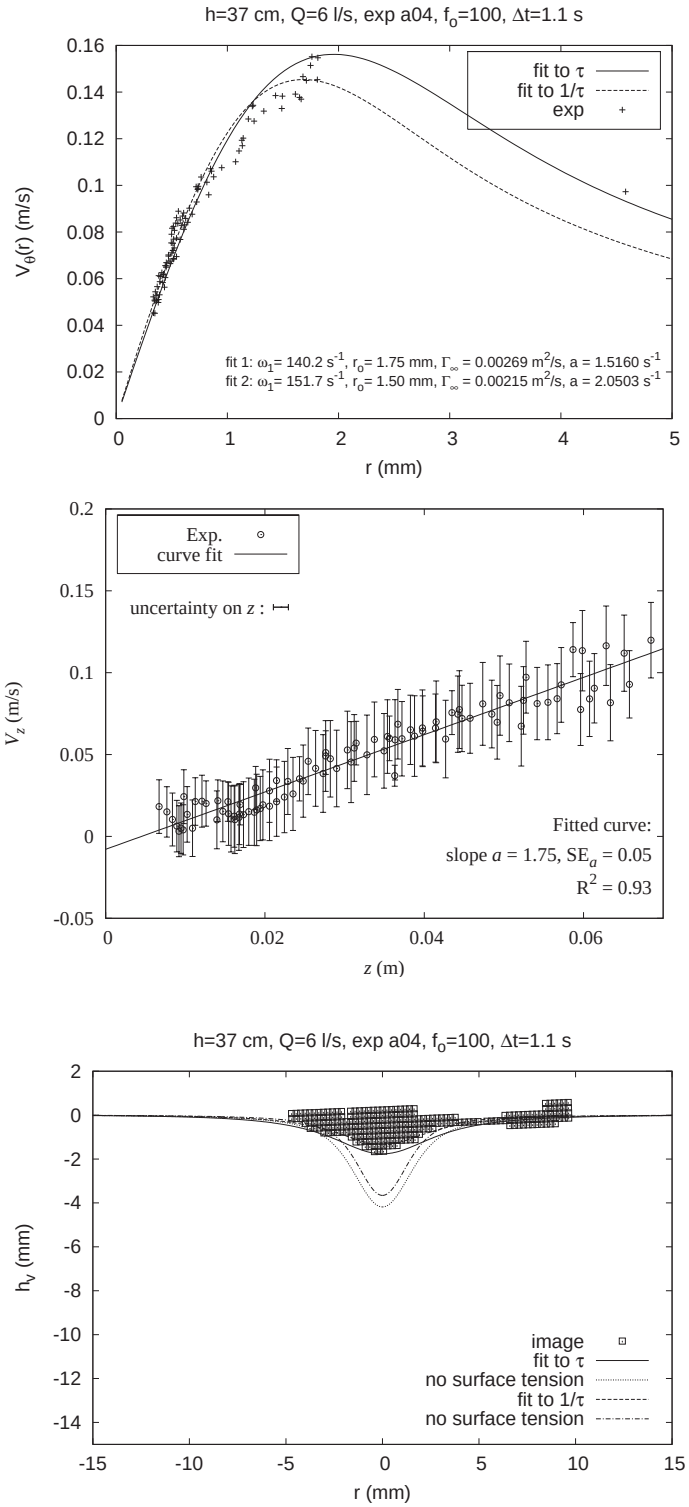

FIGURE C.4: Case 1, Film segment 2: PTV data for $V_\theta(r), V_z(z)$ with curve fits and corresponding computed free surface profile compared to the recorded one.

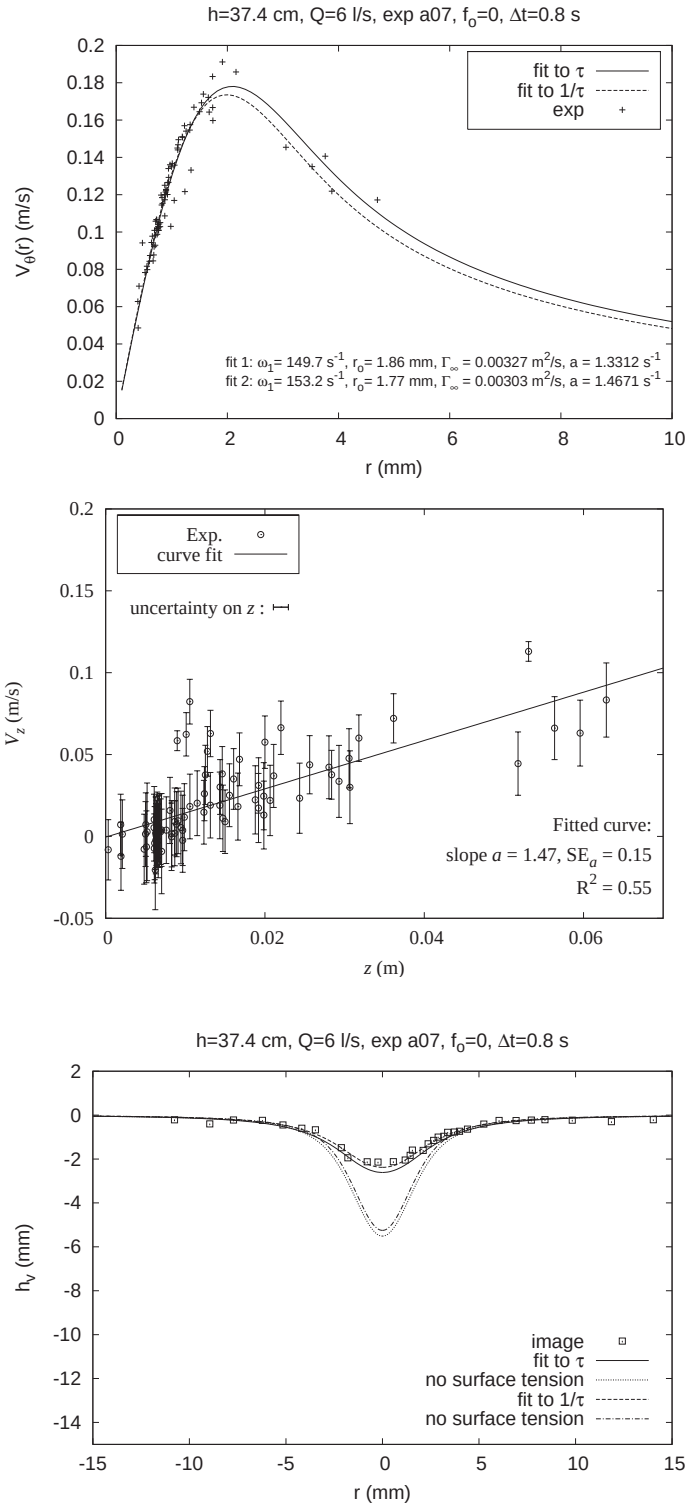

FIGURE C.5: Case 1, Film segment 3: PTV data for $V_\theta(r), V_z(z)$ with curve fits and corresponding computed free surface profile compared to the recorded one.

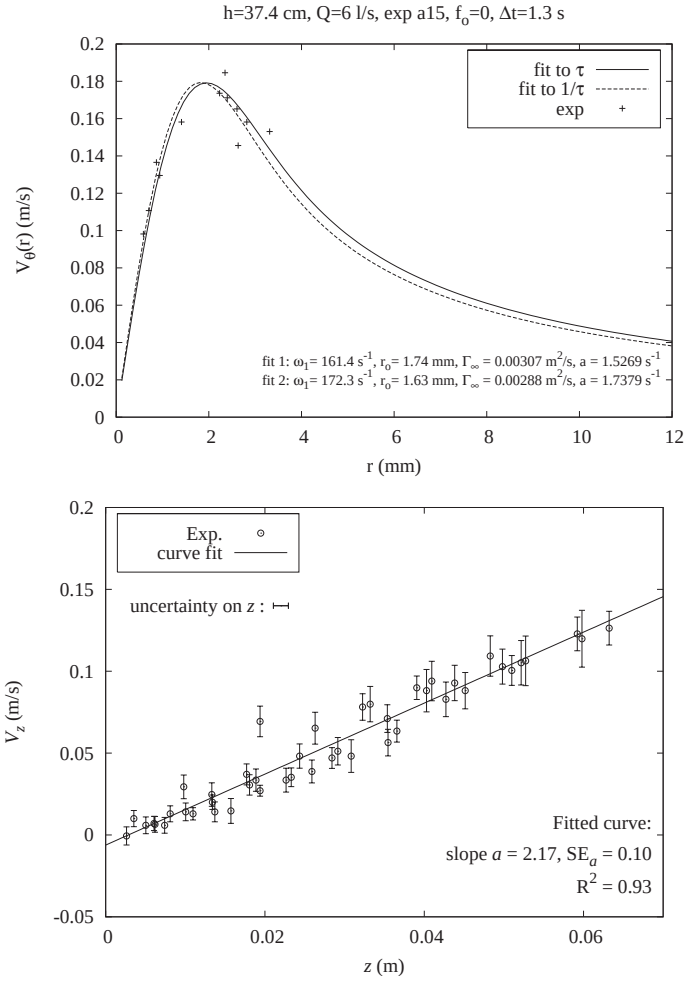

FIGURE C.6: Case 1, Film segment 4: PTV data for $V_\theta(r), V_z(z)$ with curve fits. Duplicate used for the PTV uncertainty analysis (Fig. C.1).

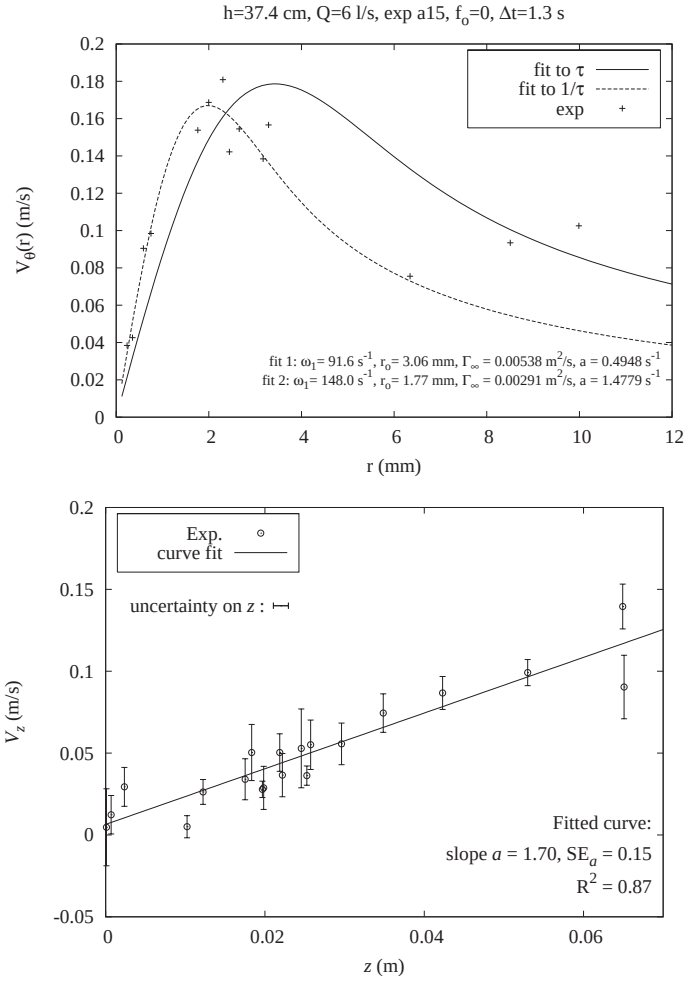

FIGURE C.7: Case 1, Film segment 5: PTV data for $V_\theta(r), V_z(z)$ with curve fits. Duplicate used for the PTV uncertainty analysis (Fig. C.1).

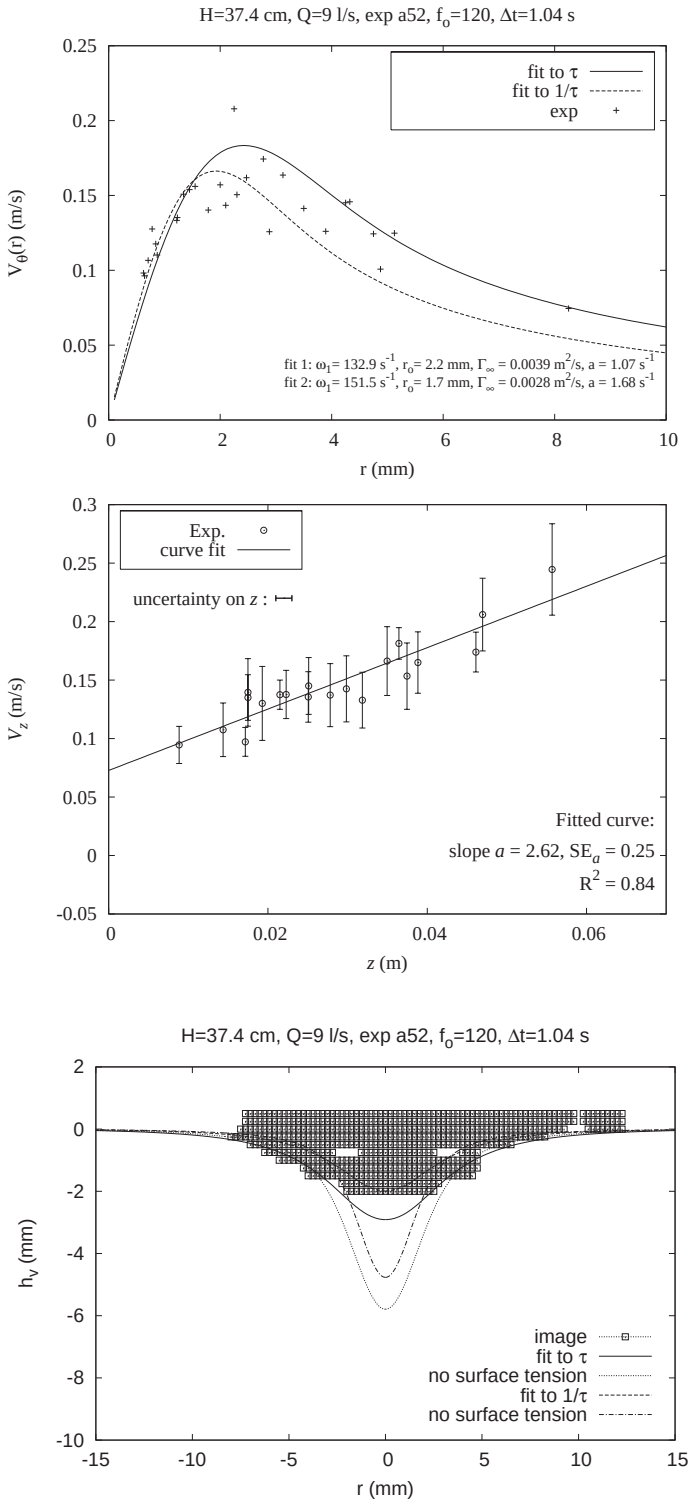

FIGURE C.8: Case 2, Film segment 1: PTV data for $V_\theta(r), V_z(z)$ with curve fits and corresponding computed free surface profile compared to the recorded one.

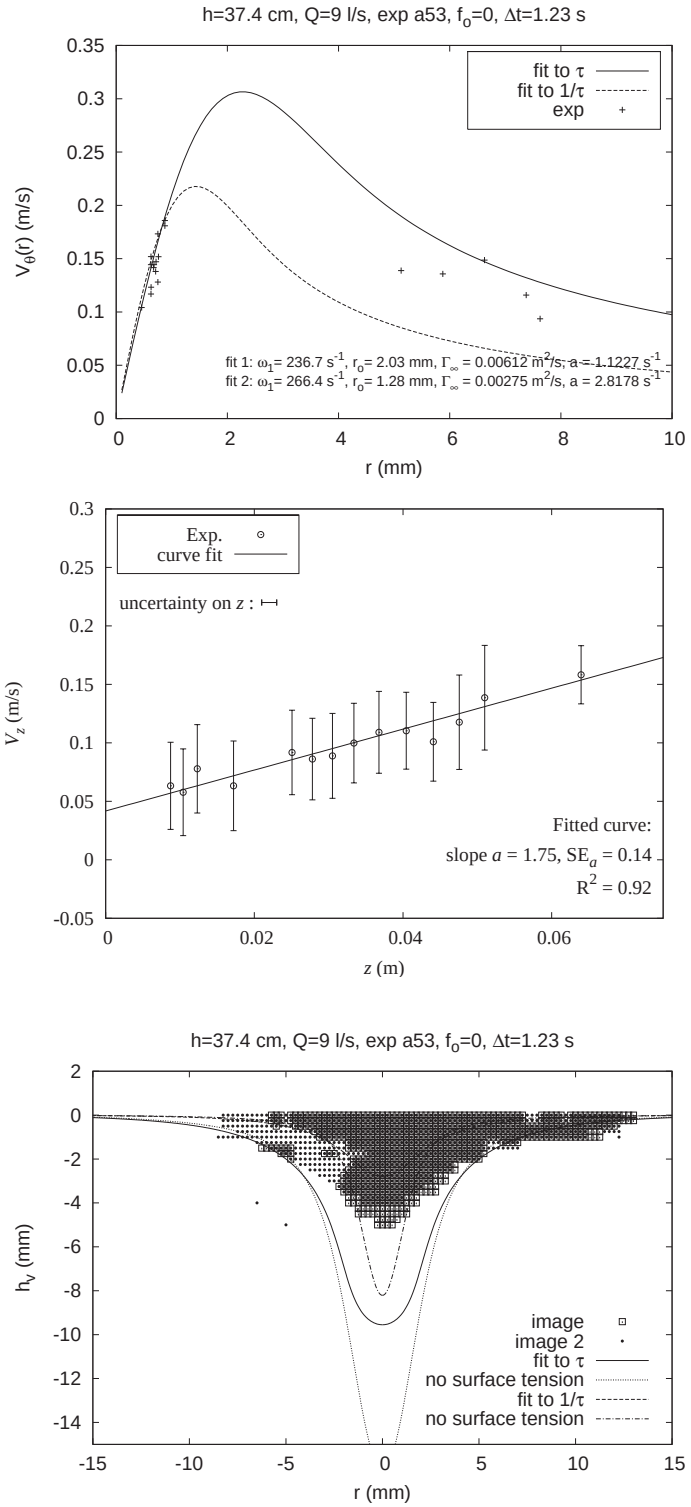

FIGURE C.9: Case 2, Film segment 2: PTV data for $V_\theta(r), V_z(z)$ with curve fits and corresponding computed free surface profile compared to the recorded one.

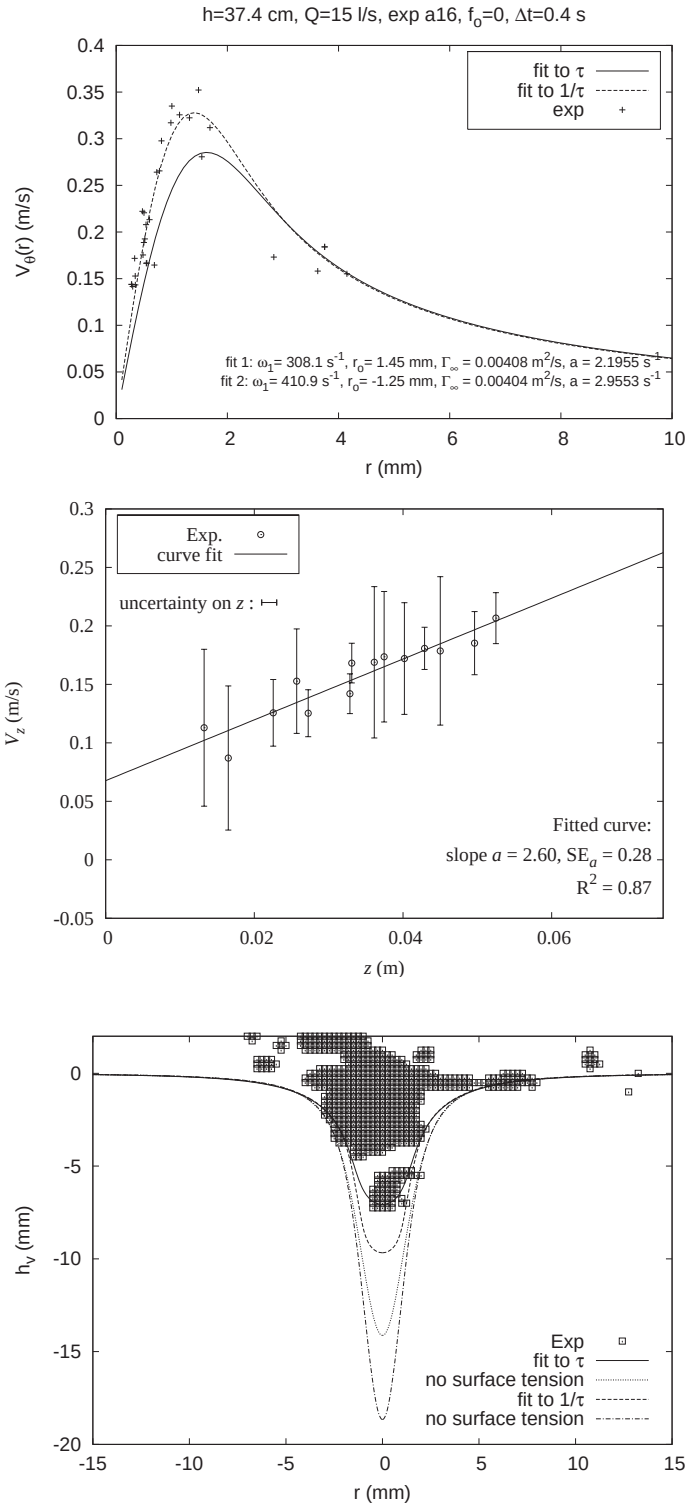

FIGURE C.10: Case 3, Film segment 1: PTV data for $V_\theta(r), V_z(z)$ with curve fits and corresponding computed free surface profile compared to the recorded one.

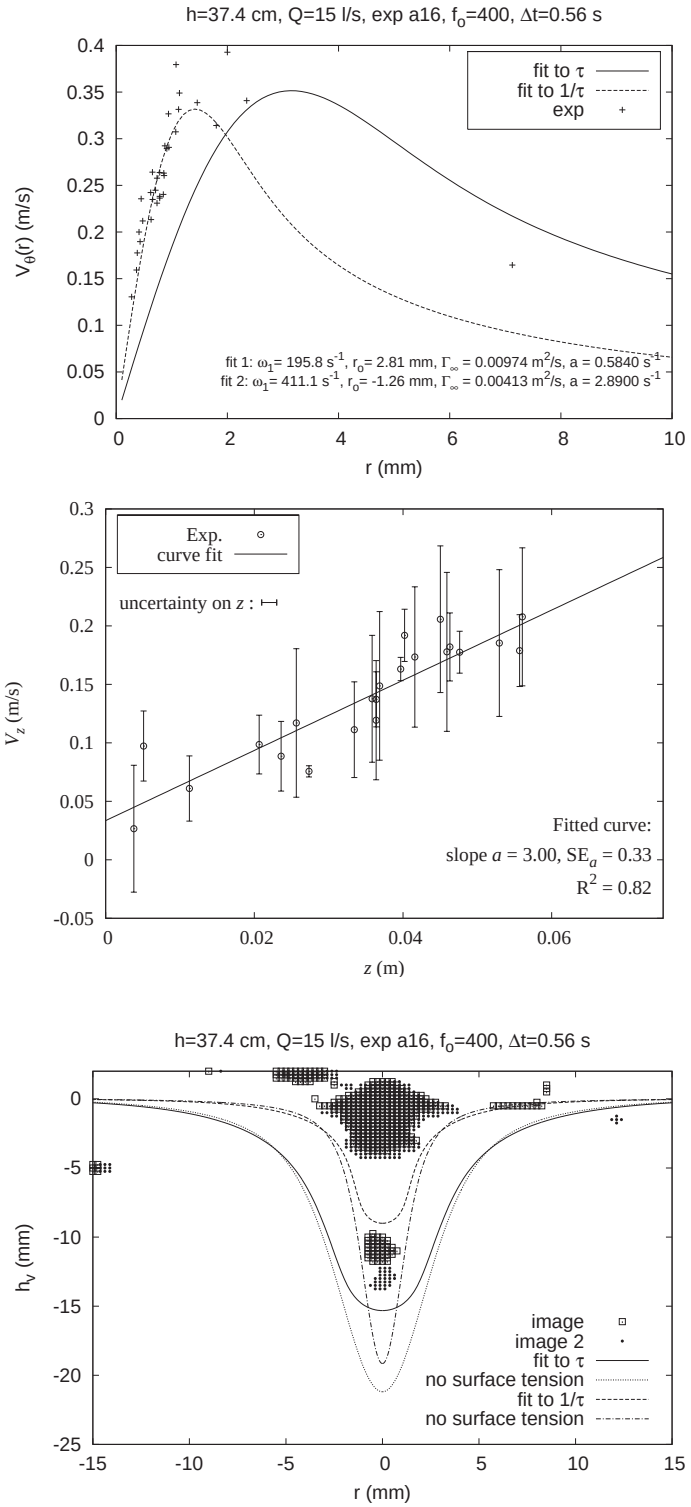

FIGURE C.11: Case 3, Film segment 2: PTV data for $V_\theta(r), V_z(z)$ with curve fits and corresponding computed free surface profile compared to the recorded one.

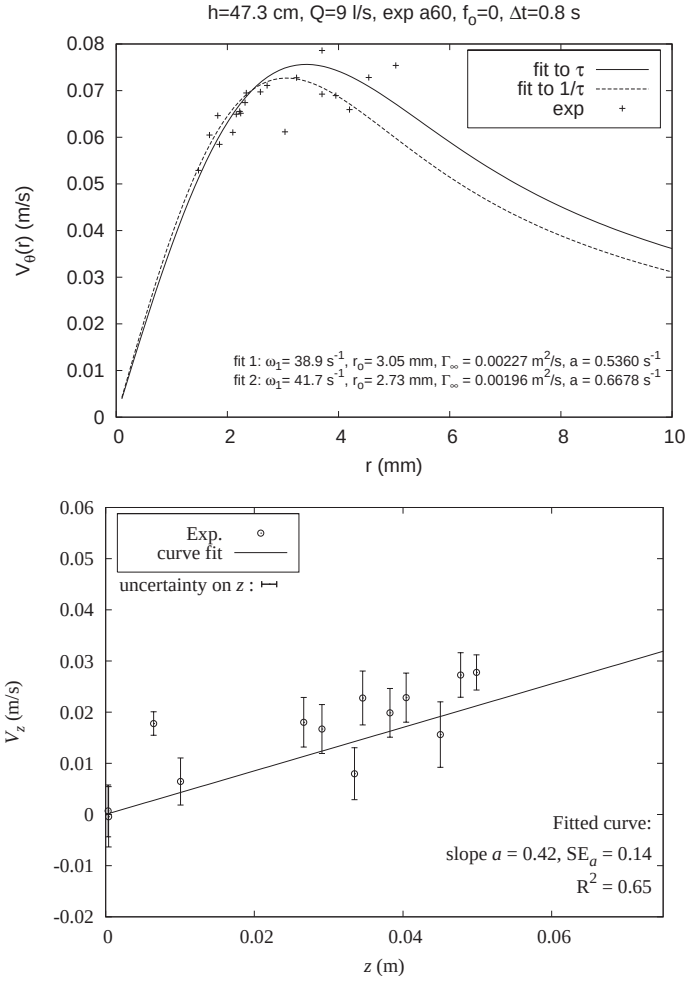

FIGURE C.12: Case 4, Film segment 1: PTV data for $V_\theta(r), V_z(z)$ with curve fits. Recorded free surface profile missing.

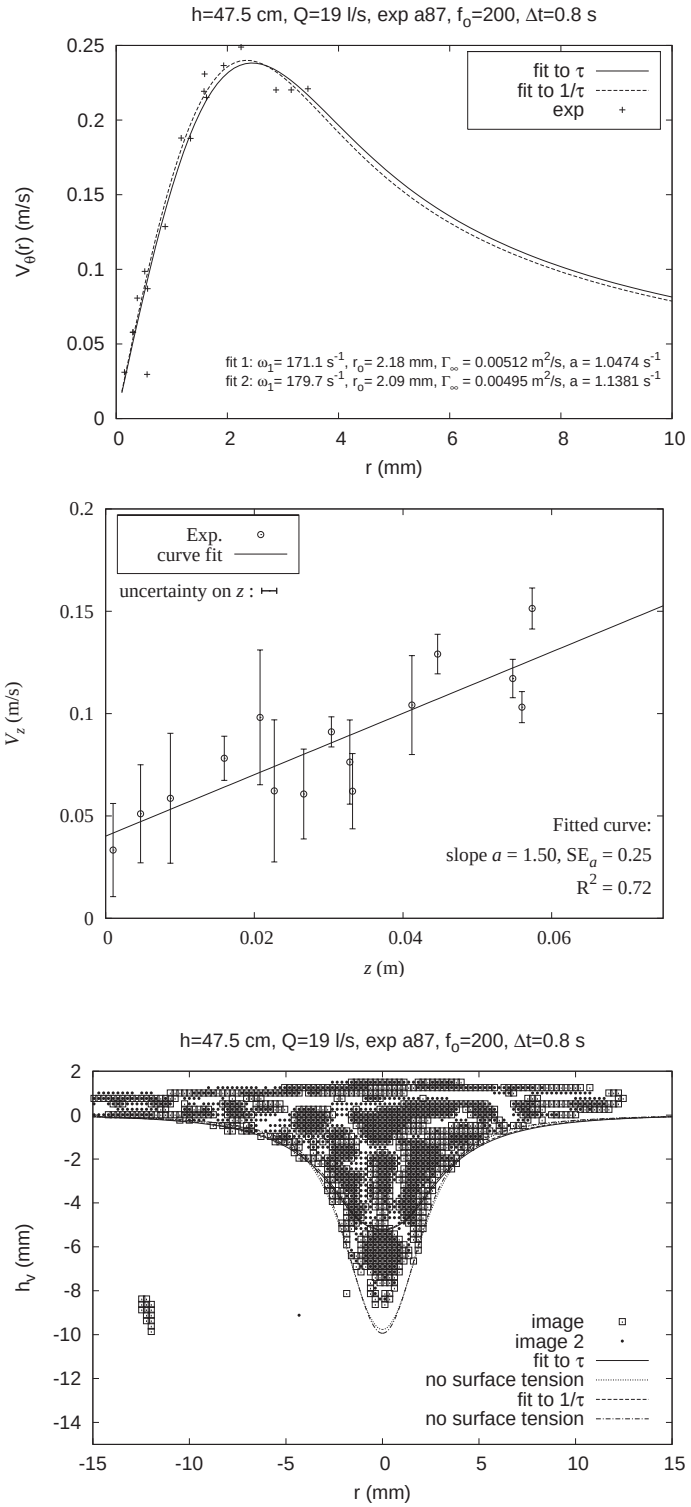

FIGURE C.13: Case 5, Film segment 1: PTV data for $V_\theta(r), V_z(z)$ with curve fits and corresponding computed free surface profile compared to the recorded one.

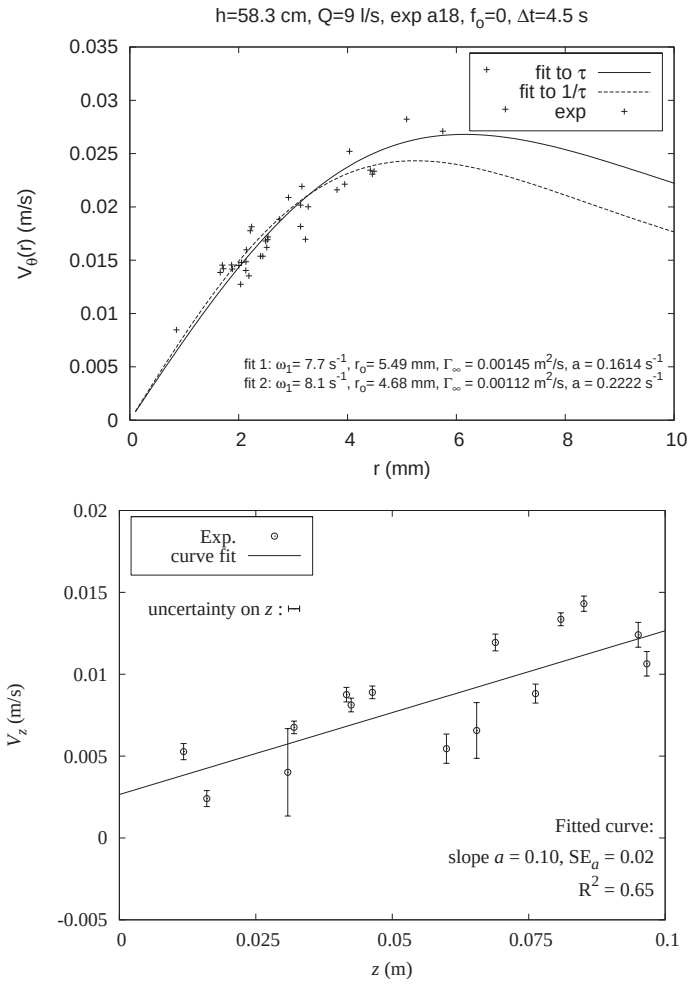

FIGURE C.14: Case 6, Film segment 1: PTV data for $V_\theta(r), V_z(z)$ with curve fits. No free surface profile is shown since the observed and measured depressions are negligible.

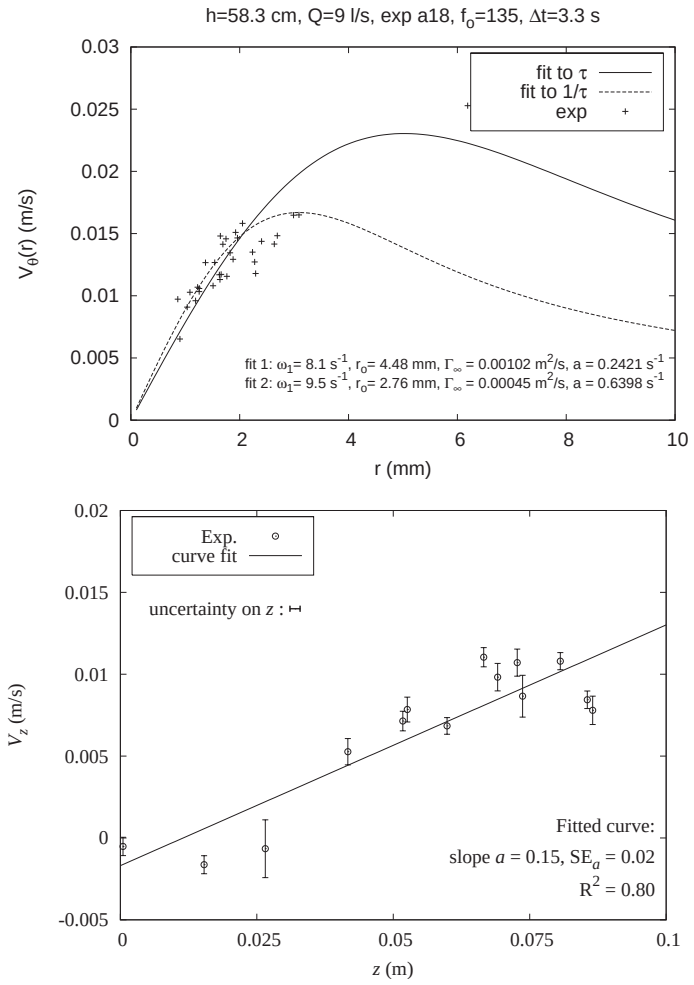

FIGURE C.15: Case 6, Film segment 2: PTV data for $V_\theta(r), V_z(z)$ with curve fits. No free surface profile is shown since the observed and measured depressions are negligible.

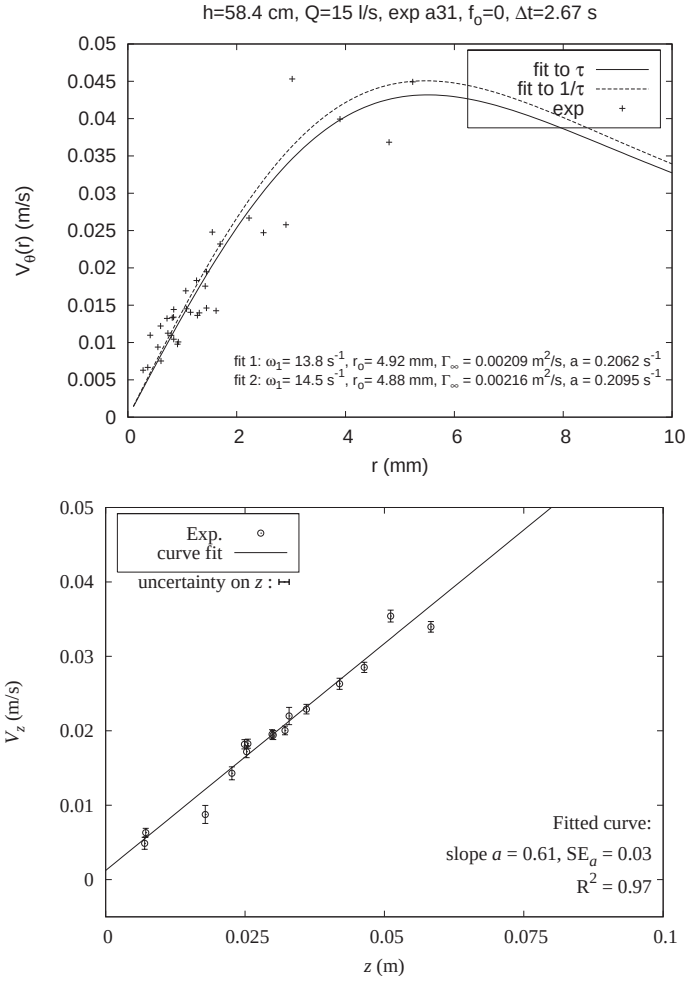

FIGURE C.16: Case 7, Film segment 1: PTV data for $V_\theta(r), V_z(z)$ with curve fits. No free surface profile is shown since the observed and measured depressions are negligible.

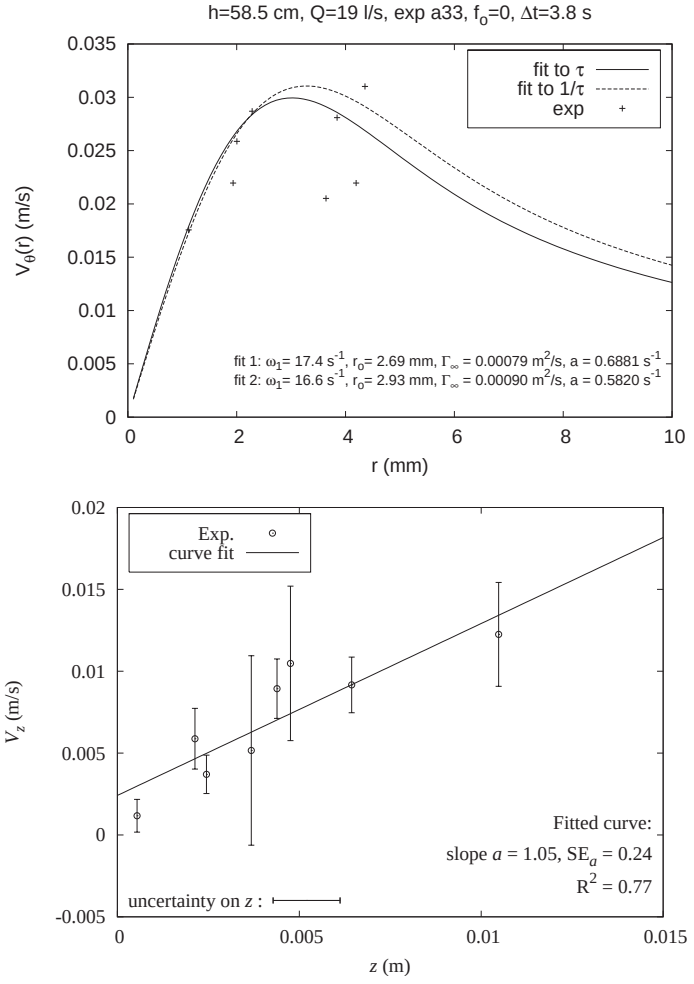

FIGURE C.17: Case 8, Film segment 1: PTV data for $V_\theta(r), V_z(z)$ with curve fits. No free surface profile is shown since the observed and measured depressions are negligible.

Appendix D

Results of ADV Measurements

A brief analysis of the uncertainty in the ADV measurements is presented, followed by the tabulated results of the measurements.

D.1 Uncertainty analysis

The signal-to-noise ratio was above 7 for all the measurements points except for 9 isolated points (3% of the points), 6 of which are at the free surface or at the channel bed or wall. The auto-correlation is above 0.7 for all the measurement points except a very small number of isolated measurement points which had autocorrelation values falling to 40 to 60% over portions of the measurement sample. The measured mean velocities at these low correlation measurement locations do not deviate significantly from those obtained at the neighboring measurement locations. These signal-to-noise and autocorrelation values should allow mean velocities to be measured with an accuracy of $\pm 10\%$ according to experiments conducted in channel flow by Rusello *et al.* (2006), where measurements with the same Sontek MicroAdV model at similar velocities were compared to PIV measurements.

The relative vertical distance between the measurement points is accurate to within 1 mm but the exact distance from the free surface or bed might be inaccurate by up to 5mm due to uncertainty about the exact distance from the probe to the measurement volume, slight changes in the water level, and mounting of the ADV. The span-wise coordinates of the measurement points might be off by up 5mm closer to the bed if the ruler is not perfectly vertical. These uncertainties would not have a significant impact on the measured velocities since the velocity gradients are relatively small over the measured distances

Tests were performed at the X=-0.055m measurement axis to examine the impact of uncertainty regarding the exact horizontal location of the ADV. When the horizontal location of the ADV was displaced by 1 cm upstream, the vertical gradient of the velocity magnitude near the free surface varied by 12%, and the magnitude of velocity 10cm below the free surface varied by 15% from the value measured at the 'correct' location. When the ADV was displaced by 0.5cm in the spanwise direction, the peak velocities varied by less than 1%. This provides an upper limit on the error that might have been generated by inaccuracy in the location of the ADV measurement axis.

D.2 Compiled data

The tabulated ADV measurement data appears on the following pages. The data from the measurements taken at $X = -0.055m$ are given first, followed by the data from the measurements at $X = -0.2m$.

	Y=0 (cm/s)					standard deviation (cm/s)		
Z (cm)	file	U_Z	U_X	U_Y	SNR	uz	ux	uy
33.4	**52	-4.725	7.898	-0.875	10.53	0.25	0.25	0.087
30.4	53	-6.736	11.692	-0.303	10.58	0.47	0.43	0.143
27.4	54	-5.646	17.839	-1.089	10.60	0.47	0.47	0.15
25.4	55	-2.782	21.054	-1.193	10.63	0.48	0.46	0.173
23.4	56	0.368	21.931	-1.319	10.60	0.51	0.48	0.126
20.4	57	5.695	20.065	-0.788	10.30	0.46	0.48	0.167
17.4	58	9.381	14.312	-0.014	8.05	0.61	0.62	0.627
14.4	59	9.176	7.899	0.547	7.29	1.05	1.01	1.16
11.4	60	7.059	4.327	0.516	7.64	0.80	0.84	0.547
8.4	61	4.547	3.010	0.100	8.34	0.70	0.79	0.631
5.4	62	2.289	2.893	-0.178	8.33	0.70	0.73	0.52
2.4	**63	0.741	2.767	-0.341	7.83	0.44	0.43	0.499
	(Range +/ - 30cm/s **=+/- 10cm/s							

FIGURE D.1: Case 1, $X = -0.055$m. $Y = 0$.

	Y=0 (cm/s)					standard deviation (cm/s)		
Z (cm)	file	U_Z	U_X	U_Y	SNR	uz	ux	uy
33.5	*2	-7.645	11.353	-1.330	8.63	0.77	0.63	0.799
30.5	*3	-11.583	16.648	-0.182	8.40	0.81	0.65	0.438
27.5	*4	-8.229	26.202	-0.275	8.48	0.60	0.57	0.337
25.5	5	-4.543	30.898	-0.188	4.46	1.12	1.10	0.328
23.5	6	0.067	32.851	-0.926	8.48	1.16	1.15	0.281
20.5	7	8.002	30.592	-1.201	8.70	1.02	1.02	0.331
17.5	*8	12.833	22.227	-0.157	9.28	0.58	0.61	0.342
14.5	*9	12.638	13.084	0.094	7.97	0.65	0.71	0.43
11.5	*10	10.439	6.264	0.650	6.74	1.03	1.26	1.11
8.5	*11	8.053	3.536	0.244	7.67	0.85	1.01	1.304
5.5	**12	4.714	3.789	-0.692	7.86	0.79	0.89	1.07
2.5	**13	1.445	4.282	-0.182	7.40	0.88	0.88	1.241
	(Range +/ - 100cm/s *+/- 30cm/s **+/-10cm/s							

FIGURE D.2: Case 2, $X = -0.055$m. $Y = 0$.

	Y=0					standard deviation		
	(cm/s)					(cm/s)		
Z (cm)	file	U_Z	U_X	U_Y	SNR	uz	ux	**uy**
33.2	52	-9.092	18.630	-3.110	10.70	2.5		
30.2	53	-18.077	25.740	-3.227	10.35	2.3		
27.2	54	-18.545	40.003	-2.635	10.00	2.97		
25.2	55	-10.143	47.421	-3.168	9.52	2.6		
23.2	56	-1.142	50.490	-2.830	9.64	1.54		
20.2	57	11.858	46.185	-2.086	11.20	1.46		
17.2	58	19.520	33.590	-0.845	12.61	1.151		
14.2	59	18.388	20.485	-0.172	14.40	0.931		
11.2	60	13.841	12.805	0.041	15.26	0.863		
8.2	61	9.587	8.587	0.096	15.23	1.173		
5.2	62	6.853	5.260	0.981	14.87	2.007		
2.2	63	4.725	7.132	0.974	14.85	2.152		

FIGURE D.3: Case 3, $X = -0.055$m. $Y = 0$.

	Y=0					stdev
	(cm/s)					(cm/s)
Z (cm)	file	U_Z	U_X	U_Y	SNR	uz
42.9	61	-4.995	11.699	-3.420	7.80	1.336
39.9	62	-9.069	16.616	-2.830	7.83	2.08
36.9	63	-6.547	24.888	-2.741	8.03	1.056
34.9	64	-2.760	28.667	-3.467	8.00	1.09
32.9	65	1.953	30.148	-3.379	8.02	1.064
29.9	66	9.101	27.307	-2.432	8.00	1.037
26.9	67	13.028	19.634	-1.040	8.00	1.007
23.9	68	12.349	11.516	-0.390	7.68	1.049
20.9	70*	9.520	6.732	-0.023	7.69	0.678
17.9	71*	7.012	3.730	0.744	7.09	0.841
14.9	72*	4.729	3.135	0.589	7.41	0.807
12.9	73**	3.586	2.565	-0.257	7.44	0.716
8.9	74**	2.143	2.385	-0.161	6.89	0.676
6.9	75**	1.043	2.741	-1.643	7.38	0.828
4.9	76**	0.075	1.924	-1.028	7.17	0.632

FIGURE D.4: Case 4, $X = -0.055$m. $Y = 0$.

	Y=0				
	(cm/s)				
Z (cm)	file	U_Z	U_X	U_Y	SNR
42.9	37	-12.600	23.102	-1.960	14.34
39.9	38	-23.800	33.000	-2.890	14.00
36.9	39	-27.600	51.220	0.480	13.60
35.9	40	-23.240	57.550	2.190	13.30
32.9	41	-2.066	67.000	4.730	13.00
29.9	42	17.366	60.130	4.550	13.78
26.9	43	26.770	42.400	4.300	14.96
23.9	44	25.710	24.720	2.930	16.76
20.9	45	20.040	14.840	2.150	17.10
17.9	46	14.760	9.590	1.766	17.58
14.9	47	10.970	5.640	1.200	17.78
11.9	48	7.590	4.300	1.610	17.40
8.9	49	4.930	4.087	0.557	17.90
5.9	50	3.690	3.620	-0.375	17.86
2.9	51	1.325	3.832	-0.804	17.44

FIGURE D.5: Case 5, $X = -0.055$m. $Y = 0$.

	Y=0 (cm/s)					standard deviation (cm/s)		
Z (cm)	file	U_Z	U_X	U_Y	SNR	uz	ux	uy
54.5	**77**	**-4.921**	**11.522**	**-1.787**	**11.90**	**0.73**	**0.70**	**0.216**
51.5	**78**	**-7.127**	**15.985**	**-2.128**	**12.10**	**0.74**	**0.71**	**0.184**
48.5	**79**	**-6.350**	**22.950**	**-2.435**	**12.06**	**0.73**	**0.73**	**0.237**
46.5	**80**	**-3.114**	**26.707**	**-2.012**	**12.20**	**0.79**	**0.75**	**0.227**
44.5	**81**	**1.315**	**28.181**	**-1.886**	**12.13**	**0.77**	**0.73**	**0.166**
41.5	**82**	**7.447**	**25.930**	**-0.942**	**12.02**	**0.73**	**0.75**	**0.22**
38.5	**83**	**11.583**	**19.133**	**0.143**	**11.77**	**0.77**	**0.75**	**0.305**
35.5	**85***	**11.330**	**11.949**	**0.276**	**11.07**	**0.48**	**0.49**	**0.37**
32.5	**86***	**9.218**	**7.207**	**0.430**	**9.60**	**0.62**	**0.77**	**0.565**
29.5	**87***	**7.016**	**4.685**	**0.069**	**9.43**	**0.78**	**1.16**	**0.737**
26.5	**88***	**5.113**	**3.225**	**0.237**	**8.86**	**0.68**	**0.69**	**0.58**
23.5	**89****	**3.892**	**2.297**	**-0.632**	**9.17**	**0.51**	**0.65**	**0.749**
20.5	**90****	**3.136**	**1.138**	**-0.453**	**9.88**	**0.49**	**0.76**	**0.975**
17.5	**91****	**1.578**	**1.669**	**-1.476**	**10.04**	**0.76**	**0.78**	**0.984**
14.5	**92****	**0.780**	**1.316**	**-0.543**	**9.88**	**0.56**	**0.66**	**0.928**
11.5	**93*****	**0.706**	**1.285**	**-0.793**	**9.77**	**0.41**	**0.56**	**0.817**
8.5	**94*****	**0.427**	**1.251**	**0.138**	**10.04**	**0.81**	**0.47**	**1.065**
5.5	**95*****	**-0.010**	**1.372**	**-0.128**	**10.02**	**0.60**	**0.38**	**0.63**
3.5	**96*****	**-0.056**	**1.134**	**0.469**	**9.60**	**0.68**	**0.34**	**0.967**
2.5	**97*****	**-0.226**	**1.156**	**-0.491**	**10.23**	**0.49**	**0.45**	**0.954**

FIGURE D.6: Case 6, $X = -0.055$m. $Y = 0$.

	Y=0 (cm/s)					standard deviation (cm/s)		
Z (cm)	file	U_Z	U_X	U_Y	SNR	uz	ux	uy
54.9	2	-8.504	17.595	-3.453	13.30	1.60	1.30	2.04
51.9	3	-14.177	24.397	-4.234	13.00	1.44	1.28	1.779
48.9	4	-13.900	36.226	-3.264	12.96	2.19	1.41	2.27
46.9	5	-7.135	42.662	-3.421	12.96	0.94	1.03	0.476
44.9	7	-0.281	45.166	-2.905	12.80	0.86	0.79	0.359
41.9	8	10.847	42.303	-1.443	12.78	0.79	0.82	0.676
38.9	9	18.524	31.520	0.001	12.86	0.79	0.79	0.449
35.9	10	18.661	19.535	0.243	13.10	0.81	0.84	0.543
32.9	11	14.920	12.095	1.009	12.87	0.97	1.05	1.308
29.9	12	11.471	7.528	0.710	12.36	1.19	1.82	1.556
26.9	13*	8.621	5.000	0.807	11.73	0.97	1.58	1.12
23.9	14*	6.331	3.510	0.656	11.64	0.85	1.42	1.562
20.9	15**	4.581	2.797	-0.053	11.84	0.56	1.29	0.911
17.9	16**	3.484	1.363	-0.096	11.49	1.01	1.57	1.411
14.9	17**	2.569	2.208	-0.939	12.40	0.59	0.97	0.786
11.9	18**	1.524	1.626	-0.693	11.89	0.69	0.84	1.394
8.9	19**	0.082	1.207	-1.501	12.24	0.99	1.41	1.233
5.9	20***	0.496	0.972	1.480	11.40	0.74	0.77	1.1
3.9	21***	-0.222	0.433	-0.205	11.10	0.70	0.84	0.936
2.9	22***	-0.303	1.424	-0.712	11.55	0.89	0.94	0.94

FIGURE D.7: Case 7, $X = -0.055$m. $Y = 0$.

	Y=0 (cm/s)					standard deviation (cm/s)		
Z (cm)	file	U_Z	U_X	U_Y	SNR	uz	ux	uy
54.8	79	-13.820	23.192	-4.387	9.34	2.36	2.35	3.768
51.8	83	-20.819	34.434	-5.241	9.05	3.01	2.23	3.353
48.8	84	-25.251	51.670	-5.420	8.06	4.01	2.32	4.796
46.8	85	-19.431	61.674	3.110	8.08	4.85	2.08	4.104
44.8	86	-3.145	65.661	2.167	7.48	3.85	1.58	2.845
41.8	87	16.530	59.086	0.670	7.31	1.80	1.33	1.306
38.8	88	26.796	41.945	0.301	8.00	1.86	1.39	1.539
35.8	89	26.042	24.887	1.150	10.57	1.22	1.20	1.01
32.8	90	20.415	14.747	0.981	11.02	1.11	1.09	0.712
29.8	91	15.498	9.592	0.997	12.25	1.14	1.31	1.062
26.8	92*	11.607	6.582	0.555	12.61	0.69	1.08	0.74
23.8	93*	8.855	4.819	0.394	13.14	0.89	1.26	1.186
20.8	94*	6.549	4.157	0.051	13.62	0.79	1.24	0.862
17.8	95**	4.850	3.665	-0.578	13.75	0.70	1.29	0.975
14.8	96**	3.618	2.801	-1.112	13.66	0.94	1.24	1.348
11.8	97**	2.061	2.682	-2.027	13.99	0.91	1.39	1.453
8.8	98**	1.086	1.620	-1.564	13.20	1.00	1.62	1.606
5.8	99**	0.440	0.481	-0.671	13.36	1.19	1.06	1.55
3.8	100**	-0.188	0.526	-0.710	14.15	1.31	1.32	1.425
2.8	101**	-0.102	0.330	0.051	13.22	1.31	1.50	1.29

FIGURE D.8: Case 8, $X = -0.055$m. $Y = 0$.

	D1						D2						D3					
	distance au mur:	4cm				Ux stdev	distance à l'axe:	25cm				Ux stdev	distance à l'axe:	10cm				Ux stdev
Z (cm)	file	U_Z	-U_X	-U_Y	SNR	std2	file	U_Z	-U_X	-U_Y	SNR	std2	file	U_Z	-U_X	-U_Y	SNR	std2
32.4	**21**	0.173	0.268	0.054	**10.540**	0.24	25	-0.238	-1.289	0.808	10.600	0.41	30	-0.265	-2.851	0.945	10.65	0.20
25.4	**22**	0.160	-0.012	0.064	**10.100**	0.24	26	-0.006	-1.917	0.886	10.600	0.19	31	-0.086	-3.179	0.931	10.6	0.23
14.4	23	0.186	0.228	0.058	**10.400**	0.36	27	-0.058	-1.982	0.754	10.200	0.19	32	0.369	-2.984	0.702	10.3	0.22
2.4	24	0.008	0.810	0.238	**9.620**	0.25	28	-0.014	-1.054	0.958	9.830	0.39	33	-0.012	-1.159	1.245	9	0.30
		(Range + ou - 3cm/s)						(Range + ou - 3cm/s)						(Range + ou - 10cm/s)				
		*pris sens inverse						*pris sens inverse						*pris sens inverse				

	Axe						G3						G2					
	distance à l'axe:	0cm				Ux stdev	distance à l'axe:	10cm				Ux stdev	distance à l'axe:	25cm				Ux stdev
Z (cm)	file	U_Z	-U_X	-U_Y	SNR	std2	file	U_Z	U_X	U_Y	SNR	std2	file	U_Z	U_X	U_Y	SNR	std2
32.4	34	-0.497	-3.375	0.003	**10.550**	0.20	48	-0.156	3.029	0.970	10.270	0.22	**44**	0.098	1.599	0.961	10.49	0.21
25.4	35	-0.137	-3.805	-0.045	**10.680**	0.19	49	0.016	3.318	1.029	10.530	0.26	45	0.160	2.021	0.884	10.4	0.21
14.4	36	0.618	-3.434	-0.015	**10.200**	0.20	50	0.544	3.106	0.739	10.200	0.22	46	-0.037	1.955	0.795	10.19	0.21
2.4	37	0.211	-1.658	-0.360	**4.800**	0.48	51	0.849	0.664	1.925	9.780	0.33	47	-0.074	0.690	1.102	9.5	0.33
		(Range + ou - 10cm/s)						(Range + ou - 3cm/s)						(Range + ou - 3cm/s)				
		*pris sens inverse																

	G1					
	distance au mur:	4cm				Ux stdev
Z (cm)	file	U_Z	U_X	U_Y	SNR	std2
32.4	40	-0.020	-0.386	0.177	**10.220**	0.23
25.4	41	0.048	-0.141	-0.089	**11.230**	0.20
14.4	42	-0.178	-0.019	0.046	**10.400**	0.28
2.4	43	0.045	-0.559	-0.105	**9.800**	0.33
		(Range + ou - 3cm/s)				

Location of measurement axes

D1 :	Y= -0.46 m
D2 :	Y= -0.25 m
D3 :	Y= -0.1 m
Axe:	Y= 0
G3 :	Y= 0.1 m
G2 :	Y= 0.25 m
G1 :	Y=0.46 m

Case1 X = -0.2 m

	D1					D2					D3				
	distance au mur:	4cm				distance à l'axe:	25cm				distance à l'axe:	10cm			
Z (cm)	file	U_Z	-U_X	-U_Y	SNR	file	U_Z	-U_X	-U_Y	SNR	file	U_Z	-U_X	-U_Y	SNR
32.4	**26**	0.667	1.073	0.335	14.42	30	-0.386	-0.728	1.896	14.13	34	-0.209	-3.659	1.686	14.13
25.4	**27**	0.480	-0.218	-0.089	14.15	31	-0.399	-2.421	1.286	14.05	35	-0.393	-4.110	1.636	14.06
14.4	28	0.213	-0.706	-0.030	13.80	32	-0.063	-2.899	1.116	14.40	36	0.268	-4.224	1.303	14.13
2.4	29	-0.300	-0.680	0.253	13.50	33	-0.058	-2.114	1.071	13.30	37	0.009	-2.798	1.096	11.30
		(Range + ou - 10cm/s)					(Range + ou - 30cm/s)					(Range + ou - 30cm/s)			
		*pris sens inverse					*pris sens inverse					*pris sens inverse			
	essai-1					essai-1					essai-1				

	Axe					G3					G2				
	distance à l'axe:	0cm				distance à l'axe:	10cm				distance à l'axe:	25cm			
Z (cm)	file	U_Z	-U_X	-U_Y	SNR	file	U_Z	-U_X	-U_Y	SNR	file	U_Z	-U_X	-U_Y	SNR
32.4	38	-0.905	-4.641	0.238	14.40	22	-0.206	3.950	1.704	15.20	17	-0.188	1.022	1.824	15.22
25.4	39	-0.466	-5.367	0.185	14.05	23	0.030	4.636	1.776	15.06	18	-0.194	2.306	1.399	15.08
14.4	40	0.441	-5.050	0.216	13.90	24	0.859	4.419	1.379	15.15	19	0.230	2.740	1.066	15.20
2.4	41	0.251	-3.105	-0.017	11.01	25	0.525	3.688	0.947	14.01	20	0.197	2.472	0.954	13.70
		(Range + ou - 30cm/s)					(Range + ou - 10cm/s)					(Range + ou - 10cm/s)			
		*pris sens inverse													
	essai-1					essai-1					essai-1				

	G1				
	distance au mur:	4cm			
Z (cm)	file	U_Z	-U_X	-U_Y	SNR
32.4	13	0.553	-0.787	0.481	14.96
25.4	14	-0.124	0.190	-0.084	24.51
14.4	15	0.440	0.899	-0.049	15.31
2.4	16	-0.001	1.077	0.099	15.00
		(Range + ou - 10cm/s)			
	essai-1				

Location of measurement axes

D1 :	Y= -0.46 m
D2 :	Y= -0.25 m
D3 :	Y= -0.1 m
Axe:	Y= 0
G3 :	Y= 0.1 m
G2 :	Y= 0.25 m
G1 :	Y=0.46 m

Case 2 X=-0.2 m

profil		D1					D2					D3				
		distance au mur:	4cm				distance à l'axe:	25cm				distance à l'axe:	10cm			
niveau	Z (cm)	file	U_Z	-U_X	-U_Y	**SNR**	#fich.	U_Z	-U_X	-U_Y	SNR	#fich.	U_Z	-U_X	-U_Y	SNR
40	**32.4**	**36**	1.313	3.147	0.822	12.90	40	0.501	0.855	4.803	11.40	44	-1.966	-2.825	4.657	10.30
110	**25.4**	**37**	1.316	-0.516	0.829	11.30	41	1.952	-4.628	2.315	10.87	45	-2.246	-6.334	3.036	9.89
220	**14.4**	38	1.121	-3.185	0.511	12.80	42	0.399	-4.495	1.702	11.44	46	0.133	-7.039	2.347	12.40
350	**1.4**	39	0.088	-3.288	0.111	15.60	43	0.010	-5.519	1.241	15.59	47	0.170	-6.906	1.373	15.60
			(Range + ou - 10cm/s)					(Range + ou - 30cm/s)					(Range + ou - 30cm/s)			
			*pris sens inverse					*pris sens inverse					*pris sens inverse			

profil		Axe					G3					G2				
		distance à l'axe:	0cm				distance à l'axe:	10cm				distance à l'axe:	25cm			
niveau	Z (cm)	#fich.	U_Z	-U_X	-U_Y	SNR	#fich.	U_Z	U_X	U_Y	SNR	#fich.	U_Z	U_X	U_Y	SNR
40	**32.4**	48	-1.625	-5.907	0.567	9.42	30	-0.836	4.137	3.677	9.78	26	0.292	-1.034	5.177	10.50
110	**25.4**	49	-1.622	-7.725	0.148	10.30	31	-1.780	6.538	2.428	10.13	27	1.441	4.923	1.229	10.30
220	**14.4**	50	0.144	-8.245	0.385	12.36	33*	0.743	7.154	1.685	13.00	28	0.737	4.334	1.620	11.80
350	**1.4**	51	0.093	-7.312	0.031	15.20	34*	0.514	6.778	1.053	15.62	29	0.444	5.378	1.023	14.48
			(Range + ou - 30cm/s)					(Range + ou - 10cm/s)					(Range + ou - 10cm/s)			
			*pris sens inverse					**+/-30cm/s								

profil		G1				
		distance au mur:	4cm			
niveau	Z (cm)	#fich.	U_Z	U_X	U_Y	SNR
40	**32.4**	22	1.082	-1.958	0.858	12.00
110	**25.4**	23	0.681	0.933	0.669	10.90
220	**14.4**	24	0.947	2.699	0.435	11.60
350	**1.4**	25	0.410	3.510	0.091	14.30
			(Range + ou - 10cm/s)			

Case3 X = -0.2 m

Location of measurement axes

D1 :	Y= -0.46 m
D2 :	Y= -0.25 m
D3 :	Y= -0.1 m
Axe:	Y= 0
G3 :	Y= 0.1 m
G2 :	Y= 0.25 m
G1 :	Y=0.46 m

	D1						D2						D3					
	distance au mur:	4cm				Ux stdev	distance à l'axe:	25cm				Ux stdev	distance à l'axe:	10cm				Ux stdev
Z (cm)	file	U_Z	-U_X	-U_Y	**SNR**	std2	file	U_Z	-U_X	-U_Y	SNR	std2	file	U_Z	-U_X	-U_Y	SNR	std2
43.3	**26**	0.021	-0.379	-0.199	8.18	0.51	31	-0.781	-0.286	1.785	7.87	0.66	36	-0.298	-3.232	1.737	8.20	0.318
36.3	**27**	0.433	-0.287	0.198	7.39	0.59	32	-0.715	-1.911	1.228	8.00	0.50	37	-0.140	-3.641	1.614	8.18	0.248
25.3	28	0.499	-0.391	0.161	7.81	0.66	33	0.198	-2.278	1.010	8.03	0.30	38	0.489	-3.529	8.300	8.31	0.26
12.3	29	0.214	-0.018	0.244	7.73	0.81	34	0.393	-2.597	0.527	8.49	0.37	39	0.715	-2.978	0.525	8.62	0.359
3.3	30	-0.170	0.059	0.256	7.50	0.55	35	-0.017	-1.353	0.714	7.70	0.55	40	0.045	-1.310	0.609	6.69	0.513
		(Range + ou - 10cm/s)						(Range + ou - 10cm/s)						(Range + ou - 10cm/s)				
		*pris sens inverse						*pris sens inverse						*pris sens inverse				
	essai-1						essai-1						essai-1					

	Axe						G3						G2					
	distance à l'axe:	0cm				Ux stdev	distance à l'axe:	10cm				Ux stdev	distance à l'axe:	25cm				Ux stdev
Z (cm)	file	U_Z	-U_X	-U_Y	**SNR**	std2	file	U_Z	U_X	U_Y	SNR	std2	file	U_Z	U_X	U_Y	SNR	std2
43.3	41	-0.541	-4.446	0.151	8.50	0.27	56	-0.042	3.700	1.748	7.90	0.28	51	0.131	1.671	1.355	7.65	0.314
36.3	42	-0.229	-4.879	0.213	8.40	0.24	57	0.246	4.139	1.731	7.63	0.26	52	0.183	1.966	1.212	7.59	0.287
25.3	43	0.917	-4.299	0.137	8.11	0.29	58	1.140	3.720	1.383	7.88	0.24	53	0.363	2.043	0.928	8.00	0.253
12.3	44	1.040	-2.968	0.075	8.14	0.30	59	1.213	2.667	0.442	7.55	0.37	54	0.469	2.136	0.528	7.25	0.336
3.3	45	0.308	-0.221	-0.580	5.60	0.40	60	0.191	0.832	0.918	6.33	0.56	55	0.096	0.275	0.926	7.20	0.552
		(Range + ou - 30cm/s)						(Range + ou - 10cm/s)						(Range + ou - 10cm/s)				
		*pris sens inverse																
	essai-1						essai-1						essai-1					

	G1					
	distance au mur:	4cm				Ux stdev
	file	U_Z	U_X	U_Y	**SNR**	std2
43.3	46	0.285	-0.233	0.305	7.50	0.41
36.3	47	-0.093	0.505	-0.074	7.30	0.41
25.3	48	0.225	0.387	0.005	8.36	0.39
12.3	49	0.369	0.641	0.048	7.70	0.64
3.3	50	-0.065	-0.718	-2.400	7.63	0.31
		(Range + ou - 10cm/s)				
	essai-1					

Case 4 X = -0.2 m

Location of measurement axes

D1 :	Y= -0.46 m
D2 :	Y= -0.25 m
D3 :	Y= -0.1 m
Axe:	Y= 0
G3 :	Y= 0.1 m
G2 :	Y= 0.25 m
G1 :	Y=0.46 m

	D1					D2					D3				
	distance au mur:	4cm				distance à l'axe:	25cm				distance à l'axe:	10cm			
Z (cm)	file	U_Z	-U_X	-U_Y	**SNR**	#fich.	U_Z	-U_X	-U_Y	SNR	#fich.	U_Z	-U_X	-U_Y	SNR
43.1	2	1.511	3.244	0.946	18.00	7	0.795	0.434	4.949	16.23	12	-1.435	-2.653	9.100	15.05
36.1	3	2.440	1.070	1.310	17.00	8	1.600	-3.500	3.810	15.24	13	1.515	-10.280	2.700	14.70
25.1	4	2.123	-2.355	0.722	17.50	9	1.655	-4.826	2.184	16.60	14	1.790	-7.857	2.679	14.86
12.1	5	1.390	-3.157	0.676	19.20	10	1.257	-5.945	1.201	18.70	15	2.047	-6.623	1.382	18.06
3.1	6	0.100	-0.625	0.566	18.67	11	0.820	-5.860	1.150	19.70	16	0.982	-5.720	0.948	18.74
		(Range + ou - 10cm/s)					(Range + ou - 10cm/s)					(Range + ou - 30cm/s)			
		*pris sens inverse					*pris sens inverse								

	Axe					G3					G2				
	distance à l'axe:	0cm				distance à l'axe:	10cm				distance à l'axe:	25cm			
Z (cm)	#fich.	U_Z	-U_X	-U_Y	SNR	#fich.	U_Z	U_X	U_Y	SNR	#fich.	U_Z	U_X	U_Y	SNR
43.1	17	-1.910	-7.440	1.550	14.10	32	-3.660	3.420	5.600	14.06	27	0.367	0.242	5.094	14.60
36.1	18	-2.613	-9.975	0.075	14.00	33	-2.280	7.900	3.300	14.32	28	1.978	4.318	2.593	13.86
25.1	19	1.400	-9.836	0.179	15.40	34	1.456	7.810	2.240	14.75	29	1.569	4.158	1.687	14.80
12.1	20	2.425	-7.132	0.178	17.70	35	2.500	6.410	1.020	17.60	30	1.663	5.121	0.941	17.29
3.1	21	1.171	-5.560	0.171	18.30		xx	xx	xx	14.34	31	1.240	4.300	0.720	18.20
		(Range + ou - 30cm/s)					(Range + ou - 10cm/s)					(Range + ou - 10cm/s)			

	G1				
	distance au mur:	4cm			
Z (cm)	#fich.	U_Z	U_X	U_Y	SNR
43.1	22	1.150	-2.148	1.056	14.59
36.1	23	1.273	0.416	0.679	13.87
25.1	24	1.773	2.541	0.249	14.24
12.1	25	1.689	2.914	0.200	16.60
3.1	26	0.105	0.192	0.048	16.00
		(Range + ou - 10cm/s)			

Case 5 X = -0.2 m

Location of measurement axes

D1 :	Y= -0.46 m
D2 :	Y= -0.25 m
D3 :	Y= -0.1 m
Axe:	Y= 0
G3 :	Y= 0.1 m
G2 :	Y= 0.25 m
G1 :	Y=0.46 m

	D1						D2								D3					
	distance au mur:	4cm			Ux stdev		distance à l'axe:	25cm			Uz stdev	Ux stdev	Uy stdev		distance à l'axe:	10cm			Uz stdev	Ux stdev	Uy stdev
Z (cm)	file	U_Z	-U_X	-U_Y	SNR	cm/s	file	U_Z	-U_X	-U_Y	SNR	cm/s	cm/s	cm/s	file	U_Z	-U_X	-U_Y	SNR	cm/s	cm/s	cm/s
54.6	**34**	0.508	0.495	0.004	12.53	0.45	40	-0.568	-0.819	1.453	12.20	0.59	0.51	0.41	46	-0.181	-3.159	1.654	12.77	0.17	0.17	**0.167**
47.6	**35**	0.147	-0.893	-0.328	12.75	0.47	41	-0.205	-1.808	1.303	12.72	0.36	0.30	0.13	47	0.047	-3.422	1.625	12.56	0.19	0.17	**0.057**
36.6	36*	**0.229**	**-0.401**	**0.16**	**12.755**	**0.316**	42	0.324	-1.912	0.938	12.85	0.29	0.20	0.06	48	0.921	-3.341	1.204	12.64	0.18	0.18	**0.059**
23.6	37	0.431	-1.154	-0.042	12.53	0.41	43	0.673	-2.093	0.505	12.74	0.31	0.22	0.08	49	1.108	-2.638	0.467	12.26	0.18	0.18	**0.08**
14.6	38	0.300	-1.022	-0.045	12.00	0.31	44	0.589	-2.234	0.331	11.99	0.25	0.33	0.21	50	0.687	-1.874	0.202	9.76	0.31	0.40	**0.21**
7.6	39	0.378	1.072	-0.140	11.70	0.43	45	0.137	-0.005	0.438	10.88	0.32	0.34	0.27	51	0.020	-0.153	0.470	10.30	0.31	0.36	**0.254**
		(Range + ou - 10cm/s)						(Range + ou - 10cm/s)								(Range + ou - 10cm/s)						

	Axe						G3								G2							
	distance à l'axe:	0cm			Ux stdev		distance à l'axe:	10cm			Uz stdev	Ux stdev	Uy stdev		distance à l'axe:	25cm			Uz stdev	Ux stdev	Uy stdev
Z (cm)	file	U_Z	-U_X	-U_Y	SNR	cm/s	file	U_Z	-U_X	-U_Y	SNR	cm/s	cm/s	cm/s	file	U_Z	-U_X	-U_Y	SNR	cm/s	cm/s	cm/s
54.6	52	-0.373	-4.275	0.218	12.78	0.23	71	-0.063	3.634	1.529	11.85	0.19	0.19	0.05	65	0.095	1.436	1.518	11.36	0.28	0.35	**0.11**
47.6	53	0.099	-4.682	0.142	12.86	0.25	72	0.311	3.926	1.519	11.50	0.23	0.23	0.05	66	0.074	1.860	1.223	11.70	0.27	0.20	**0.083**
36.6	54	1.300	-4.108	0.110	12.52	0.16	73	1.211	3.481	1.259	11.72	0.19	0.17	0.05	67	0.464	1.880	0.869	11.69	0.25	0.23	**0.059**
23.6	55	1.530	-2.407	0.010	11.36	0.39	74	1.554	2.093	0.373	10.56	0.22	0.25	0.10	68	0.694	1.620	0.360	11.30	0.32	0.29	**0.216**
14.6	56*	1.519	-0.464	0.709	9.80	0.83	75	0.868	1.221	-0.502	9.47	0.44	0.60	0.51	69*	0.420	1.054	0.200	9.85	0.32	0.46	**0.241**
7.6	57	0.187	-0.278	0.645	5.40	0.68	76*	0.045	-0.486	-0.316	9.10	0.35	0.47	0.43	70	0.130	0.138	0.259	10.10	0.26	0.35	**0.183**
		(Range + ou - 30cm/s)						(Range + ou - 10cm/s)								(Range + ou - 10cm/s)						

	G1				
	distance au mur:	4cm			Ux stdev
Z (cm)	file	U_Z	U_X	U_Y	SNR	cm/s
54.6	59	-0.023	-0.415	0.150	11.93	0.34
47.6	60	-0.035	-0.045	-0.144	11.80	0.29
36.6	61	0.150	0.187	-0.030	11.70	0.22
23.6	62	0.046	0.554	0.010	12.20	0.24
14.6	63	0.023	0.534	0.149	10.90	0.35
7.6	64	-0.209	-0.282	0.235	12.35	0.26
		(Range + ou - 10cm/s)				

Location of measurement axes

D1 :	Y= -0.46 m
D2 :	Y= -0.25 m
D3 :	Y= -0.1 m
Axe:	Y= 0
G3 :	Y= 0.1 m
G2 :	Y= 0.25 m
G1 :	Y=0.46 m

Case6 X = -0.2 m

	D1								D2								D3							
	distance au mur:	4cm							distance à l'axe:	25cm				Uz stdev	Ux stdev	Uy stdev	distance à l'axe:	10cm				Uz stde	Ux stde	Uy stdev
Z (cm)	file	U_Z	-U_X	-U_Y	SNR	std1	std2	std3	file	U_Z	-U_X	-U_Y	SNR	cm/s	cm/s	cm/s	file	U_Z	-U_X	-U_Y	SNR	cm/s	cm/s	cm/s
54.9	41	1.081	1.583	0.473	10.67	0.81	0.99	0.42	47	0.630	0.109	4.039	10.07	0.92	0.91	0.62	53	-1.608	-3.636	4.653	9.94	1.05	1.16	1.129
47.9	42	1.488	-0.048	0.606	10.06	0.62	0.88	0.45	48	0.568	-2.597	2.382	9.80	0.50	0.38	0.25	54	-1.266	-5.936	2.557	9.88	0.79	0.46	0.403
36.9	43	1.933	-1.077	0.637	10.64	0.522	0.548	0.384	49	1.183	-3.044	1.590	10.30	0.34	0.37	0.21	55	1.379	-5.531	1.951	9.83	0.32	0.30	0.249
23.9	44*	1.640	-1.045	0.137	11.20	0.69	1.08	0.57	50	1.292	-3.036	0.887	10.95	0.33	0.34	0.23	56	1.909	-3.944	0.997	10.90	0.31	0.33	0.243
14.9	45	1.029	-0.297	-0.018	11.08	0.85	0.92	0.65	51	1.120	-3.562	0.532	12.50	0.34	0.39	0.22	57	1.347	-3.504	0.509	12.18	0.34	0.41	0.335
3.9	46	-0.197	0.802	-0.055	10.94	0.50	0.61	0.56	52	0.095	-1.201	0.469	11.60	0.46	0.87	0.51	58**	0.291	-0.786	0.927	11.72	0.49	1.06	0.544
		(Range + ou - 10cm/s)								(Range + ou - 10cm/s)								(Range + ou - 10cm/s)						

	Axe								G3								G2							
	distance à l'axe:	0cm				Uz stde	Ux stde	Uy stdev	distance à l'axe:	10cm				Uz stdev	Ux stdev	Uy stdev	distance à l'axe:	25cm				Uz stde	Ux stde	Uy stdev
Z (cm)	file	U_Z	-U_X	-U_Y	SNR	cm/s	cm/s	cm/s	file	U_Z	U_X	U_Y	SNR	cm/s	cm/s	cm/s	file	U_Z	U_X	U_Y	SNR	cm/s	cm/s	cm/s
54.9	59	-1.016	-6.595	0.366	9.94	0.32	0.28	0.16	35	-0.475	5.047	2.802	10.50	0.32	0.27	0.22	29	0.117	0.663	3.270	10.20	1.05	0.91	0.578
47.9	60	-0.583	-7.512	0.322	9.84	0.27	0.32	0.16	36	-0.377	6.020	2.645	10.44	0.30	0.25	0.20	30	0.305	2.920	1.906	10.20	0.45	0.34	0.232
36.9	61	1.834	-6.935	0.132	10.14	0.32	0.24	0.16	37	1.792	5.446	1.967	10.60	0.29	0.25	0.19	31	0.938	2.870	1.437	10.90	0.30	0.33	0.193
23.9	62	2.257	-4.165	0.046	10.74	0.31	0.34	0.25	38	2.223	3.668	0.805	11.65	0.27	0.29	0.13	32	1.321	2.927	0.666	11.35	0.34	0.34	0.178
14.9	**63	1.634	-3.158	0.071	11.22	0.32	0.40	0.21	39	1.633	2.887	0.268	11.94	0.31	0.45	0.23	33	0.922	2.595	0.322	11.74	0.34	0.50	0.358
3.9	64	0.008	-1.364	0.915	11.76	0.47	0.84	0.45	40	0.107	0.242	0.357	9.97	0.44	0.81	0.35	34	0.055	0.724	-0.018	11.24	0.42	0.36	0.375
		(Range + ou - 30cm/s)								(Range + ou - 10cm/s)								(Range + ou - 10cm/s)						

	G1						
	distance au mur:	4cm				Uz stde	Ux stde	Uy stdev
Z (cm)	#fich.	U_Z	U_X	U_Y	SNR	cm/s	cm/s	cm/s
54.9	23	0.741	-0.849	0.454	10.33	0.46	0.55	0.27
47.9	24	1.011	0.402	0.595	9.89	0.46	0.61	0.27
36.9	25	1.158	0.678	0.228	10.42	0.39	0.69	0.42
23.9	26	1.072	0.516	0.220	10.70	0.50	0.80	0.45
14.9	27	0.608	0.251	0.080	11.02	0.40	0.65	0.52
3.9	28	0.213	-0.492	-0.355	10.04	0.30	0.38	0.32
		(Range + ou - 10cm/s)						

Location of measurement axes

D1 :	Y= -0.46 m
D2 :	Y= -0.25 m
D3 :	Y= -0.1 m
Axe:	Y= 0
G3 :	Y= 0.1 m
G2 :	Y= 0.25 m
G1 :	Y=0.46 m

Case7 X = -0.2 m

D1										D2										D3									
distance au mur:		4cm								distance à l'axe:		25cm								distance à l'axe:		10cm							
Z (cm)	file	U_Z	-U_X	-U_Y	SNR	std1	std2	std3		file	U_Z	-U_X	-U_Y	SNR	Uz stdev	Ux stdev	Uy stdev			file	U_Z	-U_X	-U_Y	SNR	Uz stdev	Ux stdev	Uy stdev		
54.9	36	1.518	2.411	0.815	29.53	1.52	2.41	0.82		42	-0.198	0.438	5.502	10.58	3.91	4.49	1.68			48	0.191	-4.271	7.351	9.95	cm/s	cm/s	cm/s		
47.9	37	2.697	1.208	1.360	11.80	1.19	1.46	0.87		43	1.480	-3.177	3.706	8.95	1.15	0.90	0.64			49	1.865	-7.809	2.955	8.71	1.96	1.35	0.992		
36.9	38	2.646	-1.022	0.579	10.44	0.769	0.826	0.523		44	1.862	-3.442	1.995	8.76	0.46	0.55	0.37			50	2.063	-6.744	2.040	8.20	1.36	1.07	1.11		
23.9	39	2.610	-0.517	0.902	12.28	1.32	2.08	1.22		45	2.010	-4.349	1.168	12.20	0.40	0.70	0.41			51	2.659	-5.364	1.119	11.67	0.81	0.70	0.411		
14.9	40	1.492	-1.449	0.325	12.42	0.75	1.83	0.63		46	1.564	-4.471	0.713	12.58	0.48	0.66	0.504			52	2.001	-4.529	0.644	12.54	0.68	0.69	0.577		
3.9	41	-0.085	0.502	0.282	13.23	1.02	1.74	1.31		47	0.345	-3.265	0.686	15.00	0.57	1.22	0.72			53	0.538	-3.275	0.565	15.30	0.74	1.00	0.58		
		(Range + ou - 10cm/s)									(Range + ou - 10cm/s)										(Range +/-30								

G3										G2										G1									
Axe										distance à l'axe:		10cm								distance à l'axe:		25cm							
distance à l'axe:		0cm																											
Z (cm)	file	U_Z	-U_X	-U_Y	SNR	Uz stdev	Ux stdev	Uy stdev		file	U_Z	U_X	U_Y	SNR	Uz stdev	Ux stdev	Uy stdev			file	U_Z	U_X	U_Y	SNR	Uz stdev	Ux stdev	Uy stdev		
54.9	54	-3.593	-5.603	3.710	8.97	1.81	1.96	2.31		73	-1.554	3.991	6.798	8.17	1.28	1.10	0.92			67	0.363	0.630	4.654	8.55	1.00	1.07	0.697		
47.9	55	-4.827	-9.124	-0.493	8.89	1.88	1.31	1.54		74	-0.646	8.013	1.991	7.51	1.21	0.80	0.76			68	1.148	3.443	2.961	7.23	0.67	0.50	0.321		
36.9	56	2.181	-8.630	-0.052	8.01	0.71	0.60	0.39		75	1.974	6.840	2.400	7.96	0.78	0.68	0.39			69	1.586	4.123	1.843	8.45	0.42	0.52	0.38		
23.9	57*	2.985	-5.576	0.096	11.01	0.66	0.69	0.48		76	2.791	4.971	1.099	10.89	0.66	0.62	0.40			70	1.942	3.972	0.881	10.83	0.45	0.47	0.337		
14.9	58	2.313	-4.859	0.149	12.86	0.56	0.71	0.52		77	2.180	4.299	0.515	12.86	0.56	0.71	0.47			71	1.528	4.032	0.248	13.30	0.43	0.71	0.423		
3.9	59	0.193	-1.911	0.529	13.74	0.72	1.19	0.83		78	0.459	1.491	0.333	13.13	0.72	0.92	0.58			72	-0.136	0.700	-0.007	11.93	0.64	0.95	0.478		
		(Range + ou - 30cm/s)									(Range + ou - 30cm/s)										(Range + ou - 10cm/s)								

G1								
distance au mur:		4cm						
Z (cm)	#tch.	U_Z	U_X	U_Y	SNR	Uz stdev	Ux stdev	Uy stdev
54.9	60	0.884	-1.511	0.510	9.53	0.92	1.11	0.50
47.9	62	2.007	-0.216	0.707	9.80	0.94	1.06	0.54
36.9	63	2.047	-0.363	0.819	11.34	0.87	1.29	0.82
23.9	64	1.381	0.494	0.177	10.89	0.63	1.41	0.77
14.9	65	1.280	-0.628	0.244	11.30	1.05	1.11	0.72
3.9	66	0.395	-1.359	-0.622	11.78	0.63	0.78	0.56
		(Range + ou - 10cm/s)						

Case8 X = -0.2 m

Location of measurement axes

D1 :	Y= -0.46 m
D2 :	Y= -0.25 m
D3 :	Y= -0.1 m
Axe:	Y= 0
G3 :	Y= 0.1 m
G2 :	Y= 0.25 m
G1 :	Y=0.46 m

	G1						G2					
	distance au mur:	4cm					distance à l'axe:	25cm				
Z (cm)	file	U_Z	-U_X	-U_Y	**SNR**	std2	file	U_Z	-U_X	-U_Y	SNR	std2
32.4	1	**0.039**	**1.713**	**-0.042**	**11.31**	0.208	5	0.028	1.648	-0.054	11.07	0.19
25.4	2	**0.057**	**1.723**	**-0.042**	**11.08**	0.197	6	0.054	1.743	-0.047	11.10	0.20
14.4	3	**0.064**	**1.766**	**-0.031**	**12.06**	0.203	7	0.080	1.929	-0.064	11.62	0.19
2.4	4	**0.063**	**0.868**	**0.066**	**11.88**	0.128	8	0.069	2.013	-0.066	11.24	0.20
		(Range + ou - 3cm/s)						(Range + ou - 3cm/s)				
		*										
	essai-1						essai-1					

	D1						D2						Axe					
	distance au mur:	4cm					distance à l'axe:	25cm					distance à l'axe:	0cm				
Z (cm)	file	U_Z	-U_X	-U_Y	**SNR**	std2	file	U_Z	U_X	U_Y	SNR	std2	file	U_Z	U_X	U_Y	SNR	std2
32.4	9	-0.056	-1.547	-0.043	11.10	0.16	13	-0.064	-1.750	-0.051	11.44	0.22	17	-0.071	-1.714	-0.064	11.10	0.213
25.4	10	-0.059	-1.605	-0.050	11.20	0.23	14	-0.060	-1.788	-0.052	11.28	0.22	18	-0.057	-1.678	-0.075	11.28	0.193
14.4	11	-0.043	-1.792	-0.053	11.80	0.22	15	-0.042	-1.786	-0.051	11.90	0.23	19	-0.049	-1.674	-0.035	11.50	0.215
2.4	12	-0.110	-0.667	0.040	11.42	0.13	16	-0.034	-1.924	-0.056	10.64	0.21	20	-0.059	-1.555	-0.065	9.93	0.226
		(Range + ou - 3cm/s)						(Range + ou - 3cm/s)						(Range + ou - 3cm/s)				
		*pris sens inverse						*pris sens inverse										
	essai-1						essai-1						essai-1					

Location of measurement axes

D1 :	Y= -0.46 m
D2 :	Y= -0.25 m
Axe:	Y= 0
G2 :	Y= 0.25 m
G1 :	Y=0.46 m

Case 1 X = -2 m

	G1							G2						
	4cm							25cm						
Z (cm)	distance au mur:							distance à l'axe:						
	file	U_Z	-U_X	-U_Y	SNR	std1	std2	std3	file	U_Z	-U_X	-U_Y	SNR	std1	std2	std3
32.4	44	0.098	2.475	-0.045	6.56	0.391	0.359	0.073	48	0.048	2.331	-0.045	6.533	0.354	0.347	0.08
25.4	45	0.1	2.468	-0.039	8.3	0.365	0.328	0.073	49	0.075	2.576	-0.031	7.570	0.344	0.364	0.10
14.4	46	0.074	2.545	-0.042	10.2	0.307	0.311	0.068	50	0.060	2.859	-0.048	10.255	0.311	0.335	0.13
2.4	47	0.087	2.984	-0.031	11.56	0.292	0.358	0.089	51	0.058	3.162	-0.104	12.770	0.261	0.362	0.13
		(Range + ou - 10cm/s)								(Range + ou - 10cm/s)						
	essai-1								essai-1							

	D1							D2								Axe-droite							
	distance au mur:	4cm						distance à l'axe:	25cm							distance à l'axe:	0cm						
regle	file	U_Z	-U_X	-U_Y	SNR	std1	std2	std3	file	U_Z	-U_X	-U_Y	SNR	std1	std2	std3	file	U_Z	-U_X	-U_Y	SNR	std1	std2	std3
32.4	30	-0.099	-2.253	-0.049	6.82	0.344	0.339	0.07	36	-0.094	-2.496	-0.070	6.668	0.334	0.350	0.08	40	-0.103	-2.508	-0.083	6.940	0.337	0.357	0.08
25.4	31	-0.097	-2.272	-0.052	8.11	0.315	0.345	0.06	37	-0.099	-2.626	-0.065	8.635	0.329	0.366	0.09	41	-0.110	-2.400	-0.096	7.940	0.320	0.331	0.08
14.4	33	-0.094	-2.533	-0.061	9.60	0.300	0.362	0.07	38	-0.114	-2.602	-0.059	11.020	0.291	0.324	0.09	42	-0.123	-2.433	-0.088	9.773	0.314	0.340	0.09
2.4	34	-0.168	-2.883	-0.085	11.01	0.273	0.368	0.11	39	-0.105	-3.028	-0.109	11.770	0.274	0.366	0.12	43	-0.130	-2.826	-0.124	11.670	0.262	0.354	0.11
		(Range + ou - 10cm/s)								(Range + ou - 10cm/s)								(Range + ou - 10cm/s)						
		*pris sens inverse								*pris sens inverse														
	essai-1								essai-1								essai-1							

Location of measurement axes

D1 :	Y= -0.46 m
D2 :	Y= -0.25 m
Axe:	Y= 0
G2 :	Y= 0.25 m
G1 :	Y=0.46 m

Case 2 X = -2 m

Case 3 X = -2 m

Location of measurement axes

D1 :	Y= -0.46 m
D2 :	Y= -0.25 m
Axe:	Y= 0
G2 :	Y= 0.25 m
G1 :	Y=0.46 m

	G1					G2				
	distance au mur:	4cm				distance à l'axe:	25cm			
Z (cm)	file	U_Z	-U_X	-U_Y	SNR	file	U_Z	-U_X	-U_Y	SNR
32.4	14	0.125	2.533	-0.084	9.80	18	0.082	2.289	-0.197	9.32
25.4	15	0.173	2.544	-0.076	11.12	19	0.180	3.237	-0.148	11.90
14.4	16	0.177	3.530	-0.101	14.30	20	0.088	4.452	-0.164	15.70
2.4	17	0.282	6.346	-0.362	18.00	21	0.070	6.162	-0.304	19.30
		(Range + ou - 10cm/s)					(Range + ou - 10cm/s)			
	*									
	essai-1					essai-1				

	D1					D2					Axe-droite				
	distance au mur:	4cm				distance à l'axe:	25cm				distance à l'axe:	0cm			
Z (cm)	file	U_Z	-U_X	-U_Y	SNR	file	U_Z	-U_X	-U_Y	SNR	file	U_Z	-U_X	-U_Y	SNR
32.4	5	-0.158	-2.695	0.013	10.39	9	-0.091	-2.433	-0.004	9.40	1	-0.229	-2.764	0.004	10.30
25.4	6	-0.111	-2.746	0.038	13.11	10	-0.116	-3.315	-0.064	12.37	2	-0.275	-3.037	-0.045	13.12
14.4	7	-0.173	-4.102	0.041	15.53	11	-0.244	-4.670	-0.049	16.70	3	-0.349	-3.879	0.001	16.88
2.4	8	-0.362	-6.494	-0.036	19.300	12	-0.409	-6.621	0.047	20.50	4	-0.389	-6.378	0.013	20.40
		(Range + ou - 10cm/s)					(Range + ou - 10cm/s)					(Range + ou - 10cm/s)			
	*pris sens inverse					*pris sens inverse									
	essai-1					essai-1					essai-1				

Case 4 X = -2 m

	G1						G2					
	distance au mur:	4cm					distance à l'axe:	25cm				
Z (cm)	file	U_Z	-U_X	-U_Y	SNR	**sdev2**	file	U_Z	-U_X	-U_Y	SNR	std2
43.3	1	**0.083**	**1.387**	**-0.074**	**9.37**	0.22	6	0.062	1.425	-0.081	9.13	0.220
36.3	2	**0.084**	**1.374**	**-0.067**	**9.174**	0.218	7	0.086	1.697	-0.086	9.38	0.226
25.3	3	**0.128**	**1.438**	**-0.058**	**9.42**	0.214	8	0.094	1.825	-0.095	9.67	0.254
12.3	4	**0.183**	**1.982**	**-0.036**	**10.55**	0.279	9	0.118	2.172	-0.036	11.50	0.263
3.3	5	0.161	2.493	-0.124	11.82	0.58	10	0.176	2.964	-0.114	11.96	0.369
		(Range + ou - 10cm/s)						(Range + ou - 10cm/s)				
		*										
	essai-1						essai-1					

Location of measurement axes

D1 :	Y= -0.46 m
D2 :	Y= -0.25 m
Axe:	Y= 0
G2 :	Y= 0.25 m
G1 :	Y=0.46 m

	D1						D2						Axe-droite					
	distance au mur:	4cm					distance à l'axe:	25cm					distance à l'axe:	0cm				
Z (cm)	file	U_Z	-U_X	-U_Y	SNR	std2	file	U_Z	-U_X	-U_Y	SNR	std2	file	U_Z	-U_X	-U_Y	SNR	std_2
43.3	11	-0.099	-1.522	-0.010	8.72	0.22	16	-0.102	-1.612	-0.012	7.88	0.24	21	-0.123	-1.717	-0.042	8.38	0.256
36.3	12	-0.106	-1.589	-0.014	8.34	0.24	17	-0.091	-1.654	-0.023	8.52	0.24	22	-0.097	-1.680	-0.030	8.82	0.227
25.3	13	-0.103	-1.711	-0.013	9.06	0.23	18	-0.085	-1.881	0.009	-9.49	0.26	23	-0.118	-1.769	-0.039	9.29	0.247
12.3	14	-0.077	-2.269	-0.019	11.12	0.28	19	-0.096	-2.400	-0.013	11.12	0.31	24	-0.159	-2.268	-0.003	9.82	0.308
3.3	15	-0.191	-3.069	0.067	12.83	0.33	20	-0.165	-3.358	0.039	12.52	0.28	25	-0.189	-2.711	-0.033	11.42	0.331
		(Range + ou - 10cm/s)						(Range + ou - 10cm/s)						(Range + ou - 10cm/s)				
		*pris sens inverse						*pris sens inverse										
	essai-1						essai-1						essai-1					

	G1					G2					Axe				
	distance au mur:	4cm				distance à l'axe:	25cm				distance à l'axe:	0cm			
Z (cm)	file	U_Z	-U_X	-U_Y	SNR	file	U_Z	-U_X	-U_Y	SNR	file	U_Z	-U_X	-U_Y	SNR
43.3	7	0.056	2.033	-0.097	11.70	12	0.043	1.787	-0.026	11.47	18	0.056	2.608	-0.157	11.62
36.3	8	0.122	1.861	-0.015	12.34	13	0.084	2.155	-0.134	12.20	19	0.109	2.434	-0.165	12.66
25.3	9	0.296	2.724	-0.156	15.00	14	0.275	3.672	-0.211	15.30	20	0.024	3.140	-0.101	15.10
12.3	10	0.263	4.535	-0.078	17.90	16	0.276	5.848	-0.167	5.16	21	0.154	5.315	-0.218	19.48
3.3	11	0.342	6.460	-0.221	20.40	17	0.189	6.798	-0.187	21.30	22	0.323	7.084	-0.192	21.97
		(Range + ou - 10cm/s)					(Range + ou - 10cm/s)					(Range + ou - 10cm/s)			
	*														
	essai-1					essai-1					essai-1				

	D1					D2				
	distance au mur:	4cm				distance à l'axe:	25cm			
Z (cm)	file	U_Z	-U_X	-U_Y	SNR	file	U_Z	-U_X	-U_Y	SNR
43.3	24	-0.103	-2.686	0.009	11.77	30	-0.127	-2.064	0.095	11.48
36.3	25	0.010	-1.952	0.055	13.44	31	-0.032	-2.568	0.074	13.53
25.3	26	0.002	-3.267	0.072	14.94	32	-0.020	-3.953	0.177	16.18
12.3	27	-0.121	-5.397	0.080	19.30	33	-0.199	-5.891	-0.053	20.25
3.3	28	-0.232	-6.790	-0.067	20.75	34	-2.760	-7.683	-0.059	22.47
		(Range + ou - 10cm/s)					(Range + ou - 10cm/s)			
	*pris sens inverse					*pris sens inverse				
	essai-1					essai-1				

Case 5 X = -2 m

Location of measurement axes

D1 :	Y= -0.46 m
D2 :	Y= -0.25 m
Axe:	Y= 0
G2 :	Y= 0.25 m
G1 :	Y=0.46 m

Case 6 X = -2 m

	G1						G2					
	distance au mur:	4cm					distance à l'axe:	25cm				
Z (cm)	file	U_Z	-U_X	-U_Y	SNR	std2	file	U_Z	-U_X	-U_Y	SNR	std2
54.6	2	**0.033**	**1.367**	**-0.059**	**14.4**	0.144	8	0.019	1.436	-0.061	14.05	0.190
47.6	3	**0.066**	**1.364**	**-0.055**	**14.25**	0.161	9	0.039	1.483	-0.065	13.88	0.194
36.6	4	**0.042**	**1.441**	**-0.06**	**14.56**	0.185	10	0.022	1.477	-0.070	13.84	0.176
23.6	5	**0.061**	**1.556**	**-0.06**	**14.62**	0.174	11	0.078	1.492	-0.056	13.89	0.174
14.6	6	**0.072**	**1.752**	**-0.063**	**14.46**	0.17	12	0.099	1.872	-0.067	14.70	0.174
7.6	7	0.067	1.113	-0.006	13.82	0.21	13	0.081	1.586	-0.022	13.07	0.236
		Range	+/- 3cm/s)					Range	+/- 3cm/s)			
		*										
	essai-1						essai-1					

Location of measurement axes

D1 :	Y= -0.46 m
D2 :	Y= -0.25 m
Axe:	Y= 0
G2 :	Y= 0.25 m
G1 :	Y=0.46 m

	D1						D2						Axe-droite					
	distance au mur:	4cm					distance à l'axe:	25cm					distance à l'axe:	0cm				
Z (cm)	file	U_Z	-U_X	-U_Y	SNR	std2	file	U_Z	-U_X	-U_Y	SNR	std2	file	U_Z	-U_X	-U_Y	SNR	std_2
54.6	14	-0.040	-1.276	-0.016	13.78	0.11	20	-0.025	-1.401	-0.012	13.62	0.13	26	-0.044	-1.516	-0.006	13.36	0.153
47.6	15	-0.034	-1.270	-0.020	13.78	0.11	21	-0.029	-1.399	-0.018	13.36	0.12	29	-0.049	-1.426	-0.035	13.25	0.147
36.6	16	-0.008	-1.325	-0.022	13.66	0.11	22	-0.011	-1.519	-0.015	13.27	0.18	30	-0.033	-1.511	-0.042	13.14	0.156
23.6	17	-0.030	-1.504	-0.014	14.26	0.13	23	0.004	-1.801	-0.030	13.73	0.20	31	-0.033	-1.665	-0.037	13.62	0.162
14.6	18	-0.008	-2.035	-0.023	14.54	0.22	24	0.000	-2.086	-0.004	14.50	0.19	32	-0.036	-1.886	-0.010	13.76	0.185
7.6	19	0.014	-0.897	0.099	14.07	0.16	25	-0.040	-1.894	-0.015	13.44	0.22	33	-0.052	-1.564	-0.046	11.97	0.186
		Range	+/- 3cm/s)					Range	+/- 3cm/s)					Range	+/- 10cm/s) (*=+/-3cm/s)			
	essai-1						essai-1						essai-1					

	G1						G2					
	distance au mur:	4cm					distance à l'axe:	25cm				
Z (cm)	file	U_Z	-U_X	-U_Y	SNR	std2	file	U_Z	-U_X	-U_Y	SNR	std2
54.6	86	0.051	1.853	-0.073	8.75	0.282	92	0.036	1.546	-0.067	8.80	0.239
47.6	87	0.083	1.629	-0.084	8.95	0.261	93	0.043	1.652	-0.088	8.71	0.255
36.6	88	0.073	1.754	-0.074	9.32	0.28	94	0.090	2.291	-0.114	9.83	0.273
23.6	89	0.093	2.289	-0.067	11.11	0.306	95	0.076	2.828	-0.097	12.16	0.285
14.6	90	0.129	2.692	-0.096	12.24	0.281	96	0.069	3.381	-0.157	13.70	0.343
7.6	91	0.012	2.938	-0.155	13.37	0.32	97	0.075	3.221	-0.156	14.95	0.347
		Range	+/- 3cm/s)					Range	+/- 3cm/s)			
	essai-1						essai-1					

Case 7 X = -2 m

Location of measurement axes

D1 :	Y= -0.46 m
D2 :	Y= -0.25 m
Axe:	Y= 0
G2 :	Y= 0.25 m
G1 :	Y=0.46 m

	D1						D2						Axe-droite					
	distance au mur:	4cm					distance à l'axe:	25cm					distance à l'axe:	0cm				
Z (cm)	file	U_Z	-U_X	-U_Y	SNR	std2	file	U_Z	-U_X	-U_Y	SNR	std2	file	U_Z	-U_X	-U_Y	SNR	std_2
54.6	65	-0.083	-1.806	-0.037	9.25	0.25	71	-0.062	-1.526	0.022	8.88	0.22	77	-0.099	-2.269	-0.035	9.10	0.282
47.6	66	-0.038	-1.662	-0.028	9.68	0.22	72	-0.008	-1.663	0.005	9.60	0.22	78	-0.063	-1.867	-0.061	9.52	0.287
36.6	67*	-0.027	-1.768	-0.016	9.36	0.21	73	-0.005	-2.077	0.005	10.23	0.26	79	-0.071	-2.023	-0.021	10.20	0.261
23.6	68	-0.015	-2.429	-0.019	11.55	0.37	74	-0.075	-2.968	-0.015	12.20	0.32	81	-0.060	-2.546	-0.020	11.36	0.347
14.6	69	-0.028	-3.462	0.034	13.46	0.36	75	-0.092	-3.817	0.007	14.07	0.32	82	-0.126	-3.161	-0.005	13.48	0.300
7.6	70	-0.140	-4.118	-0.002	15.02	0.25	76	-0.138	-4.862	-0.056	16.28	0.39	83	-0.201	-3.530	0.017	15.65	**0.41**
		Range	+/- 3cm/s)					Range	+/- 3cm/s)					Range	+/- 10cm/s) (*=+/-3cm/s)			
	essai-1						essai-1						essai-1					

Case 8 X = -2 m

	G1						G2					
	distance au mur:	4cm					distance à l'axe:	25cm				
Z (cm)	file	U_Z	-U_X	-U_Y	SNR	std2	file	U_Z	-U_X	-U_Y	SNR	std2
54.6	1	**0.106**	**1.867**	**-0.047**	**9.6245**	0.472	8	0.024	1.353	-0.114	9.13	0.268
47.6	3*	**0.099**	**1.587**	**-0.084**	**10.07**	0.263	9	-0.015	1.457	-0.011	8.76	0.297
36.6	4*	**0.201**	**1.929**	**0.003**	**10.1**	0.317	10	0.112	2.634	-0.071	10.60	0.343
23.6	5	**0.146**	**2.681**	**-0.095**	**11.86**	0.339	11	0.113	3.672	-0.196	13.16	0.527
14.6	6	**0.18**	**3.901**	**-0.135**	**14.6**	0.38	12	0.127	4.702	-0.187	16.06	0.398
7.6	7	0.111	4.805	-0.169	17.30	0.39	13	0.154	5.627	-0.298	17.95	0.574
		Range	+/- 10cm/s (*=+/-3)					Range	+/- 10cm/s			
	essai-1						essai-1					

Location of measurement axes

D1 :	Y= -0.46 m
D2 :	Y= -0.25 m
Axe:	Y= 0
G2 :	Y= 0.25 m
G1 :	Y=0.46 m

	D1						D2						Axe-droite					
	distance au mur:	4cm					distance à l'axe:	25cm						0cm				
Z (cm)	file	U_Z	-U_X	-U_Y	SNR	std2	file	U_Z	-U_X	-U_Y	SNR	std2	file	U_Z	-U_X	-U_Y	SNR	std_2
54.6	14	-0.055	-1.877	-0.042	8.54	0.33	21	-0.087	-1.579	0.027	8.35	0.29	30	-0.033	-1.836	-0.008	8.01	0.317
47.6	15	-0.024	-1.616	0.006	9.57	0.26	22	-0.125	-1.519	-0.032	8.60	0.37	31	-0.100	-1.734	-0.107	8.56	0.364
36.6	16	0.017	-1.778	0.026	9.80	0.29	23	-0.073	-1.961	0.097	9.23	0.33	32	-0.113	-1.849	-0.057	9.07	0.279
23.6	17	-0.040	-2.989	0.018	11.91	0.54	24	-0.117	-3.707	0.036	13.17	0.55	33	-0.212	-3.064	-0.050	11.87	0.514
14.6	18	-0.077	-4.587	0.032	14.95	0.51	25	-0.137	-5.320	-0.020	16.16	0.54	34	-0.149	-4.588	-0.075	14.64	0.637
7.6	19	-0.156	-7.368	-0.057	17.70	0.65	26	-0.159	-7.397	-0.082	19.16	0.65	35	-0.228	-6.338	0.010	18.43	**0.59**
		Range	+/- 10cm/s)					Range	+/- 10cm/s)					Range	+/- 10cm/s)			
	essai-1						essai-1						essai-1					

Appendix E

Excerpt of sample CFD startup file

This is and excerpt of the .ccl script file used to start the k-epsilon simulation. The expressions for defining the custom eddy viscosity distribution and pressure boundary conditions are listed in the EXPRESSIONS section at the end. When the custom turbulence model is employed, eddy viscosity is defined using the 'Expression' option and the eddy viscosity is set to ν*{nu ratio}. where {nu ratio} is the expression defined in EXPRESSIONS.

```
# CFX-11.0 build 2007.04.20-18.59

FLOW:
  DOMAIN:piers58q19
    Coord Frame = Coord 0
    Domain Type = Fluid
    Fluids List = Air at 25 C,Water
...
    BOUNDARY:in
      Boundary Type = INLET
      Location = IN,IN 2
      BOUNDARY CONDITIONS:
        FLOW REGIME:
          Option = Subsonic
        END
        MASS AND MOMENTUM:
          Normal Speed = uft
          Option = Normal Speed
        END
        TURBULENCE:
          Option = High Intensity and Eddy Viscosity Ratio
        END
      END
      FLUID:Air at 25 C
        BOUNDARY CONDITIONS:
          VOLUME FRACTION:
```

```
        Option = Value
        Volume Fraction = vfair
      END
    END
  END
  FLUID:Water
    BOUNDARY CONDITIONS:
      VOLUME FRACTION:
        Option = Value
        Volume Fraction = vfwat
      END
    END
  END
END
BOUNDARY:out
  Boundary Type = OPENING
  Location = OUT,OUT 2
  BOUNDARY CONDITIONS:
    FLOW DIRECTION:
      Option = Normal to Boundary Condition
    END
    FLOW REGIME:
      Option = Subsonic
    END
    MASS AND MOMENTUM:
      Option = Opening Pressure and Direction
      Relative Pressure = p out
    END
    TURBULENCE:
      Option = High Intensity and Eddy Viscosity Ratio
    END
  END
  FLUID:Air at 25 C
    BOUNDARY CONDITIONS:
      VOLUME FRACTION:
        Option = Value
        Volume Fraction = 0
      END
    END
  END
  FLUID:Water
    BOUNDARY CONDITIONS:
      VOLUME FRACTION:
        Option = Value
        Volume Fraction = 1.0
      END
    END
  END
END
BOUNDARY:overup
  Boundary Type = INLET
  Location = OVERUP,OVERUP 2
  BOUNDARY CONDITIONS:
    FLOW REGIME:
      Option = Subsonic
```

```
        END
        MASS AND MOMENTUM:
          Option = Cartesian Velocity Components
          U = -u0*0.01
          V = 0 [m s^-1]
          W = 0 [m s^-1]
        END
        TURBULENCE:
          Option = Medium Intensity and Eddy Viscosity Ratio
        END
      END
      FLUID:Air at 25 C
        BOUNDARY CONDITIONS:
          VOLUME FRACTION:
            Option = Value
            Volume Fraction = vfair
          END
        END
      END
      FLUID:Water
        BOUNDARY CONDITIONS:
          VOLUME FRACTION:
            Option = Value
            Volume Fraction = vfwat
          END
        END
      END
    END
...
    BOUNDARY:top
      Boundary Type = OPENING
      Location = TOP,TOP 2,HTOP,HTOP 2
      BOUNDARY CONDITIONS:
        FLOW REGIME:
          Option = Subsonic
        END
        MASS AND MOMENTUM:
          Option = Static Pressure for Entrainment
          Relative Pressure = 0 [Pa]
        END
        TURBULENCE:
          Option = Medium Intensity and Eddy Viscosity Ratio
        END
      END
      FLUID:Air at 25 C
        BOUNDARY CONDITIONS:
          VOLUME FRACTION:
            Option = Value
            Volume Fraction = 1.0
          END
        END
      END
      FLUID:Water
        BOUNDARY CONDITIONS:
          VOLUME FRACTION:
```

```
            Option = Value
            Volume Fraction = 1e-7
          END
        END
      END
    END
...
    FLUID:Air at 25 C
      FLUID MODELS:
        FLUID BUOYANCY MODEL:
          Option = Density Difference
        END
        MORPHOLOGY:
          Option = Continuous Fluid
        END
      END
    END
    FLUID:Water
      FLUID MODELS:
        FLUID BUOYANCY MODEL:
          Option = Density Difference
        END
        MORPHOLOGY:
          Option = Continuous Fluid
        END
      END
    END
    FLUID MODELS:
...
      TURBULENCE MODEL:
        Homogeneous Model = On
        Option = k epsilon
        BUOYANCY TURBULENCE:
          Option = None
        END
      END
      TURBULENT WALL FUNCTIONS:
        Option = Scalable
      END
    END
    FLUID PAIR:Air at 25 C | Water
      INTERPHASE TRANSFER MODEL:
        Option = Free Surface
      END
      MASS TRANSFER:
        Option = None
      END
      MOMENTUM TRANSFER:
        DRAG FORCE:
          Drag Coefficient = 0.44
          Option = Drag Coefficient
        END
      END
      SURFACE TENSION MODEL:
        Option = None
```

```
  END
END
INITIALISATION:
  Option = Automatic
  FLUID:Air at 25 C
    INITIAL CONDITIONS:
      Velocity Type = Cartesian
      CARTESIAN VELOCITY COMPONENTS:
        Option = Automatic with Value
        U = ustep
        V = 0 [m s^-1]
        W = wstep
      END
      VOLUME FRACTION:
        Option = Automatic with Value
        Volume Fraction = vfair
      END
    END
  END
  FLUID:Water
    INITIAL CONDITIONS:
      Velocity Type = Cartesian
      CARTESIAN VELOCITY COMPONENTS:
        Option = Automatic with Value
        U = ustep
        V = 0 [m s^-1]
        W = wstep
      END
      VOLUME FRACTION:
        Option = Automatic with Value
        Volume Fraction = vfwat
      END
    END
  END
  INITIAL CONDITIONS:
    EPSILON:
      Eddy Length Scale = 0.1 [m]
      Option = Automatic with Value
    END
    K:
      Fractional Intensity = 0.12
      Option = Automatic with Value
    END
    STATIC PRESSURE:
      Option = Automatic with Value
      Relative Pressure = p hydrostatic
    END
  END
END
MULTIPHASE MODELS:
  Homogeneous Model = False
  FREE SURFACE MODEL:
    Option = Standard
  END
END
```

```
  END
  OUTPUT CONTROL:
...
    MONITOR OBJECTS:
      MONITOR BALANCES:
        Option = Full
      END
      MONITOR FORCES:
        Option = Full
      END
      MONITOR PARTICLES:
        Option = Full
      END
      MONITOR POINT:bed1
        Cartesian Coordinates = -3.2 [m], 0.5 [m], 0.0001 [m]
        Option = Cartesian Coordinates
        Output Variables List = Pressure
      END
      MONITOR POINT:bed2
        Cartesian Coordinates = -2 [m], 0.5 [m], 0.0001 [m]
        Option = Cartesian Coordinates
        Output Variables List = Pressure
      END
      MONITOR POINT:bed3
        Cartesian Coordinates = -0.1 [m], 0.5 [m], 0.0001 [m]
        Option = Cartesian Coordinates
        Output Variables List = Pressure
      END
      MONITOR POINT:h1
        Expression Value = probe(Pressure)@bed1/(997[kg/m^3]*9.812[m/s^2])
        Option = Expression
      END
      MONITOR POINT:h2
        Expression Value = areaInt(Water. Volume Fraction)@outwall*0.65[m
    ]/0.54483[m^2]
        Option = Expression
      END
      MONITOR POINT:h3
        Expression Value = probe(Pressure)@bed3/(997[kg/m^3]*9.812[m/s^2])
        Option = Expression
      END
      MONITOR POINT:mout
        Expression Value = Water.massFlow()@overout
        Option = Expression
      END
      MONITOR POINT:velout
        Cartesian Coordinates = 0.53 [m], 0.501 [m], 0.14 [m]
        Option = Cartesian Coordinates
        Output Variables List = Water.Velocity u,Pressure
      END
      MONITOR POINT:vort
        Cartesian Coordinates = -0.0328 [m], 0.4451 [m], 0.57 [m]
        Option = Cartesian Coordinates
        Output Variables List = Water.Vorticity Z,Water.Velocity w
      END
```

```
    MONITOR POINT:vort 05
      Cartesian Coordinates = -0.0289 [m], 0.547 [m], 0.426 [m]
      Option = Cartesian Coordinates
      Output Variables List = Water.Vorticity Z,Water.Velocity w
    END
    MONITOR POINT:weir p
      Cartesian Coordinates = -0.2 [m], 0.501 [m], 0.14 [m]
      Option = Cartesian Coordinates
      Output Variables List = Water.Velocity u
    END
    MONITOR RESIDUALS:
      Option = Full
    END
    MONITOR TOTALS:
      Option = Full
    END
  END
  RESULTS:
    File Compression Level = Default
    Option = Standard
  END
END
SIMULATION TYPE:
  Option = Steady State
  EXTERNAL SOLVER COUPLING:
    Option = None
  END
END
SOLUTION UNITS:
  Angle Units = [rad]
  Length Units = [m]
  Mass Units = [kg]
  Solid Angle Units = [sr]
  Temperature Units = [K]
  Time Units = [s]
END
SOLVER CONTROL:
  ADVECTION SCHEME:
    Option = High Resolution
  END
  CONVERGENCE CONTROL:
    Maximum Number of Iterations = 8000
    Physical Timescale = 0.01 [s]
    Timescale Control = Physical Timescale
  END
  CONVERGENCE CRITERIA:
    Residual Target = 1e-07
    Residual Type = MAX
  END
  DYNAMIC MODEL CONTROL:
    Global Dynamic Model Control = On
  END
  MULTIPHASE CONTROL:
    Volume Fraction Coupling = Segregated
  END
```

```
  END
END

LIBRARY:
  CEL:
    EXPRESSIONS:
      dp = -1660[Pa]
      dt = 200.0[]
      eps = 0.000001 []
      h initial = 0.58[m]
      nu fs = nufs1*step(-0.43-x/1[m])+nufs2
      nu pipe = 200*step(x/1[m]-0.02)
      nu ups1 = step(-4-x/1[m])
      nu ups2 = -1/3.0*(x/1[m]+1)*step(x/1[m]+4)*step(-1-x/1[m])
      nu var = (1*(-1*(x/1[m]+1))/(3.0))*step(-1*(x/1[m]+1))*step((x/1[m]+1)
    +3)+1*step(-3-(x/1[m]+1))
      nufs1 = 1.0*exp(-((z-h initial)/0.012[m])^2)
      nufs2 = 1.0*exp(-((x+0.43[m])/0.1[m])^2)*step(x/1[m]+0.43)*nufs1
      nuturb ratio = 1.0 + nuturb upstream +max(rexp,nu pipe) + nu fs
      nuturb upstream = 500*(nu ups1 +nu ups2)
      overstep = 1.0*step(x/1[m]+4.6553)
      p hydrostatic = 997[kg/m^3]*9.812[m/s^2]*(h initial-z)*step((h initial
    - z)/1[m])
      p out = p hydrostatic -20[Pa]+dp*((atstep-t0)/dt)*step(t2-atstep)+dp*
    step(atstep-t2)
      p over out = 997[kg/m^3]*9.812[m/s^2]*(0.42[m]-z)*step((0.42[m]-z)/1[m
    ])-2[Pa]
      q = 0.0188 [m^3/s]
      rdist = sqrt((x-0[m])^2+(y-0.5[m])^2+(z-0.14[m])^2)
      rexp = 1000*exp(-rdist^2/0.003[m^2])
      t0 = 0
      t2 = t0+dt
      u0 = q/(0.106322[m^2])
      uft = u0*((atstep)/200.0)*step(200-atstep)+u0*step(atstep-200)
      ustep = (0.01[m/s]*step(-0.01-x/1[m])+0.01[m/s]*step(x/1[m]))*step(z/1[
    m])
      vfair = 1-vfwat
      vfwat = step((h initial - z)/1[m])
      wstep = 0.01[m/s]*step(-0.01-z/1[m])
    END
  END
END
```

References

Adams, G.N., Gilmore, D.C. (1972). Some observations of vortex core structure. *Can. Aeronaut. Space J.* Jun, 159–162.

Ahmad, Z., Rao, K.V., Mittal, M.K. (2008). Critical submergence of horizontal intakes in open channel flows. *J. Dam Eng.* 19(2), 71–90.

Amphlett, M.B. (1979). Discussion of vortex formation at vertical pipe intakes. *J. Hydraul. Div. ASCE* 105(HY10), 1328–1330.

Andersen, A. (2002). Vortex flows with a free surface and random matrix theory and acoustic resonances. Ph.D. thesis, Technical University of Denmark, Kongens Lyngby, Denmark.

Andersen, A., Bohr, T., Stenum, B., Rasmussen, J.J., Lautrup, B. (2003). Anatomy of a bathtub vortex. *Phys. Rev. Lett.* 91(10), 104502.

Andersen, A., Bohr, T., Stenum, B., Rasmussen, J.J., Lautrup, B. (2006). The bathtub vortex in a rotating container. *J. Fluid Mech.* 556, 121–146.

Anh, T.N., Hosoda, T. (2005). Steady free surface proile of flows with air-core vortex at vertical intake. In *Proc. 31st IAHR Cong.*, Seoul, S. Korea.

Ansar, M., Nakato, T. (2001). Experimental study of 3D pump-intake flows with and without cross flow. *J. Hydraul. Eng.-ASCE* 127(10), 825–834.

Ansar, M., Nakato, T., Constantinescu, S.G. (2002). Numerical simulations of inviscid three-dimensional flows at single- and dual-pump intakes. *J. Hydr. Research* 40(4), 153–161.

Anwar, H.O. (1965). Flow in a free vortex. *Water Power* 4, 153–161.

Anwar, H.O. (1968a). Prevention of vortices at intakes. *Water Power* October, 393–401.

Anwar, H.O. (1968b). Vortices in a viscous fluid. *J. Hydraul. Res.* 6(1), 1–13.

Anwar, H.O. (1969). Turbulent flow in a vortex. *J. Hydraul. Res.* 7(1), 1–29.

Anwar, H.O. (1983). The non-dimensional parameters of free-surface vortices measured for horizontal and vertically inverted intakes. *Houille Blanche* 1, 11–25.

Anwar, H.O., Amphlett, M.B. (1980). Vortices at vertically inverted intake. *J. Hydraul. Res.* 18(2), 123–134.

Anwar, H.O., Weller, J.A., Amphlett, M.B. (1978). Similarity of free-vortex at horizontal intake. *J. Hydraul. Res.* 18(2), 95–105.

Ash, R.L., Khorrami, M.R. (1995). Vortex stability. In S.I. Green, ed., *Fluid Vortices*, 317–369, Kluwer, Dordrecht, NL.

Batchelor, G.K. (1964). Axial flow in trailing line vortices. *J. Fluid Mech.* 20, 645–658.

Beninati, M.L., Marshall, J.S. (2005a). An experimental study of the effect of free-stream turbulence on a trailing vortex. *Exp. in Fluids* 38, 244–257.

Beninati, M.L., Marshall, J.S. (2005b). External turbulence interaction with a columnar vortex. *J. Fluid Mech.* 540, 221–245.

Benjamin, T.B. (1962). Theory of vortex breakdown phenomenon. *J. Fluid Mech.* 14(4), 593–629.

Berge, J.P. (1966). Enquête sur la formation de vortex et autres anomalies d'écoulement dans une enceinte avec ou sans surface libre. *Houille Blanche* 21(1), 13–27.

Bhat, V.I.K., Prakash, G. (2008). Life cycle analysis of run-of-river small hydro power plants in india. *Open Renew. Energ. J.* 1, 11–16.

Binnie, A.M. (1964). Some experiments on the bath-tub vortex. *J. Mech. Eng. Sci.* 6(3), 256–257.

Birch, D., Lee, T., Mokhtarian, F., Kafyeke, F. (2004). Structure and induced drag of a tip vortex. *J. Aircraft* 41(5), 1138–1145.

Blaisdell, F.W. (1982). Discussion of model-prototype comparisons of free surface vortices. *J. Hydraul. Div. ASCE* 108(HY11), 1409–1412.

Bøhling, L., Andersen, A., Fabre, D. (2010). Structure of a steady drain-hole vortex in a viscous fluid. *J. Fluid Mech.* 656, 177–188.

Bradshaw, P. (1973). Effects of streamline curvature on turbulent flow. *AGARDograph No. 169* .

Bunyawanichakul, P., Kirkpatrick, M.P., Sargison, J.E., Walker, G.J. (2006). Numerical and experimental studies of the flow field in a cyclone dryer. *J. Fluid Eng.* 128(6), 1240–1248.

Burgers, J.M. (1948). A mathematical model illustrating the theory of turbulence. *Adv. in Appl. Mech.* 1, 171–199.

Carriveau, E.C.J. (2004). Formation mechanisms of hydraulic intake vortices. Ph.D. thesis, University of Western Ontario, London, CA.

Carriveau, R. (2006). The hydraulic vortex: an autocatakinetic system. *Intl. J. General Systems* 35(6), 707–726.

Carriveau, R., Baddour, R.E., Kopp, G.A. (2002). The entrainment envelope of dye-core vortices at submerged hydraulic intakes. *Can. J. Civ. Eng.* 29, 400–408.

Carriveau, R., Kopp, G.A., Baddour, R.E. (2009). Free-surface stretching-sustained intake vortices. *J. Hydr. Res.* 47(4), 486–491.

Chang, E., Prosser, M.J. (1987). Basic results of theoretical and experimental work. In J. Knauss, ed., *Swirling flow problems at intakes*, 39–55, A.A. Balkema, Rotterdam, NL.

Cheng, Y., Li, J., Yang, J. (2007). Free surface-pressurized flow in ceiling-sloping tailrace tunnel of hydropower plant: simulation by VOF model. *J. Hydr. Research* 45(1), 88–99.

Chuang, W.L., Hsiao, S.C. (2011). Three-dimensional numerical simulation of intake model with cross flow. *J. Hydrodyn.* 23(3), 314–324.

Cotel, A.J., Breidenthal, R.E. (1999). Turbulence inside a vortex. *Phys. Fluids* 11(10), 3026–3029.

Crawley, M.J. (2012). *The R Book, Second Edition*. John Wiley & Sons, Chichester, UK.

Crow, S.C. (1970). Stability theory for a pair of trailing vortices. *AIAA J.* 8, 2172–2179.

Daggett, L.L., Keulegan, G.H. (1974). Similitude in free-surface vortex formations. *J. Hydraul. Div. ASCE* 100(HY11), 1565–1581.

de Siervi, F., Viguier, H.C., Greitzer, E.M., Tan, C.S. (1982). Mechanisms of inlet vortex formation. *J Fluid Mech.* 124, 173–207.

Denny, D.F. (1956). An experimental study of air-entraining vortices in pump sumps. *P. I. Mech. Eng.* 170, 106–116.

Duraisamy, K., Iaccarino, G. (2005). Curvature correction and application of the $v^2 - f$ turbulence model to tip vortex flows. Technical report, Center for turbulence research, Stanford, US.

Duraisamy, K., Lele, S.K. (2006). Dns of temporal evolution of isolated turbulent vortices. In *Proc. Summer Prog. 2006*, 35–47, Stanford, US.

Durbin, P. (1993). A reynolds stress model for near-wall turbulence. *J. Fluid Mech.* 249, 465–498.

Echavez, G., McCann, E. (2002). An experimental study on the free surface vertical vortex. *Exp. in Fluids* 33(3), 414–421.

Eguchi, Y., Yamamoto, K., Funada, T., Tanaka, N., Moriya, S., Tanimoto, K., Ogura, K., Suzuki, T., Maekawa, I. (1994). Gas entrainment in the IHX vessel of top-entry loop-type LMFBR. *Nucl. Eng. Des.* 146, 373–381.

Einstein, H.A., Li, H. (1951). Steady vortex flow in a real fluid. In *Proc. Heat Trans. and Fluid Mech. Inst.*, 33–43, Stanford University, Palo Alto, US.

Ezure, T., Kimura, N., Hayashi, K., Kamide, H. (2008). Transient behavior of gas entrainment caused by surface vortex. *Heat Transfer. Eng.* 29(8), 659–666.

Ferziger, J.H., Peric, M. (1999). *Computational methods for fluid mechanics, 2nd Edition*. Springer, Berlin, Germany.

Fisher, Jr, R., Franke, G. (1987). The impact of inlet flow characteristics on low head hydro projects. In *Waterpower 87: Proc. Intl. Conf. on Hydropower*, 1671–1680, Portland, OR.

G. Montilla, A.M., Castro, C. (2004). Air entrainment at guri dam intake operating at low heads. In F. Yazdandoost, J. Attari, eds., *Hydraulics of dams and river structures: Proc. Intl. Conf., Tehran,Iran*, 53–60, Taylor & Francis, London, UK.

Gatski, T.B., Rumsey, C.L. (2002). Linear and nonlinear eddy viscosity models. In B. Launder, N. Sandham, eds., *Closure strategies for turbulent and transitional flows*, 9–46, Cambridge University Press, Cambridge, UK.

Gatski, T., Speziale, C. (1993). On explicit algebraic stress models for complex turbulent flows. *J. Fluid Mech.* 254, 59–78, cited By (since 1996)414.

Goel, A. (2012). Estimation of critical submergence for horizontal intakes. *Water and Energy Intl.* 69(6), 49–54.

Gordon, J.L. (1970). Designing intakes to avoid free-surface vortices. *Water Power* Apr, 137–138.

Groupe Conseil Lasalle (2007). Aménagement la sarcelle - étude sur modèle réduit du canal d'amenée de la prise d'eau. rapport préparé pour la société d'énergie de la baie james. Technical Report 1626, Groupe Conseil Lasalle.

Gulliver, J.S. (1988). Discussion of 'Free-Surface Air Core Vortex', by A.J. Odgaard. *J. Hydraul. Div. ASCE* 114(4), 447–449.

Gulliver, J.S., Rindels, A.J., Lindblom, K.C. (1986). Designing intakes to avoid free-surface vortices. *Int. Water Power Dam Constr.* 38(9), 24–28.

Hanjalic, K., Launder, B. (1976). Contribution towards a Reynolds-Stress closure for low-Reynolds-number turbulence. *J. Fluid Mech.* 74(pt 4), 593–610.

Haque, J.N., Mahmud, T., Roberts, K.J., Rhodes, D. (2006). Modeling turbulent flows with free-surface in unbaffled agitated vessels. *Ind. Eng. Chem. Res.* 45, 2881–2891.

Haque, M.M., Constantinescu, G., Weber, L. (2007). Validation of a 3d rans model to predict flow and stratification effects related to fish passage at hydropower dams. *J. Hydraul. Res.* 45(6), 787–796.

Hatch Engineering (2008). Low head hydro market assessment - Volume 1, Main report. H-327842. Technical report, Natural Resources Canada, Ottawa, CA.

Hebaus, G.G. (1979). Discussion of vortex formation at vertical pipe intakes. *J. Hydraul. Div. ASCE* 105(HY10), 1330–1332.

Hecker, G.E. (1987). Fundamentals of vortex intake flow. In J. Knauss, ed., *Swirling flow problems at intakes*, 13–38, A.A. Balkema, Rotterdam, NL.

Hecker, G. (1981). Model-prototype comparison of free surface vortices. *J. Hydraul. Div. ASCE* 107(HY10), 1243–1259.

Heller, V. (2011). Scale effects in physical hydraulic engineering models. *J. Hydraul. Res.* 49(3), 293–306.

Helmholtz, H. (1867). On integrals of the hydrodynamical equations, which express vortex motion. *Phil. Mag. S. 4* 33(226), 485–512.

Hirt, C.W., Nichols, B.D. (1981). Volume of fluid (VOF) method for the dynamics of free boundaries. *J. Comput. Phys.* 39(1), 201 – 25.

Hisasue, N., Nakayama, A. (2011). Evaluation of vortex-suppressing devices installed in intake channel of hydropower facility using LES. In *Proc. 34th IAHR World Cong.*, Brisbane, Australia.

Hite, J.E. (1991). Vortex formation and flow separation at hydraulic intakes. Ph.D. thesis, Washington State University, Pullman, US.

Hite, J.E., Mih, W.C. (1994). Velocity of air-core vortices at hydraulic intakes. *J. Hydraul. Eng.* 120(3), 284–297.

Hoffman, E., Joubert, P. (1963). Turbulent line vortices. *J. Fluid Mech.* 16, 395–411.

Huang, S.L., Chen, H.C., Chu, C.C., Chang, C.C. (2008). On the transition process of a swirling vortex generated in a rotating tank. *Exp. in Fluids* 45, 267–282.

Hunt, J., Morrison, J. (2000). Eddy structure in turbulent boundary layers. *Eur. J. Mech. B Fluid* 19(5), 673–694, cited By (since 1996)87.

Ito, K., Ohshima, H., Sakai, T., Kunugi, T. (2010a). CFD-based evaluation of interfacial flows. In H.W. Oh, ed., *Computational fluid dynamics*, 133–156, InTech, Rijeka, HR.

Ito, K., Sakai, T., Eguchi, Y., Monji, H., Ohshima, H., Uchibori, A., Xu, Y. (2010b). Improvement of gas entrainment prediction method - introduction of surface tension effect. *J. Nucl. Sci. Technol.* 47(9), 771–778.

Jacquin, L., Fabre, D., Sipp, D., Coustols, E. (2005). Unsteadiness, instability and turbulence in trailing vortices. *C. R. Physique* 6, 399–414.

Jacquin, L., Pantano, C. (2002). On the persistence of trailing vortices. *J. Fluid Mech.* 471, 159–168.

Jain, A.K., Raju, K.G.R., Garde, R.J. (1978). Vortex formation at vertical pipe intakes. *J. Hydraul. Div. ASCE* 104(HY10), 1429–1445.

Jiming, M., Yuanbo, L., Jitang, H. (2000). Minimum submergence before double-entrance pressure intakes. *J. Hydraul. Eng.-ASCE* 126(8), 628–631.

Johnson, P.L. (1988). Hydro-power intake design considerations. *J. Hydraul. Eng.-ASCE* 114(6), 651–661.

Julien, P.Y. (1986). Concentration of very fine silts in a steady vortex. *J. Hydraul. Res.* 24(4), 255–264.

Khan, L.A., Roy, E.W., Rashid, M. (2008). Computational fluid dynamics modelling of forebay hydrodynamics created by a floating juvenile fish collection facility at the Upper Baker River Dam, Washington. *River Res. Appl.* 24(9), 1288–1309.

Kimura, N., Ezure, T., Tobita, A., Kamide, H. (2008). Experimental study on gas entrainment at free surface in reactor vessel of a compact sodium-cooled fast reactor. *J. Hydraul. Eng.-ASCE* 45(10), 1053–1062.

Kiviniemi, O., Makusa, G. (2009). A scale model investigation of free surface vortex with particle tracking velocimetry. Master's thesis, University of Oulu, Finland, and Luleå University of Technology, Oulu, Finland and Luleå, Sweden.

Klimenko, A.Y. (2007). Do we find hurricanes on other planets? In *16th Australasian Fluid Mech. Conf.*, Gold Coast, Australia.

Knauss, J. (1987). Prediction of critical submergence. In J. Knauss, ed., *Swirling flow problems at intakes*, 57–76, A.A. Balkema, Rotterdam, NL.

Kocabaş, F., Ünal, B., Ünal, S., Fedakar, H., Gemici, E. (2012). Fuzzy genetic approach for modeling of the critical submergence of an intake. *Neural Comput. Appl.* 21(8), 1–10.

Kocabaş, F., Yıldırım, N. (2002). Effect of circulation on critical submergence of an intake pipe. *J. Hydraul. Res.* 40(6), 741 – 752.

Kocabaş, F., Ünal, S. (2010). Compared techniques for the critical submergence of an intake in water flow. *Adv. Eng. Softw.* 41(5), 802 – 809.

Launder, B.E., Spalding, D.B. (1974). The numerical computation of turbulent flows. *Comput. Method. Appl. M.* 3, 269–289.

Levi, E. (1972). Experiments on unstable vortices. *J. Eng. Mech. Div. ASCE* 98(EM3), 539–559.

Lewellen, W.S. (1962). A solution for three-dimensional vortex flows with strong circulation. *J. Fluid Mech.* 14(Part 3), 420–432.

Li, H.F., Chen, H.X., Ma, Z., Yi, Z. (2008). Experimental and numerical investigation of free surface vortex. *Journal of Hydrodynamics, Ser. B* 20(4), 485 – 491.

Li, S., Lai, Y., Weber, L., Silva, J.M., Patel, V.C. (2004). Validation of a three-dimensional numerical model for water-pump intakes. *J. Hydr. Research* 42(3), 282–292.

Lundgren, T.S. (1985). The vortical flow above the drain-hole in a rotating vessel. *J. Fluid Mech.* 155, 381–412.

Marghzar, S., Montazerin, N., Rahimzadeh, H. (1956). Experiments on a small pump suction well, with particular reference to vortex formations. *P. I. Mech. Eng.* 170, 95–105.

Markland, E., Pope, J.A. (2003). Flow field, turbulence and critical condition at a horizontal water intake. *Proc. IME J. Power Energy* 217, 53–62.

Melander, M.V., Hussain, F. (1993). Coupling between a coherent structure and fine-scale turbulence. *Phys. Rev. E* 48(4), 2669–2689.

Meneveau, C., Katz, J. (2000). Scale-invariance and turbulence models for large-eddy simulation. *Ann. Rev. Fluid Mech.* 32, 1–32.

Menter, F.R. (1994). Two-equation eddy-viscosity turbulence models for engineering applications. *AIAA J.* 32, 269–289.

Mercier, A., Denault, C., Villeneuve, M. (2008). Processus de conception du canal d'amenée de la centrale de la Sarcelle. In *Canadian Dam Assoc. 2008 Annual Conf.*, Winnipeg, CA.

Miles, J. (1998). A note on the Burgers-Rott vortex with a free surface. *Z. Angew. Math. Phys.* 49, 162–165.

Moin, P., Mahesh, K. (1998). Direct numerical simulation: A tool in turbulence research. *Annu. Rev. Fluid Mech.* 30, 539–578, cited By (since 1996)448.

Möller, G., Detert, M., Boes, R. (2012a). Air entrainment due to vortices – state-of-the-art. In *Proc. 2nd IAHR Europe Cong.*, paper B16.

Möller, G., Meyer, A., Detert, M., Boes, R. (2012b). Lufteintragsrate durch Einlaufwirbel – modellfamilie nach froude. In *Internationales Wasserbausymposium*, Graz, Austria.

Monaghan, J.J. (2005). Smoothed particle hydrodynamics. *Rep. Prog. Phys.* 68, 1703–1759.

Montavon, C.A., Grotjans, H., Hamill, I.S., Phillips, H.W., Jones, I.P. (2000). Mathematical modelling and experimental validation of flow in a cyclone. In L. Svarovsky, M. Thew, eds., *Proc 5th Intl. Conf. on cyclone technologies*, 175–186, BHR Group, Bedfordshire, UK.

Montazerin, N., Rahimzadeh, H., Marghzar, S. (2001). Prediction of critical condition at a horizontal intake through pressure contours. In *Proc. 14th IAHR Cong. on hydraulics*, 434–441, Beijing, China.

Moore, D.W., Saffman, P.G. (1973). Axial flow in laminar trailing vortices. *Proc. R. Soc. Lond. A* 333, 491–508.

Morissette, D. (2009). Characterization and prediction of free surface vortices at hydro power intakes. Master's thesis, McGill University, Montreal, Québec.

Mory, M., Yurchenko, N. (1993). Vortex generation by suction in a rotating tank. *Eur J Mech B Fluid* 12(6), 729–747.

Muntean, S., Ruprecht, A., Susan-Resiga, R. (2005a). A numerical investigation of the 3d swirling flow in a pipe with constant diameter Part 1: inviscid computation. In *Proc. 3d Workshop on Vortex Dominated Flows*, Timisoara, Romania.

Muntean, S., Ruprecht, A., Susan-Resiga, R. (2005b). A numerical investigation of the 3d swirling flow in a pipe with constant diameter Part 1: turbulent computation. In *Proc. 3d Workshop on Vortex Dominated Flows*, Timisoara, Romania.

Nahas, A., Calvo, A., Piva, M. (2010). Swirling flow in a fixed container: Generation and attenuation of a vortex column. *J. Fluid Eng.-T. ASME* 132, 111204/1–9.

Nakayama, A., Hisasue, N. (2007). Large eddy simulation of vortex flow in intake channel of hydropower facility. In *Proc 32nd Conf. of the IAHR*, Venice, Italy.

Nakayama, A., Hisasue, N. (2010). Large eddy simulation of vortex flow in intake channel of hydropower facility. *J. Hydraul. Res.* 48(4), 415–427.

Nakayama, A., Jones, J. (1998). Correlation for formation of inlet vortex. *AIAA J.* 37(4), 508–510.

Nakayama, A., Matsumura, R., Hisasue, N. (2006). Large-eddy simulation of turbulent open-channel flow with free-surface fluctuations. In *Proc 7th intl conf on hydroscience and engineering*, Philadelphia, US.

Nakayama, Y., Boucher, R.F. (2000). *Introduction to Fluid mechanics*. Elsevier, Oxford, UK.

Nolan, D.S. (2001). The stabilizing effects of axial stretching on turbulent vortex dynamics. *Phys. Fluids* 13(6), 1724–1738.

Odgaard, A.J. (1986). Free-surface air core vortex. *J. Hydraul. Eng.-ASCE* 112(7), 610–620.

Padmanabhan, M., Hecker, G.E. (1984). Scale effects in pump sump models. *J. Hydraul. Eng.-ASCE* 110(HY11), 1540–1556.

Palau, G., Weitbrecht, V., Stösser, T., Bleninger, T., Hofmann, B., Maier, M., Roth, K. (2007). Numerical simulations to predict the hydrodynamics and the related mixing processes in water storage tanks. In *Proc. 32nd Conf. of the IAHR*, Venice, Italy.

Papillon, B., Sabourin, M. (2000). Atmospheric air admission in hydroturbines. In *Proc. Hydrovision 2000*, Charlotte, N.C.

Pavelyev, A., Shtarev, A. (2005). Effect of sinkhole position symmetry on the formation of nonstationary vortex funnels. *Fluid Dynamics* 40(5), 829–834.

Pennino, B.J., Hecker, G.E. (1979). A synthesis of model data for pumped storage intakes. In *Pump turbine schemes, Joint ASME-CSME Appl. Mech., Fluids Eng. and Bioeng. Conf.*, 103–112, Niagara Falls, NY.

Petit, O., Bosioc, A.I., Nilsson, H., Muntean, S., Susan-Resiga, R.F. (2010). A swirl generator case study for OpenFOAM. *IOP C. Ser. Earth Env.* 12(1), 012056/1–8.

Petitjeans, P. (2003). Stretching of a vortical structure: filaments of vorticity. *Europhysics News* 34(1), 20–23.

Petitjeans, P., Robres, J.H., Wesfreid, J.E., Kevlahan, N. (1998). Experimental evidence for a new type of stretched vortex. *Eur. J. Mech. B Fluid* 17(4), 549–560.

Pope, S. (1975). More general effective-viscosity hypothesis. *J. Fluid Mech.* 72(pt 2), 331–340, cited By (since 1996)223.

Pope, S. (2000). *Turbulent flows*. Cambridge University Press, Cambridge, UK.

Pope, S. (2004). Ten questions concerning the large-eddy simulation of turbulent flows. *New J. Phys.* 6.

Quick, M.C. (1962a). Scale relationships between geometrically similar free spiral vortices, Pt. 1. *Civ. Eng. Public Works Rev.* 57, 1135–1138.

Quick, M.C. (1970). Efficiency of air-entraining vortex formation at water intake. *J. Hydraul. Eng.-ASCE* 96(HY7), 1403–1416.

Quick, M. (1962b). Scale relationships between geometrically similar free spiral vortices, Pt. 2. *Civ. Eng. Public Works Rev.* 57, 1319–1320.

Rajendran, V.P., Constantinescu, S.G., Patel, V.C. (1999). Experimental validation of a numerical model of flow in pump-intakes bays. *J. Hydraul. Eng.-ASCE* 125(11), 1119–1125.

Rajendran, V.P., Patel, V.C. (2000). Measurement of vortices in model pump-intake bay by PIV. *J. Hydraul. Eng.-ASCE* 126(5), 322–334.

Rankine, W.J.M. (1876). *A Manual of applied mechanics.* C. Griffin & Co., London, 9th edition.

Rao, S., Diwanji, V., Srivastava, Y. (1997). Discussion of Critical submergence for intakes in open channel flow. *J. Hydraul. Eng.-ASCE* 123(6), 588–589.

Reddy, Y.R., Pickford, J.A. (1972). Vortices at intakes in conventional sumps. *Water Power* March, 108–109.

Reynolds, W. (1976). Commputation of turbulent flows. *Annu. Rev. Fluid Mech.* 8, 1976.

Rindels, A.J., Gulliver, J.S. (1983). An experimental study of critical submergence to avoid free-surface vortices at vertical intakes. Technical report, St. Anthony Falls Hydraulic Laboratory, Univ. of Minnesota, Minneapolis, US.

Rodi, W. (1993). *Turbulence models and their application in hydraulics*. IAHR Monograph series, A.A. Balkema, Rotterdam, NL.

Rossi, M., Bottausci, F., Maurel, A., Petitjeans, P. (2004). A nonuniformly stretched vortex. *Phys. Rev. Lett.* 92(5), 054504/1–4.

Roth, A., Hager, W. (1999). Underflow of standard sluice gate. *Exp. in Fluids* 27, 339–350.

Rott, N. (1958). On the viscous core of a line vortex. *Z. Angew. Math. Phys.* 9b, 543–553.

Rouse, H. (1963). On the role of eddies in fluid motion. *Am. Sci.* 51(3), 285–314.

Rusello, P.J., Lohrmann, A., Siegal, E., Maddux, T. (2006). Improvements in acoustic doppler velocimetry. In *Proc. 7th Intl. Conf. Hydrosc. Eng.*, Philadelphia, US.

Rutschmann, P., Volkart, P., Vischer, D. (1987). Design recommendations – intake structures. In J. Knauss, ed., *Swirling flow problems at intakes*, 91–100, A.A. Balkema, Rotterdam, NL.

Saffman, P.S. (1992). *Vortex Dynamics*. Cambridge University Press, Cambridge, UK.

Sakai, T., Eguchi, Y., Monji, H., Ito, K., Ohshima, H. (2008). Proposal of design criteria for gas entrainment from vortex dimples based on a computational fluid dynamics method. *Heat Transfer Eng* 29(8), 731 – 739.

Sbalzarini, I.F., Koumoutsakos, P. (2005). Feature point tracking and trajectory analysis for video imaging in cell biology. *J. Struct. Biology* 151, 182–195.

Schäfer, F., Hellman, D.H. (2005). Optimization of approach flow conditions of vertical pumping systems by physical model investigation. In *Proc of ASME FEDSM2005*, Houston, US.

Shapiro, A.H. (1962). Bath-tub vortex. *Nature* 196(4859), 1080–1081.

Skerlavaj, A., Lipej, A., Ravnik, J., Skerget, L. (2010). Turbulence model comparison for a surface vortex simulation. *IOP Conf. Ser. Earth Env.* 12.

Spalart, P.R. (1998). Airplane trailing vortices. *Annu. Rev. Fluid Mech.* 30, 107–138.

Squire, H.B. (1965). The growth of a vortex in turbulent flow. *Aeronaut. Quart.* 16(Pt.3), 302–306.

Stepanyants, Y., Yeoh, G. (2008a). Burgers-Rott vortices with surface tension. *Z. Angew. Math. Phys.* 59, 1057–1068.

Stepanyants, Y., Yeoh, G. (2008b). Stationary bathtub vortices and a critical regime of liquid discharge. *J. Fluid Mech.* 604, 77–98.

Strutt, J. (1917). On the dynamics of revolving fluids. *Proc. R. Soc. Lond. A* 93(648), 148–154.

Suerich-Gulick, F., Gaskin, S.J., Braune, A., Parkinson, E., Villeneuve, M. (2005). Free surface simulation of hydraulic turbine intakes. In *23rd CADFEM Users' Meeting*, Bonn, DE.

Suerich-Gulick, F., Gaskin, S.J., Parkinson, E., Villeneuve, M. (2007a). Numerical simulation of a free surface vortex formed in the wake of a pier at a hydropower intake. In *Proceedings of the 32nd Conference of the IAHR*, Venice, Italy.

Suerich-Gulick, F., Gaskin, S.J., Parkinson, É., Villeneuve, M. (2013a). Computational fluid dynamics modelling strategies for predicting free surface vortices at hydropower intakes. *Manuscript in preparation to submit for journal publication* .

Suerich-Gulick, F., Gaskin, S.J., Parkinson, E., Villeneuve, M., Holder, G. (2006). Experimental and numerical analysis of free surface vortices at a hydropower intake. In *Proceedings of the 7th International Conference on Hydroscience and Engineering*, Philadelphia, US.

Suerich-Gulick, F., Gaskin, S.J., Villeneuve, M. (2007b). Impact of geometry on free surface vortices in a scale model of a hydropower intake. In *Proceedings of the 5th Hydraulic Measurement and Experimental Methods Conference*, Lake Placid, NY.

Suerich-Gulick, F., Gaskin, S.J., Villeneuve, M., Parkinson, É. (2013b). Assessing the characteristics of free surface vortices at low-head hydropower intakes. *Manuscript submitted to the Journal of Hydraulic Engineering of the ASCE* .

Suerich-Gulick, F., Gaskin, S.J., Villeneuve, M., Parkinson, É. (2013c). Free surface intake vortices: Scale effects due to surface tension and viscosity. *Manuscript submitted to the Journal of Hydraulic Research* .

Suerich-Gulick, F., Gaskin, S.J., Villeneuve, M., Parkinson, É. (2013d). Free surface intake vortices: Theoretical model and measurements. *Manuscript submitted to the Journal of Hydraulic Research* .

Sweeney, C.E., Elder, R.A., Hay, D. (1982). Pump sump design experience: Summary. *J. Hydraul. Div. ASCE* 108(HY3), 361–377.

Taghvaei, S.M., Roshan, R., Safavi, K., Sarkardeh, H. (2012). Anti-vortex structures at hydropower dams. *Int. J. Phys. Sci.* 7(28), 5069–5077.

Tang, X.L., Wang, F.J., Li, Y.J., Cong, G.H., Shi, X.Y., Wu, Y.L., Qi, L.Y. (2011). Numerical investigations of vortex flows and vortex suppression schemes in a large pumping-station sump. *P I Mech Eng C-J Mec* 225(6), 1459–1480.

Tastan, K., Yıldırım, N. (2010). Effects of dimensionless parameters on air-entraining vortices. *J. Hydraul. Res.* 48(1), 57–64.

Teklemariam, E., Korbaylo, B., Groeneveld, J., Fuchs, D. (2002). Computational fluid dynamics: diverse applications in hydropower project's design and analysis. In *CWRA 55th annual conf*, Winnipeg, AB.

Tennekes, H., Lumley, J.L. (1972). *A first course in turbulence*. MIT Press, Cambridge, US.

Thomson, W.T. (1869). On vortex motion. *Trans. Roy. Soc. Edinb.* 25, 217–260.

Thomson, W.T. (1880). On the vibrations of a columnar vortex. *Phil. Mag. S. 5* 10, 155–168.

Tokyay, T., Constantinescu, S.G. (2006). Validation of a large-eddy simulation model to simulate flow in pump intakes of realistic geometry. *J. Hydraul. Eng.-ASCE* 132(12), 1303–1315.

Tokyay, T., Constantinescu, S. (2005a). Coherent structures in pump-intake flows: a large-eddy simulation (LES) study. In *31st IAHR cong*, Seoul, South-Korea.

Tokyay, T., Constantinescu, S. (2005b). Large Eddy Simulation and Reynolds Averaged Navier Stokes simulations of flow in a realistic pump intake: a validation study. In *World water and environmental resources cong*, Alaska.

Toyokura, T., Akaike, S. (1970). Vortex phenomenon in a water tank. *Bulletin of the JSME* 13(57), 373–381.

Travis, Q.B., Mays, L.W. (2011). Prediction of intake vortex risk by nearest neighbors modeling. *J. Hydraul. Eng.-ASCE* 137(6), 701–705.

Trefethen, L.M., Bilger, R.W., Fink, P.T., Luxton, R.E., Tanner, R.I. (1965). The bath-tub vortex in the southern hemisphere. *Nature* 207(5001), 1084–1085.

Trivellato, F. (2010). Anti-vortex devices: Laser measurements of the flow and functioning. *Opt. Laser Eng.* 48, 589–599.

Vatistas, G.H. (1989). Analysis of fine particle concentrations in a combined vortex. *J. Hydraul. Res.* 27(3), 417–427.

Vatistas, G.H., Li, P.M. (1988). A similar profile for the tangential velocity in vortex chambers. *Exp. in Fluids* 6, 135–137.

Vergaftik, N., Volkov, B., Voljak, L. (1983). International tables of the surface tension of water. *J. Phys. Chem. Ref. Data (USA)* 12(3), 817 – 20.

Villeneuve, M., Suerich-Gulick, F., Gaskin, S.J., Parkinson, E., Grunder, R. (2005). Optimization of intake flow conditions for compact axial turbines. In *Hydro 2005*, Villach, AT.

Vladimirov, V., Lugovtsov, B., Tarasov, V. (1980). Suppression of turbulence in the cores of concentrated vortices. *J. Appl. Mech. Tech. Phy.* 21, 632–637.

Škerlavaj, A., Škerget, L., Ravnik, J., Lipej, A. (2011). Choice of a turbulence model for pump intakes. *P I Mech. Eng. A-J. Pow.* 225, 764–778.

Walder, S., Rutschmann, P. (2007). Hybrid modeling of an intake for hydraulic optimization. In *Proc. 32nd IAHR Congress*, Venice,Italy.

Wang, Y., Jiang, C., Liang, D. (2011). Comparison between empirical formulae of intake vortices. *J. Hydraul. Res.* 49(1), 113–116.

Wang, Y.K., Jiang, C.B., Liang, D.F. (2010). Investigation of air-core vortex at hydraulic intakes. *Journal of Hydrodynamics, Ser. B* 22(5, Supplement 1), 696 – 701.

Warsi, Z.U.A. (2006). *Fluid dynamics : theoretical and computational approaches*. Taylor & Francis, London,UK.

White, A. (1964). Flow of a fluid in an axially rotating pipe. *J. Mech. Eng. Sc.* 6(1), 47–52.

Wilcox, D.C. (2006). *Turbulence Modeling for CFD*. DCW Industries, La Canada, US.

Yıldırım, N. (2004). Critical submergence for a rectangular intake. *J. Eng. Mech.-ASCE* 130(10), 1195–1210.

Yıldırım, N., Akay, H., Taştan, K. (2011). Critical submergence for multiple pipe intakes by the potential flow solution. *J. Hydraul. Res.* 49(1), 117–121.

Yıldırım, N., Eyüpoğlu, S., Taştan, K. (2012). Critical submergence for dual rectangular intakes. *J. Energ. Eng.-ASCE* 138(4), 237–245.

Yıldırım, N., Jain, S. (1981). Surface tension effect on profile of a free vortex. *J. Hydraul. Div. ASCE* 107(HY1), 132–136.

Yıldırım, N., Kocabaş, F. (1995). Critical submergence for intakes in open channel flow. *J. Hydr. Eng.* 121(12), 900–905.

Yıldırım, N., Kocabaş, F. (1998). Critical submergence for intakes in still-water reservoir. *J Hydraul. Eng.-ASCE* 124(1), 103 – 104.

Yıldırım, N., Kocabaş, F. (2000). Prediction of critical submergence for an intake pipe. *J. Hydraul. Res.* 40(4), 507–518.

Yıldırım, N., Kocabaş, F., Gülcan, S. (2000). Flow-boundary effects on critical submergence of intake pipe. *J. Hydraul. Eng.-ASCE* 126(4), 288–297.

Yoo, S., Hong, K., Hwang, M. (2002). A 3-dimensional numerical study of flow patterns around a multipurpose dam. In *Proc. 5th Intl. Conf. Hydroinformatics*, IWA Publishing, Cardiff, UK.

Zeman, O. (1995). The persistence of trailing vortices: a modeling study. *Phys. Fluids* 7(1), 135–143.

Zhan, J.M., Wang, B.C., Yu, L.H., Li, Y.S., Tang, L. (2012). Numerical investigation of flow patterns in different pump intake systems. *Journal of Hydrodynamics, Ser. B* 24(6), 873 – 882.

Zhang, Q.C., Su, X.Y. (2002). An optical measurement of vortex shape at a free surface. *Optics & Laser Techn.* 34, 107–113.

Zielinksi, P.B., Villemonte, J.R. (1968). Effect of viscosity on vortex-orifice flow. *J. Hydraul. Div. ASCE* 94(HY3), 745–752.

Zwart, P., Burns, A.D., Galpin, P.F. (2007). Coupled algebraic multigrid for free surface flow simulations. In *Proc. of OMAE2007*, OMAE2007–29080, San Diego, California.